Thèse de doctorat

pour l'obtention du titre de

DOCTEUR EN SCIENCES PHYSIQUE

délivré par

Cergy Paris Université

École doctorale n° 405 : Économie, Management, Mathématiques, Physique et Sciences Informatiques (EM2PSI)

CNRS UMR 8089

Exact Reduction of Multiscale Neural Dynamics

présentée et soutenue publiquement par

Marco Segneri

le 01 10 2020

Directeur de thèse : Monsieur Alessandro Torcini

Jury

M.	B. Gutkin	École Normale Supérieure	Rapporteur
M.	A. Destexhe	Institut de Neurosciences Paris-Saclay	Rapporteur
M.	G. Mongillo	CR-CNRS	Examinateur
M.	E. Montbrió	Universitat Pompeu Fabra	Examinateur
M.	M. Quoy	CY Cergy-Paris Université	Examinateur
M.	A. Torcini	CY Cergy-Paris Université	Examinateur

Contents

Introduction **iii**

1 Exact reduction methods for phase oscillators networks **5**
1.1 Introduction 5
1.2 Phase oscillators and Kuramoto model 7
1.3 Exact mean-field description 14
1.3.1 Watanabe-Strogatz reduction 15
1.3.2 Ott-Antonsen reduction 20
1.3.3 Comments and Limitations 24

2 QIF model and Firing Rate Equations **27**
2.1 Introduction 27
2.2 Type I and II neurons 28
2.3 Quadratic Integrate-and-Fire model 31
2.3.0.1 Tonic neuron: $\eta > 0$ 36
2.3.0.2 Excitable neuron: $\eta \leq 0$ 38
2.4 Population model of fully-coupled QIF neurons 41
2.5 Exact macroscopic reduced model for fully-coupled Network . 45
2.5.1 Heterogeneous synaptic weights 54
2.6 Validity of the Lorentzian ansatz 55

3 Theta-nested gamma oscillations in next generation neural mass models **57**
3.1 Introduction 58
3.2 Models and Bifurcation analysis 61
3.2.1 Network Models 61
3.2.2 Neural mass models 64
3.3 Dynamics in the absence of forcing 68

3.3.1 PING set-up . . . 68
3.3.2 ING set-up . . . 70
3.4 Dynamics under θ-forcing . . . 73
3.4.1 Wavelet Analysis . . . 75
3.4.2 Phase-Amplitude Locked and Unlocked States . . . 76
3.4.3 Comparison with Experimental Findings . . . 80
3.5 Discussion and Conclusions . . . 88

4 Coexistence of fast and slow gamma oscillations in one population of inhibitory spiking neurons 93
4.1 Introduction . . . 94
4.2 Methods . . . 98
4.2.1 The network model . . . 98
4.2.2 Simulation Protocols . . . 99
4.2.3 Indicators . . . 100
4.3 Effective Mean-Field model for a sparse QIF network . . . 101
4.3.1 Linear stability of the asynchronous state . . . 104
4.3.2 Phase Diagrams of the Mean-Field Model . . . 105
4.4 Network dynamics . . . 108
4.4.1 High structural heterogeneity . . . 108
4.4.2 Low structural heterogeneity . . . 112
4.5 Coexistence of slow and fast gamma oscillations . . . 115
4.5.1 Switching gamma rhythms . . . 116
4.5.2 Theta-gamma cross-frequency coupling . . . 120
4.6 Conclusions . . . 127

5 Emergence of collective oscillations in balanced neural networks due to intrinsic fluctuations 133
5.1 Introduction . . . 134
5.2 Methods . . . 135
5.2.1 The network model . . . 135
5.2.2 Simulation Protocols . . . 136
5.2.3 Indicators . . . 136
5.3 Mean-Field Approaches . . . 137
5.3.1 Fokker-Planck Approach . . . 138
5.3.2 Ott-Antonsen Ansatz . . . 140
5.3.3 Circular Cumulants' Approximation . . . 141
5.4 Homogeneous Case . . . 143

5.4.1 Asynchronous State 143
5.4.2 Linear Stability of the Asynchronous State 147
5.4.3 Bifurcation to Collective Oscillations 151
5.5 Heterogeneous case 155
5.5.1 Circular two cumulants' approach 155
5.6 Conclusions 158

Summary and perspectives **161**

A PING set-up: sub-critical Hopf **167**

B Different PING set-ups **169**

C Slow and fast gamma oscillations in Erdös-Renyi network **171**

D A general mechanism for the emergence of coexisting oscillations **173**

Bibliography **177**

Introduction

The science of complexity represents a new and extremely interdisciplinary field of research. Complex systems are systems composed of many interacting elements, whose collective behavior does not turns out to be the simple sum of all individual behaviors [1]. In the beginning the concept of complex systems has been associated with the temporal evolution of systems composed of units with highly nonlinear dynamics. In the last decade, the interest of researchers has shifted towards an even more intriguing topic: the emergence of not trivial collective dynamics in networks composed of elements whose evolution is extremely simple, such as periodic oscillators. In fact, the interaction of these oscillators can give rise to macroscopic dynamics ranging from periodic to quasi-periodic motions and included chaotic motions [2–5]. A relevant goal for applied mathematics, nonlinear dynamics and statistical mechanics is the understanding of the mechanisms that lead to the emergence of these collective behaviors in complex networks made up of simple units. It goes without saying that network organization of the brain is complex at almost every scale, from small neuronal circuits to large scale networks, where the single neurons represent the fundamental units.
In this thesis we will focus on the dynamics of complex neuronal networks, where each individual oscillator is schematized as a phase oscillator, in particular we will focus on the so-called Quadratic Integrate-and-Fire (QIF) model. In the last few years, the analysis of complex neural networks has been mainly addressed through numerical simulations with limitations imposed by computing resources, on the maximum number of neurons to consider in the network. The QIF model is widely used in neuroscience due to its simplicity, but at the same time it is able to capture the essential elements of neuronal dynamics. Furthermore, being very fast to integrate numerically, it is particularly suitable for large-scale network simulations. As we will see in Chapter 2, the QIF model represents the normal form of type I neurons [6].

Alternatively, *effective* mean field theories for neural dynamics at the population level have been formulated: the so-called *neural mass models* [7]. Neural mass models reproduce the mean dynamics of neural network in terms of macroscopic variables, for example the average activity rate of the population (the so-called average firing rate) or the average value of neuronal membrane potentials, and the equations that bind these quantities are generally derived in a phenomenological way [8, 9]. The work of this thesis is inspired by a new generation of neural mass models, developed in a recent article of E. Montbrió *et al.* [10], where the mean field equations are derived *exactly* starting from the microscopic ones for the neural population composed of QIF neurons . This innovative approach is based on recent results of statistical physics, which have shown the possibility of deriving exact macroscopic models for coupled phase oscillator networks [11, 12]. Mean field models are particularly suitable for large-scale simulations, as well as when one is interested in collective behaviors emerging from the interactions of multiple units. The reduction of a large-dimensional network dynamics to a low-dimensional mean field model, in addition to speeding up simulation times enormously, highlights macroscopic mechanisms that are difficult to foresee by the corresponding network model. However, the exact reduction derived in [10] is only valid for fully coupled networks.

In Chapter 3 of this thesis we present an application of this reduced model based on PING and ING fully coupled network configurations with the aim of reproducing the experimental data reported in [13].

To analyze the effects on the dynamics of a sparse network, in [14] an exact mean field model for sparse networks was also derived but the randomness in the couplings is only taken into account as a noise quenched terms, and it does not take into account fluctuations induced by the sparseness (endogenous noise). In Chapter 4 we use the same approach in order to analyze the dynamics of a single balanced sparse inhibitory network with a finite synaptic decay.

Since intrinsic fluctuations are necessary to give rise to the transition from asynchronous state to collective oscillations [14], in Chapter 5 of this thesis, following Brunel and Hakim's approach developed for the IF model [15], we performe a Fokker-Planck formulation of the system analyzed in [14] to take into account such intrinsic fluctuations. The limitation of this formulation consists in being high dimensional and therefore, always in Chapter 5, we try to develop a low dimensional theory that takes into account the intrinsic fluctuations following the recent results of D. Goldobin *et al.* on cumulants

approximation [16, 17].
In more detail the thesis is structured as follows. In the first chapter we introduce the concept of phase oscillator and provide a detailed analysis of the Kuramoto model [18]. We then show how it is possible to exactly reduce a system of N phase oscillators to a macroscopic system of low dimension. In this context two exact mean-field approaches have been developed. The first approach, developed in 1993 by Watanabe and Strogatz [19], is devoted to identical oscillators; while the second one, introduced in 2008 by Ott and Antonsen [11], describes the macroscopic dynamics of non-identical oscillators.
In the second chapter we introduce the single QIF neuron model by providing a detailed study of its dynamics. We then define the network model of fully coupled QIF neurons showing how to move from the microscopic description of a population of QIF neurons with instantaneous synapses, corresponding to a system of N degrees of freedom, to the exact neural mass model with only two degrees of freedom, that is in terms of the average firing rate and the average membrane potential of the network [10].
In the third chapter we examine two set-ups able to support collective gamma oscillations: the pyramidal interneuronal network gamma (PING) and the interneuronal network gamma (ING). In both set-ups we observe the emergence of theta-nested gamma oscillations by driving the system with a sinusoidal theta-forcing in proximity of a Hopf bifurcation. From our analysis it emerges that the locked states are more frequent in the ING set-up. In agreement with the experiments, we find theta-nested gamma oscillations for forcing frequencies in the range [1:10] Hz, whose amplitudes grow proportionally to the forcing one and which are clearly modulated by the theta phase. At variance with experimental findings, the gamma-power peak does not shift to higher frequencies by increasing the theta frequency. This effect can be obtained, in our model, only by incrementing, at the same time, also the noise or the forcing amplitude. This chapter contains our recent work published in Frontiers in Computational Neuroscience [20].
In the fourth chapter we study balanced sparse inhibitory networks of QIF neurons characterized by a finite synaptic time scale. As the main result, we show theoretically and numerically that a single inhibitory population can give rise to the coexistence of slow and fast gamma rhythms corresponding to collective oscillations of a balanced spiking network [21–23]. The slow and fast gamma rhythms are generated via two different mechanisms: the fast one being driven by the coordinated tonic neural firing and the slow one

by endogenous fluctuations due to irregular neural activity. We show that almost instantaneous stimulations can switch the collective gamma oscillations from slow to fast and vice versa. This chapter contains our recent paper published in Physical Review Research [24].
In the fifth chapter we consider a sparse balanced inhibitory network of QIF neurons with instantaneous synapses proving the transition from the asynchronous state to collective oscillations for large enough average connectivity by solving the associated Fokker-Planck equation. This result is in good agreement with network simulations. Moreover we try to extend the OA theory for sparse network by considering the Circular Cumulant approximation (CCs) [16]. In particular we consider CCs until the second cumulant, providing a four-dimensional system for the first and second cumulant. This low dimensional system is able to capture the transition from asynchronous state to collective oscillations, however the discrepancy with the network simulations suggests to consider major order of cumulants. This chapter contains our last paper in preparation.

Publications of the candidate based on his PhD activity

1.**Theta-nested gamma oscillations in next generation neural mass models**: Segneri M., Bi H., Olmi S. & Torcini A. (2020). Frontiers in Computational Neuroscience, 14:47.

2.**Coexistence of fast and slow gamma oscillations in one population of inhibitory spiking neurons**: Bi, H., Segneri, M., di Volo, M. & Torcini, A. (2020). Physical Review Research, 2(1), 013042.

3.**Emergence of collective oscillations in balanced neural networks due to intrinsic fluctuations**: M. di Volo, M. Segneri, D. Goldobin, A. Politi, & A. Torcini, in preparation (2020).

Chapter 1

Exact reduction methods for phase oscillators networks

Summary:

In this chapter we introduce the concept of phase oscillator and provide a detailed analysis of the Kuramoto model [18]. We then show how it is possible to exactly reduce a system of N phase oscillators to a macroscopic system of low dimension. In this context two exact mean-field approaches have been developed. The first approach, developed in 1993 by Watanabe and Strogatz [19], is devoted to identical oscillators; while the second one, introduced in 2008 by Ott and Antonsen [11], describes the macroscopic dynamics of non-identical oscillators.

1.1 Introduction

Many systems in neuroscience and biology are organised on different levels by interacting processes [25]. Networks of coupled oscillators provide models for such systems. Each node in the network is an oscillator (a dynamical process) and the network structure encodes which oscillators interact with each other [26]. In neuroscience, individual oscillators could be single neurons in microcircuits or neural masses on a more macroscopic level [27]. Other prominent examples in biology include cells in heart tissue [28], flashing fireflies [29], gait patterns of animals [30] or humans [31], cells in the suprachiasmatic nucleus in the brain generating the master clock for the

circadian rhythm [32–34], hormone rhythms [35], suspensions of yeast cells undergoing metabolic oscillations [36,37], and life cycles of phytoplankton in chemostats [38].

The function - or dysfunction - of these networks depends on the *collective dynamics* of the interacting oscillatory nodes. Hence, one major challenge is to understand how the underlying network shapes these collective dynamics. In particular, one would like to understand how the interplay of network properties (for example, connectivity and strength of interactions) and properties of the individual nodes shape the emergent dynamics. The question of relating network structure and dynamics is particularly pertinent in the study of large-scale brain dynamics, for example one can investigate how emergent functional connectivity (a dynamical property) arises from specific structural connectomes [39,40], and how each of these relates to cognition or disease. Progress in this direction not only aims to identify how healthy or pathological dynamics is linked to the network structure, but also to develop new treatment approaches [41–43].

One of the most prominent collective behaviors of an oscillator network occurs when nodes synchronize and oscillate in unison [44–46]; indeed, most of the examples given above display synchrony in some form which appears to be essential to the proper functioning of biological life processes. Here we think of synchrony in a general way: it can come in many varieties, including *phase synchrony* where the state of different oscillators align exactly, or *frequency synchrony* where the oscillators' frequencies coincide. Synchrony may be *global* across the entire network or *localized* in a particular part - the rest of the network being nonsynchronized - thus giving rise to *synchrony patterns*. How exactly the dynamics of synchrony patterns in an oscillator network relate to its functional properties is still not fully understood. In the brain, there is a wide range of rhythms but the presence of dominant rhythms in different frequency bands indicate that some level of synchrony is common at multiple scales [47,48]. Indeed, synchrony has been associated with solving functional tasks including memory [49], computational functions [50], cognition [51], attention [52,53], control of gait and motion [54], or breathing [55,56] . At the same time, abnormal synchrony patterns are associated with malfunction in disorders such as epilepsy and Parkinson's disease [57–59].

Using a detailed model of each node and a large number of nodes in the network, relating network structure and dynamics is a daunting task. Hence simplifying analytical reduction methods are needed that, rather than be-

ing purely computational, yield a mechanistic understanding of the inherent processes leading to a certain dynamic macroscopic behavior. If many biologically relevant state variables are considered in a microscopic model, each node is represented by a large dynamical system by itself. Hence, a common approach is to simplify the description of each oscillatory node to its simplest form, a *phase oscillator*; in the reduced system the state of each oscillator is given by a single periodic phase variable that captures the state of the periodic process. In this case, the complex biological process determining intrinsic dynamics are captured by the evolution of the phase variable and its interaction with the phases of the other nodes.
The main topic of this chapter is a review of recent advances that allow a reduction in the complexity of the problem: under certain assumptions, it is possible to replace a large number of nodes by a *collective* or *mean-field variable*. We focus here on phase oscillator networks that are organized into populations because of their practical importance. The mean-field reductions we present allow one to replace a network by a (low-dimensional) set of collective variables to obtain a set of dynamical equations for these variables. This set of mean-field equations describes the system exactly. Reducing to a set of mean-field equations provides a simplified - but often still sufficiently complex - description of the network dynamics that can be analyzed by using dynamical systems techniques [60]. Compared to heuristic macroscopic models, the reduced equations capture microscopic properties of individual oscillators; because of this property these reduced equations have been referred to as being *next-generation models* [61].
This chapter is organized as follows. Section (1.2) sets the stage by introducing the notion of a sinusoidally coupled network and showing the main results concerning the Kuramoto model. In Section (1.3), we give a general theory for the mean-field reductions and discuss their limitations: the methods include the Watanabe-Strogatz reduction for finite or infinite networks of identical oscillators and the Ott-Antonsen reduction for the continuum limit of nonidentical oscillators.

1.2 Phase oscillators and Kuramoto model

We consider phase oscillator networks where the state of each node is given by a single phase variable. More specifically, consider a population of N oscillators where the state of oscillator (i) is given by a phase $\theta_i \in \mathbb{T}$, where $\mathbb{T}$

indicates circle of all phases $[0, 2\pi)$. Without input, the phase of each oscillator (i) advances at its intrinsic frequency $\omega_i \in \mathbb{R}$. The input to oscillator (i) is determined by a field $\mathbb{H}_i(t) \in \mathbb{C}$ which is modulated by a sinusoidal function; this field could be due to an external driving or to network interactions between oscillators both within the same population or other populations.
In other words, we consider oscillator networks whose phases evolve according to

$$\dot{\theta}_i = \omega_i + Im\Big(\mathbb{H}_i(t)e^{-i\theta_i}\Big) \tag{1.1}$$

Since the effect of the field is mediated by a function with exactly one harmonic, we call the oscillator populations *sinusoidally coupled*.
While we allow the intrinsic frequency and the driving field to depend on the oscillator to a certain extent (i.e., they are nonidentical), we will henceforth also assume that all oscillators within any given population are *indistinguishable*: this means that the properties of each oscillator in a given population are determined by the same distribution. Specifically, suppose that the properties of each oscillator are determined by a parameter η_i - for example, the excitability in the case of a QIF neuron we will describe in the next chapter. Now let both the intrinsic frequencies and the field be functions of this parameter, that is, $\omega_i = \omega(\eta_i)$ and $\mathbb{H}_i(t) = \mathbb{H}(t; \eta_i)$. The oscillators of a given population are indistinguishable if all η_i are random variables sampled from a probability distribution with density $g(\eta)$. In the special case that all η_i are equal (in this case g is a delta-distribution) the oscillators are *identical*.
Phase oscillator networks of the form (1.1) include a range of well-known models, here we briefly review one of them relevant for the presentation of this thesis, named the *Kuramoto model* [18].
The Kuramoto model (hereafter called KM) consists of a population of N coupled phase oscillators, $\theta_i(t)$, having natural frequencies ω_i distributed with a given probability density $g(\omega)$, and whose dynamics is governed by:

$$\dot{\theta}_i = \omega_i + \sum_{j=1}^{N} K_{ij} sin(\theta_j - \theta_i), \qquad i = 1, ..., N. \tag{1.2}$$

Thus, each oscillator tries to run independently at its own frequency, while the coupling tends to synchronize it to all the others. Without loss of generality, we can consider $g(\omega)$ with zero mean, that is a system of phase oscillators

whose natural frequencies have zero mean. When the coupling is sufficiently weak, the oscillators run incoherently whereas beyond a certain threshold collective synchronization emerges spontaneously. Many different models for the coupling matrix K_{ij} have been considered such as nearest-neighbor coupling, hierarchical coupling, random long-range coupling, or even state dependent interactions [62].
The synchronization transition observable in model (1.2) was accomplished by Kuramoto in the case of *mean-field* coupling, that is taking $K_{ij} = K/N > 0$ in Eq.(1.2) [18, 63]. Such a form of network interaction is so called since the drive $\mathbb{H}(t)$ to a single oscillator is proportional to an average formed from the states of all oscillators in the network.
The model in Eq.(1.2) was then written in a more convenient form, defining the (complex-value) *order-parameter*[1]:

$$Z = re^{i\psi} = \frac{1}{N}\sum_{j=1}^{N} e^{i\theta_j}. \tag{1.3}$$

that is, the mean of all phases on the unit circle. Here $r(t)$ with $0 \leq r(t) \leq 1$ measures the coherence of the oscillator population. Its magnitude $r = |Z|$ describes the level of synchronization of the oscillator population, see Fig.(1.1): on the one hand, $r = 1$ if and only if all oscillators are phase synchronized, that is, $\theta_k = \theta_j$ for all k and j; on the other hand, we have $r = 0$ for example if the oscillators are evenly distributed around the circle. The argument ψ of the Kuramoto order parameter Z describes the "average phase" of all oscillators, that is, it describes the average position of the oscillator crowd on the circle of phases.
With this definition, Eq.(1.2) becomes:

$$\dot{\theta}_i = \omega_i + Krsin(\psi - \theta_i), \qquad i = 1, ..., N, \tag{1.4}$$

and it is clear that each oscillator is coupled to the common average phase $\psi(t)$ with coupling strength given by Kr. The order parameter (1.3) can be rewritten as:

[1]The order "parameter" Z is an observable which encodes the state of the system rather than a system parameter.

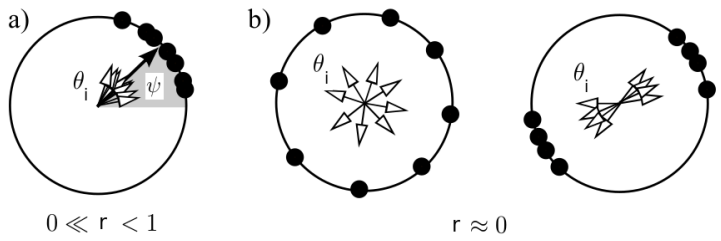

Figure 1.1: The Kuramoto order parameter (1.3) encodes the level of synchrony of a phase oscillator population. The state of each oscillator is given by a phase θ_i (black dot, empty arrow) on the circle $\mathbb{T}$. Panel (a) shows a configuration with high synchrony where $r = |Z| \approx 1$. Panel (b) shows two configurations with $r = |Z| \approx 0$: one where the oscillators are approximately uniformly distributed on the circle, the other one where they are organized into two clusters.

$$Z = re^{i\psi} = \int_{-\pi}^{+\pi} e^{i\theta} \Big(\frac{1}{N} \sum_{j=1}^{N} \delta(\theta - \theta_j) \Big) d\theta. \tag{1.5}$$

In the limit of infinitely many oscillators, they may be expected to be distributed with a probability density $\rho(\theta, \omega, t)$, so that the arithmetic mean in (1.3) becomes now an average over phase and frequency, namely:

$$Z = re^{i\psi} = \int_{-\pi}^{+\pi} \int_{-\infty}^{+\infty} e^{i\theta} \rho(\theta, \omega, t) g(\omega) d\theta d\omega. \tag{1.6}$$

This equation illustrates the use of the order parameter to measure oscillator synchronization. In fact, when $K \to 0$, Eq. (1.4) yields $\theta_i \approx \omega_i t + \theta_i(0)$, that is the oscillators rotate at angular frequencies given by their own natural frequencies. Consequently, setting $\theta \approx \omega t$ in Eq. (1.6), by the Riemann-Lebesgue lemma, we obtain that $r \to 0$ as $t \to \infty$ and the oscillators are not synchronized. On the other hand, in the limit of strong coupling, $K \to \infty$, the oscillators become synchronized to their average phase, $\theta_i \approx \psi$, and Eq. (1.6) implies $r \to 1$. For intermediate couplings, $K_c \leq K \leq \infty$, part of the oscillators are locked in phase ($\dot{\theta}_i = 0$), and part are rotating out of synchrony with the locked oscillators. This state of partial synchronization

yields $0 \leq r \leq 1$ and will be further explained below. Thus, synchronization in the mean-field KM (with $N = \infty$) is revealed by a nonzero value of the order parameter [64, 65].
The concept of order parameter as a measure of synchronization is less useful for models with short-range coupling. In these systems, other concepts are more appropriate to describe oscillator synchronization since more complex situations can happen [66, 67]. For instance, it could happen that a finite fraction of the oscillators have the same average frequency $\tilde{\omega}_i$, defined by:

$$\tilde{\omega}_i = \lim_{t\to\infty} \frac{1}{t} \int_0^t \dot{\theta}_i dt, \tag{1.7}$$

while the other oscillators may be out of synchrony or that the phases of a fraction of the oscillators can change at the same speed (and therefore partial synchronization occurs), while different oscillator groups have different speeds (and therefore their global order parameter is zero).
A continuity equation for the oscillator density can be found by noting that each oscillator in Eq.(1.2) moves with an angular or drift velocity $v_i = \omega_i + Krsin(\psi - \theta_i)$. Therefore, in the case of mean-field coupling, the one-oscillator density obeys the continuity equation:

$$\frac{\partial \rho}{\partial t} + \frac{\partial}{\partial \theta}\{[\omega + Kr\sin(\psi - \theta)]\rho\} = 0, \tag{1.8}$$

to be solved along with (1.6), with the normalization condition:

$$\int_{-\pi}^{+\pi} \rho(\theta, \omega, t) d\theta = 1, \tag{1.9}$$

and an appropriate initial condition. The system of equations (1.6) - (1.9) has the trivial stationary solution $\rho = 1/(2\pi)$, $r = 0$, corresponding to an angular distribution of oscillators having equal probability in the interval [-π, +π]. Then, the oscillators run incoherently, and hence the trivial solution is called the incoherent solution. Let us now try to find a simple solution corresponding to oscillator synchronization. In the strong coupling limit, we have global synchronization (phase locking), so that all oscillators have the same phase, $\theta_i = \psi = \omega_i t + \theta_i(0)$, which yields $r = 1$. For a finite coupling, it

may occur a smaller degree of synchronization with a stationary amplitude, i.e. $0 < r < 1$. How can be obtained this smaller value of r? A typical oscillator running with velocity $v = \omega - Krsin(\theta - \psi)$, will become stably locked at an angle such that $Krsin(\theta - \psi) = \omega$ and $-\pi/2 \leq (\theta - \psi) \leq \pi/2$. All such oscillators are locked in the natural laboratory frame of reference. Oscillators with frequencies $|\omega| > Kr$ cannot be locked. They run out of synchrony with the locked oscillators, and their stationary density obeys $v\rho = C$ (constant), according to Eq. (1.8). We have obtained a stationary state of partial synchronization, in which part of the oscillators are locked at a fixed phase while all others are rotating out of synchrony with them. The corresponding stationary density is therefore

$$\rho = \begin{cases} \delta(\theta - \psi - sin^{-1}(\frac{\omega}{Kr}))H(cos(\theta)) & |\omega| < Kr \\ \frac{C}{|\omega - Krsin(\theta - \psi)|} & elsewhere \end{cases} \tag{1.10}$$

Here $H(x) = 1$ if $x > 0$ and $H(x) = 0$ otherwise, that is $H(x)$ is the Heaviside unit step function. The normalization condition (1.9) for each frequency yields $C = \sqrt{\omega^2 - (Kr)^2}/(2\pi)$.
We can now evaluate the order parameter in the state of partial synchronization by using (1.6) and (1.10),

$$\begin{aligned} r &= \int_{-\pi/2}^{+\pi/2} \int_{|\omega|<Kr} e^{i(\theta-\psi)} \delta(\theta - \psi - sin^{-1}(\frac{\omega}{Kr})) g(\omega) d\theta d\omega \\ &+ \int_{-\pi}^{+\pi} \int_{|\omega|>Kr} e^{i(\theta-\psi)} \frac{C g(\omega)}{|\omega - Krsin(\theta - \psi)|} d\theta d\omega. \end{aligned} \tag{1.11}$$

Let us assume that $g(\omega) = g(-\omega)$. Then, the symmetry relation $\rho(\theta + \pi, -\omega) = \rho(\theta, \omega)$ implies that the second term in this equation is zero. The first term is simply:

$$\begin{aligned} r &= \int_{|\omega|<Kr} cos(sin^{-1}(\frac{\omega}{Kr})) g(\omega) d\omega \\ &= \int_{-\pi/2}^{+\pi/2} cos\theta g(Krsin\theta) Krcos\theta d\theta. \end{aligned} \tag{1.12}$$

that is,

$$r = Kr \int_{-\pi/2}^{+\pi/2} cos^2\theta g(Krsin\theta)d\theta. \tag{1.13}$$

This equation has always the trivial solution $r = 0$ corresponding to the regime of incoherence, $\rho = (2\pi)^{-1}$. However, it also has a second branch of solutions, corresponding to the partially synchronized phase (1.10), satisfying

$$1 = K \int_{-\pi/2}^{+\pi/2} cos^2\theta g(Krsin\theta)d\theta. \tag{1.14}$$

This branch bifurcates continuously from $r = 0$ at the value $K = K_c$ obtained by setting $r = 0$ in (1.14), which yields $K_c = 2/[\pi g(0)]$. Such a formula and the argument leading to it were first found by Kuramoto [18]. Considering, as an example, the Lorentzian frequency distribution:

$$g(\omega) = \frac{1}{\pi}\frac{\gamma}{\gamma^2 + \omega^2}. \tag{1.15}$$

In this case it is possible to estimate analytically the above integral (1.14). By assuming the distribution of the frequencies is Lorentzian, Kuramoto was able to find the folowing exact result [18]:

$$r = \sqrt{1 - \frac{K_c}{K}}. \tag{1.16}$$

for all $K > K_c = 2\gamma$. For a general frequency distribution $g(\omega)$, an expansion of the right-hand side of Eq. (1.13) in powers of Kr yields the scaling law

$$r \sim \sqrt{\frac{8(K - K_c)}{-K_c^3 g''(0)}}. \tag{1.17}$$

as $K \to K_c$.
According to (1.17), the partially synchronized phase bifurcates supercritically for $K > K_c$ if $g''(0) < 0$, and subcritically for $K < K_c$ if $g''(0) > 0$, see

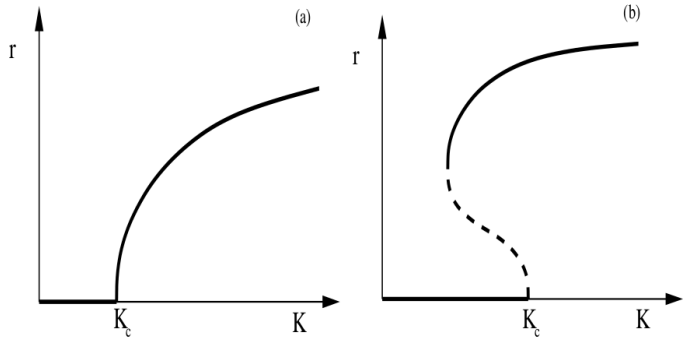

Figure 1.2: (a) Supercritical bifurcation in a diagram of r vs. K. (b) Subcritical bifurcation.

Figs.(1.2) (a) and (b). Notice that Kuramoto's calculation of the partially synchronized phase does not indicate whether this phase is stable, either globally or even locally.
The Kuramoto model (1.2) is an example of a sinusoidally coupled phase oscillator network.
Using Euler's identity $e^{i\phi} = cos(\phi) + isin(\phi)$, we have

$$\dot{\theta}_i = \omega_i + Im\Big(\frac{K}{N}\sum_{j=1}^{N} e^{i(\theta_j - \theta_i)}\Big) = \omega_i + Im\Big(KZ(t)e^{-i\theta_i}\Big)$$

where the Kuramoto order parameter $Z(t) = Z(\theta_1(t), ..., \theta_i(t))$, as defined in (1.3), depends on time through the phases. Hence, the Kuramoto model (1.2) is equivalent to (1.1) with $\mathbb{H}(t) = KZ(t)$ and the interactions between oscillators are solely determined by the Kuramoto order parameter $Z(t)$ time the coupling K. Note that the field $\mathbb{H}(t)$ is proportional to K having assumed that each oscillator is affected by a coupling equal to K/N independent of time.

1.3 Exact mean-field description

We now review how sinusoidally coupled phase oscillator networks (1.1) can be described in an exact way at a macroscopic level in terms of a *mean-field* description.

1.3.1 Watanabe-Strogatz reduction

Mean-field reductions are possible for both finite and infinite networks for populations of identical oscillators. These reductions are due to the high level of degeneracy in the system, i.e., there are many quantities that are conserved as time evolves. This degeneracy was first observed in the early 1990s for coupled *Josephson junctions*[2] arrays [68], which relate directly to Kuramoto's model of coupled phase oscillators [69].
Watanabe and Strogatz [70] show that the N Josephson junctions system has N-3 independent motion constants and there is a transformation of the variables that reduce the system to a low dimensional one. Here the phase $\theta_i(t)$ represents the quantum mechanical phase difference across the junction i, but the same reduction method can be applied to all oscillator systems that follow Eq. (1.1).
In this section we introduce a nonlinear transformation that explicitly reduces a fairly large class of N-dimensional oscillator systems ($N > 3$) to three-dimensional ones.
The general model is composed by N oscillators whose dynamics is governed by a system of differential equations of the same dimension

$$\dot{\theta}_j = f + gcos\theta_j + hsin\theta_j, \qquad j = 1, ..., N, \tag{1.18}$$

where we will find a transformation that will reduce it to a 3-dimensional system. Regarding the variables: θ_j is the phase of the j-th oscillator and f, g, h are functions of the phases of all the oscillators in the system $\theta_1, \theta_2, ..., \theta_N$, but they do not depend on the j-th index. The situation is similar to that of the mean field models except that here they are not necessarily an average of the state variables but on the contrary they are more general functions.
The phase space of (1.18) is N-dimensional, however we are going to demonstrate that each path is going to be contained in a 3-dimensional space. For this we consider the following change of variables

$$tan\Big(\frac{\theta_j(t) - \Theta(t)}{2}\Big) = \sqrt{\frac{1+\gamma(t)}{1-\gamma(t)}} tan\Big(\frac{\psi_j - \Psi(t)}{2}\Big), \tag{1.19}$$

[2]Josephson junctions are superconducting electrical devices that can generate potential difference of high frequency, typically 10^{10}-10^{11} cycles per second.

where ψ_j are known as the constants of motion and $0 \leq \gamma < 1$. The first fact that we have to highlight is that with this transformation a solution $\theta_j(t)$ of the system (1.18) has the form of (1.19) and therefore can be generated from a set of parameters ψ_j that are invariant in time. The three variables $\Theta(t)$, $\gamma(t)$ and $\Psi(t)$ are known as *WS variables* and are the ones that allow the reduction of the model. Let's show where they come from and why we introduce them, later we will see their physical interpretation and meaning. The explanation of why this variable trasformation is used is predicted from previous articles [71] where the system (1.18) is solved when f, g and h are constant, in this way we can obtain $\theta_j(t)$ explicitly and it has the form of (1.19) where $\Theta(t)$ and $\Psi(t)$ are simply proportional to t while $\gamma(t)$ is constant. So the only thing to do to solve the problem when f, g, and h are not constant, is to apply the method of variation of the parameters to get the final expression (1.19). Let's rewrite the system (1.18) in terms of the new variables according to the transformation

$$\begin{aligned} cos\theta_j &= \frac{(cos(\psi_j - \Psi) - \gamma)cos\Theta - \sqrt{1-\gamma^2}sin\Theta sin(\psi_j - \Psi)}{1 - \gamma cos(\psi_j - \Psi)}, \\ sin\theta_j &= \frac{(cos(\psi_j - \Psi) - \gamma)sin\Theta - \sqrt{1-\gamma^2}cos\Theta sin(\psi_j - \Psi)}{1 - \gamma cos(\psi_j - \Psi)}. \end{aligned} \tag{1.20}$$

Now we need to compute the derivative on time and we can do it directly from the variable change (1.19)

$$\dot{\theta}_j = \dot{\Theta} + \frac{\dot{\gamma} sin(\psi_j - \Psi) - (1-\gamma^2)\dot{\Psi}}{\sqrt{1-\gamma^2}(1 - \gamma cos(\psi_j - \Psi))}; \tag{1.21}$$

We already have all the elements necessary to express (1.18) in terms of the new variables. Using the relations (1.21) and (1.20) in equation (1.18) and rearranging we get:

$$\begin{aligned} 0 = (\dot{\Theta} - \sqrt{1-\gamma^2}\dot{\Psi} - f + g\gamma cos\Theta + h\gamma sin\Theta) +, \\ + cos(\psi_j - \Psi)(-\gamma\dot{\Theta} + \gamma f - g cos\Theta - h sin\Theta) +, \\ + sin(\psi_j - \Psi)\Big(\frac{\dot{\gamma}}{\sqrt{1-\gamma^2}} + g\sqrt{1-\gamma^2}sin\Theta - h\sqrt{1-\gamma^2}cos\Theta\Big). \end{aligned} \tag{1.22}$$

If we want equality to be verified for all j and for all t we have to cancel the coefficients accompanying 1, $cos(\psi_j - \Psi)$, $sin(\psi_j - \Psi)$. For this we have to impose three conditions on the variables γ, Θ, Ψ:

$$\begin{cases} \dot{\gamma} = -(1-\gamma^2)(gsin\Theta - hcos\Theta) \\ \gamma\dot{\Theta} = \gamma f - gcos\Theta - hsin\Theta \\ \gamma\dot{\Psi} = -\sqrt{1-\gamma^2}(gcos\Theta + hsin\Theta) \end{cases} \tag{1.23}$$

In this way we have achieved to reduce the system of N differentials equations (1.18) to one of three real differential equations (1.23) expressed only in terms of the variables ($\gamma(t)$, $\Psi(t)$, $\Theta(t)$) and the functions f, g, h.
Once seen the form that the system takes in the new variables (1.23) it is convenient clarify the meaning of these new variables that have made this drastic reduction possible in our system (see Fig. (1.3)). The variables γ, Θ and Ψ describe the reduced system and for this we refer to them as "bunch" variables. Generally speaking the change we have made is somewhat similar to a change to polar variable where γ is related to the bunch amplitude or radius, Θ is related to the bunch phase or angle and Ψ is related to the phase bunch distribution. Similar to the Kuramoto order parameter $Z = re^{i\psi}$ in Eq. (1.3), the mean amplitude γ and the mean phase Φ characterize synchrony (or equivalently, the maximum of the phase distribution); while Z and $z = \gamma e^{i\Phi}$ do not coincide in general, they do if the population is fully synchronized. The phase distribution variable Ψ determines the shift of individual oscillators with respect to Φ as illustrated in Fig. (1.3).
Thus the integration of the N-dimensional system (1.18) has been reduced to the integration of the three-dimensional system (1.23). More precisely, we have shown that (1.18) is equivalent to a (N-3)-parameter family of three-dimensional system, where the parameters are the constants of motion ψ_j.
If we look at system (1.23), we see a singularity when $\gamma = 0$. To avoid this singularity we can make a change of variables that takes us back to cartesian coordinates:

$$x = \gamma cos\Theta, \qquad y = \gamma sin\Theta, \qquad \Phi = \Theta - \Psi. \tag{1.24}$$

In these new variables (1.23) becomes:

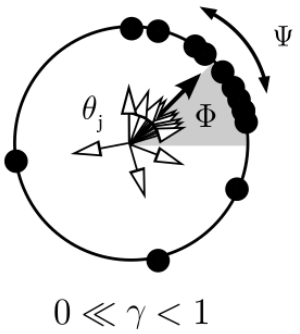

Figure 1.3: Illustration of the WS variables. Like the Kuramoto order parameter Z, the amplitude and phase in $z = \gamma e^{i\Phi}$ characterize the level of synchrony. The quantities Z and z do however only coincide if the population is fully synchronized or for uniformly distributed constants of motion in the limit $N \to \infty$. The variable Ψ is related to the phase shift and phase distribution of individual oscillators with respect to Φ.

$$\begin{cases} \dot{x} = -yf + xyg + (1-x^2)h \\ \dot{y} = xf - (1-y^2)g - xyh \\ \dot{\Phi} = f - 1 - \frac{1-\sqrt{1-\gamma^2}}{\gamma^2}(gx + hy). \end{cases} \tag{1.25}$$

If we study the case in which $\gamma = 0$ we see that the expressions of $\dot{x}$, $\dot{y}$ do not give any problem while in $\dot{\Phi}$ there is an indeterminacy but in the limit $\gamma \to 0$, the new variables take the value:

$$\dot{x} = h, \qquad \dot{y} = -g, \qquad \dot{\Phi} = f. \tag{1.26}$$

We will now turn our attention to oscillator systems where the number of oscillators tends to infinity, $N \to \infty$.
The main difference between the finite and infinite system is the way in which we see the oscillators. In the discrete case, when N is finite, the phase variables of the oscillators of the system $\theta_1, \theta_2, ..., \theta_N$ are as particles moving in the unit circle. In the continuous case, when $N \to \infty$, we are not longer able to distinguish them individually but on the contrary we will treat them as if they were a fluid characterize by a density $\rho(\theta, t)$ that indicates the

oscillators with phase θ at time t.
Not surprisingly, the transition from a discrete to a continuous system and the appearance of a density associated with system variables implies a series of extra conditions that must be checked to consistently set the problem:

- The integral through the entire domain must to be one (normalization of the probability distribution):

$$\int_0^{2\pi} \rho(\theta, t) d\theta = 1. \tag{1.27}$$

- The conservation condition of the number of oscillators implies that the dynamic is given by the transport equation[3]:

$$\frac{\partial \rho}{\partial t} + \frac{\partial}{\partial \theta}(\rho v) = 0, \tag{1.28}$$

  where $\nu(\theta, t) = f + gcos\theta + hsin\theta$ is the velocity of the fluid.

These conditions define the system in the continuous case. We now apply the reduction like the one in the system (1.18), the idea is essentially the same but the details change a little.
The main idea is to reduce (1.28) by making a change of variables that removes the dependency of time, which is exactly what we have done before when we went from θ to ψ by (1.19). Let us generalize (1.19) with the velocity removing the subscripts, namely by considering the changing $\theta_j \to \theta$. What we want to do with this change is to find conditions on (γ, Ψ, Θ) that allow to express the density $\rho(\theta, t)$ as a new time-independent density $\sigma(\psi)$, where ρ and σ are related by:

$$\rho(\theta, t) d\theta = \sigma(\psi) d\psi \qquad \forall t, \tag{1.29}$$

[3]Transport equations are common in physics. They are also known as the continuity equation (or Liouville equation in classical statistical physics describing the ensemble evolution in time) and play the important role of describing conservation laws. To visualize, in the context of fluid dynamics, the density in (1.28) plays the role of a mass density and (1.28) implies then that the total mass in the system is a conserved quantity.

to conserve oscillators in any infinitesimal interval.
Performing the same derivation as before, recalling [70] for all the mathematical details, we get the same system (1.23) that proves the validity of the reduction in the continuous case.
At this point we have reported the main aspects of the WS reduction method for a general class of coupled oscillators.

1.3.2 Ott-Antonsen reduction

The origin of the theory of Ott and Antonsen (OA) is more recent than that of WS since their most relevant works in this field [11] and [72] date from 2008 and 2009. Both works are based on the same model of oscillators that we have presented in Eq. (1.1) and the aim is to give an alternative methodology to the one proposed by WS to reduce the dimensionality of this system. In particular, they demonstrate that for Kuramoto-type systems (1.4), given a certain distribution of the frequencies, there is a single complex ordinary first-order differential equation (2 degrees of freedom) that determines the dynamics of the system and also, given an initial conditions, they find their exact solution analytically.
The Ott-Antonsen reduction applies to the continuum limit of populations of indistinguishable sinusoidally coupled phase oscillators (1.1). We first outline the basic steps to derive the macroscopic equations and highlight the assumptions made along the way.
We now consider the dynamics of (1.1) in the (continuum) limit of infinitely large networks, $N \to \infty$. To simplify the exposition, we consider the classical case in which the intrinsic frequency, $\omega_k = \eta_k$, is a random parameter and the driving field, $\mathbb{H}_k$, is the same for all oscillators. Hence, suppose that the intrinsic frequencies ω_k are randomly drawn from a distribution with density $g(\omega)$ on $\mathbb{R}$. In the continuum limit, the state of a population at time t is not given by a collection of oscillator phases, but rather by a probability density $\rho(\omega, \theta; t)$ for an oscillator with intrinsic frequency $\omega \in \mathbb{R}$ to have phase $\theta \in \mathbb{T}$ at time t. For a set of phases $\mathbb{B} \subset \mathbb{T}$ the integral $\int_{\mathbb{B}} \int_{\mathbb{R}} \rho(\theta, \omega; t) d\omega d\theta$ determines the fraction of oscillators whose phase is in $\mathbb{B}$ at time t. Moreover, we have $\int_{\mathbb{T}} \rho(\theta, \omega; t) d\theta = g(\omega)$ for all times t by our assumption that the intrinsic frequencies do not change over time.
The conservation of the total number N of the oscillators implies that the

dynamics of (1.1) in the continuum limit is given by the transport equation[4]

$$\frac{\partial \rho}{\partial t} + \frac{\partial}{\partial \theta}(v\rho) = 0 \qquad \text{with} \qquad v = \omega + Im\Big(\mathbb{H}(t)e^{-i\theta}\Big) \tag{1.30}$$

exactly as we have shown in the case of WS.
Because the number of oscillators is conserved, the change of the phase distribution over time is determined by the change of phases given by the velocity v through (1.1) at time t of an oscillator with phase θ and intrinsic frequency ω.
Ott and Antonsen [11] showed that there exists a manifold of invariant probability densities for the transport equation (1.30). Specifically, if $\rho(\theta, \omega, 0)$ satisfies the condition of the manifold (we will specify these conditions later), so the density $\rho(\theta, \omega, t)$ will satisfies the condition of the manifold as well, for any time $t \geq 0$.
Let

$$Z = \int_{-\infty}^{+\infty} \int_{-\pi}^{+\pi} \rho(\theta, \omega, t) e^{-i\theta} d\theta d\omega \tag{1.31}$$

denote the Kuramoto order parameter (1.3) in the continuum limit. We will see below that the evolution on the invariant manifold is now described by a simple ordinary differential equation for Z.
In the following we outline the key steps to derive a set of reduced equations and refer to [11, 72, 76] for further details. Suppose that $\rho(\theta, \omega, t)$ can be expanded into a Fourier series in the phase angle θ of the form

$$\rho(\theta, \omega, t) = \frac{g(\omega)}{2\pi}\Big(1 + \rho^+ + \rho^-\Big) \;\text{ where }\; \rho^+ = \sum_{n=1}^{+\infty} \rho^{(n)}(\omega, t) e^{in\theta} \tag{1.32}$$

Here it is assumed that ρ^+ has an analytic continuation into the complex half plane { Im(θ)$>$ 0 } (and $\rho^- = \rho^{+*}$ into { Im(θ) $<$ 0 }); even with this assumption we can solve a large class of problems, but it poses a restriction to a number of practical cases discussed in the section (1.3.3) below. Ott and

[4] If the oscillators are subject to noise, the continuity equation is a Fokker-Planck equation which contains an additional diffusive term [64, 73–75].

Antonsen now imposed the ansatz that Fourier coefficients are *powers of a single function* $a(\omega, t)$,

$$\rho^{(n)}(\omega, t) = [a(\omega, t)]^n \tag{1.33}$$

where $|a(\omega, t)| < 1$ to avoid divergence (this ansatz is equivalent to the Poisson kernel structure for the unit disk, $\rho^+ = \frac{ae^{i\theta}}{1-ae^{i\theta}}$). Substitution of (1.32) into (1.30) yields

$$\frac{\partial a}{\partial t} + i\omega a + \frac{1}{2}(\mathbb{H}a^2 - \mathbb{H}^*) = 0. \tag{1.34}$$

Thus, the ansatz (1.33) reduces the integral partial differential equation (1.30) to a single complex ordinary differential equation in a. Finally, with (1.33) we obtain

$$Z = \int_{-\infty}^{+\infty} g(\omega) a(\omega, t) d\omega, \tag{1.35}$$

which relates a and the order parameter Z in (1.31). Assuming analyticity, this integral may be evaluated using the residue theorem of complex analysis. We now clarify under which conditions the OA ansatz is applicable. First of all, performing the summation of the Fourier series and using $\sum_{n=1}^{\infty} x^n = x/(1-x)$ in (1.32) :

$$\rho(\theta, \omega, t) = \frac{g(\omega)}{2\pi} \frac{(1-|\alpha|)(1+|\alpha|)}{(1-|\alpha|)^2 + 4\,|\alpha|\, sin^2[\frac{1}{2}(\theta - \psi)]}, \tag{1.36}$$

where $\alpha \equiv |\alpha|\, e^{-i\psi}$ and ψ real. In order that Eqs. (1.34) and (1.35) represent a solution of Eq. (1.31) for all time, we require that, as $\alpha(\omega, t)$ evolves under Eq. (1.34) and Eq. (1.35), $|\alpha(\omega, t)| \leq 1$ continues to be satisfied. This can be shown by substituting $\alpha = |\alpha|\, e^{-i\psi}$ into Eq. (1.34), multiplying by $e^{i\psi}$, and taking the real part of the result, thus obtaining :

$$\frac{\partial\, |a|}{\partial t} + \frac{1}{2}(|a|^2 - 1) Re[\mathbb{H}e^{-i\psi}] = 0. \tag{1.37}$$

We see from Eq. (1.37) that $\partial |a| / \partial t = 0$ at $|a| = 1$. Hence a trajectory of Eq. (1.34), starting with an initial condition satisfying $|\alpha(\omega, 0)| < 1$ cannot cross the unit circle in the complex α-plane, and we have $|\alpha(\omega, t)| < 1$ for all finite time, $0 \leq t < +\infty$.

To proceed further, we now introduce another restriction on our assumed form of ρ; we require that $\alpha(\omega, t)$ can be analytically continued from real ω into the complex ω-plane, and that this continuation has no singularities in the lower half ω-plane, and that $|\alpha(\omega, t)| \to 0$ as $Im(\omega) \to -\infty$. If these conditions are satisfied for the initial condition, $\alpha(\omega, 0)$, then they are also satisfied for $\alpha(\omega, t)$ for $0 < t < \infty$. To see that this is so, we first note that for large negative $\omega_i = Im(\omega)$, Eq. (1.34) is approximately $\partial\alpha/\partial t = -|\omega_i|\,\alpha$, and thus $\alpha(\omega, t) \to 0$ as $\omega_i \to -\infty$ will continue to be satisfied if $\alpha(\omega, 0) \to 0$ as $\omega_i \to -\infty$.

We can now exactly specify the invariant manifold M on which our dynamics takes place. It is the space of functions of the real variable (ω, t) of the form given by Eq. (1.36) where $|\alpha(\omega, t)| \leq 1$ for real ω; $\alpha(\omega, t)$ can be analytically continued from the real $\omega-$axis into the lower half ω-plane; and, when continued into the lower half ω-plane, $\alpha(\omega, t)$ has no singularities there and approaches zero as $\omega_i \to -\infty$.

These equations take a particularly simple form if the distribution of intrinsic frequencies $g(\omega)$ is Lorentzian with mean $\hat{\omega}$ and width Δ, i.e.,

$$g(\omega) = \frac{1}{\pi} \frac{\Delta}{(\omega - \hat{\omega})^2 + \Delta^2} \tag{1.38}$$

since $g(\omega)$ has poles at $\hat{\omega} \pm i\Delta$ and thus (1.35) gives $Z = a(\hat{\omega} - i\Delta, t)$. As a result, we obtain the two-dimensional differential equation for the order parameter of the population:

$$\dot{Z} = -(\Delta + i\hat{\omega})Z + \frac{1}{2}\mathbb{H}^* - \frac{1}{2}\mathbb{H}Z^2 \tag{1.39}$$

know as **Ott-Antonsen equations**.

We note that this reduction method also works for other frequency distribution g as outlined in [76], in which the authors show that the OA reduction also applies for Maxwellian distribution ($g_M(\omega) \sim e^{-(\omega-\bar{\omega})^2/[2(\Delta\omega)^2]}$) and sech distribution ($g_s(\omega) \sim sech[(\omega - \bar{\omega})/\Delta\omega]$). In [11] it is showed that the OA reduction also is possible for Lorentzian-type distribution as $g_L(\omega) \sim \frac{1}{\omega^4+1}$

which decreases as ω^{-4} in contrast of the Lorentzian distribution (1.38). Moreover in [72] the autors discuss that past numerical experiments comparing results obtained using Lorentzian $g(\omega)$ and using Gaussian $g(\omega)$ were found to yield qualitatively identical bifurcation structures. However, the resulting mean field equation will not always be a single complex ordinary equation but could be a set of coupled complex ordinary equations. For example, for multi-modal frequency distributions g the Ott-Antonsen equations will have an equation for each mode; see [77–79] .

The derivation above only states that there is an invariant manifold of densities ρ for the transport equation (1.30). What happens to densities ρ that are not on the manifold as time evolves? Under some assumptions on the distribution in intrinsic frequencies g, Ott and Antonsen also showed in [72] that there are densities ρ that are attracted to the invariant manifold. In particular in [72] they show that for a Lorentzian distribution of the form (1.38), for $\Delta > 0$, the long time dynamics of the order parameter $Z(t)$ is governed by the ordinary differential equation (1.39) that describes its dynamics for distribution functions $\rho(\theta, \omega, t)$ on the reduced manifold. Thus, even if our desired condition $Im(\omega) \to -\infty$ is not satisfied initially, in many cases, the result that the long time dynamics of $Z(t)$ is described by (1.39) may still apply.

In other words, the dynamics of the Ott-Antonsen equations capture the long-term dynamics of a wider range of initial phase distributions $\rho(\theta, \omega, 0)$, whether they satisfy (1.33) initially or not.

We close this section showing as an example the Ott-Antonsen (OA) mean field equations for the Kuramoto model.

Consider the continuum limit of the Kuramoto model (1.4) with a Lorentzian distribution of intrinsic frequencies. Recall that the driving field for the Kuramoto model is $\mathbb{H}(t) = KZ(t)$. Substituting this into (1.39) we obtain Ott-Antonsen formulation for the Kuramoto model:

$$\dot{Z} = -(\Delta + i\hat{\omega})Z + \frac{K}{2}Z - \frac{K}{2}|Z|^2 Z \tag{1.40}$$

1.3.3 Comments and Limitations

Before we apply the mean field reductions to particular neural model networks in the next chapter, let's close this chapter with some comments on the limitations of these approaches.

As stated above, the main assumption for the validity of the OA reduction is that the interactions is restricted to pure sinusoidal coupling function and that the number of oscillators is infinite. Moreover the network must be fully-coupled. There are explicit examples that show that the reductions become invalid if these assumptions are not verified. This does not mean that the reductions break down completely, and there may still be some degeneracy in the system if the interaction is of a specific form; see [80] for a more detailed discussion. It remains a challenge to identify which part of the mean-field reduction (if any) remains valid for more general interaction functions and phase response curves. Another example [17] come up considering the collective dynamics in large populations of coupled phase oscillators with intrinsic noise.

The Ott-Antonsen reduction for the continuum limit allows for the oscillators to be nonidentical. By contrast, the Watanabe-Strogatz reduction of finite networks requires oscillators to be identical. Neither of these approaches applies to finite networks of nonidentical oscillators, and understanding such networks remains a challenge. There has also been some recent progress analyzing situations in which the Ott-Antonsen or Watanabe-Strogatz equations do not apply exactly, using perturbation approach for weakly nonidentical oscillators ensembles [81].

Finally, Ott and Antonsen showed that the manifold of oscillator densities ρ on which the reduction holds is attracting [72]. Their method of proof has been shown to apply to a wider class of systems [77]. As pointed out by Mirollo [82], their proof is based on a strong smoothness assumption on the density ρ which implies limitations to this approach. More precisely, to be able to evaluate contour integrals using the residue theorem, it is typically assumed that the density is holomorphic. This assumption is only valid for distributions g that allow for arbitrarily large (or small) intrinsic frequencies with nonzero probability. Any distribution for which the intrinsic frequencies are bound to a finite interval - the intrinsic frequencies of any finite collection of oscillators will lie in a finite interval - are excluded. Hence, while the manifold described by Ott and Antonsen attracts some class of oscillator densities (which include some commonly used ones like Lorentzians and Gaussians), it is not clear how large this class actually is.

Chapter 2

QIF model and Firing Rate Equations

Summary:

In this chapter we introduce the single QIF neuron model providing a detailed study of its dynamics. We then define the network model of fully coupled QIF neurons showing how to move from the microscopic description of a population of QIF neurons with instantaneous synapses, corresponding to a system of N degrees of freedom, to the exact neural mass model with only two degrees of freedom, that is in terms of the average firing rate and the average membrane potential of the network.

2.1 Introduction

Neurons, of various types and morphologies, are connected in very complex networks through chemical and electrical synapses in the various areas of the brain, present in all vertebrates and in many invertebrates. For example, the human brain contains about 100 billion neurons and each neuron can be connected to a large number of other neurons, up to 10,000. The complexity of the network brain is such that it cannot be studied numerically (or theoretically) with a direct approach, i.e. by making the most faithful reproduction of the brain or portions of it, since going into extreme neural network description details risks, due to the presence of a very high number

of parameters to be calibrated, to make the state of the network very sensitive to small variations of the parameters themselves, both because from a numerical point of view, the simulation of this network would become very expensive in terms of calculation, making possible only simulations for very short time intervals.
The understanding of any complex system goes through the choice of a description level that captures the fundamental properties of the system and overlooks those that are not essential to its purpose. In particular, if we are interested in studying the collective phenomena of a neuronal network, for example phenomena of synchronization, clustering, information coding, memory formation, etc., then it is reasonable to use a simplified microscopic representation of the neuron [83]. In neuroscience, the so-called *formal spiking neuronal* models are used to perform theoretical analyses and simulations of large-scale networks [84].
In this chapter we analyze one of these *formal spiking models*, the so-called *Quadratic Integrate-and-Fire model* (QIF). In addition, given that there are multiple simplified single models neuron, we will try to give a justification for the reason for this choice.
In particular, in Section 2.2 we define the variables that describe the dynamics of a neuron and we describe qualitatively the distinction between type I and II neurons. Starting from this distinction we derive, in Section 2.3, the QIF model providing a detailed description of its dynamics. In Section 2.4 we define the fully-coupled network model of QIF neurons and in Section 2.5 we illustrate how to reduce, under certain hypotheses, the detailed network microscopic dynamics to a few simple equations that describe its macroscopic dynamics. Finally, in Section 2.6, we discuss the validity of this reduction method.

2.2 Type I and II neurons

Before moving on to the description of the QIF model, it is useful to summarize how the dynamics of the individual neuron (i.e. its activity) originates, through the illustration of some basic notions of neurophysiology.
The *membrane potential* of a neuron is defined as the difference potential measured at the ends of two electrodes, one placed inside the neuronal cell and one placed in the surrounding extracellular liquid. When we talk about neuronal signal we refer to the temporal and spatial variation of the mem-

brane potential. When the neuron is at *rest*, that is, it is not somehow excited from the outside, the membrane potential assumes a characteristic value called *resting potential*, typically of the order of $-65\ mV$, i.e. the interior of the cell is at a lower potential than on the outside.
Action potentials are typical voltage impulses generated during neuronal dynamics; they have an almost stereotyped form and are not subject to attenuation or distortion during its propagation. The action potential is the elementary unit associated with the transmission of neuronal signals. Typically when we refer to the signal emitted by a neuron we mean the time sequence of these action potentials, called *spike train*.
We can schematize the emission of an action potential by a neuron i as follows. The neuron i receives a certain number of impulses from the neurons pre-connected to it (called *presynaptic neurons*). If these impulses are received in a sufficiently short time window, the neuron i responses roughly linear, in the sense that its membrane potential increases approximately proportionally to the input it receives. When the potential of neuron i reaches a typical value, V_{th}, called the *activation threshold*, the behavior of the neuron becomes highly not linear: it is generated an action potential that has a stereotyped form and therefore unrelated to the stimuli that produced it; moreover the neuron, for the entire duration of the emission of the action potential, becomes insensitive, namely *refractory*, to the stimuli that come from the other neurons.
In *formal spiking models*, the form of the action potential is not reproduced and it is formally assumed that the neuron emits an impulse towards the neurons connected to it at the precise moment when the value of the potential reaches a certain value. The idea behind the formal spiking models is to describe the sub-threshold evolution of the membrane potential and to treat the emission of the action potential as a stereotype event.
In the brain there are multiple types of neurons with different dynamics. Despite this we can classify neurons into two general classes based on the response of neuronal cells stimulated by a constant current [6, 85]:

- **Type I**: action potentials can be emitted with arbitrarily small frequency, based on the intensity of the applied current.

- **Type II**: action potentials can only be emitted with a frequency above a certain value and this frequency is relatively insensitive to the intensity of the applied current.

Experimental data comparing the two types of neuron are shown in Figure (2.1). In the left panel of Fig. (2.1) we observe the data relating to a neuron of the primary visual cortex of the rat[1] which represents an example of neuron type I while on the right the data relating to a neuron of the rat midbrain, as an example of the type II. In the figure are reported the respective empirical curves that express the Current-Frequency relationship. Generally, type I neurons fire with one frequency that can vary continuously covering a range from 2 Hz to 100 Hz, and even more depending on the specific class of neuron. The qualitative important distinction is that for type I neurons the Current-Frequency relationship is comparable to one continuous function, while for type II neurons, the transition from the quiescent state to the tonic state of periodic emission of action potentials, occurs through a discontinuous jump.
Due to this biological distinction, the mathematical models of a single neuron are classified according to how such oscillations arise. In general, as explained by Ermentrout and Rinzel in [87] and [88], the transition from the silent state to the oscillatory state occurs through, typically, two different bifurcations that correspond to the two types of neuron just illustrated. For type II models, the transition occurs due to a Hopf bifurcation (supercritical or subcritical), while for type I neurons, it occurs through a Saddle-Node bifurcation on an invariant circle (SNIC).

In this thesis we will focus on type I behavior and therefore we report here just an explanation of how the SNIC bifurcation occurs.
The SNIC bifurcation takes place in a space of at least 2 dimensions and is illustrated in Fig. (2.2) in the planar case. It is called invariant because any solution starting on the circle remains on the circle. Initially there are 3 points of equilibrium: a stable node (blue point), an unstable saddle point (red point) and an unstable focus (white point). The unstable variety of the saddle point is formed by two heterocline trajectories which, rising from the saddle point, tend in infinite time towards the stable node. The combination of these two trajectories forms a closed curve in the phase plane that contains the unstable focus. The stable variety of the saddle point (colored green in Fig. (2.2)) represents the "threshold-variety" in the sense that an initial condition on the left of this is attracted directly to the stable point, while an

[1] In the cerebral cortex of mammals there are many type I pyramidal neurons [6] and this area of the brain is generally referred to as the area responsible for higher cognitive functions [86].

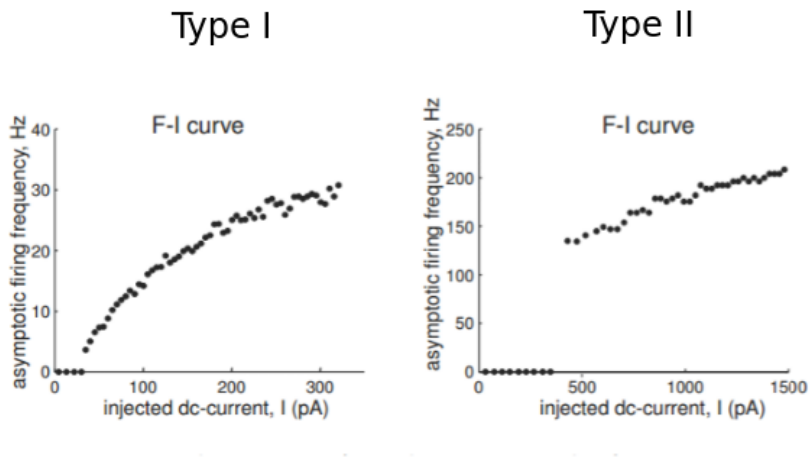

Figure 2.1: Comparison between a type I neuron and a type II neuron belonging to the brain of a rat. In the left column the data related to a type I neuron, in the right column the data related to a type II neuron. Figure taken from [6] and readjusted.

initial condition to the right of it is dragged around the unstable focus before converging towards the stable node. This particular situation configures the *excitable state* of the neuron. The "long" path around the repulsive focus corresponds to the mechanism of generation of the action potential, while the "short" path configures relaxation towards the resting state of the neuron. The central picture in Fig. (2.2) shows the dynamics exactly on the critical bifurcation value: the node and the saddle merge and at the same time the heteroclinic orbit closes in on itself in a homoclinic orbit, that is a cycle of infinite duration. Exceeded the critical bifurcation value (picture on the right), the node and the saddle annihilate and, as a consequence, the homoclinic orbit becomes a limit cycle. Therefore the oscillations in this cycle arise with zero frequency and grow continuously.

2.3 Quadratic Integrate-and-Fire model

In this section we define the so-called Quadratic Integrate-and-Fire (QIF) neuronal model, which will be the single neuron model that we will use in the following to analyze the dynamics of neural populations. The QIF neuron

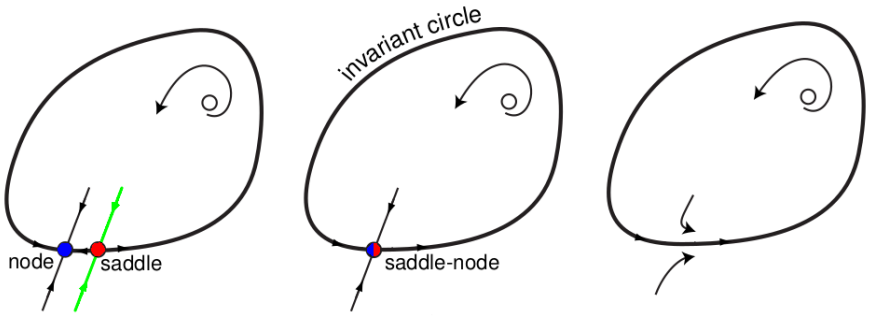

Figure 2.2: Illustration of the SNIC bifurcation. Figure taken from [6] and readjusted.

is the prototype of type I neurons, as it represents in paradigmatic way the transition from a quiescent to an oscillatory state.
In [89] Ermentrout and Kopell demonstrate rigorously how to reduce the equations of a dynamical system, near a SNIC bifurcation, to the following quadratic ordinary differential equation:

$$\dot{x}(t) = x^2(t) + I \tag{2.1}$$

being I the controller parameter.
In order to avoid discontinuities, it is convenient to rewrite such equation introducing the phase-variable $\theta = 2\arctan(x)$, obtaining the following equation:

$$\dot{\theta} = [1 - cos(\theta(t))] + [1 + cos(\theta(t))]I \tag{2.2}$$

As explained in the previous paragraph, the SNIC bifurcation, by definition, is a global bifurcation in which multiple structures interact (heterocline orbits, fixed points, etc.) in at least a two-dimensional space. However, the universal dynamic that occurs on the invariant circle near an SNIC bifurcation is one-dimensional. The one-dimensional equation (2.2) describes exactly this universal dynamic.
Equation (2.2) defines the so-called Theta-model (hereafter indicated as Θ-model). The variables θ and I in (2.2) represent dimensionless the membrane potential and the current injected into the neuron. In this representation neurons are seen as simple phase oscillators characterized by an angular variable.

Since the function $\theta(t)$ always appears as an argument of the periodic cosine function, it is convenient to visualize the model on the unit circle.
We represent the curve (2.2) in the plane $(\theta, \dot{\theta})$, considering $|I|$ constant and not too large. We can distinguish three qualitatively different cases: $I < 0$, $I = 0$ and $I > 0$.
In the case $I < 0$, see Fig. (2.3), we have an unstable equilibrium solution θ_{inst} close to zero (red point in Fig. (2.3)) and one stable θ_{stab} close to 2π (blue point in Fig. (2.3)).

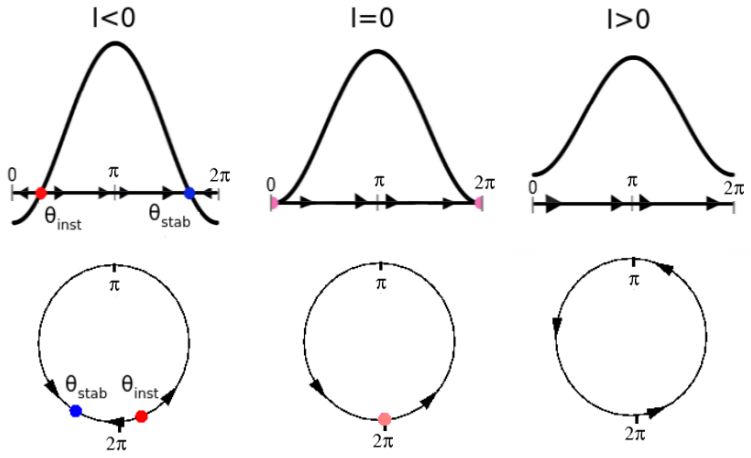

Figure 2.3: SNIC of the Θ-model. The three figures above show the curve in Eq.(2.2), for different values of I, and its intersections with the axis $\dot{\theta} = 0$. The three figures below show the same dynamic displayed on the unit circle. The blue (red) point represents the stable (unstable) equilibrium point, the pink one the neutral equilibrium point. Figures taken from [90] and readjusted.

In this case, if we start with an initial condition slightly smaller than the position of the unstable equilibrium point, $\theta(t_0) < \theta_{inst}$, then the flow on the circle transports the system towards the stable solution θ_{stab}. If instead we start with a slightly larger initial condition, $\theta(t_0) > \theta_{inst}$, then the flow rotates the system along the whole circle, with a peak of speed in $\theta = \pi$, towards the stable solution. We can interpret the stable solution as the resting potential value, while the unstable solution plays the important role of the threshold value beyond which the mechanism for generating the action potential is triggered, which we formally assume to be issued at the time t_{fire}

such that $\theta(t_{fire}) = \pi$.
Fig. (2.3) illustrates, varying I from negative to positive, the 3 characteristic phases of the saddle-node bifurcation. For $I < 0$ there is the coexistence of a stable and an unstable equilibrium point. As the current increases, these equilibrium points merge exactly for $I = 0$, and then disappear for $I > 0$. We model this event as the onset of the oscillatory state of the neuron.
In the case $I > 0$ the system rotates incessantly along the circle emitting a train of periodic impulses. To calculate the frequency of this oscillatory system suppose that we have at time t_0 the initial condition $\theta(t_0) = 0$ and let T be the time spent to make a lap. Therefore, $\theta(T) = 2\pi$ and we can express T through the integral relation:

$$T = \int_0^{2\pi} \frac{d\theta}{1 - cos(\theta(t)) + [1 + cos(\theta(t))]I} \tag{2.3}$$

To obtain an explicit expression of the period it is sufficient to solve the last integral, for example through the transformation;

$$V = \tan\Big(\frac{\theta}{2}\Big) \tag{2.4}$$

which maps the angle variable $\theta \in [0,+2\pi]$ in $V \in [-\infty,+\infty]$.
Equation (2.2) becomes:

$$\frac{2}{1+V^2}\dot{V} = [1 - \frac{1-V^2}{1+V^2}] + [1 + \frac{1-V^2}{1+V^2}]I \tag{2.5}$$

from which we obtain:

$$\dot{V}(t) = V^2(t) + I. \tag{2.6}$$

The integral (2.3) takes now the form:

$$T = \int_{-\infty}^{+\infty} \frac{dV}{I + V^2}, \tag{2.7}$$

from which we get:

$$T = \frac{1}{\sqrt{I}}\Big[\arctan(\frac{V}{\sqrt{I}})\Big]_{-\infty}^{+\infty} = \frac{\pi}{\sqrt{I}}. \tag{2.8}$$

Therefore, in the Θ-model the oscillations arise continuously with the increase of I given by the formula:

$$\nu = \frac{1}{T} = \frac{\sqrt{I}}{\pi}, \tag{2.9}$$

and therefore, according to the definition given in the previous section, this model belongs to type I neurons.
Noteworthy is the fact that, experimentally, the Current-Frequency relationship of type I neurons is well reproduced with a "square root" function (see Fig. (2.1)), and this adds further value to the Θ-model.
The Θ-model is often presented with another name: the QIF model because of the quadratic term in the equation of the voltage. The QIF model is preferred because it has a more natural interpretation in terms of membrane potential of the neuron. The equation governing the evolution of the QIF model is exactly (2.6), which we rewrite below for clarity, where we denote the constant I with η:

$$\dot{V}(t) = V^2(t) + \eta \tag{2.10}$$

some solutions of equation (2.10) reach the infinite in a finite time. This is a geometric consequence of the change of variable (2.4), in fact, equation (2.10) describes the same dynamics of the Θ-model but "observed" from the local point of view in which the fusion of the saddle and the node takes place. As much as it is true that equation (2.10) turns out exactly the normal form obtained by approximating any dynamic system around a fixed point that forks through a saddle-node. To capture the essence of the oscillation, which occurs when the saddle-node bifurcation occurs on an invariant circle, we accompany equation (2.10) with a reset rule: whenever the membrane potential reaches the value V_{th}, then we reset the potential to the V_{reset} value such that $V_{reset} < V_{th}$.
In the following of this thesis we set $V_{th} = +\infty$ and $V_{reset} = -\infty$, and therefore it is perfectly equivalent to the Θ-model through the transformation

(2.4).
Equation (2.10) can be solved analytically, the sign of the parameter η defines two different types of behavior, represented in the phase plan $(V, \dot{V})$ in Fig. (2.4).

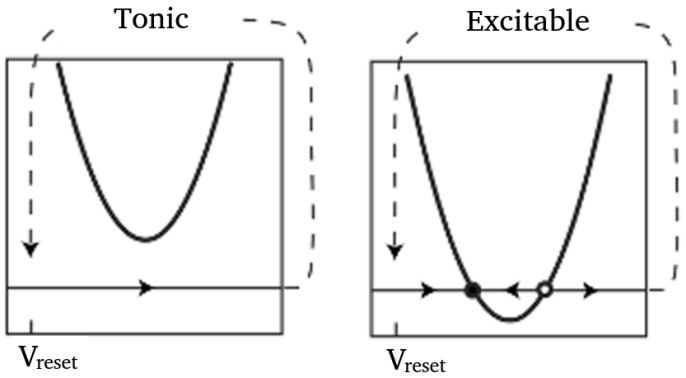

Figure 2.4: Phase plan $(V, \dot{V})$ of the QIF model. On the left the case $\eta > 0$, on the right the case $\eta \leq 0$. Figures taken from [6] and readjusted.

2.3.0.1 Tonic neuron: $\eta > 0$

In the case $\eta > 0$, we have $V^2(t) + \eta > 0$, $\forall t$. Therefore, by separation of the variables in equation (2.10), we get the relation: $\frac{\dot{V}(t)}{V^2(t)+\eta} = 1$. Given an initial condition $(t_0, V(t_0))$ and a time $t_1 > t_0$, we get:

$$\int_{t_0}^{t_1} \frac{\dot{V}(t)}{V^2(t) + \eta} dt = \int_{t_0}^{t_1} dt = t_1 - t_0, \tag{2.11}$$

The integral on the left can be solved with elementary methods, providing:

$$\frac{1}{\sqrt{\eta}} \Big[\arctan\Big(\frac{V(t_1)}{\sqrt{\eta}}\Big) - \arctan\Big(\frac{V(t_0)}{\sqrt{\eta}}\Big) \Big] = t_1 - t_0, \tag{2.12}$$

which, in particular, only makes sense if we assume $(t_1 - t_0) \in [0, \frac{\pi}{\sqrt{\eta}}]$.
By solving equation (2.12) for $V(t_1)$, we get:

$$V(t_1) = \sqrt{\eta}\tan\Big(\sqrt{\eta}(t_1 - t_0) + \arctan\Big(\frac{V(t_0)}{\sqrt{\eta}}\Big)\Big) \tag{2.13}$$

whose graph is illustrated in Fig. (2.5).

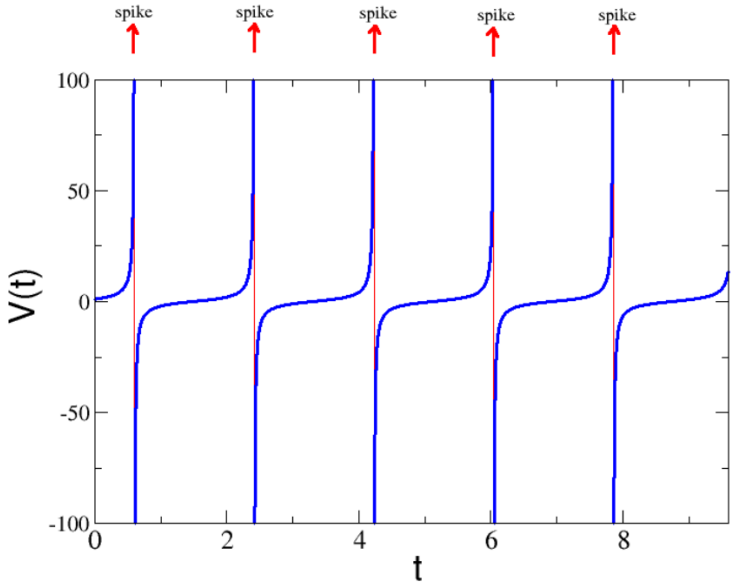

Figure 2.5: Tonic neuron. In red, the vertical asymptotes representing the firing times t_{fire}, expressed by (2.15), in which the neuron emits an action potential. Function graph of $V(t)$ in (2.13) with $\eta = 3$, $V(t_0) = 1$.

Clearly the inversion makes sense as long as the argument of the tangent is less than $\frac{\pi}{2}$, since for this value the tangent has a singularity.
So in case $\eta > 0$, fixed an initial condition $(t_0, V(t_0))$, we can analytically extend the solution of equation (2.10) up to time t_{fire} such that $\sqrt{\eta}(t_{fire} - t_0) + \arctan\Big(\frac{V(t_0)}{\sqrt{\eta}}\Big) = \frac{\pi}{2}$ and therefore up to the time :

$$t_{fire} = t_0 + \frac{1}{\sqrt{\eta}}\Big(\frac{\pi}{2} + \arctan\frac{V(t_0)}{\sqrt{\eta}}\Big). \tag{2.14}$$

At this moment the neuron emits an action potential and the value of the membrane potential is instantly reset to minus infinity:

- $V(t_{fire}^{-}) = +\infty \rightarrow$ emission of the action potential[2];
- $V(t_{fire}^{+}) = -\infty$: resetting of the membrane potential.

At this point the neuron restarts with an initial condition given by ($t_0 = t_{fire}^{+}, V(t_0) = -\infty$) and we can repeat exactly the same procedure of before integrating for a time interval $\frac{\pi}{\sqrt{\eta}}$ until a new singularity is encountered. We therefore deduce that a QIF neuron with $\eta > 0$ emits periodic pulse trains at times t_{fire} given by:

$$t_{fire} = \frac{1}{\sqrt{\eta}}\Big(\frac{\pi}{2} + \arctan\frac{V(t_0)}{\sqrt{\eta}}\Big) \pm k\frac{\pi}{\sqrt{\eta}} \qquad k \in \mathbb{Z}, \tag{2.15}$$

and we find again the important formula that expresses the dependence of the period as a function of the value of η:

$$T = \frac{\pi}{\sqrt{\eta}} \tag{2.16}$$

2.3.0.2 Excitable neuron: $\eta \leq 0$

As in the case of a tonic neuron, by separation of the variables, we obtain the equation (2.12). Since now $\eta \leq 0$, we must exclude the instants of time that provide constant solutions such that $V(t) = V_{stab}$ and $V(t) = V_{inst}$. So, let's take an initial condition $(t_0, V(t_0))$ and choose a time t_1 such that the interval (t_0, t_1) do not contain the above mentioned times which achieve constant solutions. We have to distinguish two cases.

Sub-threshold dynamics: $|V(t_0)| \leq \sqrt{|\eta|}$

In this case $V(t_0)$ lies in the segment relative to the negative part of the parabola in Fig. (2.4) and therefore the trend of the solution $V(t)$ will be strictly monotonous decreasing and will tend asymptotically to the resting membrane value. Solving the integral in (2.11), being $V(t_0) > V(t_1)$, we finally obtain:

[2]the expression t_{fire}^{-} (t_{fire}^{+}) means the limit that tends to t_{fire} from the left (right).

$$V(t_1) = -\sqrt{|\eta|}\tanh\Big(\sqrt{|\eta|}(t_1 - t_0) + \operatorname{arctanh}\Big(\frac{V(t_0)}{\sqrt{|\eta|}}\Big)\Big) \tag{2.17}$$

whose graph is illustrated in Fig. (2.6).
In particular, a QIF neuron with $\eta < 0$ and initial condition $|V(t_0)| \leq \sqrt{|\eta|}$, if isolated, will never emit any action potential.

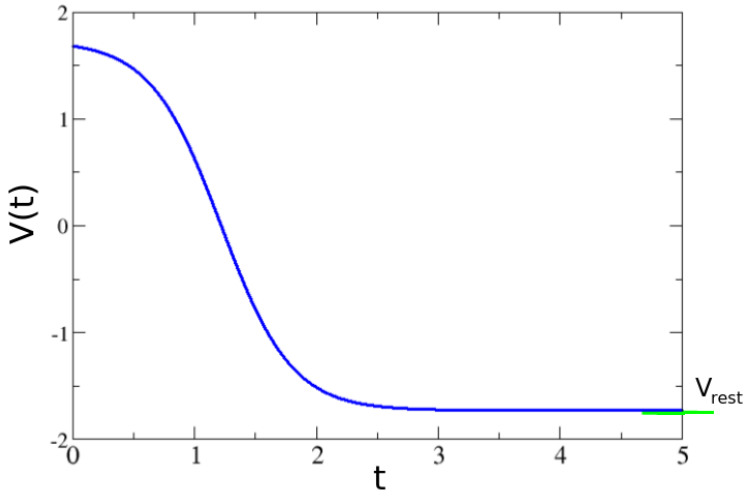

Figure 2.6: Excitable neuron, Sub-threshold dynamics. In green the value of the resting membrane potential, $V_{rest} = -\sqrt{-\eta}$, to which the neuron tends. Trend of $V(t)$ in (2.17) with $\eta = -3$, $V(t_0) = -\eta - 0.05$.

Supra-threshold dynamics: $|V(t_0)| \geq \sqrt{|\eta|}$

Assume that $V(t_0) > \sqrt{|\eta|}$ and therefore that $V(t_0)$ lies in the right half-line of the positive part of the parabola in Fig. (2.4). In this case, from equation (2.11), is possible to show that there exists a finite time t_f such that $V(t_f) = +\infty$, giving by:

$$t_f = t_0 + \frac{1}{\sqrt{|\eta|}}\operatorname{arctanh}\Big(\frac{\sqrt{|\eta|}}{V(t_0)}\Big). \tag{2.18}$$

This means that if the neuron at time t_0 has a membrane value $V(t_0) \geq \sqrt{|\eta|}$, then at the instant of time t_f it will emit an action potential and instantly reset its membrane value to -∞.
At this point, as already observed, the value of $V(t)$ will tend to value $V_{stab} = -\sqrt{|\eta|}$ strictly monotonously increasing and the analytical form of the solution can be obtained from the equation (2.11) writing:

$$\int_{t_0}^{t_1} \frac{\dot{V}(t)}{V^2(t)+\eta} dt = \int_{t_0}^{t_f} \frac{\dot{V}(t)}{V^2(t)+\eta} dt + \int_{t_f}^{t_1} \frac{\dot{V}(t)}{V^2(t)+\eta} dt, \tag{2.19}$$

being $V(t_1) = +\infty$. Solving equation (2.19) and inverting we get:

$$V(t_1) = -\sqrt{|\eta|}\text{cotanh}\Big(\sqrt{|\eta|}(t_1 - t_0) - \text{arctanh}\Big(\frac{\sqrt{|\eta|}}{V(t_0)}\Big)\Big) \tag{2.20}$$

whose graph is illustrated in Fig. (2.7).

Limit case: $|V(t_0)| = \sqrt{|\eta|}$

In this particular case the differential equation of the QIF model takes the form : $\dot{V}(t) = V^2(t)$. Choosing an initial condition $V(t_0) = 0$ we can proceed with the separation of the variables and obtain the analytical solution:

$$V(t) = \frac{V(t_0)}{1 - V(t_0)(t - t_0)}. \tag{2.21}$$

So if $V(t_0) > 0$ then the neuron spikes at the time:

$$t_f = t_0 + \frac{1}{V(t_0)}. \tag{2.22}$$

The QIF neuron with $\eta = 0$ has a qualitatively similar dynamic to that of the hyperbolic cotangent in Fig. (2.7), although the analytical solution is different.

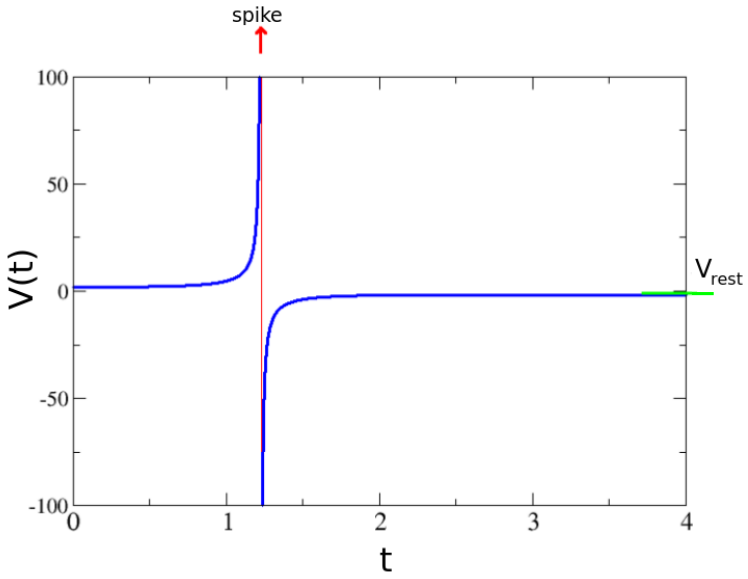

Figure 2.7: Excitable neuron, Supra-threshold dynamics. In red the vertical asymptote represents the spiking time t_f, expressed by (2.18), in which the neuron emits an action potential. In green the value of the resting membrane potential, $V_{rest} = -\sqrt{-\eta}$, to which the neuron tends asymptotically after the emission of the action potential. Trend of $V(t)$ in (2.20) with $\eta = -3$, $V(t_0) = -\eta + 0.05$.

2.4 Population model of fully-coupled QIF neurons

In this section we discuss the fully-coupled network model of QIF neurons with instantaneous synapses, that is, each neuron interacts instantaneously with everyone else.
To define a neural network we have to model the coupling between the individual QIF neurons of the network, taking into consideration the electrophysiology of the biological synapses. In particular, we will deal with two types of networks: one with synapses completely impulsive and one with impulsive growth synapses and exponential decay.
A neural network is, formally, a graph whose nodes are made up of neurons and whose connections represent synapses; in particular, each connection is weighed with the corresponding synaptic efficiency [91]. The synaptic weights

can be fixed or they can also evolve in the time (synaptic plasticity), according with the past of the two nodes connected by the synapse [92, 93].
The synapses thus constitute a graph with unidirectional and oriented connections. Each node is characterized by an evolution equation in which the state of the neuron depends on the neurons connected to it, namely the presynaptic neurons. In this thesis we assume that the synaptic weights remains unchanged over time, that is, we do not take into account the presence of synaptic plasticity.
Under these hypotheses the evolution equation of each node, of a network composed of N QIF neurons, takes the form:

$$\dot{V}_i(t) = V_i^2(t) + \eta_i + JS(t) + I_e(t), \qquad i = 1, ..., N, \tag{2.23}$$

We can interpret the elements of equation (2.23) as follows:

- the *excitability* η_i of the i-th QIF neuron of the network should be thought as a parameter that grossly incorporates everything that characterizes a specific neuron, i.e. in this constant all the internal characteristics of the particular neuron are condensed (particular surface, microscopic structure of the membrane, gating processes etc.), as well as the external characteristics of the network that are attributable to the particular area in which this neuron is located (presence of intense electrical activity due to other neurons close to which it is not connected, chemical composition of the extracellular liquid locally to the neuron, etc.);

- the parameter J represents the *synaptic weight*, equal for all synapses of the network, while $S(t)$ is a function of time which represents the average field of synaptic activation, that is a function that takes into account the effective coupling between all the neurons of the network at instant t. The sign of the constant J defines whether the impulse received is of an excitatory type ($J > 0$), or inhibitory ($J < 0$). Furthermore, since the synapses of the network are all the same, we can define on the basis of the sign of J a completely excitatory or completely inhibitory network;

- Clearly the field $S(t)$ must be defined as a function of the impulses emitted by neurons in the network. Therefore, assuming that $t_1, ..., t_M$

are the past instants of time, i.e. preceding the current time t, in which some neuron in the network has emitted an impulse, then we define the evolution of the *average synaptic field* through the following linear differential equation:

$$\tau_d \dot{S}(t) + S(t) = \frac{1}{N} \sum_{k=1}^{M} \delta(t - t_k), \tag{2.24}$$

where $\delta(t - t_k)$ is the Dirac delta function centered on the instant of the impulse and τ_d is the decay time of the synaptic field. A positive value of τ_d stands for an exponential decay of the synaptic field, while $\tau_d = 0$ stands for an instantaneous decay. In this case we say that the synaptic is impulsive.
We observe that in this formulation the interaction between neurons is taken instantaneously, that is every time a neuron emits an impulse at the instant t_k then all the neurons of the network receive it, through the field S, at that same instant. Moreover, this model provides for self-stimulation, i.e. the possibility of the neuron being influenced by its own impulse[3].

- the time-dependent function $I_e(t)$ represents a possible external current applied to all the neurons of the network.

Therefore, given the initial network condition $(V_1(t_0), ..., V_N(t_0), S(t_0))$ the dynamics of the network model is formally defined by the following system of $N + 1$ ordinary differential equations:

$$\begin{cases} \dot{V}_i(t) = V_i(t)^2 + \eta_i + JS(t) + I_e(t), & i = 1, ..., N, \\ \tau_d \dot{S}(t) + S(t) = \frac{1}{N} \sum_{k=1}^{M} \delta(t - t_k), \end{cases} \tag{2.25}$$

together with the resetting rule $\forall k = 1, ..., M$, $V_i(t_k^-) = +\infty$ then $V_i(t_k^+) = -\infty$, where, $\forall t > t_0$ fixed, the finite number of instants t_k with $k = 1, ..., M$ are implicitly defined by $V_j(t_k^-) = +\infty$ for some $j \in \{1, ..., N\}$.

[3]There are studies showing the existence of synapses between a neuron and a branch of its own axon [94], and the presence of these links has an inhibitory functional role [95].

The equation (2.25) can be easily generalized if there are multiple interacting populations. Denoting with A and B two populations formed by, respectively, N_A and N_B QIF neurons. Population A (B) is therefore described by the membrane potentials of the individual neurons $\{V_i^A\}$ $i = 1, ..., N_A$ ($\{V_i^B\}$ $i = 1, ..., N_B$) and by the mean field of synaptic activation S_A (S_B). If $t_1, ..., t_M^A$ ($t_1, ..., t_M^B$) are the moments in which any neuron of population A (B) emits a spike, then we describe the evolution of the two QIF networks coupled through non instantaneous synapses (exponentially decaying) with the following system of $N_A + N_B + 2$ differential equations:

$$\begin{cases} \dot{V}_i^A(t) = V_i^A(t)^2 + \eta_i^A + J_{AA}S^A(t) + J_{BA}S^B(t), & i = 1, ..., N_A, \\ \tau_d^A \dot{S}^A(t) + S^A(t) = \frac{1}{N_A} \sum_{k=1}^{M_A} \delta(t - t_k^A), & \\ \dot{V}_i^B(t) = V_i^B(t)^2 + \eta_i^B + J_{BB}S^B(t) + J_{AB}S^A(t), & i = 1, ..., N_B, \\ \tau_d^B \dot{S}^B(t) + S^B(t) = \frac{1}{N_B} \sum_{k=1}^{M_B} \delta(t - t_k^B), & \end{cases} \tag{2.26}$$

more the reset rule to each neuron.
In the system (2.26), the parameters J_{BA} and J_{AB} define the intensity with which, respectively, the network B influences the network A and the network A influences the network B. The term J_{AA} (J_{BB}) represents the weight of the internal connections of network A (B).
To obtain, in practice, a macroscopic quantity that measures the intensity of the activity of the neural network, we can proceed as follows: we divide the time interval $[t_0, t]$, in which we observe the evolution of the network, in L equispaced subintervals, $I_1, ..., I_L$, of length $W = \frac{t-t_0}{L}$. For each of these subintervals I_l, with $l = 1, ..., L$, we count the number of impulses K_l that are emitted by neurons in the network in that time interval. Then the following quantity

$$R_l = \frac{1}{N} \frac{K_l}{W}, \tag{2.27}$$

is an average index of the state of activity of the network. For $L \to +\infty$, that is measuring on increasingly smaller intervals $W \to 0$, (2.27) can be written, in a distributional sense, as a linear superposition of delta functions centered on the instants $\{t_1, ..., t_M\}$ in which the pulses are emitted in the time interval $[t_0, t]$.

$$r(t) = \frac{1}{N}\sum_{k=1}^{M}\delta(t - t_k), \tag{2.28}$$

This object is defined as *instantaneous population rate* or *population firing rate*, that is, the average instantaneous rate of emission of impulses by neurons in the population. Therefore we can rewrite the equation of the field $S(t)$ in (2.24) as

$$\tau_d \dot{s}(t) + s(t) = r(t), \tag{2.29}$$

where we just recall the capital S with the lowercase s since we are referring to the macroscopic variable. Eq. (2.29) expresses the important relation between the firing rate $r(t)$ and the field $s(t)$.
Another macroscopic quantity of particular interest is the average membrane potential of the network, defined as:

$$v(t) = \frac{1}{N}\sum_{j=1}^{N} V_j(t), \tag{2.30}$$

that is, as the average of the membrane potentials of all neurons of the network.

2.5 Exact macroscopic reduced model for fully-coupled Network

In this section we show how to reduce, *exactly*, in the thermodynamic limit $N \to \infty$, the infinite system of equations given by (2.25) to a system of few differential equations, which express the evolution of the average macroscopic quantities of the network: the instantaneous population rate $r(t)$ defined in (2.28), the mean membrane potential $v(t)$ defined in (2.30) and the synaptic activation field $s(t)$ defined in (2.29).
The results showed in this section are the content of the article by Montbrió-Pazó-Roxin [10], which extended the results obtained previously by Ott-Antonsen for a phase oscillator network [11] to a network of QIF neurons.

In the limit of infinite neurons we consider the network as a continuum, that is, as a *neural mass* described through a probability density function $\rho(V, \eta, t)$. The parameters η_i become a continuous random variable η distributed according to a certain probability density function $g(\eta)$ which remains unchanged in time. In this context $\rho(V|\eta, t)dV$ is the fraction of neurons, characterized by a given value of η, which, at a given time t, have a membrane potential between V and $V + dV$. Therefore $\int_{-\infty}^{+\infty} \rho(V|\eta, t)dV = g(\eta)$ represents the fraction of neurons characterized by a given value of η at time t and hence this quantity is time-independent.
We consider η as a fixed parameter that, for shortness, we will not explicitly indicate in the text when not necessary.
Let be:

$$[a, b] = \{V \in \mathbb{R} : \quad V = V(t, V_0) \quad for \quad V_0 \in [a_0, b_0]\} \tag{2.31}$$

the interval of the points $V = V(t, V_0)$ reached at the instant t by the paths that originate from the interval $[a_0, b_0]$ at the initial instant $t = t_0$.
Since each trajectory corresponds to a neuron, we can assume that the number of neurons is conserved:

$$\int_{a_0}^{b_0} \rho(V_0, t_0)dV_0 = \int_a^b \rho(V, t)dV. \tag{2.32}$$

By changing the variable $V = V(t, V_0)$ in the integral of the member to the right of equation (2.32) we obtain

$$\int_{a_0}^{b_0} \rho(V_0, t_0)dV_0 = \int_{a_0}^{b_0} \rho(V(t, V_0), t)\frac{\partial V}{\partial V_0}dV_0 \tag{2.33}$$

from which it follows, for the arbitrariness of the interval $[a_0, b_0]$ that

$$\rho(V_0, t_0) = \rho(V(t, V_0), t)\frac{\partial V}{\partial V_0}. \tag{2.34}$$

Finally, deriving with respect to t we obtain

$$\begin{aligned} 0 &= \Big(\frac{\partial \rho}{\partial V}\dot{V} + \frac{\partial \rho}{\partial t}\Big)\frac{\partial V}{\partial V_0} + \rho\frac{\partial}{\partial t}\frac{\partial V}{\partial V_0} = \Big(\frac{\partial \rho}{\partial V}\dot{V} + \frac{\partial \rho}{\partial t}\Big)\frac{\partial V}{\partial V_0} + \rho\frac{\partial \dot{V}}{\partial V_0} = \\ &= \Big(\frac{\partial \rho}{\partial V}\dot{V} + \frac{\partial \rho}{\partial t}\Big)\frac{\partial V}{\partial V_0} + \rho\frac{\partial V}{\partial V_0}\frac{\partial \dot{V}}{\partial V} \end{aligned} \tag{2.35a}$$

from which follows the continuity equation :

$$\frac{\partial}{\partial t}\rho + \frac{\partial}{\partial V}\Big[\rho(V^2 + \eta + JS + I_e)\Big] = 0 \tag{2.36}$$

where we explicitly expressed the velocity field

$$\dot{V} = V^2 + \eta + JS + I_e \tag{2.37}$$

according with the equation (2.23). The continuity equation (2.36) and the synaptic field equation (2.24) represent together the continuous formulation of the neuronal network (2.25) in the thermodynamic limit ($N \to +\infty$).
We observe that equation (2.36) admits a trivial stationary solution in the case of external constant current. In fact, a time independent density function, $\rho_0(V|\eta)$, solves equation (2.36) if and only if it satisfies $\partial_V[(V^2 + \eta + JS + I_e)\rho] = 0$. This is trivially true when the density ρ_0, for any given value of η, has the form

$$\rho_0(V|\eta) \propto \frac{1}{V^2 + \eta + JS + I_e}; \tag{2.38}$$

this corresponds to a Lorentzian distribution with respect to the membrane potential. Physically, Lorentzian density distribution simply means that the tonics neurons characterized by the same η value will be distributed on the axis V with a density inversely proportional to the speed $\dot{V}$ they possess.
Proceeding as in [10], we also assume in the non-stationary case that, regardless of the initial conditions, equations (2.36) and (2.24) redistribute the membrane potentials of the QIF neural mass in a form similar to the stationary solution (2.38). More precisely we proceed with the following ansatz:

Regardless of the form of the initial distribution $\rho(V, \eta, 0)$, the solutions of (2.36) and (2.24) converge to a Lorentzian density function with respect to the membrane potentials:

$$\rho(V|\eta, t) = \frac{1}{\pi} \frac{x(\eta, t)}{[V - y(\eta, t)]^2 + x(\eta, t)^2} \tag{2.39}$$

where $x(\eta, t) \geq 0$ is the half width at half maximum (HWHM).

In practice, this Lorentzian Ansatz (LA) consists of an assumption on the form of the attractor of the system. This attractor is a sub-variety of all possible density functions. Assuming that this hypothesis is valid, we can therefore focus on the study of the dynamics on this subvariety, that is, study how the statistical quantities $x(\eta, t)$ and $y(\eta, t)$ evolve. As we shall see, under certain hypotheses the macroscopic dynamics on the attractor admits a finite-dimensional description, although it has an infinite dimension (the set of all possible $x(\eta, 0)$, $y(\eta, 0)$, the initial conditions). We will discuss the validity of the Lorentzian Ansatz at the end of this chapter.
Applying the LA, we can express the quantities $r(t)$ e $v(t)$ in the following way. Since the Lorentzian distribution of the membranes is symmetric and centered on $y(\eta, t)$, for each η and t fixed, then the following relationship holds:

$$v(\eta, t) = y(\eta, t) = P.V \int_{-\infty}^{+\infty} \rho(V|\eta, t) V dV \tag{2.40}$$

where $P.V$ indicates the Cauchy principal value of the integral.
Therefore the average membrane potential of the network is expressed through the following integral relation

$$v(t) = \int_{-\infty}^{+\infty} y(\eta, t) g(\eta) d\eta \tag{2.41}$$

In the QIF model a neuron emits a pulse when it reaches the infinite potential value. Therefore we can calculate the firing rate, for each value of η and t, as the limit for the value of membrane potential that tends to infinity of the flow of the neural mass

$$r(\eta,t)=\rho(V\to+\infty|\eta,t)\dot{V}(V\to+\infty|\eta,t) \tag{2.42}$$

that we can write through the relations (2.39) and (2.37) as

$$r(\eta,t)=\lim_{V\to+\infty}\Big[\frac{1}{\pi}\frac{x(\eta,t)}{[V-y(\eta,t)]^2+x(\eta,t)^2}(V^2+\eta+JS+I_e)\Big] \tag{2.43}$$

In the limit in (2.43) the dominant infinite terms of the second order in V are compensated, therefore we deduce the following important relation

$$r(\eta,t)=\frac{x(\eta,t)}{\pi}. \tag{2.44}$$

Finally, the instantaneous population rate is expressed through the following integral

$$r(t)=\frac{1}{\pi}\int_{-\infty}^{+\infty}x(\eta,t)g(\eta)d\eta. \tag{2.45}$$

We proceed by replacing the LA relationship expressed by (2.39) within the continuity equation (2.36) and we rewrite the continuity equation as

$$-\frac{\partial}{\partial t}\rho=\frac{\partial}{\partial V}\Big[\rho(V^2+\Lambda)\Big] \tag{2.46}$$

where $\Lambda=\eta+JS+I_e$, independent of V. The member of left, through (2.39), becomes:

$$-\frac{1}{\pi}\frac{1}{[(V-y)^2+x^2]^2}\Big\{\dot{x}[(V-y)^2+x^2]-x[-2\dot{y}(V-y)+2x\dot{x}]\Big\}. \tag{2.47}$$

The right member becomes:

$$\begin{aligned}\Big(\frac{\partial}{\partial V}\rho\Big)(V^2+\Lambda)+2V\frac{1}{\pi}\frac{x}{(V-y)^2+x^2}=\\ =\frac{1}{\pi}\Big(\frac{-2(V-y)x}{[(V-y)^2+x^2]^2}(V^2+\Lambda)+\frac{2Vx}{(V-y)^2+x^2}\Big).\end{aligned} \tag{2.48}$$

Therefore, by equating (2.47) and (2.48), and assuming $(x, V-y) \neq (0,0)$, we get the following relation

$$\begin{aligned} -\dot{x}[(V-y)^2 + x^2] + 2x[x\dot{x} - \dot{y}(V-y)] = \\ = -2(V-y)x(V^2+\Lambda) + 2Vx[(V-y)^2 + x^2], \end{aligned} \tag{2.49}$$

which must be satisfied $\forall\ V \in (-\infty, +\infty)$. Necessarily, the terms of each power order of the variable V must vanish. Cubic terms in variable V vanish. The vanishing of square order terms means that the following equation holds

$$\dot{x} = 2xy. \tag{2.50}$$

From those of the first order we get $2\dot{x}y - 2x\dot{y} = 2xy^2 + 2x^3 - 2x\Lambda$, from which applying the equation (2.50) and assuming $x \neq 0$ finally we obtain:

$$\dot{y} = y^2 - x^2 + \Lambda. \tag{2.51}$$

The zero-order term vanish if the equations (2.50) and (2.51) are satisfied, therefore it does not contain any further information than the first and second order terms.
Introducing the complex variable $w = x + iy$ we can write in compact form the (2.50) and (2.51) in the following way

$$\dot{w} = i(\Lambda - w^2). \tag{2.52}$$

Summarizing, under the hypothesis that the dynamics of the continuous system formed by (2.36) and (2.24) distributes the membrane potentials of neurons in a Lorentzian form as in (2.39), then the macroscopic dynamics can be described exactly by the following reduced system

$$\begin{aligned} \frac{\partial}{\partial t} w(\eta, t) = i[\eta + Js(t) + I_e(t) - w(\eta, t)^2], \\ \tau_d \frac{\partial}{\partial t} s(t) + s(t) = \frac{1}{\pi} \int_{-\infty}^{+\infty} x(\eta, t) g(\eta) d\eta, \end{aligned} \tag{2.53}$$

in terms of average quantities $w(\eta,t) = x(\eta,t) + iy(\eta,t)$ and $s(t)$.
We observe that for the correct derivation of the macroscopic model (2.53) it is necessary to assume $x(\eta,t) \neq 0\ \forall \eta \in \mathbb{R}$, $t > 0$. To ensure that $w(\eta,0) = x(\eta,0) + iy(\eta,0)$, evolving with the law (2.53), really represents a physical solution of our problem for any $t > 0$ we must impose that $Re(w(\eta,t)) \geq 0$, $\forall t > 0$, as it defines the size of the distribution, namely, through (2.45), the firing rate. It can be shown [11], that if the real functions $x(\eta,0), y(\eta,0)$ of real variable η satisfy

1. $x(\eta,0) \neq 0 \qquad \forall \eta \in \mathbb{R}$;
2. $x(\eta,0)$ and $y(\eta,0)$ are analytically continued from $\eta \in \mathbb{R}$ to $\eta \in \bar{\mathbb{I}}^- = z \in \mathbb{C} : Im(z) \leq 0$ without singularities and these extensions satisfy

$$\lim_{Im(\eta)\to-\infty} x(\eta,0) = \lim_{Im(\eta)\to-\infty} y(\eta,0) = 0 \tag{2.54}$$

then $w(\eta,t)$, evolving through (2.53), satisfies (1), (2), for all $t > 0$. In (2) the lower half-plane is chosen to ensure that the quantity $x(\eta,t) = Re(w(\eta,t))$ remains positive. In fact from equation (2.53), extending η to a complex variable, $\eta = Re(\eta) + iIm(\eta)$, we have $\frac{\partial}{\partial t}x(\eta,t) = -Im(\eta) + 2x(\eta,t)y(\eta,t)$ which is positive in $x = 0$. The law of evolution described by (2.53) prevents w from crossing the imaginary axis and therefore ensures to remain confined in $Re(w) \geq 0$. We can therefore precisely define the shape of the LA attractor as:

$$M = \Big\{\rho(V|\eta,0) = \frac{1}{\pi}\frac{x(\eta,0)}{[V - y(\eta,0)]^2 + x(\eta,0)^2} : w = x + iy\ satisfy\ (1),(2)\Big\}.$$

To eliminate the dependence in η in (2.45) and (2.41), we assume that it is distributed according to a Lorentzian density

$$g(\eta) = \frac{1}{\pi}\frac{\Delta}{(\eta - H)^2 + \Delta^2}, \tag{2.55}$$

where H is the position of the peak and $\Delta \geq 0$ the amplitude parameter. We underline that this hypothesis is uncorrelated with the previous LA on

the distribution of membrane potentials. The reason why we assume (2.55) is because, with this particular choice, we are able to express analytically the integral (2.45) and (2.41).
We extend the real variable η in a complex variable, $\eta = \eta_r + i\eta_i$, and we extend analytically $w(\eta, t)$ and $g(\eta)$ from $\eta \in \mathbb{R}$ to the complex half-plane with negative imaginary part, $\eta \in \bar{\mathbb{I}}^-$. The function $g(\eta) : \bar{\mathbb{I}}^- \to \mathbb{C}$ admits a single pole of order 1 in $\eta = H - i\Delta$, as shown by the following decomposition

$$g(\eta) = \frac{1}{\pi} \frac{\Delta}{[\eta - (H + i\Delta)][\eta - (H - i\Delta)]}. \tag{2.56}$$

We proceed by calculating the integrals (2.45) and (2.41) through the residue theorem. We consider the curve $\gamma = \gamma_1\gamma_2$ — where $\gamma_1(s) = s$ with $s \in [-|\eta|, +|\eta|]$ parameterizes the real segment and $\gamma_2(s) = |\eta| e^{-is}$ with $s \in [0, \pi]$ parameterizes a semicircle — that winds the pole of $g(\eta)$ clockwise. By integrating on this curve and calculating the limit for $|\eta| \to +\infty$ we get

$$r(t) = \frac{1}{\pi} \int_{-\infty}^{+\infty} x(\eta, t) g(\eta) d\eta = \frac{1}{\pi} [-2i\pi Res_x(H - i\Delta)] = \frac{x(H - i\Delta)}{\pi}, \tag{2.57}$$

$$v(t) = \int_{-\infty}^{+\infty} y(\eta, t) g(\eta) d\eta = [-2i\pi Res_y(H - i\Delta)] = y(H - i\Delta), \tag{2.58}$$

from which it follows

$$w(H - i\Delta, t) = \pi r(t) + iv(t), \tag{2.59}$$

and therefore the firing rate $r(t)$ and the average membrane potential $v(t)$ depend only on the value of w calculated on the pole of $g(\eta)$ located in the lower half-plane. Consequently, to get one relation dependent only on time t it is sufficient to evaluate the equation (2.53) for $\eta = H - i\Delta$.

$$\begin{aligned} \frac{\partial}{\partial t}[\pi r(t) + iv(t)] &= i\Big\{H - i\Delta + Js(t) + I_e(t) - [\pi^2 r(t)^2 - v(t)^2 + i2\pi r(t)v(t)]\Big\}, \\ \tau_d \frac{\partial}{\partial t} s(t) + s(t) &= \frac{1}{\pi} \int_{-\infty}^{+\infty} x(\eta, t) g(\eta) d\eta, \end{aligned} \tag{2.60}$$

At this point, depending on the assumptions we make about the synaptic dynamics, we get different *reduced models* for the population of QIF neurons.

Instantaneous synapses, $\tau_d = 0$:

We assume that the interaction between two neurons is a completely impulsive event. In this case, therefore, in the field equation (2.29) we choose $\tau_d = 0$, obtaining $s(t) = r(t)$. So, breaking down the equation (2.60) in real and imaginary part we obtain the following real two-dimensional system:

$$\begin{cases} \dot{r} = \frac{\Delta}{\pi} + 2rv \\ \dot{v} = v^2 + H + Jr + I_e - \pi^2 r^2 \end{cases} \tag{2.61}$$

The nonlinear system (2.61) describes exactly, in macroscopic terms, a population of QIF neurons within the limit of an infinite number of neurons. The equation of $v(t)$ looks like the equation (2.10) of evolution of a single QIF neuron of the network characterized by the average H value of the excitability η_i of the network neurons. In this equation, the nonlinear term $\pi^2 r^2$, together with the evolution of the equation of $r(t)$, formalizes the reset rule at the network level; in fact, this term prevents an uncontrolled growth of the variable $v(t)$ by acting as a negative correction which leads to a decrease in $v(t)$ when network activity (namely $r(t)$) increases.

Exponentially decaying synapses, $\tau_d > 0$:

Now we assume the interaction between neurons as an impulsive event that decays exponentially. In this case, therefore, in the field equation (2.29) we choose $\tau_d > 0$. We can reduce, in the thermodynamic limit of infinite QIF neurons, the system of equations (2.25) to the following system of ordinary differential equations

$$\begin{cases} \dot{r} = \frac{\Delta}{\pi} + 2rv \\ \dot{v} = v^2 + H + Js + I_e - \pi^2 r^2 \\ \dot{s} = \frac{1}{\tau_d}[-s + r]. \end{cases} \tag{2.62}$$

The variable s models the average dynamics of the synapses, which in this case results in an exponential decay, with decay constant τ_d, perturbed by the positive action of the firing rate r. Furthermore, the s field affects the

average membrane of the network by acting negatively or positively on it according to the type of inhibitory synapses ($J < 0$) or excitatory ($J > 0$). The fixed points of the system (2.62) are exactly the same as in the case of instantaneous synapses. In fact, from $\dot{s} = 0$ it follows that $s = r$. So the introduction of an exponentially decaying synapse does not change the values of the fixed points but it can change the stability and the bifurcation process.

2.5.1 Heterogeneous synaptic weights

Equation (2.60) has been derived assuming the currents η_i randomly distributed in according with (2.55). Let us now distribute the coupling J_i, that is, we consider heterogeneity on the synaptic weights of the network. In this case the network dynamics of QIF neurons is given by:

$$\begin{cases} \dot{V}_i(t) = V_i(t)^2 + \eta + J_i S(t) + I_e(t), \qquad i = 1, ..., N, \\ \tau_d \dot{S}(t) + S(t) = \frac{1}{N} \sum_{k=1}^{M} \delta(t - t_k), \end{cases} \tag{2.63}$$

where now η is a fixed parameter and the couplings J_i are distributed in according with:

$$h(J) = \frac{1}{\pi} \frac{\Gamma}{(J - \bar{J})^2 + \Gamma^2}. \tag{2.64}$$

We can now repeat exactly the procedure of the previous paragraph to obtain the firing rate equations:

$$\begin{cases} \dot{r} = \frac{\Gamma r}{\pi} + 2rv \\ \dot{v} = v^2 + \eta + \bar{J}s + I_e - \pi^2 r^2 \\ \dot{s} = \frac{1}{\tau_d}[-s + r], \end{cases} \tag{2.65}$$

where the difference with the model (2.62) lies in the term $\frac{\Gamma}{\pi}$ which is now multiplied by $r(t)$.
Equations (2.65) constitute the exact reduced model for a fully-coupled network of QIF neurons with heterogeneity on the synaptic weights and exponential synaptic decay.

2.6 Validity of the Lorentzian ansatz

In this section we clarify why the Lorentzian Ansatz (2.39) holds for ensembles of QIF neurons.
In the first chapter we explained how, through the Ott Antonsen's ansatz, it is possible to derive an exact finite-dimensional model from a system of coupled oscillators, in the thermodynamic limit of infinite oscillators. As we have already shown, the link between the QIF neurons and the phase oscillators is highlighted by the change of variable $V_i = tan(\theta_i/2)$. In terms of phase variables, the QIF neuron system given by (2.23) takes the form:

$$\dot{\theta}_i = (1 - cos\theta_i) + (1 + cos\theta_i)[\eta_i + JS(t) + I], \qquad i = 1, ..., N. \tag{2.66}$$

In this new reference the LA on the form of the distribution of membrane potentials in (2.39) becomes the following Ott-Antonsen (OA) ansatz on the distribution of the oscillator phases on the unit circle:

$$\tilde{\rho}(\theta|\eta, t) = \frac{1}{2\pi} Re\Big(\frac{1 + \alpha(\eta, t)e^{i\theta}}{1 - \alpha(\eta, t)e^{i\theta}}\Big) \tag{2.67}$$

where the function $\alpha(\eta, t)$ is related to our $w(\eta, t) = x(\eta, t) + iy(\eta, t)$ through the relation

$$\alpha(\eta, t) = \frac{1 - w(\eta, t)}{1 + w(\eta, t)}. \tag{2.68}$$

The conformal map $W(z) = \frac{1-z}{1+z}$ transforms the complex right half-plane into the complex unit disk $\{Re(z) \geq 0\} \to \{|z| \leq 1\}$. Using the conformal map W, the density in terms of phase oscillators of the OA ansatz in (2.67) is transformed into the density in terms of membrane potentials of the LA for QIF neurons in (2.39); they are two equivalent representations of the Poisson kernel, one defined in the right half-plane and the other in the unit disk.
The key observation supporting the applicability of the LA is the fact that Eq. (2.67) turns out to be the ansatz discovered by Ott and Antonsen [11]. According to the OA theory in the thermodynamic limit, the dynamics of the class of systems 1.1 generally converges to the OA manifold [Eq. (2.67)]. In the original work of Ott-Antonsen, showed in Section. 1.3.2, this result

has been proven if the phase dynamics $\mathbb{H}(t)$ does not depend on the specific oscillator η_i. On the other hand, in our case, for Eq. (2.66), we have $\omega_i = 1 + \eta_i + JS + I$ and $\mathbb{H}_i(\eta_i, t) = i(-1 + \eta_i + JS + I)$, involving an intrinsic dependence between an oscillator's phase and its dynamics. The extent of the OA ansantz for this type of parameter-dependent oscillatory systems $\mathbb{H}_i(\eta_i, t)$ is proven in [77]. This result proves the equivalence between the Lorentzian ansatz (2.39) for network of QIF neurons and the OA ansatz.

Chapter 3

Theta-nested gamma oscillations in next generation neural mass models

Abstract:

Theta-nested gamma oscillations have been reported in many areas of the brain and are believed to represent a fundamental mechanism to transfer information across spatial and temporal scales. In a series of recent experiments in vitro it has been possible to replicate with an optogenetic theta frequency stimulation several features of cross-frequency coupling among theta and gamma rhythms observed in behaving animals. In order to reproduce the main findings of these experiments we have considered a new class of neural mass models able to reproduce exactly the macroscopic dynamics of spiking neural networks. In this framework, we have examined two set-ups able to support collective gamma oscillations: the pyramidal interneuronal network gamma (PING) and the interneuronal network gamma (ING). In both set-ups we observe the emergence of theta-nested gamma oscillations by driving the system with a sinusoidal theta-forcing in proximity of a Hopf bifurcation. These mixed rhythms display always phase amplitude coupling. However 2 different types of nested oscillations can be identified: one characterized by a perfect phase locking between theta and gamma rhythms, corresponding to an overall periodic behavior; another one where the locking is imperfect and the dynamics is quasi-periodic or even chaotic. From our analysis it emerges that the locked states are more frequent in the ING set-up. In agreement

with the experiments, we find theta-nested gamma oscillations for forcing frequencies in the range [1:10] Hz, whose amplitudes grow proportionally to the forcing one and which are clearly modulated by the theta phase. At variance with experimental findings, the gamma-power peak does not shift to higher frequencies by increasing the theta frequency. This effect can be obtained, in or model, only by incrementing, at the same time, also the noise or the forcing amplitude.

3.1 Introduction

Oscillations in the brain, reflecting the underlying dynamics of neural populations, have been measured over a broad frequency range [96]. Particularly studied are γ-rhythms (30-120 Hz), due to their ubiquitous presence in many regions of the brain, irrespectively of the species [97], and for their relevance for cognitive tasks [98] and neuronal diseases [57, 99].
Inhibitory networks have been shown to represent a fundamental ingredient for the emergence of γ oscillations [97, 100]. Indeed, inhibition is at the basis of the two most known mechanisms: pyramidal interneuronal network gamma (PING) and interneuronal network gamma (ING) [101]. The ING mechanism is observable in purely inhibitory networks in the presence of few ingredients: recurrent connections, a time scale associated with the synaptic $GABA_A$ receptors and an excitatory drive sufficiently strong to lead the neurons supra-threshold [97]. The collective oscillations (COs) emerge when a sufficient number of neurons begins to fire within a short time window and generate almost synchronous inhibitory post-synaptic potentials (IPSPs) in the post-synaptic interneurons. The inhibited neurons fire again when the IPSPs have sufficiently decayed and the cycle will repeat. Thus, the main ingredients dictating the frequency of the COs in the ING set-up are: the kinetics of the IPSPs and the excitatory drive [102]. On the other hand the PING mechanism is related to the presence of an excitatory and an inhibitory population, in this case COs emerge whenever the drive on the excitatory neurons is sufficiently strong to induce an almost synchronous excitatory volley that in turn elicits an inhibitory one. The period of the COs is thus determined by the recovery time of the pyramidal neurons from the stimulus received from the inhibitory population [8]. A peculiarity of this mechanism, observed both *in vivo* and *in vitro* experiments, is that there is a delay between the firing of the pyramidal cells and the interneuronal burst [97].

In several parts of the brain, one can observe that γ oscillations are modulated by θ oscillations, with θ frequencies corresponding to 4-12 Hz in rodents and to 1-4 Hz in humans. Specific examples have been reported for the hippocampus of rodents in behaving animals and during rapid eye movement (REM) sleep [103–107], for the visual cortex in alert monkeys [108], for the neocortex in humans [109] etc. This is an example of a more general mechanism of cross-frequency coupling (CFC) between a low and a high frequency rhythm, which is believed to have a functional role in the brain [110]. In particular, low frequency rhythms (such as θ) are usually involving broad brain regions and are entrained to external inputs and/or to cognitive events; on the other hand the high frequency activity (e.g. the γ-rhythm) reflects local computation activity. Thus CFC can represent an effective mechanism to transfer information across spatial and temporal scales [110, 111]. Four different types of CFC of interest for electrophysiology, have been listed in [112]: phase-phase, phase-frequency, phase-amplitude and amplitude-amplitude couplings (PPC, PFC, PAC, and AAC). Two more types of CFCs have later been added as emerging from the analysis of coupled nonlinear oscillators [113] and coupled neural mass models [114]: frequency-frequency and amplitude-frequency coupling (FFC and AFC).

In this chapter we will consider θ-nested γ oscillations, where specific features of the γ oscillations are correlated to the θ phase. In particular we will analyze PPC, PFC and PAC between θ and γ rhythms. The most studied CFC mechanism is the PAC, which corresponds to the modification of the amplitude (or power) of γ-waves induced by the phase of the θ-oscillations. This mechanism has been reported in the primary visual cortex of anaesthetized macaques subject to naturalistic visual stimulation [115], as well as during the formation of new episodic memories in the human hippocampus [116]. As discussed in [112], the θ phase can often modulate both amplitude (PAC) and frequency (PFC) of the γ oscillations, therefore these two mechanisms can occur at the same time. PPC, which refers to n:m phase locking between γ and θ phase oscillations [117], has been identified in the rodent hippocampus during maze exploration [105].

Our study is mostly motivated by recent optogenetic experiments revealing PAC in areas CA1 and CA3 of the hippocampus and in the medial enthorinal cortex (MEC) [13, 118–120]. These experiments have shown that a sinusoidal optogenetic stimulation at θ-frequency of the circuits *in vitro* is able to reproduce several features of θ-nested γ oscillations, usually observed in behaving rats [121]. All these experiments suggest that inhibition has a key

role in generating this cross-frequency rhythm; however both ING [119] and PING [13,120] mechanisms have been invoked to explain locally generated γ oscillations.

PING and ING oscillation mechanisms have been qualitatively reproduced by employing heuristic neural mass models [8, 122]. However, these standard firing rate models do not properly describe the synchronization and desynchronizaton phenomena occurring in neural populations [61, 123, 124]. In Section [2.5] we have delineated a new generation of neural mass models, which are able to exactly reproduce the network dynamics of spiking neurons of type I, for any degree of synchronization among the neurons [10,125–127]. In particular, for purely inhibitory networks, these mean-field models have been able to reproduce the emergence of COs, observed in the corresponding networks, without the inclusion of an extra time delay [123], as well as the phenomenon of event related synchronisation and desynchronisation [61].

Our main aim is to understand how θ-nested γ oscillations can emerge when a PING or ING mechanism is responsible for the fast oscillations and which differences can be expected in the population dynamics in the two cases. Therefore we will consider the new class of neural mass models introduced in [10] in two configurations: namely, a purely inhibitory population (ING set-up) and two coupled excitatory-inhibitory populations (PING set-up). In both configurations we will examine the system response to an external sinusoidal θ-drive.

Section 3.2 is devoted to the introduction of different spiking network configurations of Quadratic Integrate-and-Fire (QIF) neurons able to generate γ COs via PING and ING mechanisms and to the introduction of their corresponding exact neural mass formulations. A detailed bifurcation analysis of the neural mass models for the PING and ING set-ups, in the absence of any external forcing, is reported in Section 3.3. The PAC mechanism is analysed and discussed in Section 3.4. First, by considering different types of PAC states (namely, phase locked or unlocked) and second, by comparing our numerical results for PAC dynamics with experimental findings reported in [13] and [120], for the CA1 region of the hippocampus under sinusoidal optogenetic stimulations. Finally, a discussion of our results and of their implications, as well as of possible future developments, will be presented in Section 3.5. The results reported in the chapter are mostly devoted to supercritical Hopf bifurcations, however a specific example of a sub-critical Hopf bifurcation leading to COs is discussed for the PING set-up in Appendix A. Further network configurations ensuring the emergence of COs via PING

mechanism are presented in Appendix B.

3.2 Models and Bifurcation analysis

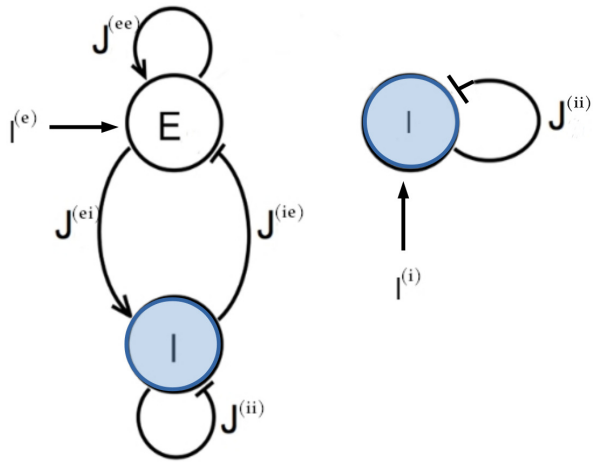

Figure 3.1: **Network topologies** Two different network configurations have been investigated: on the left side, an excitatory population (E) and an inhibitory population (I) form a circuit that can generate oscillatory output (PING set-up); on the right side one inhibitory population (I) is coupled to itself with an inhibitory coupling (ING set-up). In both cases an external current $I^{(l)}$ impinging on one single population has been considered.

3.2.1 Network Models

In this chapter we want to compare the two principal mechanisms at the basis of the emergence of collective oscillatory dynamics in neural networks: namely, the PING and ING mechanisms. Therefore we will consider QIF neurons in the two following set-ups: an excitatory and an inhibitory population coupled via instantaneous synapses (PING configuration) and a single inhibitory population interacting via post-synaptic potentials (PSPs) with exponential profile (ING configuration). The corresponding network configurations are shown in Fig. (3.1). Moreover, the neurons are assumed to be fully coupled. As we will show in the following, both these two configurations

support the emergence of COs.
The dynamics of the membrane potentials of the QIF neurons in the PING configuration is given by

$$\begin{aligned}
\tau_m^{(e)}\dot{V}_k^{(e)} &= \left(V_k^{(e)}\right)^2 + \eta_k^{(e)} + \tau_m^{(e)}\left[J^{(ee)}S^{(e)} - J^{(ie)}S^{(i)}\right] + I^{(e)}(t) \quad k = 1, \ldots, N^{(e)} \\
\tau_m^{(i)}\dot{V}_j^{(i)} &= \left(V_j^{(i)}\right)^2 + \eta_j^{(i)} + \tau_m^{(i)}\left[J^{(ei)}S^{(e)} - J^{(ii)}S^{(i)}\right] + I^{(i)}(t) \quad j = 1, \ldots, N^{(i)} \\
S^{(l)} &= \frac{1}{N^{(l)}}\sum_{t_m^{(l)}} \delta(t - t_m^{(l)}) \qquad l \in \{e, i\} \quad ; \qquad (3.1)
\end{aligned}$$

where the super-scripts e (i) denote the excitatory (inhibitory) population, $\tau_m^{(e)} = 20$ ms ($\tau_m^{(i)} = 10$ ms) is the excitatory (inhibitory) membrane time constant, $\eta_k^{(l)}$ is the excitability of the k-th neuron of population l, $J^{(ln)}$ is the strength of the synaptic coupling of population l acting on population n. The term $I^{(l)}(t)$ represents a time-dependent external current applied to the population l; usually we have considered the external drive to be applied to the excitatory population only, i.e. $I^{(e)}(t) \neq 0$ and $I^{(i)}(t) = 0$. The synaptic field $S^{(l)}(t)$ is the linear super-position of all the pulses $Y(t)$ emitted in the past within the l population, $Y(t)$ being δ-functions in the present case. Furthermore, since the neurons are fully coupled, each neuron will be subject to the same synaptic field [4]. The emission of the m-th spike in the network occurs at time $t_m^{(l)}$ whenever the membrane potential of a generic neuron j reaches infinity, i.e. $V_j^{(l)}(t_m^{(l)-}) \to +\infty$, while the reset mechanism is modeled by setting $V_j^{(l)}(t_j^{(l)+}) \to -\infty$, immediately after the spike emission.
The main part of our analysis of the PING set-up will be devoted to networks with self-activation only (i.e. where $J^{(ii)} = 0$), a configuration which is known to favour the emergence of collective oscillations [8, 128, 129]. However, as discussed in Appendix B, we have found that COs can arise in different PING set-ups: in the presence of self-inhibition only (i.e. with $J^{(ii)} \neq 0$ and $J^{(ee)} = 0$) and in the absence of both self-activation and inhibition (i.e. with $J^{(ee)} = J^{(ii)} = 0$).
For what concerns the purely inhibitory network, the membrane potential dynamics of the j-th neuron is ruled by the following equations:

$$\begin{aligned}\tau_m^{(i)}\dot{V}_j^{(i)} &= \left(V_j^{(i)}\right)^2 + \eta_j^{(i)} - \tau_m^{(i)} J^{(ii)} s^{(i)} + I^{(i)}(t) \\ \tau_d \dot{S}^{(i)} &= -S^{(i)} + \frac{1}{N^{(i)}} \sum_{t_m^{(l)}} \delta(t - t_m^{(i)}) \quad ,\end{aligned} \tag{3.2}$$

where $\tau_m^{(i)} = 10$ ms. In this case the synaptic field $S^{(i)}(t)$ is the super-position of the exponential IPSPs $Y(t) = \mathrm{e}^{-t/\tau_d}/\tau_d$ emitted in the past, where we set $\tau_d = 10$ ms.
As often done in previous chapters, we assume that the neuron excitabilities $\eta_i^{(l)}$ are randomly distributed according to a Lorentzian probability density function (PDF)

$$g^{(l)}(\eta) = \frac{1}{\pi} \frac{\Delta^{(l)}}{(\eta - H^{(l)})^2 + (\Delta^{(l)})^2} \ , \tag{3.3}$$

where $H^{(l)}$ is the median and $\Delta^{(l)}$ is the half-width half-maximum (HWHM) of the PDF. Therefore each population will be composed of neurons supra- (with $\eta_j^{(l)} > 0$) and sub-threshold (with $\eta_j^{(l)} < 0$), the percentage of one group with respect to the other being determined by the Lorentzian parameters. For the PING set-up we fix $\Delta^{(e)} = \Delta^{(i)} = 1$, whereas varying $H^{(e)}$ and $H^{(i)}$. For the ING set-up we fix $\Delta^{(i)} = 0.3$ and analyze the dynamics by varying $H^{(i)}$.
The dynamical equations are integrated by employing a 4th order Runge-Kutta method in the absence of noise with a time step $dt = 0.002$ ms ($dt = 0.001$ ms) for the PING (ING) set-up. Moreover, we define a threshold $V_p = 100$ and a reset value $V_r = -100$. Whenever the membrane potential V_j of the j-th neuron overcomes V_p at a time t_p, it is reset to V_r for a refractory period equal to $2/V_j$. At the same time the firing time is estimated as $t_p + 1/V_j$; for more details see [10]. The membrane potentials are initialized from a random flat distribution defined over the range $[-100 : 100]$, while the excitabilities are randomly chosen from the Lorentzian distribution (3.3). For instantaneous synapses, we will only employ the following two indicators to characterize the macroscopic dynamics:

$$r^{(l)}(t) = \frac{M^{(l)}(\Delta t)}{N^{(l)} \Delta t} \quad , \quad v^{(l)}(t) = \frac{1}{N^{(l)}} \sum_j^{N^{(l)}} V_j^{(l)}(t), \tag{3.4}$$

which represent the average population activity and the average membrane potential of the l-th population, respectively. In particular the average population activity of the $l-$network $r^{(l)}(t)$ is given by the number of spikes $M^{(l)}(\Delta t)$ emitted in a time window Δt, divided by the total number of neurons in such population. For finite IPSPs we also consider the synaptic field $s^{(l)}(t)$. Furthermore, the emergence of COs, corresponding to periodic motions of $r^{(l)}(t)$ and $v^{(l)}(t)$, are characterized in terms of their frequencies $\nu^{(l)}$. We assume that the driving current, mimicking the θ-stimulation in the optogenetic experiments, is a purely sinusoidal excitatory current of the following form

$$I_\theta(t) = \frac{I_0}{2}[1 - \cos(2\pi\nu_\theta t)] \tag{3.5}$$

where ν_θ is the forcing frequency, usually considered within the θ-range, i.e. $\nu_\theta \in [1 : 10]$ Hz. In this context a theta phase associated with the forcing field can be defined as $\theta(t) = \mathrm{mod}(2\pi\nu_\theta t, 2\pi)$. For the PING configuration we set $I^{(e)}(t) = I_\theta(t)$ and $I^{(i)}(t) \equiv 0$ and for the ING set-up $I^{(i)}(t) = I_\theta(t)$.

3.2.2 Neural mass models

As discussed in Chapter 2, an exact neural mass model has been derived in [10] for a fully coupled network of QIF neurons with instantaneous synapses and with Lorentzian distributed neuronal excitabilities. In this case the macroscopic neural dynamics of a population l is described by two collective variables: the mean field potential $v^{(l)}(t)$ and the instantaneous firing rate $r^{(l)}(t)$. In this context, the neural mass model for two coupled $E - I$ populations with instantaneous synapses, corresponding to the microscopic model reported in Eq. (3.1), can be written as

$$
\begin{aligned}
\dot{r}^{(e)} &= \frac{\Delta^{(e)}}{\left(\tau_m^{(e)}\right)^2 \pi} + \frac{2 r^{(e)} v^{(e)}}{\tau_m^{(e)}} \\
\dot{v}^{(e)} &= \frac{\left(v^{(e)}\right)^2 + H^{(e)} + I^{(e)}(t)}{\tau_m^{(e)}} - \tau_m^{(e)} \left(\pi r^{(e)}\right)^2 \\
&+ J^{(ee)} r^{(e)} - J^{(ie)} r^{(i)} + A \xi^{(e)} \\
\dot{r}^{(i)} &= \frac{\Delta^{(i)}}{\left(\tau_m^{(i)}\right)^2 \pi} + \frac{2 r^{(i)} v^{(i)}}{\tau_m^{(i)}} \\
\dot{v}^{(i)} &= \frac{\left(v^{(i)}\right)^2 + H^{(i)} + I^{(i)}(t)}{\tau_m^{(i)}} - \tau_m^{(i)} \left(\pi r^{(i)}\right)^2 \\
&+ J^{(ei)} r^{(e)} - J^{(ii)} r^{(i)} + A \xi^{(i)} \quad .
\end{aligned}
\tag{3.6}
$$

In the equations for the evolution of the average membrane potentials we have also inserted an additive noise term of amplitude A, employed in some of the analysis to mimic the many noise sources present in the brain dynamics. In particular the noise terms $\xi^{(e)}$ and $\xi^{(i)}$ are both δ-correlated and uniformly distributed in the interval $[-1:1]$.
In case of finite synapses, the exact derivation of the corresponding neural mass model is still feasible for QIF neurons, but the macroscopic evolution now contains further equations describing the dynamics of the synaptic field characterizing the considered synapses [61, 123]. In particular, for a single inhibitory population with exponential synapses, the corresponding neural mass model reads as:

$$
\begin{aligned}
\dot{r}^{(i)} &= \frac{\Delta^{(i)}}{(\tau_m^{(i)})^2 \pi} + \frac{2 r^{(i)} v^{(i)}}{\tau_m^{(i)}} \\
\dot{v}^{(i)} &= \frac{(v^{(i)})^2 + H^{(i)} + I^{(i)}(t)}{\tau_m^{(i)}} - \tau_m^{(i)} (\pi r^{(i)})^2 \\
&- J^{(ii)} s^{(i)} + A \xi^{(i)} \\
\dot{s}^{(i)} &= \frac{1}{\tau_d} [-s^{(i)} + r^{(i)}].
\end{aligned}
\tag{3.7}
$$

In the present case the equation for the average membrane potential contains, as already shown before in Eqs. (3.6), an additive noise term of amplitude

A.
It should be noticed that in Eqs. (3.6) and (3.7) the noise has been added in an effective manner and not with a consistent procedure, that would amount to take into account the effect of microscopic noise on the mean-field formulation. This can be achieved by considering a Fokker-Planck description for the distribution of the membrane potentials, e.g. as done in [15], or by considering a reduced approach in terms of circular cumulants [16,17]. However, all these formulations will lead to much more complicated evolution equations for the macroscopic quantities.
To analyse the stability of the macroscopic solutions of Eqs. (3.6) and (3.7), one should estimate the corresponding Lyapunov spectrum (LS) [130]. This can be done by considering the time evolution of the tangent vector, which for the PING set-up turns out to be four dimensional, i.e. $\delta = \left\{\delta r^{(e)}, \delta v^{(e)}, \delta r^{(i)} \delta v^{(i)}\right\}$. The dynamics of the tangent vector is ruled by the linearization of the Eqs. (3.6), namely

$$\begin{aligned}
\delta\dot{r}^{(e)} &= \frac{2\left(r^{(e)}\delta v^{(e)} + v^{(e)}\delta r^{(e)}\right)}{\tau_m^{(e)}} \\
\delta\dot{v}^{(e)} &= \frac{2v^{(e)}\delta v^{(e)}}{\tau_m^{(e)}} - 2\tau_m^{(e)}\pi^2 r^{(e)}\delta r^{(e)} + J^{(ee)}\delta r^{(e)} - J^{(ie)}\delta r^{(i)} \\
\delta\dot{r}^{(i)} &= \frac{2\left(r^{(i)}\delta v^{(i)} + v^{(i)}\delta r^{(i)}\right)}{\tau_m^{(i)}} \\
\delta\dot{v}^{(i)} &= \frac{2v^{(i)}\delta v^{(i)}}{\tau_m^{(i)}} - 2\tau_m^{(i)}\pi^2 r^{(i)}\delta r^{(i)} + J^{(ei)}\delta r^{(e)} - J^{(ii)}\delta r^{(i)} \quad .
\end{aligned} \tag{3.8}$$

For the ING set-up the tangent vector is three dimensional, $\delta = \left\{\delta r^{(i)}, \delta v^{(i)}, \delta s^{(i)}\right\}$, and its time evolution can be obtained by the linearization of Eqs. (3.8), which reads as

$$\begin{aligned}
\delta\dot{r}^{(i)} &= \frac{2\left(r^{(i)}\delta v^{(i)} + v^{(i)}\delta r^{(i)}\right)}{\tau_m^{(i)}} \\
\delta\dot{v}^{(i)} &= \frac{2v^{(i)}\delta v^{(i)}}{\tau_m^{(i)}} - 2\tau_m^{(i)}\pi^2 r^{(i)}\delta r^{(i)} - J^{(ii)}\delta s^{(i)} \\
\delta\dot{s}^{(i)} &= \frac{1}{\tau_d}[-\delta s^{(i)} + \delta r^{(i)}] \quad .
\end{aligned} \tag{3.9}$$

Please notice that the presence of additive external noise or of forcing terms in Eqs. (3.6) and (3.7) does not modify the evolution equations in the tangent space Eqs. (3.8) and (3.9).
The LS is composed by 4 (3) Lyapunov exponents (LEs) $\{\lambda_i\}$ for the PING (ING) set-ups, which quantify the average growth rates of infinitesimal perturbations along the orthogonal manifolds. In details, LEs are estimated as follows

$$\lambda_i = \lim_{t\to\infty} \frac{1}{t} \log \frac{|\delta_{\mathbf{i}}(t)|}{|\delta_{\mathbf{i}}(0)|}, \tag{3.10}$$

where the technique described in [131] to maintain the tangent vectors δ_i orthonormal during the evolution is employed. The autonomous system will be chaotic for $\lambda_1 > 0$, while a periodic (quasi-periodic) dynamics will be characterized by $\lambda_1 = 0$ ($\lambda_1 = \lambda_2 = 0$) and a fixed point by $\lambda_1 < 0$. In a non-autonomous system in the presence of an external forcing, one Lyapunov exponent will be necessarily zero, therefore a periodic behaviour corresponds to $\lambda_1 < 0$ and a quasi-periodic dynamics to $\lambda_1 = 0$ [130].
In the absence of noise, neural mass models have been directly integrated by employing a Runge-Kutta 4th order integration scheme, while in the presence of additive noise with a Heun scheme. In both cases the time step has been set to $dt = 0.01$ ms. In order to estimate the Lyapunov spectra we have integrated the direct and tangent space evolution with a Runge-Kutta 4th order integration scheme with $dt = 0.001$ ms, for a duration of 200 s, after discarding a transient of 10 s.
Besides LEs, in order to characterize the macroscopic dynamics of the model, we have estimated the frequency power spectra $P_S^{(e)}(F)$ ($P_S^{(i)}(F)$) of the mean excitatory (inhibitory) membrane potential $v^{(e)}(t)$ ($v^{(i)}(t)$) for the PING (ING) set-up. The power spectra have been obtained by calculating the temporal Fourier transform of the mean membrane potentials sampled at time intervals of 2 ms. In the deterministic (noisy) case, time traces composed of 2048 (1024) consecutive intervals have been considered to estimate the spectra, which are obtained at a frequency resolution of $\Delta F = 0.244$ Hz ($\Delta F = 0.488$ Hz). Finally, the power spectra have been averaged over 12 (488) independent realizations for the deterministic (noisy) dynamics. To compare our numerical findings with the experimental results reported in [13], as a measure of the power of the γ oscillations, we have estimated the area of the power spectrum P_γ in an interval ± 15 Hz around the main peak position

F_r of the corresponding power spectrum.

3.3 Dynamics in the absence of forcing

Due to the low dimensionality of the neural mass models we have been able to obtain the corresponding bifurcation diagrams by employing the software MATCONT developed for orbit continuation [132].
In particular, we have derived the bifurcation diagrams in the absence of forcing ($I^{(e)} = I^{(i)} \equiv 0$) as a function of the medians $H^{(e)}$ and $H^{(i)}$ of the excitability distributions for the PING and ING configuration. In general, we observe either asynchronous dynamics, corresponding to a stable fixed point (a focus) of the neural mass equations, or COs, corresponding to stable limit cycles for the same set of equations.

3.3.1 PING set-up

For the excitatory-inhibitory set-up, as already mentioned, we usually fix $H^{(i)} = -5$ and we vary $H^{(e)}$. In this case the inhibitory neurons are mostly below threshold (apart from 6-7 % of them) and they can be driven supra-threshold from the activity of the excitatory population for sufficiently large values of $H^{(e)}$. COs emerge when a sufficient number of neurons is supra-threshold, i.e. when $H^{(e)}$ becomes positive enough. Indeed, as shown in Fig. 3.2 (a), at negative or low values of $H^{(e)}$, one can observe asynchronous dynamics, where the neurons fire independently and without any collective behaviour (as an example see Fig. 3.2 (c)). By increasing $H^{(e)}$, a supercritical Hopf bifurcation occurs at $H_c^{(e)} \simeq 1.5$ leading to the emergence of COs. The COs regime is characterized in the network by almost periodic population bursts, where the neurons in one population partially synchronize over a short time window in the order of a few milliseconds. An example for $H^{(e)} = 5$ is shown in Fig. 3.2 (d), where one can observe two salient characteristics of the oscillatory dynamics. Firstly, the excitatory anticipates always the inhibitory burst by a certain time interval T_a (in this case $T_a \simeq 5$ ms), as usually observed for the PING mechanism [101]. Secondly, the bursts of the excitatory population have a temporal width ($\simeq 8$ ms) which is two or three times larger than those of the inhibitory ones ($\simeq 2 - 3$ ms). This is also due to the fact that a large part of the inhibitory neurons is sub-threshold, therefore most of them fire within a short time window, irrespective of their excitabilities,

due to the arrival of the synaptic stimulation from the excitatory population. Instead, the excitatory neurons, which are mostly supra-threshold, recover from silence, due to the inhibitory stimulation received during the inhibitory burst, over a wider time interval, driven by their own excitabilities. It is evident that the CO frequency of the excitatory and inhibitory population coincide in this set-up.

Moreover, it is important to investigate the bifurcation diagram of the system at fixed median excitatory drive by varying $H^{(i)}$. The corresponding bifurcation diagram is displayed in Fig. 3.2 (b) for $H^{(e)} = 10$. By increasing $H^{(i)}$, COs emerge from the asynchronous state via a sub-critical Hopf bifurcation at $H^{(i)}_{c1} \simeq -8.4$ and they disappear via a super-critical Hopf bifurcation at $H^{(i)}_{c2} \simeq 0.20$. Since the first transition is hysteretical, COs disappear via a saddle-node of the limit cycles at a value $H^{(i)}_{SN} \simeq -10.00$ lower than $H^{(i)}_{c1}$. Indeed, in the interval $[H^{(i)}_{SN}; H^{(i)}_{c1}]$ we have the coexistence of a stable focus with a stable limit cycle. In summary, COs are clearly observable as long as $H^{(i)}$ is negative or sufficiently small. If the inhibitory neurons become mostly supra-threshold, this destroys the collective behavior associated with the PING mechanism.

It is worth noticing that the frequencies of the COs are in the γ-range, namely $\nu^{(e)} \in [22 : 71]$ Hz (as shown in the inset of Fig. 3.2 (a)): in this set-up the maximum achievable frequency $\simeq 100$ Hz, since the decay time of inhibition is dictated by $\tau^{(i)}_m = 10$ ms [101]. On the other hand, the influence of $H^{(i)}$ on the frequency of the COs is quite limited. As shown in the inset of Fig. 3.2 (b) for a specific case corresponding to $H^{(e)} = 10.0$, $\nu^{(i)} \equiv \nu^{(e)}$ varies by few Hz (namely, from 42.8 to 46.9 Hz), when $H^{(i)}$ is varied by an order of magnitude.

For what concerns the delay T_a between the excitatory and inhibitory bursts, we observe a decrease of T_a with the increase of the excitatory drive $H^{(e)}$, from $T_a \simeq 10$ ms at the Hopf bifurcation, towards 2 ms for large $H^{(e)}$ value, see Fig. 3.2 (e). The largest value of T_a is of the order of $\tau^{(i)}_m$. This can be explained by the fact that the excitatory stimulations should reach the inhibitory population within a time interval of (at most) $\simeq \tau^{(i)}_m$ to be able to sum up in an effective manner and to ignite the inhibitory burst. As shown in the inset of Fig. 3.2 (e), the increase of $H^{(i)}$ has in general the effect to reduce T_a; this should be expected since for larger excitabilities (larger $H^{(i)}$), the inhibitory neurons are faster in responding to the excitatory stimulations. However, this is not the case in proximity of the saddle-node bifurcation at

$H_{SN}^{(i)}$ and for positive $H^{(i)}$, where the effect is reversed and T_a increases with $H^{(i)}$.
It is worth noticing that the same parameters as in panel (a) are used for the main panel (e), while in the inset of Fig. 3.2 (e), the data shown are calculated for the same parameters as in panel (b).
For the PING set-up we can also observe sub-crtical Hopf bifurcations. A specific example is discussed in some detail in Appendix A.

3.3.2 ING set-up

As shown in [123], in order to observe COs in globally coupled inhibitory QIF networks and in the corresponding neural mass models, it is sufficient to include a finite synaptic time scale τ_d. On the other hand, in sparse balanced QIF networks, COs are observable even for instantaneous synapses [14]. Indeed, for the set of parameters here employed, by varying the median of the inhibitory excitabilities $H^{(i)}$, we observe a super-critical Hopf bifurcation at $H_c^{(i)} \simeq 2.4$, from an asynchronous state to COs (see Fig. 3.3 (a)). Analogously to the PING set-up, the frequencies of the COs observable in the ING set-up are within the γ-range, namely $\nu^{(i)} \in [26 : 83]$ Hz. In particular, we observe an almost linear increase of $\nu^{(i)}$ with $H^{(i)}$.
Therefore, the PING and ING set-ups considered here are ideal candidates to analyze the influence of θ-forcing on γ-oscillatory populations, which represents the main focus of this chapter. In particular, the response of the system to the excitatory θ-forcing current (3.5) can be interpreted in terms of the bifurcation diagrams for the model in the absence of forcing shown, respectively, in Fig. 3.2 (a) for the PING set-up and in Fig. 3.3 (a) for the ING set-up. The interpretation is possible due to the fact that the response of the system to the sinusoidal current (3.5) can be considered as almost adiabatic, because the forcing frequencies $\nu_\theta \in [1 : 10]$ Hz are definitely slower than those of the COs ($\nu^{(e)}$ and $\nu^{(i)}$), which lie in the γ-range.

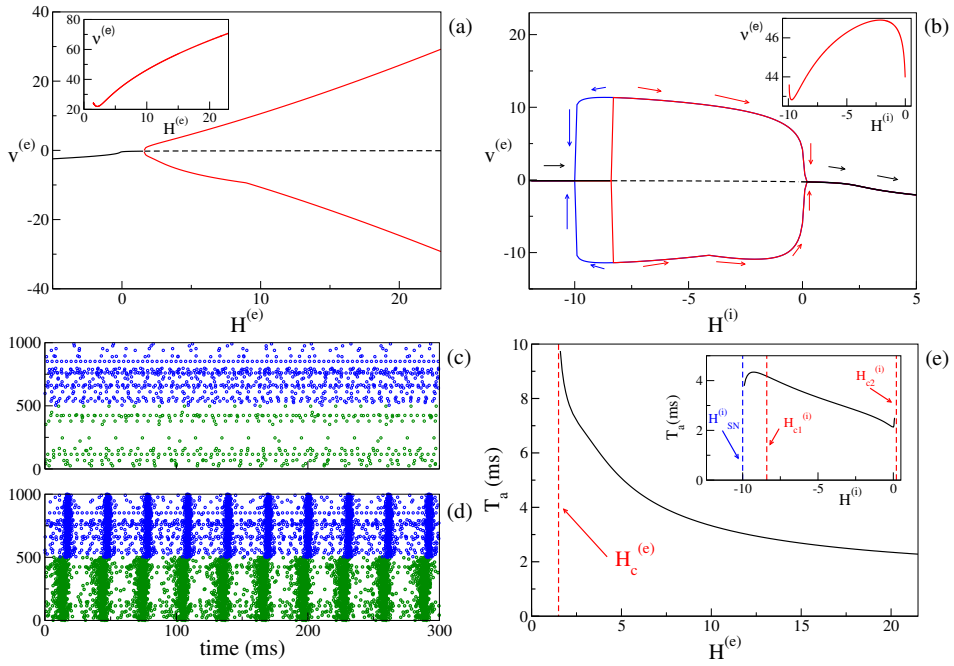

Figure 3.2: (**PING set-up**) (a) Bifurcation diagram of the average membrane potential $v^{(e)}$ as a function of $H^{(e)}$, for $H^{(i)} = -5.0$. The black continuous (dashed) line identifies the stable (unstable) fixed point. The red lines denote the maxima and minima of the limit cycles. The supercritical Hopf bifurcation occurs at $H_c^{(e)} = 1.5$. The inset shows the frequency $\nu^{(e)}$ of the COs versus $H^{(e)}$. (b) Bifurcation diagram of the average membrane potential $v^{(e)}$ versus $H^{(i)}$ for $H^{(e)} = 10$. The Hopf bifurcations are located at $H_{c1}^{(i)} = -8.4$ and $H_{c2}^{(i)} = 0.20$, while the saddle-node bifurcation of limit cycles occurs at $H_{SN}^{(i)} = -10.0$. The inset show the frequency $\nu^{(i)} \equiv \nu^{(e)}$ of the COs versus $H^{(i)}$. (c-d) Raster plots of the excitatory (green dots) and inhibitory (blue dots) networks are calculated in correspondence with the stable fixed point for $H^{(e)} = -5.0$ (c) and with the limit cycle for $H^{(e)} = +5.0$ (d) for the case analyzed in (a). For a better visualization, the activity of only 500 neurons of each population is shown. (e) Delay T_a as a function of $H^{(e)}$. The red dashed line denotes $H_c^{(e)}$. Here we have used the same parameters as in panel (a). In the inset is reported the dependence of T_a versus $H^{(i)}$ for the parameters in panel (b). The other parameters of the system are $J^{(ee)} = 8$, $J^{(ie)} = J^{(ei)} = 10$, $J^{(ii)} = 0$ and the sizes of the networks are $N^{(e)} = 5000$, $N^{(i)} = 5000$.

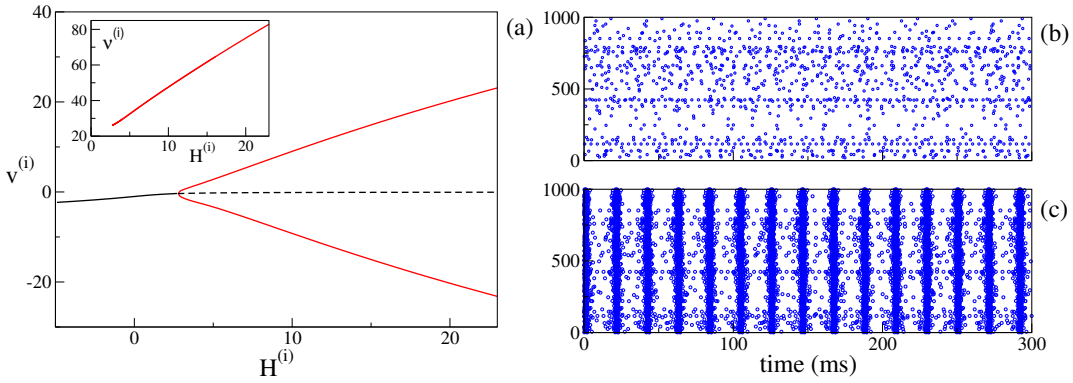

Figure 3.3: (**ING set-up**) (a) Bifurcation diagram of the average membrane potential $v^{(i)}$ as a function of $H^{(i)}$. The black continuous (dashed) line identifies the stable (unstable) fixed point. The red lines denote the maxima and minima of the limit cycles. The supercritical Hopf bifurcation occurs at $H_c^{(i)} \simeq 2.4$. The inset shows the COs' frequency $\nu^{(i)}$ of the inhibitory population as a function of $H^{(i)}$. (b-c) Raster plots of the inhibitory network (blue dots) are calculated in correspondence with the stable fixed point at $H^{(i)} = 0.0$ (b) and with the limit cycle at $H^{(i)} = +10.0$ (c). Only the firing activity of 1000 neurons is displayed. Parameters of the system: $J^{(ii)} = 21.0$, $H^{(i)} = 2.0$, $\Delta^{(i)} = 0.3$, $\tau_m^{(i)} = 10.0$ ms, $\tau_d = 10.0$ ms, $A = 0$. The system size for the purely inhibitory network is $N^{(i)} = 10000$.

3.4 Dynamics under θ-forcing

As a first step, we have verified that the reduced mean-field models are able to reproduce the macroscopic evolution of the spiking network in both considered set-ups, under the external forcing (3.5). In particular, we set the unforced systems in the asynchronous regime in proximity of a super-critical Hopf bifurcation, by choosing $H_0^{(e)} = 1.3 < H_c^{(e)}$ and $H_0^{(i)} = -5$ ($H_0^{(i)} = 2.0 < H_c^{(i)}$) and considered a forcing term with frequency $\nu_\theta = 5$ Hz and amplitude $I_0 = 10$ ($I_0 = 9$) for the PING (ING) set-up.
The comparisons, reported in Figs. 3.4 (a) and (c), reveal a very good agreement in both set-ups between the network and the neural mass simulations, for the mean membrane voltages and the instantaneous firing rates. Furthermore, in both cases, we clearly observe COs, whose amplitudes are modulated by the amplitude of the θ-forcing term (3.5), suggesting that we are in the presence of a Phase-Amplitude Coupling (PAC) mechanism [133]. The corresponding spectrograms shown in Figs. 3.4 (b) and (d) reveal that the frequencies of the COs are in the γ-range with the maximum power localized around 50-60 Hz. Moreover, the spectrograms indicate that the process is stationary and due to the external stimulation. The gamma oscillations repeat during each θ-cycle and they arrest when the external stimulation is stopped. The characteristics of these COs resemble θ-nested γ-oscillations reported in many experiments for neural systems *in vitro* under optogenetic stimulation [13, 118–120] as well as in behaving animals [134].

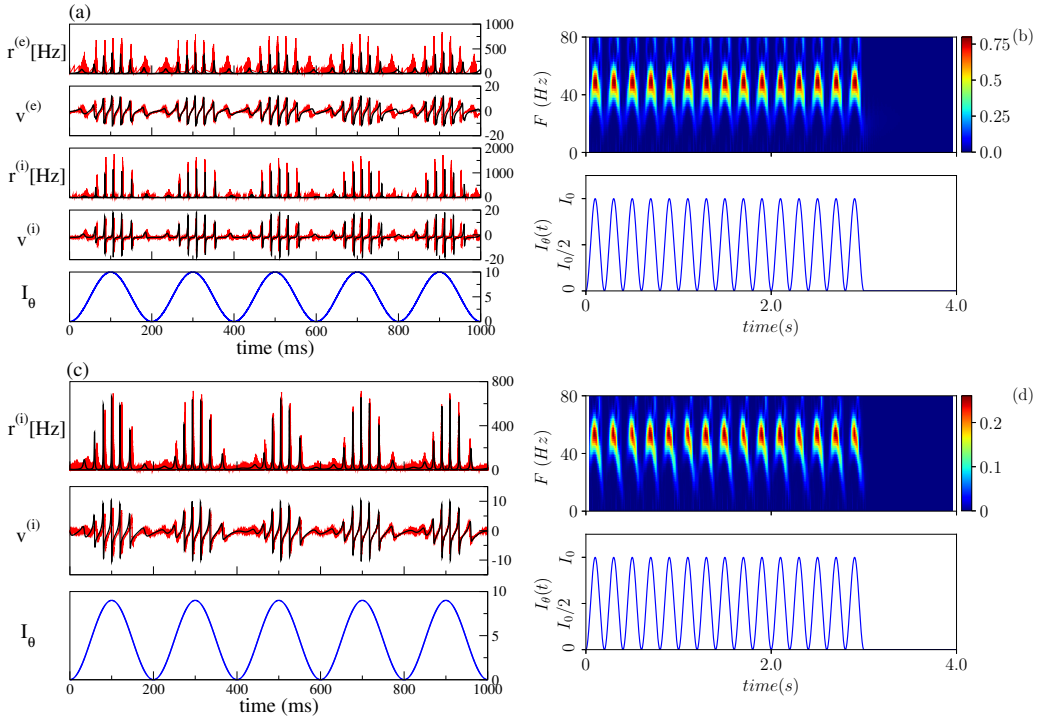

Figure 3.4: **Theta-nested gamma oscillations** (**PING set-up**) (a) From top to bottom: temporal traces of $r^{(e)}$, $v^{(e)}$, $r^{(i)}$, $v^{(i)}$, for the spiking network (red curves) and the neural mass model (black curves). I_θ, reported in the bottom panel in blue, is the external current (3.5). For the neural mass model the average rates and membrane potentials are solutions of Eq. 3.6, while for the network they are calculated according to Eq. 3.4. (b) Spectrogram of the mean membrane potential $v^{(e)}$ (top) as a function of the external forcing (bottom). The amplitude of the forcing is $I_0 = 10$ and its frequency is $\nu_\theta = 5$ Hz. Parameters of the system: $J^{(ee)} = 8$, $J^{(ie)} = J^{(ei)} = 10$, $J^{(ii)} = 0$, $H_0^{(e)} = 1.3$, $H_0^{(i)} = -5.0$, $\Delta^{(e)} = 1$, $\tau_m^{(e)} = 20$, $\Delta^{(i)} = 1$, $\tau_m^{(i)} = 10.0$, $A = 0$, network size $N^{(e)} = N^{(i)} = 5000$. The average firing rates are $\bar{R}^{(e)} \simeq 37$ Hz, $\bar{R}^{(i)} \simeq 36$ Hz. (**ING set-up**) (c) From top to bottom: temporal traces of $r^{(i)}$, $v^{(i)}$ where the line colors have the same meaning as in panel (a). For the neural mass model, average rates and membrane potentials are solutions of Eq. 3.7. (d) Spectrogram of the mean membrane potential $v^{(i)}$ (top) as a function of the external forcing (bottom). The amplitude of the forcing is $I_0 = 9$ and its frequency is $\nu_\theta = 5$ Hz. Parameters of the system: $J^{(ii)} = 21.0$, $H_0^{(i)} = 2.0$, $\Delta^{(i)} = 0.3$, $\tau_m^{(i)} = 10.0$ ms, $\tau_d = 10.0$ ms, $A = 0$, system size for the purely inhibitory network $N^{(i)} = 10000$. The corresponding average firing rate is $\bar{R}^{(i)} \simeq 28$ Hz.

3.4.1 Wavelet Analysis

To get a deeper insight into these dynamics we have estimated the continuous wavelet transform of the average membrane potential on each θ-cycle. As an example, we report in Fig. 3.5 the wavelet spectrogram of the mean potential within a single θ-cycle for the previously examined PING (panel (a)) and ING (panel (b)) set-ups. Indeed, from the comparison of panel (a) and (b) in Fig. 3.5, we practically do not observe any difference: the system responds with COs in the range $[40, 80]$ Hz and it exhibits alternating maxima and minima in the wavelet spectrogram as a function of the θ-phase. Similar results have been reported in Fig. 4G in [13] for the CA1-region of rat hippocampus under optogenetic sinusoidal θ-stimulation.

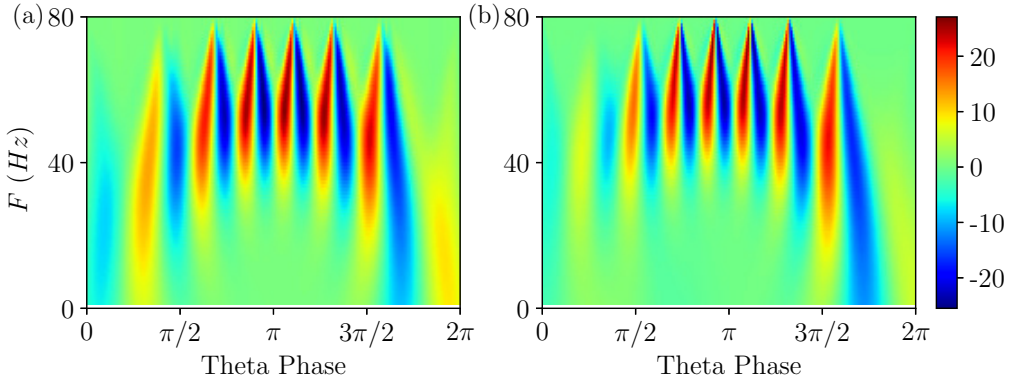

Figure 3.5: **Wavelet Analysis** Continuous wavelet transform over a single θ-cycle of the mean membrane potentials $v^{(e)}$ and $v^{(i)}$ appearing in the neural mass models for PING (a) and ING (b) set-up, respectively. This analysis allows for accurate automated detection and extraction of γ activity without the need for bandpass filtering. Parameters as in Fig. 3.4.

Differences among the two cases appear when one considers the wavelet spectrograms averaged over many θ-periods: for the PING case the spectrogram remains unchanged, instead for the ING set-up the spectrogram smears out and it does not present anymore the clear oscillations reported in Fig. 3.5 (b). This difference indicates that, in the PING case, the observed pattern repeats exactly over each cycle: γ-oscillations and θ-oscillations are perfectly phase locked. This is not the case for the ING set-up: although the PAC

patterns appear quite similar in successive cycles, as shown in Fig. 3.4 (c), indeed they do not repeat exactly. From the point of view of nonlinear dynamics, the PING case would correspond to a perfectly periodic case, while the other case could be quasi-periodic or even chaotic. Therefore, we can observe PAC with an associated phase locking, but also in the absence of phase locking.
Furthermore, according to the data shown in Fig. 3.5, this can also represent an example of PFC, since COs with frequencies $\simeq 40$ Hz occur at small and large θ-phases, while in the middle range $\pi/2 < \theta < 3\pi/2$ one observes similar oscillations with $F \simeq 60$ Hz.
For what concerns the wavelet analysis obtained from optogenetic experiments and shown in Fig. 4G in [13], we should stress two important aspects: (i) the wavelet spectrogram, averaged over several θ cycles (namely 30), displays clear correlations among the θ-phase and the γ-oscillations; (ii) the spectrogram is highly asymmetric indicating that γ-oscillations emerge in proximity of θ-phase $\simeq \pi$ and disappear $\simeq 3/2\pi$. The former aspect reveals that θ and γ oscillations were perfectly locked in the experiment, while the latter suggests that the bifurcation associated with the emergence of COs in the experiment is probably hysteretic. This would explain the asymmetry that we do not observe here for super-critical Hopf bifurcations in Fig. 3.5, but that emerges for sub-critical Hopf bifurcations, as discussed in Appendix A.

3.4.2 Phase-Amplitude Locked and Unlocked States

To better examine the dynamical regimes emerging in our set-ups, we have first estimated the maximal Lyapunov exponent λ_1 associated with the neural mass models, for the same parameters considered in Fig. 3.4, over a wide range of forcing amplitudes, that is $0 \leq I_0 \leq 20$. From the results reported in Fig. 3.6 (a) and (b), it is clear that λ_1 is almost always zero, apart from some limited intervals where it is negative and a few values of I_0 for the ING set-up, where it can be even positive. This means that the dynamics is usually quasi-periodic, apart from some Arnold tongues where there is perfect locking between the external forcing and the forced system.

We notice that for small amplitudes the forcing entrains the system in a $1:1$ periodic locking, therefore the instantaneous firing rate displays one peak for each θ-period with the same frequency as the forcing ν_θ. This locking is

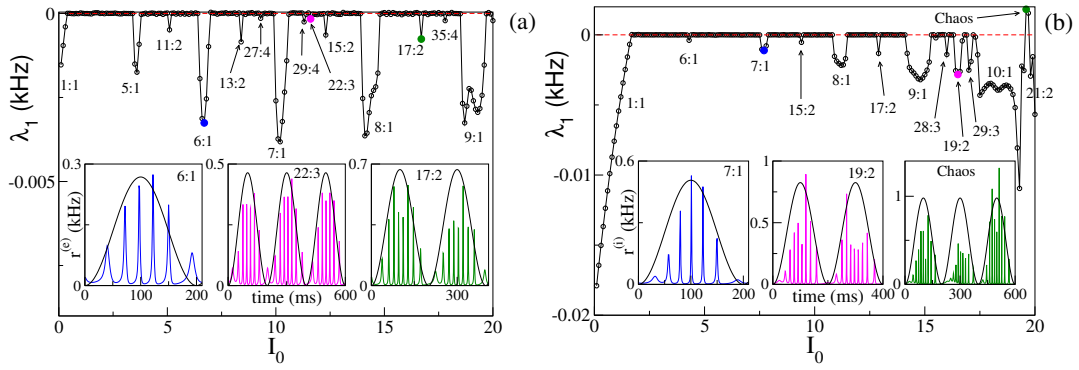

Figure 3.6: **Maximal Lyapunov exponent** λ_1 estimated for the neural mass models as a function of the forcing amplitude I_0, for the PING (a) and ING (b) set-ups. In both cases the system is subject to a forcing frequency $\nu_\theta = 5$ Hz. Insets in panel a (b) report the instantaneous firing rate $r^{(e)}(t)$ ($r^{(i)}(t)$) versus time for the PING (ING) set-up respectively. The three cases shown are representative of the states identified by circles in the main panels. The color code is the same, i.e. the color used in the inset identifies the corresponding circle in the main panel. The black continuous lines in the inset correspond to I_θ in arbitrary units. Parameters are the same as in Fig. 3.4.

present in a wider region in the ING case (namely, $I_0 < 1.70$) with respect to the PING set-up (namely, $I_0 < 0.40$). More interesting locking regimes, where the forced populations oscillate in the γ-range, emerge at larger I_0. These locking regimes can be considered as θ-nested γ-oscillations; most of them are of the type $m : 1$, with $m \in [5 : 10]$, which means that, for each θ-period, the firing rate of the forced populations has m maxima (for specific examples see the insets of Fig. 3.6 (a) and (b)). In extremely narrow parameter intervals other, more complex, kinds of locking of the type $m : n$ emerge, where exactly m maxima in the population activity appear for every n θ-oscillations. In the examined cases we have identified locked patterns with n up to four. Moreover, for the ING case, we have even observed a chaotic region (see Fig. 3.6 (b)), which emerges at quite large forcing amplitude $I_0 \simeq 19$. On the basis of our analysis we cannot exclude that chaos could emerge also in the PING set-up, for sufficiently strong forcing.
Let us now focus on the $m : 1$ perfectly locked states with $m > 1$, which

are worth investigating due to their relevance for θ-γ mixed oscillations, as well as to their relative large frequency of occurrence with respect to more complex $m : n$ locked states. In particular, we have examined the response of the system to different forcing amplitudes $I_0 \in [0 : 20]$ and frequencies $\nu_\theta \in [1 : 10]$ Hz. The $m : 1$ locked oscillations are reported in Figs. 3.7 (a) and (b) and characterized by the number m of oscillations displayed within a single θ-cycle.
These locked states appear only for $\nu_\theta > 2 - 3$ Hz. Moreover, the states with equal m are arranged in stripes in the (ν_θ, I_0)-plane. Locked states in the PING configuration occur in separated stripes whose order m increases for increasing I_0; in particular, states with $3 \leq m \leq 10$ are clearly identifiable. In the ING set-up, for sufficiently large ν_θ and I_0, we have a continuum of locked states, thus indicating that, for the ING set-up, phase locking to the forcing frequency is easier to achieve. In this case the order of occurrence of m-order states is not clearly related to the forcing amplitude; however locked states with order m and $2m$ are often nested within each other as shown in Fig. 3.7 (b).
To examine which frequencies are excited in these states we have measured for each amplitude I_0 the minimal, the maximal and the average frequency of the COs associated with $m : 1$ locked states over the whole range of examined forcing frequencies ν_θ. These frequencies are reported in Figs. 3.7 (c) and (d). The analysis clearly reveals that the minimal CO frequency is essentially independent from I_0 and its value is around 20 Hz, while the maximal and the average grow with I_0. However all these frequencies stay within the γ-range for the examined forcing amplitudes.
To better understand the mechanism underlying the emergence of θ-nested γ oscillations, we have reported in Figs. 3.7 (c) and (d) the COs frequencies $\nu^{(e)}$ ($\nu^{(i)}$) (green solid lines) obtained from the adiabatic bifurcation analysis of the neural mass models (these frequencies are also shown in the insets of Figs. 3.2 (a) and 3.3 (a)). The very good agreement between $\nu^{(e)}$ and $\nu^{(i)}$ and the maximal frequency measured for the locked states suggests that the nested COs are induced by the crossing of the super-critical Hopf bifurcation during the periodic stimulation. In particular, during forcing, the maximal achievable γ-frequency is the one corresponding to the maximal stimulation current $I_0 + H_0^{(e)}$ ($I_0 + H_0^{(i)}$) for the unforced PING (ING) set-ups. Furthermore, under sinusoidal forcing, the system spends a longer time in proximity of the maximal stimulation value, since it is a turning point. This explains why this frequency is always present in the response of the driven system for

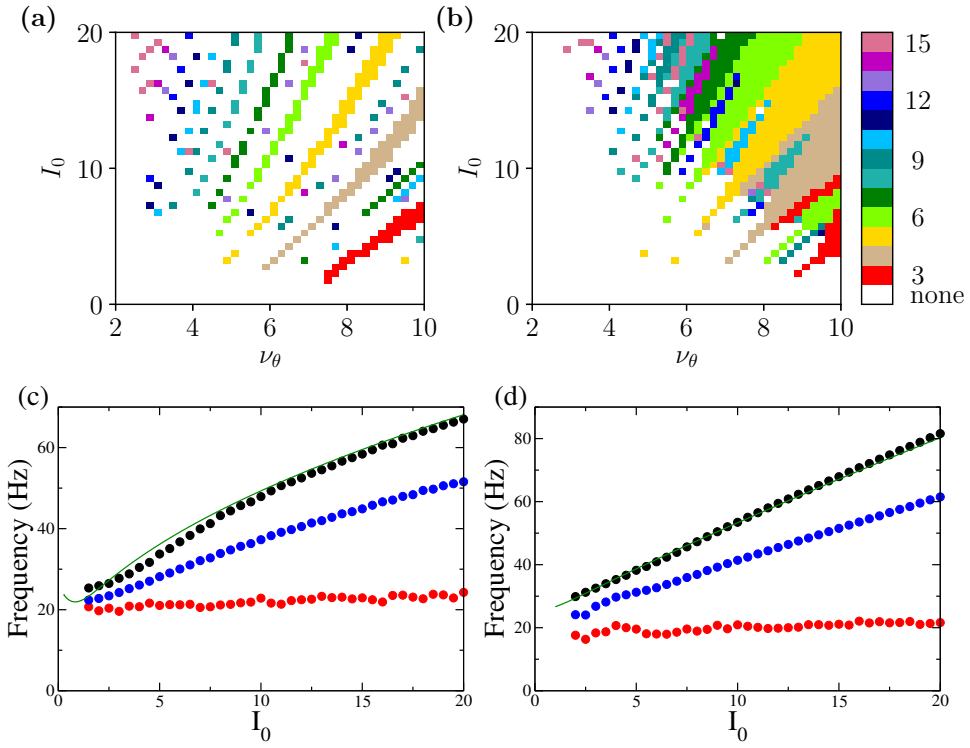

Figure 3.7: **Phase locked** $m:1$ **states** Locked states for the neural mass models are displayed in panels (a) and (b) for the PING and ING set-ups, respectively. The color code identifies the locked states according to the value of m, from 3 to 15. (c,d) Minimal (red circles), average (blue circles) and maximal (black circles) frequencies of the COs as a function of the forcing amplitude I_0 for PING (c) and ING (d) set-ups. These values are obtained by considering all possible $m:1$ locked states corresponding to the examined I_0. The frequencies $\nu^{(e)}$ ($\nu^{(i)}$) (green solid lines) of the COs obtained from the bifurcation analysis in the adiabatic set-up are reported as a function of $H^{(e)} - H_0^{(e)}$ ($H^{(i)} - H_0^{(i)}$) for the PING (ING). Parameters are the same as in Fig. 3.4.

the considered locked states.

3.4.3 Comparison with Experimental Findings

In a series of recent optogenetic experiments on the mouse enthorinal-hippocampal system, clear evidence has been reported that phase-amplitude coupled γ-rhythms can be generated locally in brain slices *ex vivo* in the CA1-region, as well as in the CA3 and MEC, under sinusoidal θ stimulations [13, 118–120]. In particular, in [120] the authors reported evidence that, for all the regions CA1, CA3 and MEC, the generation of the γ-rhythms, under θ-rhythmic activation of pyramidal neurons, is due to a PING mechanism.
However, due to the fact that pyramidal neurons are directly activated during experiments, their result cannot exclude that tonic activation of interneurons contributes to θ-γ oscillations *in vivo*. Furthermore, in [119] the authors affirm that θ-nested γ-oscillations due to the optogenetic θ-frequency drive, are generated, in MEC, by local feedback inhibition without recurrent excitation, therefore by a ING mechanism. In this Section we try to reproduce some of the analyses reported in these experimental studies by employing both the PING and ING set-ups, in order to understand if these two set-ups give rise to different dynamical behaviors.
By following the analysis performed in [13, 120], we have considered the response of the two set-ups to forcing of different frequencies ν_θ and amplitudes I_0. The results reported in Fig. 3.8 reveal that the phenomenon of PAC is present for all the considered frequencies $\nu_\theta \in [1, 10]$ Hz and amplitudes $I_0 \in [1, 20]$ in both set-ups. Moreover, analogously to what was reported in [13,120], the amplitude of the γ-oscillations increases proportionally to I_0, while the number of nested oscillations in each cycle increases for decreasing ν_θ. On the basis of this comparison, the forced PING and ING set-ups display essentially the same dynamics.
To get a more detailed information about the dynamics in the two set-ups, we will now consider the features of the power spectra $P_S^{(e)}$ ($P_S^{(i)}$) of the mean excitatory (inhibitory) potential for the PING (ING) set-up. These features are obtained for different forcing amplitudes and frequencies, somehow similar to the analysis performed for the power spectra of the Local Field Potential (LFP) in [13, 120].

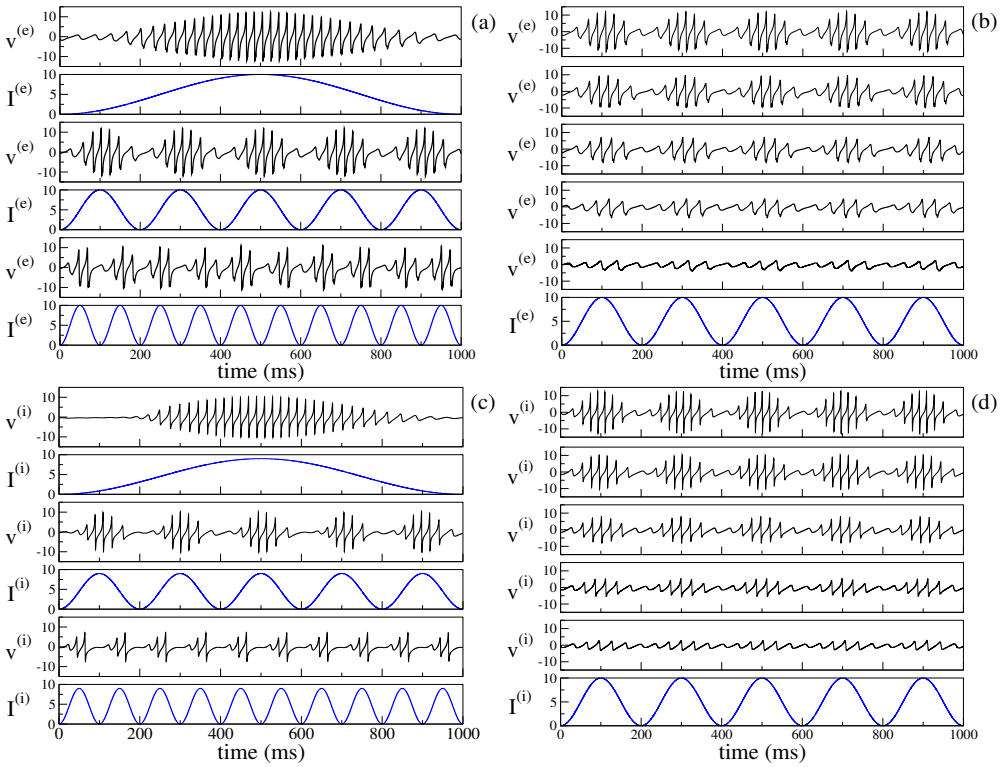

Figure 3.8: **Theta-Nested Gamma COs for PING (a-b) and ING set-up (c-d)** Left column: dependence of the mean membrane potential of the excitatory (inhibitory) population $v^{(e)}$ ($v^{(i)}$) on the frequency ν_θ of the external forcing $I^{(e)} = I_\theta$ ($I^{(i)} = I_\theta$) with $I_0 = 10$ ($I_0 = 9$) for the PING (ING) set-up. The current profiles (blue lines) are displayed immediately below the corresponding membrane potential evolution. From top to bottom, the frequency ν_θ is 1 Hz, 5 Hz and 10 Hz. Right column: dependence of the mean membrane potential $v^{(e)}$ ($v^{(i)}$) on the amplitude I_0 of the external current. Here the forcing frequency is kept constant at the value $\nu_\theta = 5Hz$. The amplitude is changed from 100% of maximum (top) to 20% of maximum (bottom) in 20% increments, the maximum being given by $I_0 = 10$. The data refer to the evolution of neural mass models, the parameters are the same as in Fig. 3.4.

Let us first consider, as an example of the obtained power spectra, the case corresponding to the PING set-up with a forcing characterized by $\nu_\theta = 5$ Hz and amplitude $I_0 = 10$, shown in Fig. 3.9 (a). In the spectrum we observe very well defined spectral lines located at frequencies which can be obtained as a linear combination of the forcing frequency $\nu_\theta = 5$ Hz and of the response frequency $F_r = 45$ Hz. In particular F_r is associated with the main peak and should correspond to the intrinsic frequency of the forced system. In the present case, the adiabatic bifurcation diagram reported in Fig. 3.2 (a) tells us that the maximal achievable frequency is $\nu^{(e)}_{max} \simeq 49.3$ Hz, corresponding to $H^{(e)} = I_0 + H^{(e)}_0 = 11.3$. Indeed $F_r < \nu^{(e)}_{max}$ due to the interaction with the forcing current that eventually induces a locking phenomenon at a frequency that is exactly a multiple of ν_θ, as it happens in the present case. However, in general, a spectrum as the one shown in Fig. 3.9 (a), is the emblem of a quasi-periodic motion characterized by two incommensurate frequencies. This can be easily observable in most cases in our system, where ν_θ and F_r are usually incommensurate.
The spectra obtained from optogenetic stimulation, reported in [13, 120], do not resemble the one shown in Fig. 3.9 (a); indeed they present only two peaks: one corresponding to the stimulation frequency and one, quite broad, associated with the γ-oscillations. We can expect that the difference is due to the multiple noise sources that are always present in an experimental analysis (in particular for neurophysiological data), but that are absent in our model. Indeed, by considering the neural mass model for the PING set-up with additive noise on the membrane potentials of suitable amplitude, that is $A = 1.4$, we get a power spectrum resembling the experimental one, as shown in Fig. 3.9 (b). The presence of noise induces the merging of the principal peaks in a unique broad one and the shift of the position of the main peak towards some larger values ($F_r = 54$ Hz in the present case) with respect to the fully deterministic case.

Let us now consider the power spectra obtained for different forcing frequencies $\nu_\theta \in [1 : 10]$ Hz in the θ-range, in case of fixed forcing amplitude and in the absence of noise. The position of the main and auxiliary peaks are shown in Fig. 3.10 (a) (Fig. 3.10 (c)) for the PING (ING) set-up and compared with the experimental results (red circles) obtained for the CA1 region of the hippocampus in [13]. It is clear that, for both set-ups, the position of the main peak F_r (green squares) has a value $\simeq 50$ Hz and it does not show any clear dependence on ν_θ. This is in contrast with the experimental

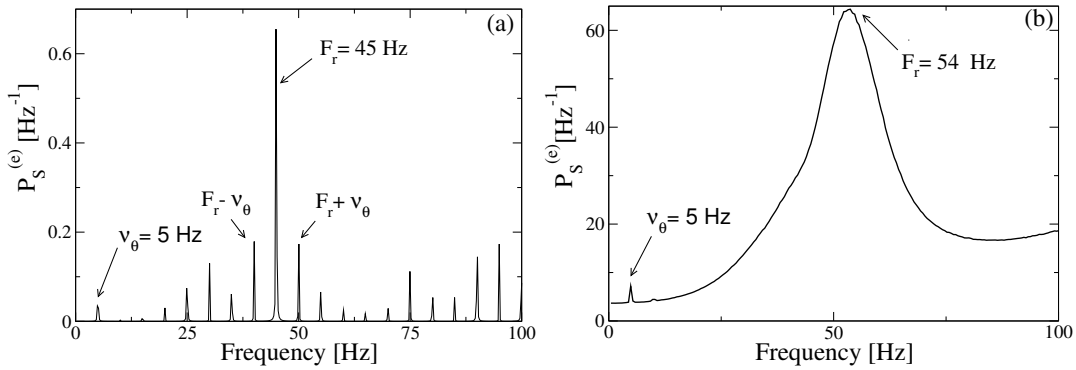

Figure 3.9: **Power spectra for the PING set-up** Spectra $P_S^{(e)}$ of the mean membrane potential $v^{(e)}$ of the neural mass model estimated when the excitatory population is subject to an external drive with frequency $\nu_\theta = 5$ Hz and amplitude $I_0 = 10$, in the absence of noise (a) and for additive noise with amplitude $A = 1.4$ (b). The data refer to the evolution of neural mass models, the parameters are as in Fig. 3.4.

data, which reveal an increase proportional to ν_θ from 49 Hz to 60 Hz. The same trend is displayed in our simulation from the subsidiary peak located at $F_r + \nu_\theta$ (black stars), showing an increase with ν_θ.
Let us now take into account the power of the γ oscillations P_γ as defined in Section 3.2.2. As shown in the insets of Fig. 3.10 (b) and (d), this quantity remains essentially constant for low frequencies (namely, for $\nu_\theta \leq 5$ Hz in the PING and for $\nu_\theta \leq 7$ Hz in the ING), while it drops to smaller values at larger frequencies. On the other hand, the experimental results (red circles) reveal a similar decrease at frequencies $\nu_\theta > 5$ Hz, but they also reveal an increase at low frequencies, not present in our numerical data, thus suggesting a sort of resonance at 5 Hz. For what concerns the dependence of P_γ on the forcing amplitude, we have fixed $\nu_\theta = 5$ Hz and varied I_0 in the range $[4 : 10]$ ($[8 : 20]$) for the PING (ING) set-up. In both cases and analogously to experimental data, P_γ increases proportionally to I_0, see Fig. 3.10 (b) and (d).
In both set-ups, our model is unable to reproduce, in the absence of noise and for fixed forcing amplitude I_0, the steady increase of F_r with ν_θ reported in the experiments for the mice CA1 in [13]. Therefore, in order to cope with this problem, we will now investigate how a similar trend can emerge in our

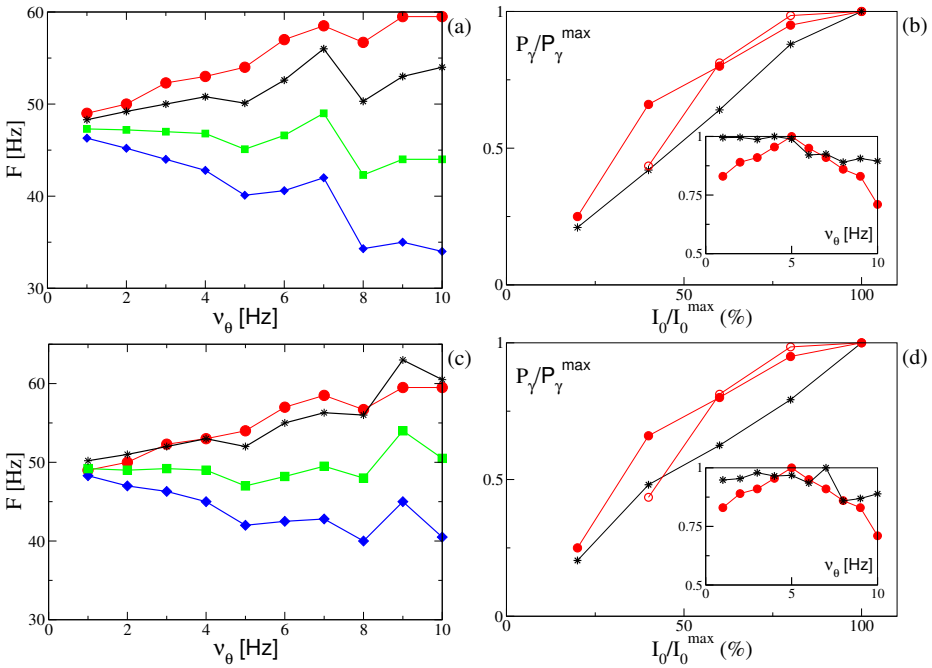

Figure 3.10: **Power spectra features** (**PING set-up**) (a) Frequencies of the peaks of the power spectrum $P_S^{(e)}$ as a function of the stimulation frequency ν_θ. Green squares correspond to the main peak frequency F_r, while the black stars to $F_r + \nu_\theta$ and the blue diamonds to $F_r - \nu_\theta$. The red circles are the experimental data extrapolated from Fig. 4C of [13]. The amplitude of the forcing is $I_0 = 10$. (b) Normalized power of the γ oscillations $P_\gamma / P_\gamma^{max}$ associated with the signal $v^{(e)}$ as a function of the amplitude stimulation, where we set $I_0^{max} = 20$ and the frequency of stimulation at $\nu_\theta = 5$ Hz. In the inset we report the same quantity as a function of the frequency stimulation ν_θ for $I_0 = 10$. The black stars correspond to our simulations, while the red circles to experimental data extrapolated from Fig. 4E (Fig. 4B for the inset) of Ref. [13] (filled circles) and from Fig. 4C of Ref. [120] (empty circles). The other parameters are as in Fig. 3.4. (**ING set-up**) (c) Same as in panel (a) for the power spectrum $P_S^{(i)}$ with $I_0 = 9$. (d) Same as panel (b) for the signal $v^{(i)}$ with $I_0^{max} = 40$. The data refer to the evolution of neural mass models. For the inset we set $I_0 = 9$, other parameters as in Fig. 3.4.

data. In particular, in the remaining part of the chapter we consider noisy dynamics, to have a better match with experiments where is unavoidable. In Fig. 3.10 (a) we report, for the PING set-up, the estimated power spectra for different noise levels, under constant external sinusoidal forcing. The effect of noise is to render the spectrum more flat and to shift the position of the peak in the γ-range towards higher frequencies. As shown in the inset of Fig. 3.10 (a), the frequency F_r is almost insensitive to the noise up to amplitudes $A \simeq 1.0$, then it increases steadily with A from $\simeq 45$ Hz to $\simeq 62$ Hz. The effect of varying the forcing amplitude I_0, for constant forcing frequency $\nu_\theta = 5$ Hz and noise amplitude $A = 1.4$, is shown in Fig. 3.10 (b). In this case the amplitude increase of the forcing leads to more defined peaks in the γ-range and to an almost linear increase with I_0 of F_r, as reported in the inset. In the same inset we also have reported the results related to two optogenetic experiments for the CA1-region of the mice hippocampus. In particular, the data-sets refer to two successive experiments performed by the same group: namely, red filled circles refer to [13] and red open circles to [120]. While in one experiment (red open circles) a constant increase of F_r with the forcing amplitude is observable from 60 to 70 Hz, in the other one (red filled circles) the frequency initially increases with I_0 and then decreases with it. As a matter of fact in the latter case, F_r remains around $45 - 50$ Hz for a variation of I_0 from 40 to 100 % of the maximal amplitude I_0^{max}. From the comparison with our results, we can affirm that our data reproduce the correct range of frequencies in both experiments and also the dependence on the forcing amplitude for $I_0/I_0^{max} \geq 60\%$ reported in [120]. The decrease of F_r for I_0/I_0^{max} larger than the 50% reported in [13] is inconsistent with our data, but also with the experimental results of the same group published in [120].

From this last analysis we have understood that, for constant forcing frequency, the γ-peak shifts towards higher frequencies by increasing the forcing amplitude or the noise level, i.e. by increasing the stimulation power.

Therefore, to obtain an increase of F_r with the forcing frequency ν_θ, analogously to the results reported in [13] (and displayed as filled red circles in Fig. 3.10(a) and (c)), we perform numerical experiments where ν_θ increases together with A or I_0. The simplest protocol is to assume that A (I_0) will increase linearly with ν_θ. The results obtained for the PING (ING) set-up are reported in Fig. 3.12 (a) (Fig. 3.12 (b)). As evident from the figures, in both set-ups and for both protocols we obtain results in reasonable agreement with the experiments. In the present framework, we have also analyzed the

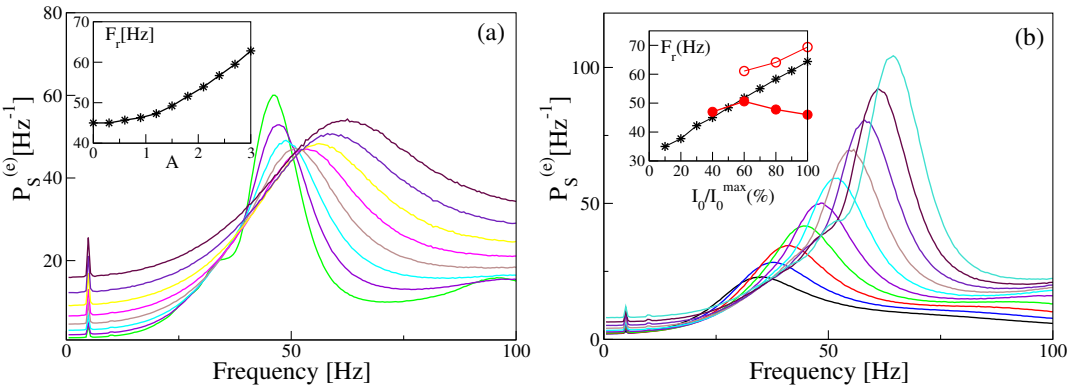

Figure 3.11: **Power spectra dependency on noise and forcing amplitudes** (**PING set-up**) Power spectra $P_S^{(e)}$ for different noise level A (a) and different amplitude of the external input I_0 (b), for a fixed forcing frequency $\nu_\theta = 5$ Hz. In the insets are reported the frequencies F_r of the main peak as a function of the noise level (a) and of the amplitude of the external drive I_0 (b). In the inset of panel (b) are also reported experimental data extracted from Fig. 4F of Ref [13] (filled red circles) and from Fig. 4D of Ref. [120] (open red circles). The curves in (a) are obtained by varying the noise amplitude $A \in [0.9 : 3.0]$ with a step of 0.3, while keeping $I_0 = 10$ fixed. On the other hand the curves in (b) refer to different forcing amplitudes $2 \leq I_0 \leq 20$, varied in steps of 0.2, with fixed noise amplitude $A = 1.4$. The other parameters are as in Fig. 3.4. Data have been obtained by the integration of neural mass models.

dependence of the γ-power P_γ on ν_θ. In particular, this quantity increases almost linearly with the forcing frequency, at variance with the experimental results in [13] which revealed a sort of resonance with an associated maximal γ-power around $\nu_\theta = 5$ Hz (the experimental data are displayed as red circles in the insets of Fig. 3.10 (b) and (d)).

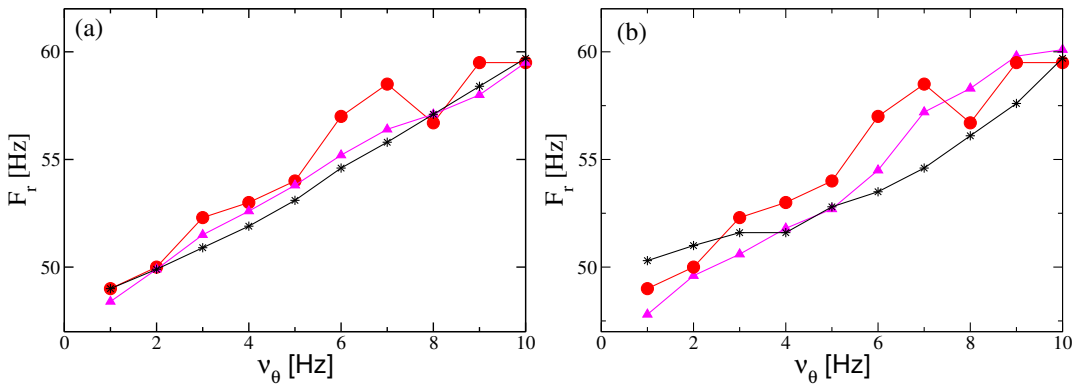

Figure 3.12: **Influence of the theta frequency on the gamma oscillations** Frequency F_r of the main peak of the power spectrum $P_S^{(e)}$ versus ν_θ for the PING (a) and ING (b) set-ups. Red filled circles represent the experimental data extrapolated from Fig. 4C in [13]. Black stars (magenta triangles) refer to numerical data obtained by varying linearly the noise amplitude A (the forcing amplitude I_0) as a function of ν_θ and maintaining the forcing amplitude I_0 (the noise amplitude A) constant. The data shown as black stars for the PING (ING) set-up in panel (a) (panel (b)) are obtained by adding white noise to the evolution of the mean membrane potentials and by varying linearly its amplitude in the interval $A \in [1.4 : 2.9]$ as a function of ν_θ with $I_0 = 10$ ($I_0 = 9$). The magenta triangles refer to data obtained by keeping fixed the noise amplitude at the value $A = 1.4$ and by varying linearly with ν_θ the forcing amplitude I_0 in the range $[9.5 : 18]$ ($[8 : 14]$) for the PING (ING) set-up in panel (a) (panel (b)). Other parameters for as in Fig. 3.4. Data are obtained from neural mass models integration.

3.5 Discussion and Conclusions

In this chapter we have analyzed the dynamics of a new class of neural mass models arranged in two different set-ups: an excitatory-inhibitory network (or PING set-up) and a purely inhibitory network (or ING set-up). These neural mass models are extremely relevant to mimick neural dynamics for two reasons. On one side, because they are not derived heuristically, since they reproduce exactly the dynamics of excitatory and inhibitory networks of spiking neurons for any degree of synchronization [10, 123, 135]. On other side, these neural masses reproduce the macroscopic dynamics of quadratic integrate-and-fire neurons, which are normal forms of type I neurons, therefore they are expected to represent the dynamics of this large class of neurons [89].

In this present work we have shown that θ-nested γ oscillations can emerge both in the PING and ING set-up under an external excitatory θ-drive whenever the system, in the absence of forcing, is in a regime of asynchronous dynamics, but in proximity of a Hopf bifurcation towards collective γ oscillations. The external forcing drives the system across the bifurcation inside the oscillatory regime, thus leading to the emergence of γ oscillations. The amplitude of these collective oscillations is related to the distance from the bifurcation point, therefore it depends on the phase of the θ-forcing term. These nested oscillations can arise in proximity of a super-critical and also a sub-critical Hopf bifurcations. As shown in Appendix A, in the latter case the amplitudes are no more symmetric with respect to the maximum value of the theta stimulation, analogously to the experimental findings reported in [13].

Equivalent results have been reported for an excitatory-inhibitory network with a recurrent coupling among the excitatory neurons, by considering the Wilson-Cowan rate model [129]. However, at variance with our neural mass model, the Wilson-Cowan model fails to reproduce the emergence of γ-oscillations, displayed by the corresponding spiking networks, in several other set-ups. In particular, the Wilson-Cowan model is unable to display COs for purely inhibitory populations (the ING set-up), without the addition of a delay in the IPSPs transmission, delay that is not required in the network model. Moreover, the Wilson-Cowan model is unable to display COs even for excitatory-inhibitory coupled populations in the absence of a recurrent excitation [123, 129]. As shown in Appendix B, the considered neural mass model in the PING set-up displays clear θ-nested γ-oscillations in the

absence of any recurrent coupling or with recurrent couplings only among the inhibitory neurons.
Furthermore, we have identified two different types of phase amplitude couplings. One characterized by a perfect locking between θ and γ-rhythms, corresponding to an overall periodic behaviour dictated by the slow forcing. The other one where the locking is imperfect and the dynamics is quasi-periodic or even chaotic. The perfectly locked θ-nested γ oscillations display in turn two types of cross-frequency coupling: phase-phase and phase amplitude coupling [133]. These states arise for ν_θ larger than 2-3 Hz and for sufficiently large forcing amplitudes. From the results reported in [13] for the CA1-region of the hippocampus under sinusoidal forcing *in vitro*, it is evident that perfectly phase locked PACs have been observed in each single slice. However, *in vivo* this perfect phase-phase locking cannot be expected, see the detailed discussion of phase-phase coupling reported in [136], where the authors clarify that phase locking is indeed observable, but only over a limited number of successive θ-cycles. Therefore, PAC with an underlying chaotic (or noisy) dynamics is the scenario usually expected in behaving animals.
From our analysis it also emerges that locked states are more frequent in the ING set-up. The purely inhibitory population is more easily entrained by the forcing with respect to the coupled excitatory-inhibitory population system, where the forcing is applied to the excitatory population. This result is somehow in agreement with recent findings based on the analysis of phase response curves, which suggest that stimulating the inhibitory population facilitates the entrainment of the gamma-bands with an almost resonant frequency [137, 138]. However, these analyses do not consider θ-γ entrainment: this will be a subject of future studies based on exact macroscopic phase response curves [138, 139].
Our modelization of the PAC mechanism induced by an external θ-forcing is able to reproduce several experimental features reported for optogenetic experiments concerning the region CA1, CA3 of the hippocampus, as well as MEC [13, 118–120]. In agreement with the experiments, we observe nested γ COs for forcing frequencies in the range $[1 : 10]$ Hz, whose amplitude grows proportionally to the forcing one. Furthermore, the γ-power and the frequency of the γ peak increase almost linearly with the forcing amplitude, i.e. with the input θ-power. Moreover these findings are consistent with recent results for behaving rats, where it has been shown that hippocampal γ-frequency and the associated power increase proportionally to the animal

speed [140,141]. In addition, in [142], the authors have clearly demonstrated that the hippocampal θ-power and the mouse speed are positively correlated. This proportionality between the θ-power and the mouse speed has been recently employed to develop a computational model able to successfully reproduce CA1 network activity [143].
However, the neural mass model in all the examined PING and ING set-ups is unable to reproduce the increase in frequency of the γ-power peak with ν_θ reported in [13]. Indeed, such effect was expected by the observation that during movement, both the frequencies of hippocampal θ oscillations [144] and γ oscillations [140] increase with the running speed of the animal. However, the variation of the γ frequency reported in [140] for behaving animals amounts to 40-60 Hz, while in the optogenetic experiment by [13], the increase was limited to $\simeq$ 10 Hz. In order to get a similar increase in the neural mass model, we have been obliged to assume that the stimulation power (namely, the noise or the forcing amplitude) increases proportionally to ν_θ. On one side, further experiments are required to clarify if, during optogenetic experiments, the forcing (or noise amplitude) affecting the neural dynamics is indeed dependent on ν_θ. This could be due to a reinforcement of the synaptic strengths for increasing forcing frequencies, or to the fact that higher θ frequencies can favour neural discharges in regions different from CA1, thus being assimilated to external noise. On another side it should be analyzed if other bifurcation mechanisms, beside the Hopf one, here considered, can give rise to such a dependence of γ power on θ forcing.
Finally, experiments on behaving rodents report clear evidence that θ-power and ν_θ, as well as the power of the γ-peak and the corresponding frequency, increase all proportionally to the animal speed [140–142, 144]. Furthermore, in [141] the authors report evidence of the increase of the phase-amplitude coupling with the speed. This scenario is consistent with the results reported in our analysis, where we have shown that an increase of ν_θ and of the stimulation power leads to an increase of P_γ and of the frequency of the γ peak as well as of the PAC. It is worth noting that the mean field models we have adopted in this chapter are far from being biologically realistic in this state. The enrichment of these models with more real biological features constitutes a necessary step if we want to reach a deeper contact with the experimental data. For this reason, the choice of the parameters made long this analysis tries to be on the one hand as close as possible to the typical values of the parameters obtained experimentally (such as for the membrane time constants and the synaptic time decay), on the other hand to give rise to

complex dynamical behavior, as for the case of the excitabilities and synaptic strengths, for which there are no corresponding experimentally measurable quantities with our model. Our aim is mostly to propose simple models capable of giving rise to complex mechanisms. As we have shown, for example, the increase of noise in our model induces, counterintuitively, an increase in the response frequency of the system. Although the biological reason for this is not clear to our knowledge, we think that the analysis of this mechanism deserves to be addressed from a mathematical point of view.

Author Contributions:
Marco Segneri, Hongjie Bi and Simona Olmi performed the simulations and data analysis. Simona Olmi and Alessandro Torcini were responsible for the state-of-the-art review and the paper write-up. All the authors conceived and planned the research.

Chapter 4

Coexistence of fast and slow gamma oscillations in one population of inhibitory spiking neurons

Abstract:

Oscillations are a hallmark of neural population activity in various brain regions with a spectrum covering a wide range of frequencies. Within this spectrum gamma oscillations have received particular attention due to their ubiquitous nature and to their correlation with higher brain functions. Recently, it has been reported that gamma oscillations in the hippocampus of behaving rodents are segregated in two distinct frequency bands: slow and fast. These two gamma rhythms correspond to different states of the network, but their origin has been not yet clarified. Here, we show theoretically and numerically that a single inhibitory population can give rise to coexisting slow and fast gamma rhythms corresponding to collective oscillations of a balanced spiking network. The slow and fast gamma rhythms are generated via two different mechanisms: the fast one being driven by the coordinated tonic neural firing and the slow one by endogenous fluctuations due to irregular neural activity. We show that almost instantaneous stimulations can switch the collective gamma oscillations from slow to fast and vice versa. Furthermore, to make a closer contact with the experimental observations, we consider the modulation of the gamma rhythms induced by a slower (theta)

rhythm driving the network dynamics. In this context, depending on the strength of the forcing, we observe phase-amplitude and phase-phase coupling between the fast and slow gamma oscillations and the theta forcing. Phase-phase coupling reveals different theta-phases preferences for the two coexisting gamma rhythms.

4.1 Introduction

The emergence of collective oscillations in complex system has been a subject largely studied in the last decades from an experimental as well as from a theoretical point of view, for a recent review see [145]. In particular, the transition from asynchronous to collective dynamics in networks of heterogeneous oscillators has been characterized in terms of methods borrowed from statistical mechanics [25, 146, 147] and nonlinear dynamics [74, 148, 149].
Oscillatory dynamics is fundamental for the functioning of the mammalian brains, rhythms ranging from 1 to 500 Hz have been measured at a mesoscopic level, corresponding to the dynamics of neural populations, by employing electroencephalography (EEG), magnetoencephalography (MEG), or local field potential (LFP) [96].
In particular, gamma oscillations (30-100 Hz) have been suggested to underlie various cognitive and motor functions. Oscillations in the gamma band have been related to attention selection [150], memory formation and retrieval [121, 151], binding mechanisms for sensory awareness [152], and human focal seizures [153].
Gamma oscillations have been observed in many areas of the brain and their emergence has been shown to be crucially dependent on inhibitory networks [97, 100]. By following [97] gamma oscillations in purely inhibitory networks can emerge only via two mechanisms: the single neurons can fire periodically locked in phase [154] or each neuron can have irregular activity, but sufficiently strong recurrent interactions can render the asynchronous state unstable against fluctuations and collective oscillations (COs) can arise [14, 15, 155]. On one hand, the role of the synaptic mechanisms in promoting tonic synchronization in the gamma range has been clarified in [100, 156]. On the other hand, fast network oscillations with irregular neural discharges can emerge when the neurons are operating in the so-called balanced state [157–161], a typical cortical state, where the balance of excitation and inhibition allows for a healthy activity of the brain. The balanced

state has been observed *in vitro* and *in vivo* experiments in the cerebral cortex [162, 163] and reported in simulations of networks of excitatory and inhibitory spiking neurons [155, 164, 165] as well as of purely inhibitory circuits driven by external excitatory currents [23, 166].
Recently, the co-existence of gamma oscillations in three distinct bands has been reported for the cornu ammonis area 1 (CA1) of the hippocampus [105]: namely, a slow one ($\simeq$ 30-50 Hz), a fast (or intermediate) one ($\simeq$ 50-90 Hz), and a so called ε-band ($\simeq$ 90-150 Hz). However, only the two lower bands show a clear correlation (P-P coupling) with the theta rhythm during maze exploration and REM sleep, thus suggesting their functional relevance [105]. There are several further evidences that these two gamma bands correspond to different states of the hippocampal network [167]. In particular, in freely behaving rats place cells code differently the space location and the running speed during theta-nested slow or fast gamma rhythms [167–169]. Moreover, gamma rhythms with similar low and high frequencies subtypes occur in many other brain regions, besides the hippocampus [170, 171]. Despite their relevance, the mechanisms behind the emergence of these two distinct gamma bands are not yet clarified.
For what concerns the hippocampus, experiments show that slow gamma rhythms couple the activity of the CA1 area to synaptic inputs from CA3, while fast gamma rhythms in CA1 are entrained by inputs from medial Entorinhal Cortex (mEC) [171]. Slow and fast oscillations have been recorded also in CA3, where fast gamma are entrained by synaptic inputs from mEC [104]. These findings suggest that CA3-activated interneurons drive slow gamma, while mEC-activated interneurons drive fast gamma. Nonetheless, it has been shown that a substantial proportion of CA1 interneurons phase-lock to both slow and fast gamma LFP oscillations [104, 105, 172]. Therefore, as suggested by L.L. Colgin in [171], such interneurons may be part of a network that can generate either slow or fast gamma, depending on the state of the network. Furthermore there are experimental evidences that gamma rhythms can be generated locally *in vitro* in the CA1, as well as in the CA3 and mEC, thanks to optogenetic stimulations [13, 118, 119] or pharmacological manipulations, but at lower gamma frequencies with respect to optogenetics [173–176]. A recent theoretical work has analyzed the emergence of gamma oscillations in a neural circuit composed by two populations of interneurons with fast and slow synaptic time scales [177, 178]. Based on the results of this idealized rate model and on the analysis of experimental data sets for the CA1 area the authors showed that multiple gamma bands can

arise locally without being the reflection of feedforward inputs.
In the present work, we show, for the first time to our knowledge, that a single inhibitory population, characterized by only one synaptic time, can display coexisting fast and slow gamma COs corresponding to different network states. In particular, the slow gamma oscillations are associated to irregular spiking behaviors and fluctuations driven, while the fast gamma oscillations coexist with a much more regular neural dynamics and they can be characterized as mean driven [179, 180]. Furthermore, in presence of theta forcing we observe different theta-gamma cross-frequency coupling scenarios depending on the forcing amplitude. For small amplitudes we have theta-nested gamma oscillations resembling those reported for various brain areas *in vitro* under optogenetic sinusoidal theta-stimulation [13, 118, 119]. At larger amplitudes the two types of gamma COs phase lock to the theta rhythm, similarly to what has been reported experimentally for the CA1 region of the hippocampus [104, 105]. More specifically we have studied balanced sparse inhibitory networks of quadratic integrate-and-fire (QIF) neurons pulse coupled via inhibitory post-synaptic potentials (IPSPs), characterized by a finite synaptic time scale. For this sparse network we derived an effective mean-field (MF) by employing recently developed reduction techniques for QIF networks [10,14,61,123]. In the MF model, in proximity of the sub-critical Hopf bifurcations, we report regions of bistability involving one stable focus and one stable limit cycle. In direct simulations of the corresponding spiking network we observe the coexistence of two distinct COs with frequencies in the slow and fast gamma band. The slow gamma COs are due to the microscopic irregular dynamics, characteristic of the balanced dynamics, which turns the damped oscillations towards the MF focus in sustained COs. The fast gamma COs are instead related to the oscillatory branch emerging via the sub-critical Hopf bifurcation from the asynchronous state. The network can be driven from one kind of COs to the other by transiently stimulating the neurons. In presence of a theta forcing nested gamma oscillations characterized by a P-A coupling appear for small forcing amplitudes, while at intermediate amplitudes slow and fast gamma phases lock to the theta phase displaying P-P coupling between the rhythms. For even larger amplitudes only fast gamma are observables with a maximal power in correspondence of the maximum of the stimulation.
The chapter is organized as follows. In Section (4.2), we introduce the model for an inhibitory sparse balanced network of QIF neurons as well as the macroscopic and microscopic indicators employed to characterize its dynam-

ics. Section (4.3) is devoted to the derivation of the corresponding effective MF model and to the linear stability analysis of the asynchronous state. Simulation results for the network for high and low structural heterogeneity are reported in Section (4.4) and compared with MF forecasts. The coexistence and transitions from slow (fast) to fast (slow) gamma oscillations is analyzed in Section (4.5) together with the cross-frequency coupling between theta and gamma oscillations. A concise discussion of the results and of possible future developments is reported in Section (4.6). Finally, Appendix C is devoted to the analysis of coexisting gamma oscillations in Erdös-Renyi networks, while Appendix D discusses of a general mechanism for the coexistence of noise-driven and tonic oscillations.

4.2 Methods

4.2.1 The network model

We consider N inhibitory pulse-coupled QIF neurons [89] arranged in a random sparse balanced network. The membrane potential of each neuron evolves according to the following equations:

$$\tau_m \dot{V}_i(t) = I + V_i^2(t) - \tau_m J S_i(t) \tag{4.1a}$$

$$\tau_d \dot{S}_i(t) = -S_i(t) + \sum_j \epsilon_{ji} \delta(t - t_j(m)) \ , \tag{4.1b}$$

where $\tau_m = 15\ ms$ represents the membrane time constant, I an external DC current, encompassing the effect of distal excitatory inputs and of the internal neural excitability. The last term in (4.1a) is the inhibitory synaptic current, with J being the synaptic coupling and S_i the synaptic field seen by neuron i. Whenever the membrane potential V_i reaches infinity a spike is emitted and V_i resetted to $-\infty$. The field S_i is the linear superposition of all the exponential IPSPs $Y(t) = e^{(-t/\tau_d)}$ received by the neuron i from its pre-synaptic neurons in the past, namely

$$S_i(t) = \frac{1}{\tau_d} \sum_{j \in pre(i)} \sum_{m | t_j(m) < t} \epsilon_{ji} H(t - t_j(m)) Y(t - t_j(m)) \tag{4.2}$$

where τ_d is the synaptic time constant, $t_j(m)$ the spike time of the m-th spike delivered by the j-th neuron, $H(t)$ is the Heaviside function and ϵ_{ji} is the adjacency matrix of the network. In particular, $\epsilon_{ji} = 1$ (0) if a connection from node j to i exists (or not) and $k_i = \sum_j \epsilon_{ji}$ is the number of pre-synaptic neurons connected to neuron i, or in other terms its in-degree.
In order to compare the simulation results with the exact MF recently derived [10,14,123], we consider sparse networks where the in-degrees k_i are extracted from a Lorentzian distribution

$$P(k) = \frac{\Delta_k}{(k - K)^2 + \Delta_k^2}, \tag{4.3}$$

peaked at K and with a half-width half-maximum (HWHM) Δ_k, the parameter Δ_k measures the level of structural heterogeneity in the network,

and analogously to Erdös-Renyi networks we assumed the following scaling for the HWHM $\Delta_k = \Delta_0\sqrt{K}$. The DC current and the synaptic coupling are rescaled with the median in degree K as $I = I_0\sqrt{K}$ and $J = J_0/\sqrt{K}$, as usually done to achieve a self-sustained balanced state for sufficiently large in degrees [157–159,161,165]. In this chapter we will usually consider $I_0 = 0.25$, $N = 10000$ and $K = 1000$, unless stated otherwise.

4.2.2 Simulation Protocols

The network dynamics is integrated by employing a standard Euler scheme with an integration time step $\Delta t = \tau_m/10000$. The coexistence of solutions in proximity of a sub-critical Hopf bifurcation is analyzed by performing adiabatic network simulations where a control parameter (e.g. the synaptic time τ_d) is slowly varied. In particular, these are performed by starting with an initial value of $\tau_d^{(0)}$ and arriving to a final value $\tau_d^{(1)}$ in M steps, each time increasing τ_d by $\Delta\tau_d = (\tau_d^{(1)} - \tau_d^{(0)})/(M-1)$. Once the final value $\tau_d^{(1)}$ is reached, the synaptic time is decreased in steps $\Delta\tau_d$ down to $\tau_d^{(0)}$. Each step corresponds to a simulation for a time $T_s = 90$ s during which the quantities of interest are measured, after discarding a transient $T_t = 15$ s. The initial condition for the system at each step is its final configuration at the previous step.
For what concerns the analysis of the crossing times t_c from slow (fast) to fast (slow) gamma in a bistable regime, reported in Section (4.5.1), we proceeded as follows. Let us first consider the transition from slow to fast gamma COs. We initialize the system in the slow gamma state at a current $I_0 \equiv I_1$ ensuring the bistability of the dynamics. Then we increase the DC current to a value $I_0 \equiv I_2$ for a time interval T_P , after that time we return to the original value $I_0 \equiv I_1$ and we check, after a period of 1.5 s, if the system is in the slow or fast gamma regime. Then we repeat the process $M = 30$ times for each considered value of T_P and we measure the corresponding transition probability. The crossing time t_c is defined as the minimal T_P giving 80% of probability that the transition will take place. To analyze the transition from fast to slow, we initialize the system in the fast gamma state at a DC current I_1, we decrease the current to a value $I_0 \equiv I_3$ for time T_P and then we proceed as before. To examine the influence of noise on such transitions we added to the membrane potential evolution a noise term of zero average and amplitude A_n.

4.2.3 Indicators

To characterize the collective dynamics in the network we measure the mean membrane potential $v(t) = \sum_{i=1}^{N} V_i(t)/N$, the instantaneous firing rate $r(t)$, corresponding to the number of spikes emitted per unit of time and per neuron, as well as the mean synaptic field $s(t) = \sum_{i=1}^{N} S_i(t)/(NK)$[1].
The microscopic activity can be analyzed by considering the inter-spike interval (ISI) distribution as characterized by the coefficient of variation cv_i for each neuron i, which is the ratio between the standard deviation and the mean of the ISIs associated to the train of spikes emitted by the considered neuron. In particular, we will characterize each network in terms of the average coefficient of variation defined as $CV = \sum_i cv_i/N$. Time averages and fluctuations are usually estimated on time intervals $T_s \simeq 90s$, after discarding a transients $T_t \simeq 15s$.
Phase entrainment between an external forcing characterized by its phase $\theta(t)$ and the collective oscillations induced in the network can be examined by considering the following phase difference:

$$\Delta_{nm}(t) = n * \theta(t) - m * \gamma(t); \tag{4.4}$$

where $\gamma(t)$ is the phase of the COs defined by considering the time occurrences T_k of the k maximum of the instantaneous firing rate $r(t)$ of the network, namely $\gamma(t) = 2\pi(t - T_k)/(T_{k+1} - T_k)$ with $t \in [T_k, T_{k+1}]$[2].
We have a $n : m$ phase locking whenever the phase difference (4.4) is bounded during the time evolution, i.e. $|\Delta_{nm}(t)| < const.$
This somehow qualitative criterion can be made more quantitative by considering statistical indicators measuring the level of $n : m$ synchronization for irregular/noisy data. In particular, an indicator based on the Shannon entropy has been introduced in [117], namely

$$e_{nm} = \frac{(E_{max} - E)}{E_{max}} \quad with \quad E = -\sum_{k=1}^{M} p_k ln(p_k) \tag{4.5}$$

[1] In the definition of the mean synaptic field we have divided the sum also by the median in-degree K, because on average a neuron is subject to K spike trains.

[2] This definition of the phase avoids spurious phase locking indications in terms of the Kuramoto order parameter arising with not perfectly harmonic signals as pointed out in [136]

where E is the entropy associated to the distribution of $\Delta_{nm}(t)$ and $E_{max} = ln(M)$ with M number of bins.
The degree of synchronization among the phases can be also measured by the Kuramoto order parameter, namely [64, 105]

$$\rho_{nm} = \left| \frac{1}{L} \sum_{k=1}^{L} e^{i\Delta_{nm} t_k} \right| \tag{4.6}$$

where $|\cdot|$ represents the modulus and $t_k = k\frac{T_W}{L}$ are L successive equispaced times within the considered time window T_W. For completely desynchronized phases $\rho_{nm} \propto 1/L$, while partial (full) synchronization will be observable whenever ρ_{nm} is finite (one).
To assess the stationarity and the statistical significance of the obtained data we measured the above indicators within a time window T_W and we averaged the results over several distinct time windows in order to obtain also the corresponding error bars. Furthermore, to avoid the detection of spurious phase locking due to noise or band-pass filtering one should derive significance levels $e_{nm}^{(S)}$ and $\rho_{nm}^{(S)}$ for each $n : m$ phase locking indicators e_{nm} and ρ_{nm} [117,136]. The significance levels have been estimated by considering surrogate data obtained by randomly shuffling the original time stamps of one of the two considered phases. Moreover, by following [136] we considered also other two types of surrogates for the generation of $\Delta_{nm}(t)$ (4.4) within a certain time window T_W. These are the time-shift surrogate, obtained by time shifting the origin of one time series for the phases with respect to the original one in the definition of (4.4) and the random permutation surrogate, obtained by randomly choosing the origins of two time windows of duration T_W to estimate $\Delta_{nm}(t)$.

4.3 Effective Mean-Field model for a sparse QIF network

By following [14] we derive an effective MF formulation for the model (4.1). As a starting point we consider the exact macroscopic model derived in (2.65) for fully coupled networks of pulse-coupled QIF [10], in particular we focus on inhibitory neurons coupled via exponentially decaying IPSPs [123]. As reported in (2.5.1), for a structurally inhomogeneous network made of identical

QIF neurons, with the synaptic couplings randomly distributed according to a Lorentzian, the MF dynamics can be expressed in terms of only three collective variables (namely, v, r and s), as follows:

$$\begin{aligned} \tau_m \dot{r} &= 2rv + \frac{\Gamma}{\pi} s & (4.7a) \\ \tau_m \dot{v} &= v^2 + I + \bar{g}\tau_m s - (\pi \tau_m r)^2 & (4.7b) \\ \tau_d \dot{s} &= -s + r & (4.7c) \end{aligned}$$

where $\bar{g}$ is the median and Γ the HWHM of the Lorentzian distribution of the synaptic couplings.
At a mean-field level, the above formulation can be applied to a sparse network, indeed the quenched disorder in the connectivity distribution can be rephrased in terms of a random synaptic coupling. Namely, each neuron i is subject in average to an inhibitory synaptic current of amplitude $g_0 k_i s/(\sqrt{K})$ proportional to its in-degree k_i. Therefore at a first level of approximation we can consider the neurons as fully coupled, but with random values of the coupling distributed as a Lorentzian of median $\bar{g} = -J_0\sqrt{K}$ and HWHM $\Gamma = J_0\Delta_0$. The MF formulation (4.7) takes now the expression:

$$\begin{aligned} \tau_m \dot{r} &= 2rv + \frac{\Delta_0 J_0}{\pi} s & (4.8a) \\ \tau_m \dot{v} &= v^2 + \sqrt{K}(I_0 - J_0 \tau_m s) - (\pi \tau_m r)^2 & (4.8b) \\ \tau_d \dot{s} &= -s + r. & (4.8c) \end{aligned}$$

As verified in [14] for instantaneous PSPs this formulation represents a quite good guidance for the understanding of the emergence of sustained COs in the network, despite the fact that the MF asymptotic solutions are always stable foci. Instead in the present case, analogously to what found for structurally homogeneous networks of heterogeneous neurons in [123], we observe that for IPSPs of finite duration oscillations can emerge in the network as well as in the mean-field, as shown in Fig. (4.1). The data reported in the figure confirm that the MF formulation (4.8), despite not including current fluctuations, reproduces quite well the macroscopic evolution of the network in the oscillatory regime also for a sparse network.
Therefore we can safely employ such effective MF model to interpret the phenomena observed in the spiking network and to obtain theoretical predictions

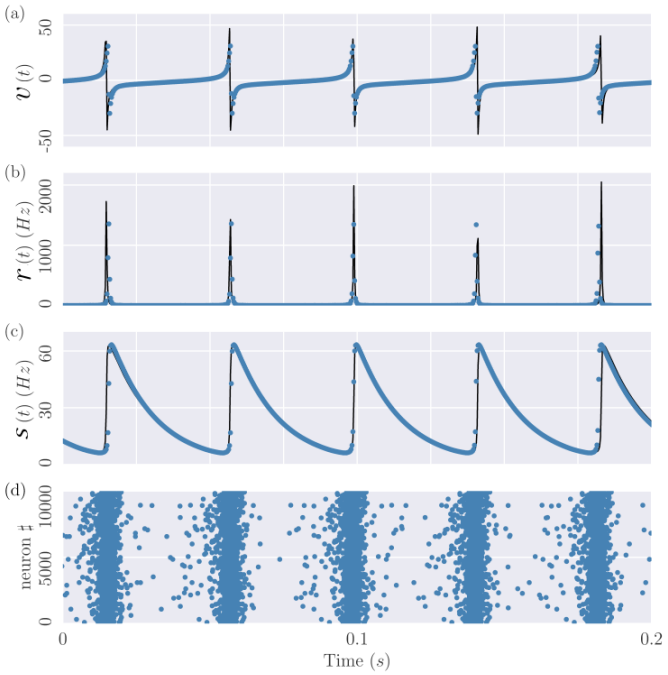

Figure 4.1: **Comparison of the spiking dynamics with the mean-field results.** Collective variables v (a), r (b) and s (c) versus time, obtained from simulations of the spiking network (4.1a) (blue circles) as well as from the MF formulation (4.8) (black line). In (d) the corresponding raster plot is also displayed, revealing clear COs with frequency $\nu_{OSC} \simeq 24$ Hz. Dynamics of the network of $N = 10000$ neurons with median in-degree $K = 1000$ and $\Delta_0 = 0.3$. Other parameters are $I_0 = 0.25$, $J_0 = 1.0$ and $\tau_d = 15$ ms.

for its dynamics.
In the next two subsections we will firstly study analytically the linear stability of the asynchronous state, which corresponds to a fixed point of (4.8), and then we will describe the bifurcation and phase diagrams associated to the MF model (4.8).

4.3.1 Linear stability of the asynchronous state

The fixed point solution (v^*, r^*, s^*) of (4.8) is given by:

$$v^* = -\frac{\Delta_0 J_0}{2\pi} \ , \tag{4.9a}$$

$$r^*\tau_m = \frac{J_0\sqrt{K}}{2\pi^2}\left(\sqrt{1+\frac{4\pi^2}{\sqrt{K}}\frac{I_0}{J_0^2}+\frac{\Delta_0^2}{K}}-1\right) \ , \tag{4.9b}$$

$$s^* = r^* \ . \tag{4.9c}$$

By performing a linear stability analysis around the fixed point solution (v^*, r^*, s^*) we obtain the following secular equation:

$$\begin{vmatrix} 2v^*-\Lambda\tau_m & 2r^* & -2v^* \\ -2(\pi\tau_m)^2 r^* & 2v^*-\Lambda\tau_m & -J_0\sqrt{K}\tau_m \\ 1 & 0 & -1-\Lambda\tau_d \end{vmatrix} = 0. \tag{4.10}$$

in a more explicit form this is

$$\begin{aligned} & (1+\Lambda\tau_d)\left[(\Lambda\tau_m-2v^*)^2+(2\pi r^*\tau_m)^2\right] \\ + \ & 2v^*(\Lambda\tau_m-2v^*)+2J_0\sqrt{K}r^*\tau_m = 0 \end{aligned} \tag{4.11}$$

In the present case, for inhibitory coupling (i.e. $J_0 > 0$) the solutions of the cubic equation (4.11) are one real and two complex conjugates. The real one is always negative therefore irrelevant for the stability analysis, while the couple of complex eigenvalues $\Lambda = \Lambda_R \pm i\Lambda_I$ can cross the imaginary axes giving rise to oscillatory behaviours via Hopf bifurcations. The presence of the two complex conjugate eigenvalues implies that whenever the asynchronous state is stable, this is always a focus characterized by a frequency of relaxation towards the fixed point given by $\nu_D = \Lambda_I/2\pi$. For excitatory coupling, the real eigenvalue can become positive with an associated saddle-node bifurcation and the emergence of collective chaos [5, 181].
By following [123], the Hopf boundaries can be identified by setting $\Lambda = i2\pi\nu_O$ in (4.11) and to zero the real and imaginary part of the resulting equation, namely one gets

$$\begin{aligned} \tfrac{(1-4\tau_d v^*)(2\pi\nu_O)^2}{r^*} - (2\pi)^2 r^*\tau_m - 2J_0\sqrt{K} = 0 \\ [(2\pi\nu_O)^2\tau_m - 4(v^*)^2 - (2\pi r^*\tau_m)^2] - 2\tfrac{\tau_m v^*}{\tau_d} = 0 \ . \end{aligned} \tag{4.12}$$

4.3.2 Phase Diagrams of the Mean-Field Model

Apart from the linear stability of the asynchronous state and the associated Hopf boundaries which can be worked out analytically, the limit cycle solutions of the MF model and the associated bifurcations have been obtained by employing the software XPP AUTO developed for orbit continuation [182]. The MF model (4.8), apart from the membrane time constant τ_m, which sets the system time scale, and the median in-degree K, which we fixed to 1000, is controlled by four independent parameters: namely, Δ_0, J_0, I_0, τ_d. In the following we will give an overview of the possible behaviors of the MF model in terms of two parameters phase diagrams for the most relevant combinations of the four mentioned parameters. The results of these analysis are summarized in Figs. (4.2) and (4.3).

Our analysis of the stationary solutions has revealed three possible regimes: stable foci (I); stable COs (II); coexistence of these two stable solutions (III). The stability boundaries of the COs are delimited by three kind of bifurcations: super-critical Hopf (black lines in the figures); sub-critical Hopf (red lines) and saddle-node (SN) of limit cycles (blue lines). Stable (unstable) COs emerge from stable foci at super-critical (sub-critical) Hopfs, while stable and unstable limit cycles merge at the SNs.

A fundamental parameter controlling the emergence of COs in the MF model is the synaptic time τ_d, indeed in absence of this time scale no oscillations are present at the MF level [14]. On the other hand too large values of τ_d also lead to COs suppression, since the present model reduces to a Wilson-Cowan model for a single inhibitory population, that it is know to be unable to display oscillations [123]. As shown in Figs. (4.2) and (4.3), oscillations are observable for intermediate values of τ_d and not too large J_0, since large inhibition leads to a quite reduced activity of the neurons not sufficient to ignite a collective behaviour. This is in agreement with the fundamental role played by gamma-Aminobutyric acid (GABA) in the emergence of epileptic seizures, characterized by an anomalous level of synchronization among the neurons, indeed the occurence of seizures seems strongly correlated with a GABA deficit, corresponding to a reduction of J_0 in our case [183, 184]. Moreover, in order to observe COs the excitatory drive I_0 should be larger than some critical value, as shown in Fig. (4.2) (c-d). This is consistent with the observation of the emergence of gamma oscillations in hippocampal slices induced through the acetylcoline agonist charbachol [173, 185], which leads to a decrease of the conductances of potassium channels, which can

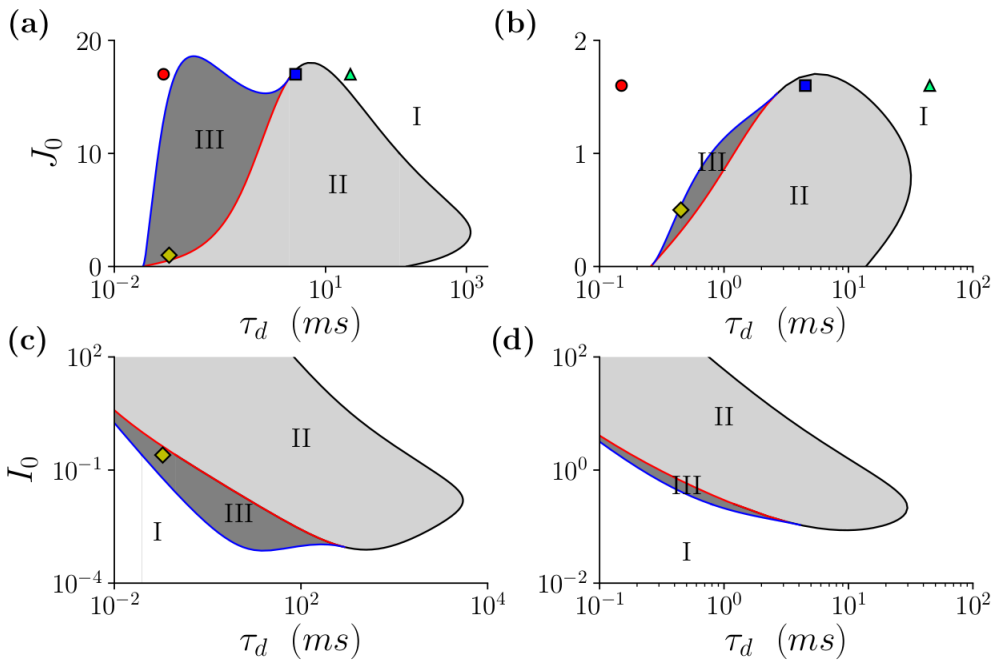

Figure 4.2: **Phase diagrams of the mean-field model in the (τ_d, J_0)-plane (a-b) and in the (τ_d, I_0)-plane (c-d)**. The left panels refer to $\Delta_0 = 0.3$ and the right ones to $\Delta_0 = 3$. The red (black) line corresponds to sub-critical (super-critical) Hopf bifurcations, while the blue curve indicates saddle-node bifurcations of limit cycles. In the region I (white) the only stable solutions are foci and in the region II (light shaded) these are limit cycles. The dark shaded area (III) represents the region of coexistence of stable foci and limit cycles. The colored symbols indicate the states analyzed in Section 4.4. The parameters are $I_0 = 0.25$ in (a-b) and $J_0 = 1.0$ in (c-d) and $K = 1000$.

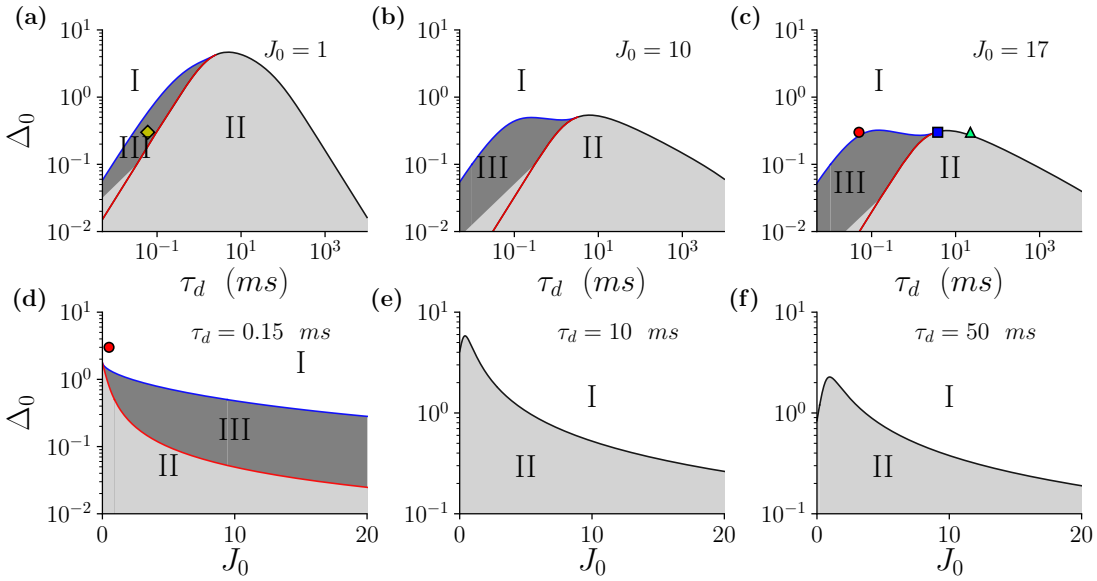

Figure 4.3: **Phase diagrams of the mean-field model in the (τ_d, Δ_0)-plane (a-c) and in the (J_0, Δ_0)-plane (d-f)** The line colors, the colored symbols and regions are defined as in Fig. (4.2). For the parameters we fixed $I_0 = 0.25$ and K=1000.

be mimicked as an increase of I_0 [186, 187]. Indeed, by increasing the structural heterogeneity (measured by Δ_0), which acts against coherent dynamics, larger values of I_0 are required for COs as well as smaller synaptic couplings (see Figs. (4.2) (b),(d) and (4.3) (d-f)). Therefore the emergence of COs can be triggered by self-disinhibition as well as by an external excitatory drive, and we expect to observe in both cases the same scenarios.
As already mentioned, for infinitely fast synapses ($\tau_d \to 0$) the only possible solutions of the MF are foci characterized by two complex conjugate eigenvalues. Nevertheless, in the corresponding network the irregular firings of the neurons, due to the dynamical balance, can sustain COs, which are predicted to relaxed toward the fixed point in the MF. In the next Section we will analyze the role of these microscopic fluctuations in triggering the network dynamics also for finite τ_d.

4.4 Network dynamics

We investigate in this Section the dynamics of the network by considering the parameter plan (τ_d, J_0). In particular, we want to examine the role of structural heterogeneity (measured by Δ_0) in shaping the dynamical behaviours. This characteristic of the network structure is extremely relevant, as it can determine even if the system is in a balanced or in an imbalanced regime [14, 188, 189].

4.4.1 High structural heterogeneity

We consider first a relatively high value for the structural heterogeneity, namely $\Delta_0 = 3.0$. For sufficiently large synaptic time constant τ_d, the bifurcation diagram reveals the emergence of oscillations in the MF model (4.8) via super-critical Hopf bifurcations, analogously to what has been reported for globally coupled networks [123]. An example of the bifurcation diagram, displaying the extrema of the mean membrane potential v as a function of τ_d is reported in Fig. (4.4) (a) for $J_0 = 1.6$. In particular, we observe for instantaneous synapses ($\tau_d \to 0$) a stable focus, as expected from the analysis previously reported in [14]. The focus is stable up to $\tau_1^{(H)}$ where it is substituted by a stable oscillatory state via a super-critical Hopf bifurcation. Oscillations are observable up to $\tau_2^{(H)}$, where via a second super-critical Hopf bifurcation they disappear and the unique stable solution for the MF system remains a focus. The typical stable regimes are denoted in Fig. (4.4) (a) by three capital letters: namely, (A) corresponds to a focus, (B) to a limit cycle and (C) to another focus. The network dynamics corresponding to these typical MF solutions is examined in the remaining panels of Fig. (4.4). For the focus solutions the network dynamics is asynchronous, as clearly visible from the corresponding raster plots in Fig. (4.4) (b) and (d). Furthermore, the dynamics of the neurons is quite regular in this case, as testified from the values of the average coefficients of variation, namely $CV \simeq 0.14$ and $CV \simeq 0.04$ corresponding to the distributions reported in Fig. (4.4) (e) and (f), respectively. At intermediate values of τ_d, as predicted by the MF analysis, we observe COs with frequency $\nu_{OSC} \simeq 34$ Hz in the network dynamics, see Fig. (4.4) (c). However, also in this case the dynamics is dominated by supra-threshold neurons with an associated very low CV, as evident from the large peak present at $cv_i \simeq 0$ in the distribution $P(cv_i)$ shown in Fig. (4.4) (g).

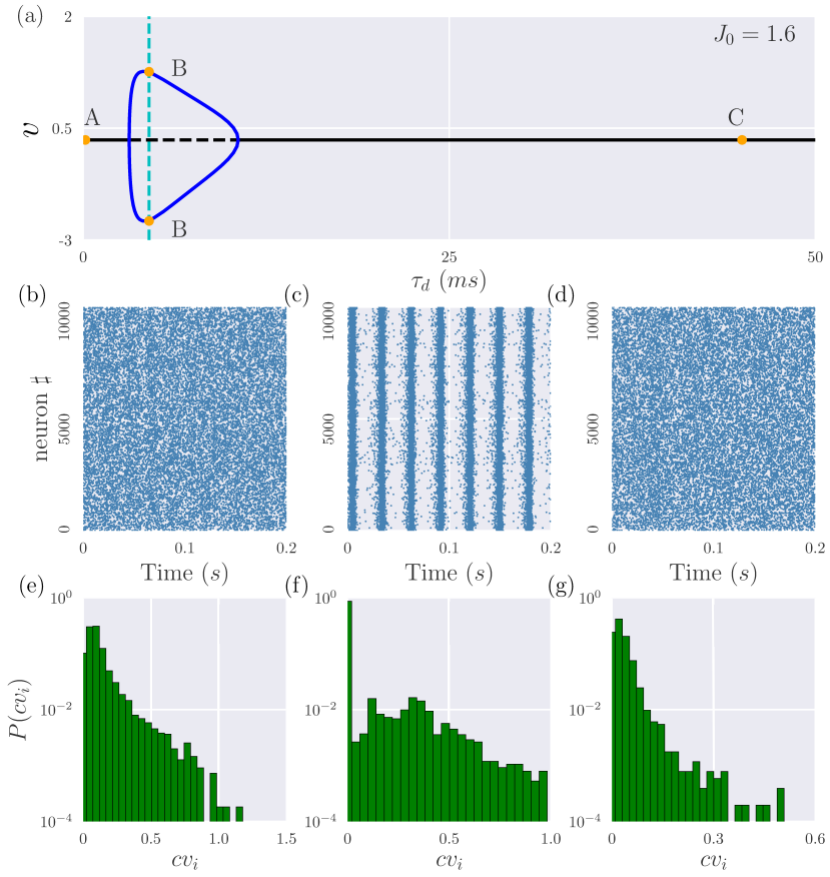

Figure 4.4: **High Structural heterogeneity: super-critical Hopf bifurcation.** (a) Bifurcation diagram of the MF model (4.8) displaying the extrema of v versus τ_d, black solid (dashed) lines refer to the stable (unstable) focus, while blues solid lines to the oscillatory state. The supercritical Hopf bifurcations take place for $\tau_1^{(H)} = 3.14$ ms and $\tau_2^{(H)} = 10.59$ ms. The capital letters in (a) denote three stationary states corresponding to different synaptic time scales, namely: (A) $\tau_d = 0.15$ ms, (B) $\tau_d = 4.5$ ms and (C) $\tau_d = 45$ ms. The network dynamics corresponding to these states is reported in the panels below: the left column corresponds to (A), the central to (B) and the right one to (C). For each column, the top panels are the corresponding raster plots (b,c,d) and the bottom ones the distributions of the $\{cv_i\}$ of the single neurons (e,f,g). The average firing rates $\bar{r}$ are: (A) $\bar{r} = 11.68$ Hz, (B) $\bar{r} = 24.89$ Hz and (C) $\bar{r} = 10.39$ Hz. Network parameters are $N = 10000$, $K = 1000$ and $\Delta_0 = 3.0$. Other parameters are $I_0 = 0.25$ and $J_0 = 1.6$.

For lower synaptic coupling J_0 the phase portrait changes, as shown in Fig. (4.5) (a) for $J_0 = 0.5$. In this case the MF analysis indicates that the transition from a stable focus to the oscillatory state occurs by increasing τ_d via a sub-critical Hopf bifurcation. At large synaptic time constant, the stable focus is recovered via a super-critical Hopf bifurcation taking place at $\tau_2^{(H)}$, analogously to what has been seen for larger coupling. An interesting regime is observable between $\tau^{(S)}$, where the stable and unstable limit cycle merge via a saddle-node bifurcation, and $\tau_1^{(H)}$, where the focus become unstable. In this interval the MF model displays two coexisting stable solutions: a limit cycle and a focus. It is important to verify if also the finite size sparse network displays this coexistence, indeed as shown in Fig. (4.5) depending on the initial conditions the network dynamics can converge towards COs or towards an asynchronous state. In particular, we observe that the asynchronous dynamics is associated to extremely low cv-values (see Fig. (4.5) (d)) suggesting that this can be considered as a sort of irregular splay state [190]. However, also the COs with $\nu_{OSC} \simeq 58$ Hz are characterized by a low average coefficient of variation, namely $CV \simeq 0.014$ indicating that the dynamics is mean driven. The sub-critical Hopf, as expected, is associated to a hysteretic behavior, this effect can be revealed by considering simulations concerning an adiabatic variation of τ_d. The results of these simulations are reported in Fig. (4.5) (b), where the maximal values of the instantaneous firing rate r_M are reported as a function of τ_d for the adiabatic protocol and compared with the MF estimations of r_M. From the figure it is clear that the transition from the focus to the stable limit cycle occurs at $\tau_d < \tau_1^{(H)}$ and the system returns from the oscillatory state to the asynchronous one at τ_d definitely smaller than $\tau^{(S)}$. These are finite size (and possibly also finite time) effects, indeed as shown in Fig. (4.5) (b) by increasing N the transition points approach the MF ones.

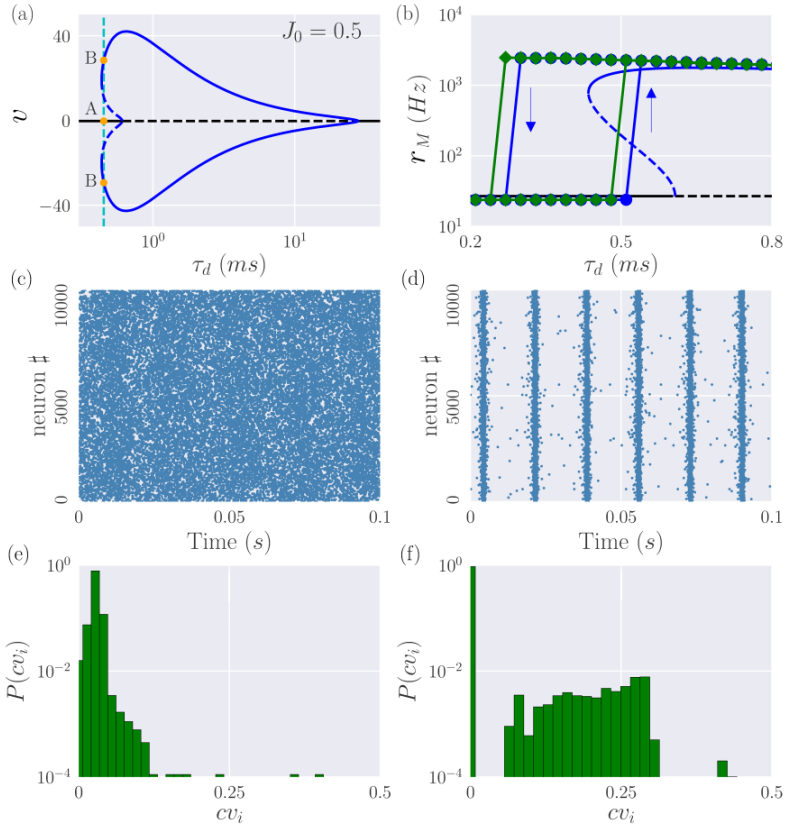

Figure 4.5: **High structural heterogeneity: sub-critical Hopf bifurcation.** (a) Bifurcation diagram of the MF model analogous to the one reported in Fig. (4.4) (a). The super-critical (sub-critical) Hopf bifurcation takes place at $\tau_2^{(H)} = 27.96$ ms ($\tau_1^{(H)} = 0.61$ ms), the saddle node of limit cycles at $\tau^{(S)} = 0.43$ ms. The capital letters in (a) denote two stationary states corresponding to the same synaptic time scales $\tau_d = 0.45$ ms. The network dynamics corresponding to these states is reported in the panels below: the left column correspond to (A) and the right one to (B). For each column, the top panels display the raster plots (c,d) and the bottom ones the distribution of the $\{cv_i\}$ of the single neurons (e,f). In panel (b) are reported the maximal values of the rate r_M obtained by performing adiabatic simulations by first increasing and then decreasing the synaptic time τ_d (green) diamonds for $N = 10000$ and (blue) circles for $N = 20000$, the arrows denote the jump from one state to the other. The MF results are also displayed: solid (dashed) black lines refer to stable (unstable) foci, while solid (dashed) blue lines to stable (unstable) limit cycles. The average firing rates $\bar{r}$ are: (A) $\bar{r} = 26.16\ Hz$ and (B) $\bar{r} = 57.35\ Hz$. Parameters are the same as in Fig. (4.4), apart for $J_0 = 0.5$, the parameters for the adiabatic simulations are $\Delta\tau_d = 0.03$ ms, $\tau_d^{(0)} = 0.21$ ms and $\tau_d^{(1)} = 0.81$ ms.

4.4.2 Low structural heterogeneity

We consider now a relatively low value of the structural heterogeneity, i.e. $\Delta_0 = 0.3$, which for instantaneous synapses can sustain a dynamically balanced state [14]. Let us first consider a relatively large coupling, namely $J_0 = 17.0$, the corresponding bifurcation diagram for the MF model is reported in Fig. (4.6) (a). This is quite similar to the one previously shown for high structural heterogeneity in Fig. (4.4) (a). However, peculiar differences are observable at the level of network simulations. Indeed in this case COs are present for all the considered τ_d-values, even if these correspond to stable foci in the MF (states (A) and (C) in Fig. (4.6) (a)) as evident from the raster plots reported in Fig. (4.6) (b) and (d). In particular we measured the following frequencies for the observed COs: $\nu_{OSC} \simeq 57$ Hz for state (A), $\nu_{OSC} \simeq 30$ Hz for (B) and $\nu_{OSC} \simeq 16$ Hz for (C). Furthermore, the network dynamics is now definitely more irregular than for high Δ_0 with distributions $P(cv_i)$ centered around $cv_i = 1$ for the states (A) and (C) in Fig. (4.6) (a) corresponding to stable foci in the MF formulation (see Fig. (4.6) (e) and (g)) and with $P(cv_i)$ extending towards values around $cv_i \simeq 1$ for the oscillatory state (B), as shown in Fig. (4.6) (i). This irregularity in the spike emissions is a clear indication that now the dynamics is mostly fluctuation driven due to the dynamically balanced dynamics observable in the sparse network for sufficiently low structural heterogeneity. Furthermore, as shown in [14] for instantaneous synapses, these current fluctuations are able to turn the macroscopic damped oscillations towards the stable foci, observable in the MF model, in sustained COs in the network. The origin of the COs observable for the state (B) is indeed different, since in this case sustained oscillations emerge due to a super-critical Hopf bifurcation both in the MF and in the network dynamics.

By decreasing the synaptic coupling J_0 (Fig. (4.7) (a)) we observe in the MF phase diagram the emergence of regions where the oscillations coexist with the stable focus in proximity of a sub-critical Hopf bifurcation, analogously to what has been reported for high heterogeneity (see Fig. (4.5) (a)). At variance with that case, we have now in the network a bistability between two COs whose origin is different: one emerges via a Hopf bifurcation and it is displayed in Fig. (4.5) (d), while the other is sustained by the irregular spiking associated to the balanced state and the corresponding raster plot is reported in Fig. (4.5) (c).

In particular, the latter COs are associated to large cv-values (Fig. (4.7) (e))

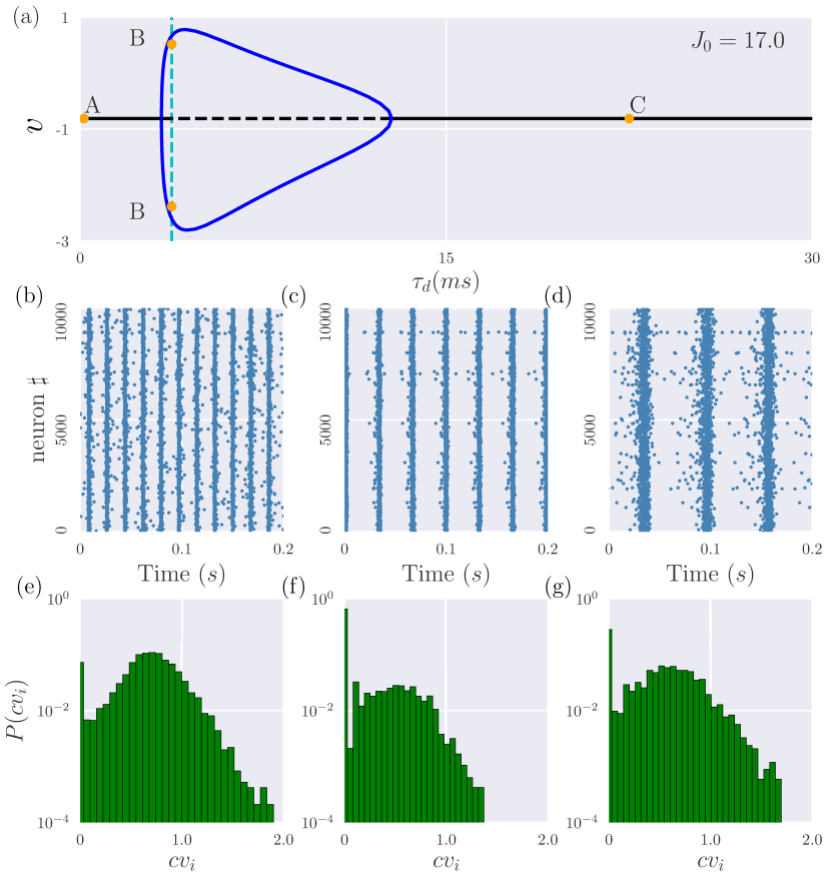

Figure 4.6: **Low structural heterogeneity: super-critical Hopf bifurcation.** The panels here displayed are analogous to the ones in Fig. (4.4). In this case the super-critical Hopf bifurcations occur for $\tau_1^{(H)} = 3.33$ ms and $\tau_2^{(H)} = 12.61$ ms and the stationary states in (a) corresponding to the capital letter (A), (B) and (C) refer to $\tau_d = 0.15$ ms, $\tau_d = 3.75$ ms and $\tau_d = 22.5$ ms, respectively. The average firing rates $\bar{r}$ are: (A) $\bar{r} = 4.92\ Hz$, (B) $\bar{r} = 11.31\ Hz$ and (C) $\bar{r} = 1.93\ Hz$. The parameters are the same as in Fig. (4.4), apart $\Delta_0 = 0.3$. and $J_0 = 17$.

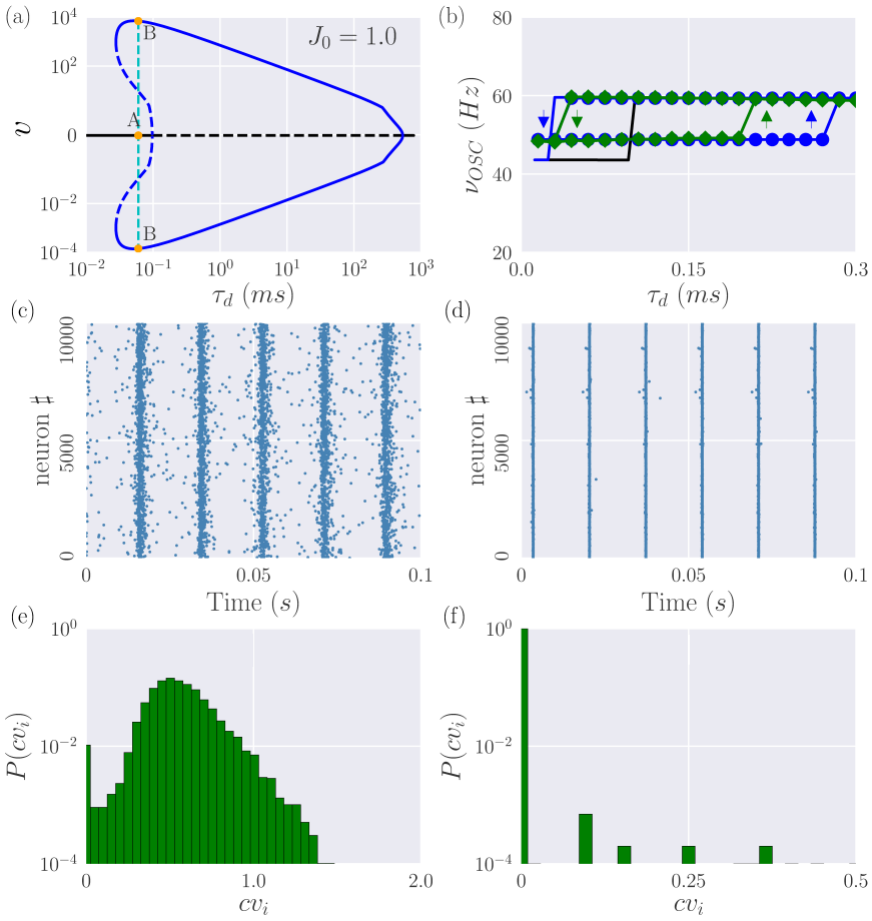

Figure 4.7: **Low structural heterogeneity: sub-critical Hopf bifurcation.** The panels here displayed, apart panel (b), are analogous to the ones in Fig. 4.5. In the present case the sub-critical Hopf occurs at $\tau_1^{(H)} = 0.097$ ms, while the super-critical Hopf at $\tau_2^{(H)} = 531.83$ ms and the saddle-node of limit cycles at $\tau^{(S)} = 0.028$ ms, and the coexisting states (A) and (B) shown in (a) refer to $\tau_d = 0.06$ ms. Panel (b) reports the frequency of collective oscillations as measured via adiabatic simulations for $N = 2000$ by considering $T_s = 90$ ms (blue circles) and $T_s = 1500$ ms (green diamonds), the transient time $T_t = 15$ ms is unchanged. The solid lines in (b) refer to the MF results, namely the black line to ν_D and the blue one to the limit cycle frequency ν_O. The average firing rates $\bar{r}$ are: (A) $\bar{r} = 22.75\ Hz$ and (B) $\bar{r} = 59.9\ Hz$. The parameters are as in Fig. (4.6) apart for $J = 1.0$ and for the adiabatic simulations are $\Delta\tau_d = 0.015$ ms, $\tau_d^{(0)} = 0.015$ ms and $\tau_d^{(1)} = 0.30$ ms.

typical of a balanced regime, while the other COs are extremely regular as shown in Fig. (4.7) (f) resembling the dynamics of a highly synchronized system.
In order to analyze the coexistence region, we report in Fig. (4.7) (b) the frequencies ν_{OSC} of the collective oscillations as measured via adiabatic simulations of the network (symbols). Furthermore, the MF results for ν_D associated to the foci and the frequencies ν_O of the limit cycles are also reported in the figure as black and blue solid line, respectively. The frequencies of the COs in both states are reasonably well captured by the MF approach, furthermore the two frequencies can be quantitatively associated to fast and slow gamma oscillations. The comparison reveals that the COs induced by microscopic irregular firing exist far beyond $\tau_1^{(H)}$, despite here the unique stable solution predicted by the MF should be the almost synchronized bursting state shown in Fig. (4.7) (d). On the other hand the backward transition is almost coincident with the MF prediction for $\tau^{(S)}$ as displayed in Fig. (4.7) (b). As reported in Fig. (4.7) (b), we observe that also the forward transition value approaches to $\tau_1^{(H)}$ by increasing the duration T_s of the adiabatic steps. Therefore this result suggest that the observed discrepancies are due to finite time (and possibly finite size) effects affecting the network simulations.

4.5 Coexistence of slow and fast gamma oscillations

In the previous Section we have shown, for a specific choice of the parameters, that fast and slow collective gamma oscillations can coexist. However, the phenomenon is observable in the whole range of coexistence of the stable foci and of the stable limit cycles. In particular, in Fig. (4.8) we report in the (τ_d, J_0)-plane the frequencies ν_D associated to the damped oscillations towards the MF focus in panel (a) and the frequencies ν_O of the limit cycles in panel (b). It is evident that $\nu_D \simeq 30 - 40$ Hz, while the frequencies of the limit cycle ν_O are of the order of 60 Hz, thus in the network we expect to observe coexisting COs characterized by slow and fast rhythms in a wide range of parameters.
For this parameter set ν_D seems to depend only slightly on τ_d and J_0. On the contrary the frequency ν_O, characterizing the more synchronized events, is influenced by these parameters. In particular, ν_O decreases for increasing

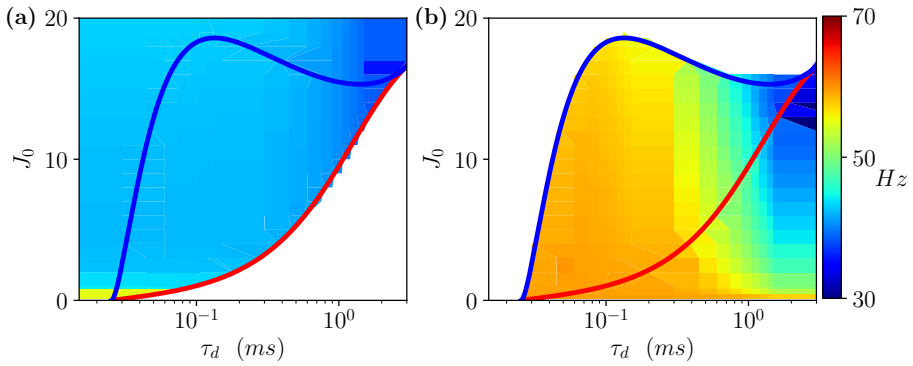

Figure 4.8: **Coexisting fast and slow gamma oscillations** (a) Frequencies ν_D associated to the damped oscillations towards the stable foci; (b) frequencies ν_O of the limit cycles. Red lines refer to the sub-critical Hopf boundaries, while the blue ones to saddle-node bifurcations of limit cycles. Parameters as in Fig. (4.2)

IPSP time duration, similarly to what observed experimentally for cholinergic induced gamma oscillations in the hippocampus *in vitro* [173]. Moreover, barbiturate, a drug often used as anxiolytic, is known to increase IPSP time duration [191] and slow down gamma oscillations [192], in accordance with our scenario. Furthermore, for $\tau_d > 1$ ms the increase of J_0 leads to a decrease of ν_D, similarly to the effect of alcohol that induces an increase of inhibition associated to a decrease in gamma oscillation frequencies measured in the human visual cortex [193].
The coexistence of fast and slow gamma COs is a quite general phenomenon not limited to the specific network topology we employed, i.e. that associate to the Lorentzian in-degree distribution. Indeed, as shown in Appendix C it can be observed also for a sparse Erdös-Renyi network.

4.5.1 Switching gamma rhythms

As a further aspect, we will consider the possibility to develop a simple protocol to drive the system from slow gamma COs to fast ones (and vice versa) in the bistable regime. Let us consider the case where the network is oscillating with slow gamma frequency as shown in Fig. (4.9) for $I_0 \equiv I_1 = 0.25$. The protocol to drive the system in the fast gamma band consists in

delivering a step current I_2 to all the neurons for a very limited time interval T_{sh}. In this way the system is transiently driven in a regime where oscillatory dynamics is the only stable solution, as a matter of fact the neurons remain in a high frequency state even after the removal of the stimulation, when I_0 returns to the initial value I_1 (see Fig. (4.9)). In order to desynchronize the neurons and to recover the slow gamma COs , we delivered random quenched DC currents $I_0(i)$ (with $i = 1, \ldots, N$) to the neurons for a time period T_{sl}. The currents $I_0(i)$ are taken from a flat distribution with a very low average value I_3 and a width ΔI_3 corresponding to a parameter range where the MF foci are the only stable solutions. As shown in Fig. (4.9) in this case to drive the system from fast to slow gamma oscillations it was sufficient to apply the perturbation for a much smaller period $T_{sl} << T_{sh}$.
Let us now try to characterize in more details the observed switching transitions. This can be done by considering the MF bifurcation diagram in terms of the external DC current I_0 reported in Fig. (4.10) (a) for the examined parameters. The diagram reveals a sub-critical Hopf bifurcation taking place at $I^{(H)} \simeq 0.43$ and a region of bistability extending from $I^{(S)} \simeq 0.06$ to $I^{(H)}$. Therefore, if we consider a DC current in the bistable interval (namely, $I_0 \equiv I_1 = 0.25$) and we prepare the system in the slow gamma regime a transition to the fast gamma COs will be observable whenever the DC current is increased to a value $I_0 \equiv I_2 > I^{(H)}$. However, if we return in the bistable regime at $I_0 \equiv I_1$, after delivering the perturbation I_2 for a time interval T_P, it is not evident in which regime (fast or slow) the system will end up. Thus we have measured the transition probability from slow to fast gamma for different T_P and I_2 by following the protocol reported in Section 4.2.2. We analyzed these transitions in presence of a small additive noise on the membrane potentials of amplitude A_n, somehow encompassing the many sources of noise present in neural circuits.
The results shown in Fig. (4.10) (b) for $I_2 = 1.0$ and $A_n = 0.05$ reveal that even if $I_2 > I^{(H)}$ the perturbation should be applied for a minimal time interval $T_P > t_c \simeq 0.12$ s to induce the transition to the fast gamma COs in at least the 80% of cases. It is interesting to note that the noise amplitude can play a critical role on the switching transition, indeed the increase of A_n can desynchronize the fast gamma regime even for $T_P > t_c$, see Fig. (4.10) (c). Therefore t_c depends critically not only on I_2 but also on A_n: as expected by increasing I_2 the crossing time drops rapidly towards zero, while the switching transition is delayed to longer times for larger A_n (see Fig. (4.10) (d)).

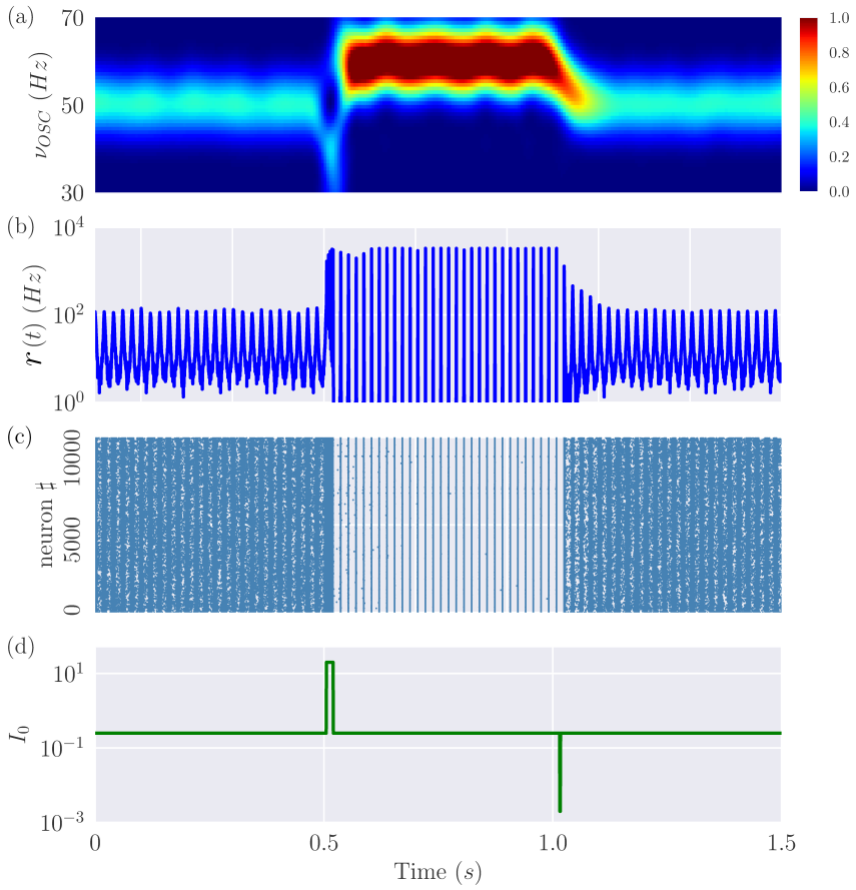

Figure 4.9: **Switching from fast (slow) to slow (fast) gamma oscillations** Results of the switching experiments described in the text, from top to bottom: (a) spectrogram of the mean membrane potential v; (b) the firing rate $r(t)$; (c) the raster plot and (d) the stimulation protocol reporting the average external DC current. The parameters are the same as in Fig. (4.7) (in particular $\tau_d = 0.06$ ms), apart $T_{sh} = 0.015$ s, $T_{sl} = 0.0015$ s, $I_1 = 0.25$, $I_2 = 20.0$, $I_3 = 0.012$, $\Delta I_3 = 0.01$.

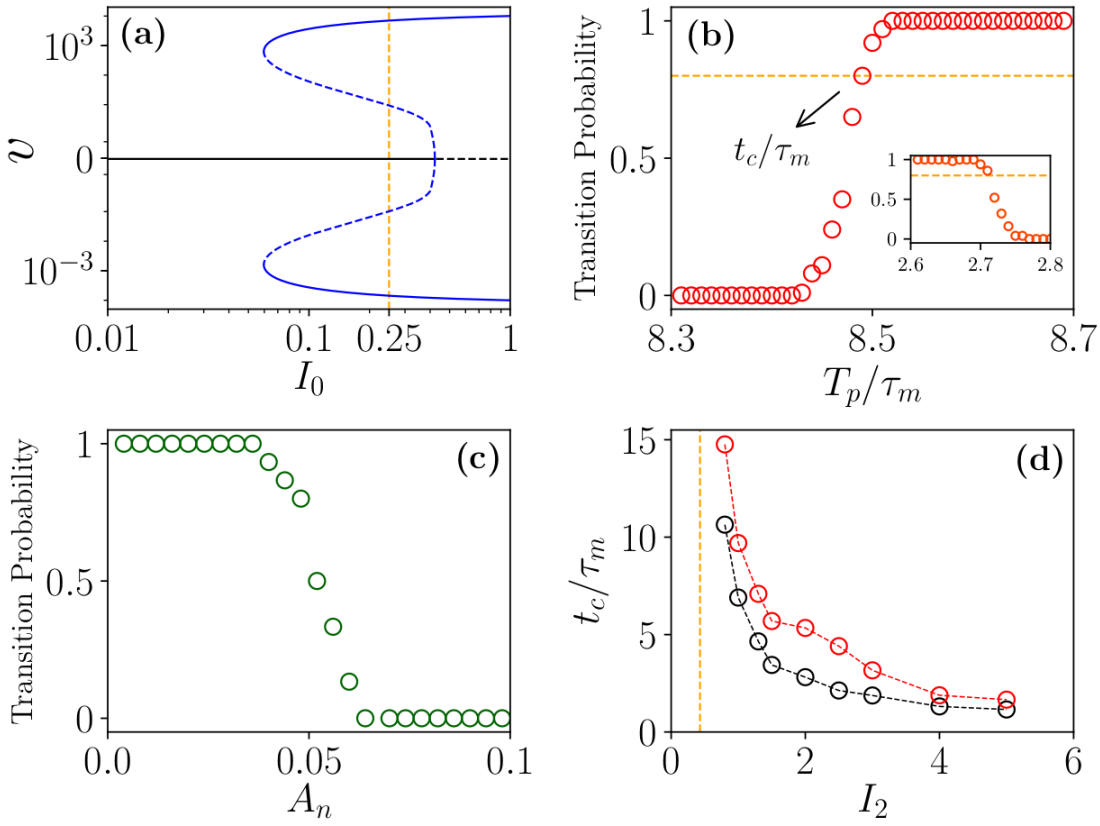

Figure 4.10: **Statistics of the switching transitions** (a) Bifurcation diagram of the MF model reporting the extrema of the mean membrane potential v as a function of I_0 displaying stable (solid line) and unstable solutions (dashed lines) for foci (black) and limit cycles (blue). The vertical dashed (orange) line refers to $I_0 = 0.25$. (b) Transition probability as a function of T_P, the orange dashed line denotes the 80 % for $I_2 = 1.0$, in the inset the data for the transition from fast to slow gamma is reported for $I_3 = 0.03$, in both cases $A_n = 0.05$ (c). Transition probability as a function of the noise amplitude A_n for $I_2 = 1$ and $T_P = 8.48\tau_m$. (d) Crossing times t_c versus the perturbation amplitude I_2 for various noise levels: $A_n = 0.02$ (black circles) and 0.07 (red circles). The vertical orange line indicates the value $I^{(H)}$. Panels (c-d) refer to the transition from slow to fast gamma COs, while the inset in (b) to the transition from fast to slow gamma. The parameters are the same as in Fig. (4.7).

For what concerns the transition from fast to slow gamma, this occurs in an irreversible manner only for amplitude of the perturbation $I_3 < I^{(S)}$, an example is shown in the inset of Fig. (4.10) (b). Despite the switching transition can be observed also for $I_3 > I^{(S)}$ this will be much more complex due to the competition of the two stable states in the interval $I_0 \in [I^{(S)} : I^{(H)}]$ and more specific protocols should be designed to obtain the desynchronization of the system.

4.5.2 Theta-gamma cross-frequency coupling

So far we have described a simple protocol where external constant stimulations to the inhibitory network can drive the neural population from one state to the other. However, gamma oscillations are usually modulated by theta oscillations in the hippocampus and in the neocortex during movement and REM sleep [170, 194]. This has recently inspired a series of optogenetic experiments *in vitro* intended to reproduce the effect of the theta forcing and the activity observed *in vivo* [13, 118, 119]. To make a closer contact with these experiments we decided to consider a periodic stimulation of all neurons in the network as follows:

$$I_0(t) = I_\theta[1 - cos(2\pi\nu_\theta t)] \quad ; \tag{4.13}$$

where the phase of the theta forcing is defined as $\theta(t) = 2\pi\nu_\theta t$. The term appearing in (4.13) corresponds to the synaptic input received by the neurons, in order to compare this forcing term with the LFPs experimentally measured in [104, 105] and which reveals theta oscillations, one should remember that the LFP corresponds to the electrical potential measured in the extracellular medium around neurons [195]. Therefore for a meaningful comparison with the synaptic input (4.13) the sign of the LFP should be reversed. This is consistent with the observations reported in [104, 105] that the maximum of activity of the excitatory (pyramidal) cells is observed in correspondence of the minimum of the LFP.
We considered the network dynamics in presence of the periodic forcing (4.13) and additive noise on the membrane potentials (with zero mean and amplitude A_n). As shown in Fig. (4.11), the response of the system to the forcing is controlled by the value of the amplitude I_θ in (4.13): for small $I_\theta \leq 0.20$ one observes only slow gamma COs; for intermediate values of the amplitude $0.20 < I_\theta \leq 0.32$ one has the coexistence of slow and fast gamma COs; while

for $I_\theta \geq 0.32$ only fast oscillations are present.
For small I_θ, as one can appreciate from the raster plot in panel (m), the firings of the neurons, despite being partially synchronized, are quite irregular. Furthermore the corresponding spectrogram in Fig. (4.11) (k) reveals that the power is concentrated at frequencies below 50 Hz and that the amplitude of the spectrum has a modulated structure as a function of the phase. This is confirmed by the analysis of the power of the spectrum PS (PF) restricted to the slow (fast) gamma band (see Fig. (4.11) (n)). These are indications of theta-nested gamma oscillations, as confirmed by the instantaneous firing rate reported in Fig. (4.11) (l), which reveals also an evident P-A coupling between the gamma phases and the theta forcing.
These results resemble experimental observations of theta-nested gamma oscillations induced *in vitro* by sinusoidal optical stimulation at theta frequency in the medial entorhinal cortex (mEC) [119] and in the areas CA1 [13] and CA3 [118] of the hippocampus. In all these experiments single neurons spiked quite irregularly, while the collective dynamics was oscillatory, analogously to our dynamics as shown in Fig. (4.11) (l) and (m). As previously discussed, these COs are induced by intrinsic fluctuations and characterized at a MF level by frequencies $\simeq \nu_D$ (green solid line), which represents a reasonable estimation of the position of the maxima of the spectrogram as shown in Fig. (4.11) (k).
The situation is quite different for sufficiently large forcing amplitude, where the neuronal dynamics becomes quite regular and highly synchronized, as evident from Figs. (4.11) (d) and (e). In this case the power is concentrated in the fast gamma band and it is maximal in correspondence of the largest value of I_0 occuring at $\theta = \pi$ (see Figs. (4.11) (c) and (f)). Furthermore the profile of the maximal power in the spectrogram follows reasonably well the MF values ν_O (red solid line) expected for fast gamma COs, as evident from Fig. (4.11) (c). For these large currents we have a sort of pathological synchronization usually observable in connection with neuronal diseases. In particular, highly synchronized fast gamma oscillations have been observed in patients with neocortical epilepsy [196].
The most interesting situation occurs for intermediate amplitudes, specifically we considered $I_\theta = 0.30$. As evident from Figs. (4.11) (h) and (i) in this case the network dynamics can vary noticeably from one theta cycle to the next, due to the switching from one gamma regime to the other occurring erratically. However by averaging over a sufficiently large number of cycles we can identify stationary features of this dynamics. In particular, we

observe that the values of maximum power in the averaged spectrum correspond to different theta phases for the slow and fast gamma COs: namely, for slow gamma the maximal activity is observable at small angles, while for fast gamma this corresponds to the largest value of the forcing current (4.13) (see Figs. (4.11) (g) and (j)).
These findings resemble the experimental results reported in [104] for the region CA1 of the hippocampus in freely moving rats, where it has been reported that slow gamma power were peaked around $\theta \simeq 0.4\pi$ and fast gamma power around $\theta \simeq \pi$, corresponding also to the maximum of activity of excitatory place cells. Similar results have been reported in [105] for what concerns the slow gamma rhythm, however in those experiments fast gamma (referred in as intermediate gamma) occurs earlier in the theta cycle.
The network response to the external periodic forcing (4.13) can be interpreted in terms of an adiabatic variation of the external current whenever the time scale of the forcing term is definitely slower with respect to the neuronal time scales (i.e. τ_m and τ_d). Since this is the case, we can try to understand the observed dynamics at a first level of approximation by employing the bifurcation diagram of the MF model obtained for a constant DC current I_0, which is shown in Fig. (4.11) (a) for the set of parameters here considered. The diagram reveals that the system bifurcates via a sub-critical Hopf from the asynchronous state to regular oscillatory behavior at a current $I^{(H)} \simeq 0.159$ and that the region of coexistence of stable foci and limit cycles is delimited by a saddle-node bifurcation occurring at $I^{(S)} \simeq 0.012$ and by $I^{(H)}$.
The forcing current (4.13) varies over a theta cycle from a value $I_0 = 0$ at $\theta = 0$ up to a maximal value $I_0 = 2I_\theta$ at $\theta = \pi$ and returns to zero at $\theta = 2\pi$. Since the forcing current will start from a zero value, we expect that the network will start oscillating with slow gamma frequencies associated to the stable focus which is the only stable solution at small $I_0 < I^{(S)}$. Furthermore, if $I_\theta < I^{(H)}/2$ the system will remain always in the slow gamma regimes during the whole forcing period, since the focus is stable up to the current $I^{(H)}$.
For amplitudes $I_\theta > I^{(H)}/2$ we expect a transition from slow to fast COs for a theta phase $\theta^{(H)} = \arccos\left[(I_\theta - I^{(H)})/I_\theta\right]$ corresponding to the crossing of the sub-critical Hopf. Since this transition is hysteretic the system will remain in the fast regime until the forcing current does not become extremely small, namely $I_0 < I^{(S)}$, corresponding to a theta phase $\theta^{(S)} = 2\pi - \arccos\left[(I_\theta - I^{(S)})/I_\theta\right]$.

The performed analysis is quasi-static and does not take into account the time spent in each regime. If $I_\theta >> I^{(H)}$ the time spent by the system in the slow gamma regime is extremely reduced, because $\theta^{(H)} \simeq 0$ and $\theta^{(S)} \simeq 2\pi$, and this explains why for large I_θ we essentially observe only fast gamma. On the other hand, we find only slow gamma COs for I_θ up to 0.20, a value definitely larger than $I^{(H)}/2$, and this due to the fact that a finite crossing time is needed to jump from one state to the other as discussed in the previous subsection.

Let us now focus on the case $I_\theta = 0.3$, where we observe the coexistence of fast and slow gamma COs. As already mentioned we have stable foci in the range $I_0 \in [0 : I^{(H)}]$, this in terms of θ-angles obtained via the relationship (4.13) for $I_\theta = 0.3$ corresponds to an interval $\theta/\pi \in [0 : 0.34]$, roughly matching the region of the spectrogram reported in Fig. (4.11) (g) where the maximum power of slow gamma oscillations is observable. As already mentioned, even if the forcing current $I_0(\theta)$ decreases for $\theta \to 2\pi$, we would not observe slow gamma at large θ-angles due to the hysteretic nature of the sub-critical Hopf transition. Slow gamma COs are associated to fluctuation driven dynamics with frequency $\simeq \nu_D$ (green solid line), as confirmed also by the comparison with the maxima of the power spectrum reported in Fig. (4.11) (g).

For currents $I_0 > I^{(H)}$ only the limit cycles (corresponding to fast gamma COs with frequencies ν_O) are stable, indeed the maximum of the power spectrum for fast gamma COs occurs for $\theta \simeq \pi$ where $I_0 \simeq 0.6 > I^{(H)}$ is maximal. As expected, the CO frequency associated to the maximum of the power spectrum is well reproduced by ν_O (see the red solid line in Fig. (4.11) (g)).

As a last point, let us examine if the coexistence of fast and slow gamma COs is related to some form of P-P locking between theta forcing and gamma oscillations [105,117]. As evident from Fig. (4.12) (a) and (b) the theta forcing at $\nu_\theta = 10$ Hz locks the collective network dynamics, characterized by the mean membrane potential and by the γ-phase defined in Section 4.2.3. In particular, for this specific time window we observe for each θ-oscillations exactly six γ-oscillations of variable duration: slower at the extrema of the θ-window and faster in the central part. In agreement with the expected coexistence of γ rhythms of different frequencies.

Let us quantify these qualitative observations by considering statistical indicators measuring the level of $n : m$ synchronization for irregular/noisy data over a large number of theta cycles. In particular, we will employ the Kuramoto order parameter ρ_{nm} and the normalized entropy e_{nm} introduced in

Section 4.2.3 measured over time windows of duration T_W and averaged over many different realizations.
As shown in Fig. (4.12) (c) and (d), both these indicators exhibit two maxima showing the existence of two different locking between θ and γ oscillations for $n : m$ equal to $\simeq 3 - 4$ and $\simeq 8$, thus corresponding to slow and fast gamma (being $\nu_\theta = 10$ Hz). By following [136], in order to test if the reported P-P couplings are significant, we have estimated ρ_{nm} over time windows of increasing duration, namely from 0.1 s to 1 s. As shown in Fig. (4.12) (c) the measured values do not vary substantially even by increasing T_W by a factor 10. This is a clear indication of the stationarity of the P-P locking phenomenon here analysed [136]. Furthermore, we measured e_{nm} also for surrogate data obtained by random permutation and by time-shift (for the exact definitions see Section 4.2.3 and [136]), the values obtained for these surrogate data are almost indistinguishable from the original ones (see Fig. (4.12) (d)). These results demand for the development of more effective approaches able to distinguish true locked state from spurious locking.
Finally, the significance level of the reported measurements have been evaluated by randomly shuffling the time stamps of the γ-phases and denoted as $\rho^{(S)}$ and $e^{(S)}$, respectively (dashed lines in Fig. (4.12) (c) an (d)). The values of $\rho^{(S)}$ and $e^{(S)}$ are definitely smaller than those of the corresponding indicators in correspondence of the observed P-P lockings, thus confirming their significance.

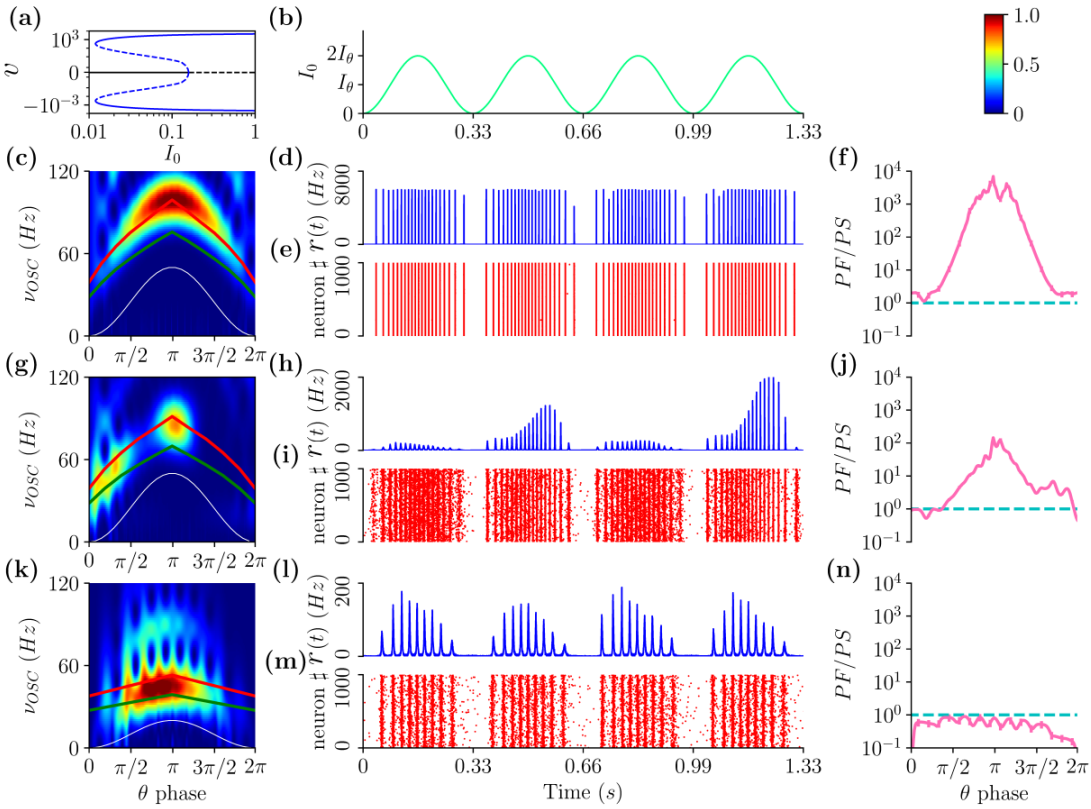

Figure 4.11: **Fast and slow gamma oscillations entrainement with the theta forcing** (a) Bifurcation diagram of the MF model analogous to the one reported in Fig. (4.10) (a). (b) Theta forcing (4.13) versus time. The three lower rows refer from top to bottom to $I_\theta = 0.35$, 0.3 and 0.1. In the left column are reported the averaged spectrograms as a function of the theta phase. In the same panels are reported ν_D (solid green line), ν_O (solid red line) as a function of θ, as well as the forcing in arbitrary units (white solid line). The central column displays an instance of a short time interval of the corresponding raster plots and instantaneous firing rates $r(t)$. The right column reports the ratio PF/PS of the power contained in the fast ($50 < \nu_{OSC} < 100$ Hz) and slow ($30 \leq \nu_{OSC} \leq 50$ Hz) gamma bands as a function of the θ phase. In this case the error bars are displayed, but are almost invisible on the reported scale. Parameters are $J_0 = 1$, $\tau_d = 0.15$ ms, $\Delta = 0.3$ and $K = 1000$, for the simulations we considered $N = 10000$, and $\nu_\theta = 3$ Hz and $A_n = 1.1 \times 10^{-3}$, the data for the spectrograms (left row) have been obtained by averaging over 30 theta cycles and those for PF/PS (right row) over 400 cycles.

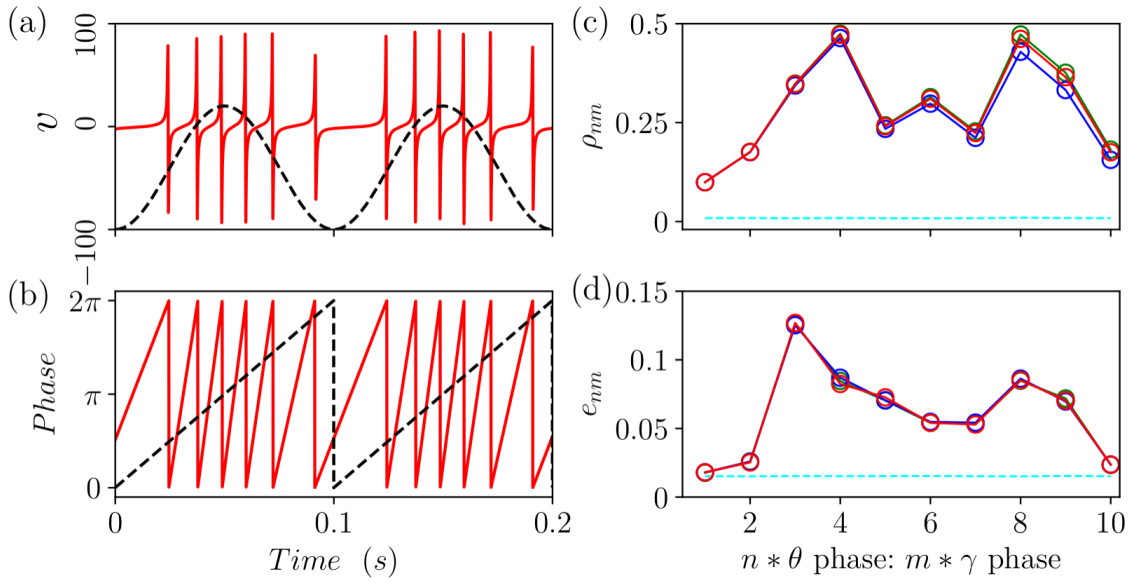

Figure 4.12: **Phase-phase coupling $n : m$ between theta forcing and gamma oscillations** (a-b) Locking of the gamma oscillations to the external theta forcing: (a) average membrane potential v versus time, the black dashed line is the forcing (4.13) in arbitrary units; (b) gamma (red solid) and theta (black dashed) phases for the corresponding time interval. (c) Kuramoto order parameter ρ_{nm} for the phase difference $\Delta_{nm}(t)$ for time windows of duration $T_W = 0.1$ s (green), 0.5 s (red) and 1 s (blue) averaged over $70 < M < 700$ different realizations. (d) Normalized entropy e_{nm} for a time window $T_W = 0.5$ s averaged over $M = 140$ realizations (green), surrogate data are also reported corresponding to random permutation (red) and time shift (blue) of the original data averaged over $M = 100$ independent realizations. The reported data refer to the simulation of the spiking network subject to the external forcing (4.13) with additive noise on the membrane potentials. Parameters are the same as in Fig. (4.11), apart for $I_\theta = 0.3$, $\nu_\theta = 10$ Hz and $A_n = 1.0 \times 10^{-3}$, the histogram of $\Delta_{nm}(t)$ employed for the estimation of e_{nm} have been evaluated over $M = 50$ bins. The results refer only to phases associated to gamma frequencies in the band $30 - 100$ Hz. The error bars in (c) and (d) are of the order of the size of the symbols and the significance levels are reported as dashed cyan lines in (b) $\rho^{(S)} = 0.009$ and (c) $e^{(S)} = 0.016$.

4.6 Conclusions

In this chapter we have shown in terms of an effective mean-field that in a sparse balanced inhibitory network with finite synaptic decay COs can emerge via super or sub-critical Hopf bifurcations from a stable focus. Furthermore, in the network (for sufficiently low structural heterogeneity) the macroscopic focus turns out to be unstable towards microscopic fluctuations in the firing activity leading to the emergence of COs characterized by a frequency corresponding to that of the damped oscillations towards the MF focus. Therefore in proximity of the sub-critical Hopf bifurcations the coexistence of two COs with different origins is observable: slow (fast) gamma oscillations being fluctuation (mean) driven.
From our analysis it emerges that two ingredients are needed to observe coexisting slow and fast gamma COs: the sparseness in the connections and the dynamical balance of the network activity. In particular, the sparseness has a twofold effect at the macroscopic and at the microscopic level. In a mean-field framework the randomness in the in-degree distribution can be reinterpreted as a quenched disorder in the synaptic couplings, which gives rise to the coexistence of stable foci and limit cycles. However, in a fully coupled network with heterogeneous parameters we would not observe strong irregular fluctuations at the level of single neurons, analogous to Poissonian-like firings ususally observed in the cortex [123, 180, 197]. These can emerge only in sparsely connected networks [15, 155]. Moreover, the balance mechanism guarantees that the irregular spiking dynamics will not disappear in the thermodynamic limit [14, 157–159]. These persistent microscopic fluctuations are able to trigger slow gamma COs in the network, which coexist with fast gamma COs corresponding to the limit cycle solutions in the MF. These two ingredients usually characterize real brain networks, where our prediction that slow (fast) gamma oscillations are associated to more (less) irregular neuronal dynamics can be experimentally tested e.g. by measuring the coefficient of variation associated to these two states. Furthermore, previous theoretical analysis of gamma oscillations based on two interacting Wilson-Cowan rate models with different synaptic times revealed only the possible coexistence of two stable limit cycles both corresponding to tonic collective firing (i.e. mean driven COs) [177, 178].
Our model is not meant to explicitly replicate the dynamics of specific brain areas, but rather to illustrate fundamental mechanisms by which slow and fast gamma oscillations may arise and coexist due to local network inhibitory

features. However, several phenomena we reported resemble experimental results obtained for different brain regions *in vitro* as well as *in vivo* and our findings can stimulate new experiments or lead to novel interpretation of the existing data.
Of particular interest is the possibility, analysed in Section (4.5.1), to switch from a gamma rhythm to the other by performing transient stimulations. This mechanism can allow a single inhibitory population to pass from a coding task to another following an external sensory stimulus. Indeed it has been shown that distinct gamma rhythms are involved in different coding processes: namely, fast gamma in new memory encoding, while slow gamma has been hypothized to promote memory retrieval [198].
On one side, pathological synchronization is usually associated to neuronal diseases [58, 153, 199]. On another side, aberrant gamma oscillations have been observed in several cognitive disorders, including Alzheimer's disease, Fragile X syndrome and neocortical epilepsy [196, 198]. Furthermore, deep brain stimulation (DBS) techniques have been developed along the years to treat some of these diseases, e.g. essential tremor and Parkinsons' disease [200–202]. We have presented a simple model exhibiting the coexistence of highly synchronized states and asynchronous or partially synchronized regimes. Therefore, our model can represent a simple benchmark where to test new DBS protocols to obtain eventually less invasive technique to desynchronize pathological states [203–205] or to restore healthy gamma rhythms, as suggested in [198].
Moreover, the richness of the dynamical scenario present in this simple model indicates possible future directions where intrinsic mechanisms present in real neural networks like spike frequency adaptation could permit a dynamical alternation between different states. In this direction, a slow variable like adaptation could drive the system from "healthy" asynchronous or oscillatory dynamics to periods of pathological extremely synchronous regimes, somehow similar to epileptic seizure dynamics [206].
In Section (4.5.2), we have analyzed the emergence of COs in our network in presence of an external theta forcing. This in order to make a closer contact with recent experimental investigations devoted to analyze the emergence of gamma oscillations in several brain areas *in vitro* under sinusoidally modulated theta-frequency optogenetic stimulations [13, 118, 119]. For low forcing amplitudes, our network model displays theta-nested gamma COs at frequencies $\simeq 50$ Hz joined with irregular spiking dynamics. These results are analogous to the ones reported for the CA1 and CA3 areas of the hippocam-

pus in [13,118], moreover theta-nested oscillations with similar features have been reported also for the mEC [119], but for higher gamma frequencies.
Furthermore, for intermediate forcing amplitudes we observe the coexistence of slow and fast gamma oscillations, which lock to different phases of the theta rhythm, analogously to what reported for the rat hippocampus during exploration and REM sleep [104,105]. The theta-phases preferences displayed in our model by the different gamma rhythms are due to the hysteretic nature of the sub-critical Hopf bifurcation crossed during the theta stimulation. Finally, for sufficiently strong forcing, the model is driven in the fast gamma regime.
Our analysis suggests that a single inhibitory population can generate locally different gamma rhythms and lock to one or the other in presence of a theta forcing. In particular, we have shown that fast gamma oscillations are locked to a strong excitatory input, while slow gamma COs emerge when excitation and inhibition balance. These results can be useful in revealing the mechanism behind slow and fast gamma oscillations reported in several brain areas: namely, hippocampus [171], olfactory bulb [207], ventral striatum [208], visual cortical areas [209] and neocortex [170]. Particularly interesting are the clear evidences reported in [170] that different gamma rhythms, phase locked to the hippocampal theta rhythm, can be locally generated in the neocortex. Therefore future studies could focus on this brain region to test for the validity of the mechanisms here reported.
For what concerns the CA1 area of the hippocampus, where most of the experimental studies on theta-gamma oscillations have been performed. Despite the experimental evidences that different gamma oscillations emerging in CA1 area at different theta phases are a reflection of synaptic inputs originating from CA3 area and mEC [104, 172] this does not exclude the possibility that a single CA1 inhibitory population can give rise to different gamma rhythms depending on the network state [171]. This hypothese is supported by experimental evidences showing that a large part of CA1 interneurons *in vivo* can lock to both slow and fast gamma [104, 105, 172] and that *in vitro* gamma rhythms can be locally generated in various regions of the hippocampus due to optogenetic stimulations [13, 118, 119] or pharmalogical manipulation [173–176]. However, much work remains to be done to clarify if local mechanisms can give rise to coexisting gamma rhythms also in the CA1 area.
At variance with previous results for purely inhibitory populations reporting noise sustained COs in the range $100 - 200$ Hz [97] our model displays

slow gamma rhythms characterized by irregular firing of the single neurons. Therefore in our case it is not necessary to add an excitatory population to the inhibitory one to slow down the rhythm and to obtain oscillations in the gamma range as done in [164, 210]. Evidences have been recently reported pointing out that gamma oscillations can emerge locally in the CA1 induced by the application of kainate due to purely inhibitory mechanisms [176]. However, other studies point out that in the same area of the hippocampus excitatory and inhibitory neurons should interact to give rise to oscillations in the gamma range [13,175]. Preliminary results obtained for QIF networks with a sinusoidal theta forcing show that theta-nested gamma oscillations with similar features can emerge for purely inhibitory as well as for mixed excitatory-inhibitory networks [20].

As shown in Section (4.3.2) the same kind of bifurcation diagram can be observed by considering the external excitatory drive as well as the self-disinhibition of the recurrently coupled inhibitory population. This suggests that in our model the same scenarios reported in Section (4.5) for an excitatory theta forcing can be obtained by considering an external inhibitory population which transmits rhythmically its activity to the target population. This somehow mimicks the pacemaker theta activity of a part of the medial septum interneurons on the interneurons of the hippocampus experimentally observed in [211]. This subject will be addressed in future studies due to its relevance in order to clarify the origin of theta-gamma oscillations in the hippocampus, however it goes beyond the scopes of the present analysis.

In this chapter we considered a model including the minimal ingredients necessary to reproduce the phenomenon of coexisting gamma oscillations corresponding to quite simple (namely, periodic) collective regimes. However, the introduction of synaptic delay in the model can lead to more complex coexisting states, like quasi-periodic and even chaotic solutions, as recently shown for fully coupled networks in [181, 212]. The inclusion of delay in our model can enrich the dynamical scenario maybe allowing to mimic further aspects of the complex patterns of activity observed in the brain, like e.g. sharp-wave ripples observed in the hippocampus and which are fundamental for memory consolidation [213]. Due to the large variety of interneurons present in the brain and in particular in the hippocampus [214] a further step in rendering our model more realistic would consist in considering multiple inhibitory populations characterized by different neuronal parameters. By manipulating the influence of a population on the others it would be interesting to investigate the possible mechanisms to switch COs from one

gamma rhythm to another, following the richness of the bifurcation scenarios presented in Figs. (4.2) and (4.3).
The generality of the phenomena here reported is addressed in Appendix C and D. In particular in Appendix C we show that the mechanisms leading to the coexistence scenario of fast and slow gamma oscillations are not peculiar of Lorentzian in-degree distributions (that we employed to allow a comparison of the network simulations with the MF results), but that they are observable also in the more studied Erdös-Renyi sparse networks. Appendix D is devoted to the analysis of a suitable normal form, which reproduces the dynamics of the MF in proximity of the sub-critical Hopf bifurcation. In particular, the noisy dynamics of the normal form reveals coexisting oscillations of different frequencies. More specifically the addition of noise leads from damped oscillations towards the stable focus to sustained oscillations characterized by the same frequency. This latter result links our findings to the more general context of noise-induce oscillations for non-excitable systems examined in various fields of research: namely, single cell oscillations [215], epidemics [216], predator-prey interactions [217] and laser dynamics [218]. At variance with all previous studies we have analyzed noise-induced oscillations coexisting and interacting with oscillations emerging from the Hopf bifurcation. Furthermore, the mechanism leading to the irregular fluctuations in our case is quite peculiar. Single cells oscillations are believed to be driven by molecular noise, induced by the small number of molecules present in each cell, and therefore disappearing in the thermodynamic limit [219]. Recently, another possible mechanism leading to fluctuation amplification in a feed-forward chain has been suggested as a pacemaking mechanism for biological systems, in this context the amplitude of the oscillations grows with the system size [220]. Instead in our case, the dynamical balance provides intrinsic noise and oscillations of constant amplitude, essentially independent from the number of synaptic inputs (in-degree) and from the number of neurons in the network.

Author Contributions:
Hongjie Bi, Marco Segneri and Matteo di Volo performed the simulations and data analysis. Matteo di Volo and Alessandro Torcini were responsible for the state-of-the-art review and the paper write-up. All the authors conceived and planned the research.

Chapter 5

Emergence of collective oscillations in balanced neural networks due to intrinsic fluctuations

Abstract:

Collective oscillations have been observed in sparse balanced inhibitory networks of QIF neurons with instantaneous synapses for sufficiently connected network. Their origin is due to the microscopic irregular firings that is able, in the balanced state, to sustain collective oscillations. Effective mean field models have been proposed in order to capture the transition from asynchronous to oscillatory behavior. However they failed to include noise fluctuations that are present at the network level. These fluctuations can be considered by developing a Fokker-Planck formulation for the distribution of the membrane potentials of the QIF neurons. Here we analytically solve the Fokker-Planck equation associated to a sparse network and we prove the transition from asynchronous state to collective oscillations. However, since this approach is infinite dimensional, we also employ the Circular Cumulant Approximation in order to derive a mean field model that takes into account noise fluctuation.

5.1 Introduction

Oscillations are a hallmark of neural population activity in various brain regions with a spectrum covering a wide range of frequencies. In particular, gamma oscillations (30-100 Hz) have been suggested to underlie various cognitive and motor functions, as already pointed out in Chapter 3 and 4.
Due their relevance, many mechanisms have been proposed in order to achieve such dynamical regime. For example, in [123] it has been shown that a single fully-coupled inhibitory population with finite synaptic decay is able to generate self-sustained oscillations in the gamma-band. In Chapter 3 we have shown that gamma oscillations can emerge in a fully-coupled inhibitory population coupled with an excitatory population (PING set-up) without any synaptic decay. In Chapter 4 we have shown that a sparse balanced inhibitory population with finite synaptic decay can give rise to the coexisting slow and fast gamma rhythms.
In particularly in Chapter 4 we discussed that the presence of sparseness in a balance network can give rise to collective oscillations (COs) but the corresponding effective mean-field model does not capture the emergence of such COs. This peculiar aspect had been already noticed in [14], where the authors showed that a single sparse balanced inhibitory network of QIF neurons with instantaneous synapses gives rise to COs by increasing the network connectivity (in-degree). They showed that the COs can survive only in the presence of irregular spiking dynamics due to the dynamical balance, suggesting that the presence of sparseness in the connections is a key ingredient for the transition from the asynchronous state to COs. Actually, the presence of the sparseness in the network can be reinterpreted as an intrinsic noise term describing the irregular microscopic fluctuations of the input current on the single neuron and these fluctuations trigger COs from the asynchronous state.
In [14] an effective mean-field model is also employed for sparse balanced networks whose analytic stability analysis reveals that the asymptotic solution is a stable focus. This means that such mean-field model is not able to reproduce the transition to COs observed in the corresponding network since it takes into account the sparseness as a noise quenched term, but it neglects the dynamic current fluctuations.
In this chapter we want to develop a mean-field model of a sparse balanced inhibitory network of QIF neurons with instantaneous sinapses, the same network set-up analyzed in [14], able to reproduce the transition between the

asynchronous and the oscillatory states. For this aim, we solve the corresponding Fokker-Planck equation (FPE). In this way the sparseness of the network is taken into account by considering an irregular fluctuating input current in the microscopic dynamic of the single neuron. Since the FPE formulation is still high-dimensional, we also try to extend the OA reduction by considering the Circular Cumulant approximation (CCs) that represents a recently developed approach [16] useful to study the impact of weak intrinsic noise on the network dynamics. In [16], the authors show that, in presence of noise, the OA equations 1.39 can be generalized to a system of infinite equations written in terms of circular cumulants. For non-vanishing noise, generally all the infinite cumulants are non-zero. However, for weak noise, one can expect the cumulants with orders larger than one to be small and neglect them, providing a closed low-dimensional system of equations for the leading cumulants.

5.2 Methods

5.2.1 The network model

We consider N inhibitory pulse-coupled QIF neurons [89] arranged in a random sparse balanced network. The membrane potential of each neuron evolves according to the following equations:

$$\tau_m \dot{V}_i(t) = I + V_i^2(t) - \tau_m J \sum_j \epsilon_{ji} \delta(t - t_j(m)) \tag{5.1}$$

where $\tau_m = 15$ ms represents the membrane time constant, I an external DC current, encompassing the effect of distal excitatory inputs and of the internal neural excitability. The last term in (5.1) is the inhibitory synaptic current, with J being the synaptic coupling. The synaptic current is the linear super-position of all the instantaneous IPSPs $S(t) = \delta(t)$ received by the neuron i from its pre-synaptic neurons in the past, $t_j(m)$ is the spike time of the m-th spike delivered by the j-th neuron, and ϵ_{ji} is the adjacency matrix of the network. In particular, $\epsilon_{ji} = 1$ (0) if a connection from node j to i exists (or not) and $k_i = \sum_j \epsilon_{ji}$ is the number of pre-synaptic neurons connected to neuron i, or in other terms its in-degree.
Whenever the membrane potential V_i reaches infinity a spike is emitted and V_i resetted to $-\infty$. In absence of the synaptic coupling the QIF model displays

excitable dynamics for $I < 0$, while for positive DC currents it behaves as an oscillator with period $T_0 = \pi/\sqrt{I}$, as shown in Chapter 2.
In order to compare the simulation results with an exact MF recently derived [10,14,123], we consider sparse networks where the in-degrees k_i are extracted from a Lorentzian distribution

$$L(k) = \frac{\Delta_k}{(k-K)^2 + \Delta_k^2} \tag{5.2}$$

peaked at K and with a half-width half-maximum (HWHM) Δ_k, the parameter Δ_k measures the level of structural heterogeneity in the network, and analogously to Erdös-Renyi networks we assumed the following scaling for the HWHM $\Delta_k = \Delta_0\sqrt{K}$. The DC current and the synaptic coupling are rescaled with the median in-degree K as $I = i_0\sqrt{K}$ and $J = g_0/\sqrt{K}$, as usually done to achieve a self-sustained balanced state for sufficiently large in-degrees [157–159, 161, 165].

5.2.2 Simulation Protocols

The network dynamics is integrated by employing a standard Euler scheme with an integration time step $\Delta t = \tau_m/10000$.

5.2.3 Indicators

To characterize the collective dynamics in the network we measure the mean membrane potential $v(t) = \sum_{i=1}^{N} V_i(t)/N$ and the instantaneous firing rate $r(t)$, corresponding to the number of spikes emitted per unit of time and per neuron.
In order to measure the level of coherence in the network dynamics, a commonly used order parameter is [221]

$$\rho^2 \equiv \frac{\overline{\langle v\rangle^2} - \overline{\langle v\rangle}^2}{\langle \overline{v^2} - \overline{v}^2\rangle} \; ; \tag{5.3}$$

where the overbar denotes a time average. In practice, ρ is the rescaled amplitude of the standard deviation of the average $\langle v\rangle$. When all neurons behave in exactly the same way (perfect synchronization), the numerator and the denominator are equal to one another and $\rho = 1$. If instead, they are

independent as in an asynchronous regime, $\rho \approx 1/\sqrt{N}$ due to the central limit theorem.
The degree of synchronization among the phases can be also measured by the Kuramoto order parameter, namely [64]

$$z_1 = \left| \frac{1}{N} \sum_{k=1}^{N} \mathrm{e}^{i\theta_k} \right| \quad ; \tag{5.4}$$

where $|\cdot|$ represents the modulus. For completely desynchronized phases $|z_1| \propto 1/\sqrt{N}$, while partial (full) synchronization will be observable whenever $|z_1|$ is finite (one).
The microscopic activity can be analyzed by considering the inter-spike interval (ISI) distribution as characterized by the coefficient of variation cv_i for each neuron i, which is the ratio between the standard deviation and the mean of the ISIs associated to the train of spikes emitted by the considered neuron. In particular, we will characterize each network in terms of the average coefficient of variation defined as $CV = \sum_i cv_i/N$. Time averages and fluctuations are usually estimated on time intervals $T_s \simeq 90$ s, after discarding transients $T_t \simeq 15$ s.

5.3 Mean-Field Approaches

At a mean-field level the evolution equation (5.1) can be rewritten for the subpopulation of neurons with in-degree k_j as the following Langevin equation

$$\dot{V}_j = V_j^2 + A_{g_j}(t) + \sigma_{g_j}(t)\xi_j(t) \tag{5.5}$$

where ξ_j is a δ-correlated Gaussian noise with unitary variance (i.e. $\langle \xi_j(t)\xi_m(t) \rangle = \delta_{jm}\delta(t)$) and

$$A_{g_j}(t) = \sqrt{K}\,[i_0 - g_j r(t)] \tag{5.6}$$

$$\sigma_{g_j}(t) = \sqrt{g_0 g_j r(t)} \tag{5.7}$$

where $r(t)$ is the instantaneous firing rate and A_{g_j} is the total input current. The amplitude of the synaptic current fluctuations σ_{g_j} is estimated for a sufficiently sparse network within the Poissonian approximation [155] and we have defined an effective synaptic coupling $g_j = g_0 k_j/K$, which is obviously

distributed as a Lorentzian $L(g)$ peaked at g_0 with HWHM $\Delta_g = \Gamma/\sqrt{K}$ with $\Gamma = \Delta_0 g_0$.
In a more general framework the variance of the current fluctuations is given by $\sigma^2_{g_j}(t) = \mathcal{FF} g_0 g_j r(t)$, where $\mathcal{FF}$ is the Fano factor measuring the ratio between the variance of the spike count and its average [222, 223]. For a stationary renewal process $\mathcal{FF} = (CV)^2$, where CV is the coefficient of variation of the spike train [222]. Therefore at a first level of approximation the effect of non Possonian distributions can be taken into account by rewriting the amplitude of the current fluctuations as

$$\sigma^{(R)}_{g_j}(t) = CV\sqrt{g_0 g_j r(t)} \quad . \tag{5.8}$$

5.3.1 Fokker-Planck Approach

The Langevin equation (5.5) for the dynamics of the membrane potential of neurons of the sub-population with effective coupling g can be transformed into a Fokker-Planck equation describing the evolution of the probability distribution $P_g(V,t)$, namely:

$$\partial_t P_g(V,t) = -\partial_V[(V^2 + A_g(t))P_g(V,t)] + D_g(t)\partial^2_{V^2} P_g(V,t) \tag{5.9}$$

where $D_g = \sigma^2_g/2$. This can be rewritten as a continuity equation as follows:

$$\frac{\partial P_g(V,t)}{\partial t} = -\frac{\partial}{\partial v} F_g(V,t) \tag{5.10}$$

where $F_g(V,t)$ represents the flux

$$F_g(V,t) = (V^2 + A_g)P_g(V,t) - D_g\frac{\partial P_g}{\partial V} \tag{5.11}$$

with the boundary condition $\int dg F_g(V = +\infty, t)L(g) = r(t)$.
In order to solve the FP, we will transform the membrane potential in a phase variable by performing the transformation from QIF to θ-neuron model [89], namely:

$$V = tg(\theta/2) \quad \text{with} \quad \theta \in [-\pi : \pi] \tag{5.12}$$

The new variable θ is associated to the following PDF :

$$R_g(\theta) = P_g(V)\frac{dV}{d\theta} \qquad \text{where} \quad \frac{dV}{d\theta} = \frac{1}{2\cos^2(\theta/2)} \tag{5.13}$$

and the Fokker-Planck equation (5.9) can be rewritten as:

$$\partial_t R_g(\theta,t) = -\partial_\theta\left[\psi_0(\theta)R_g(\theta,t)\right] + \partial_\theta\left[Z_0(\theta)\partial_\theta R_g(\theta,t)\right] \tag{5.14}$$

with

$$\begin{aligned} \psi_0(\theta) &= (1-\cos(\theta)) + (A_g + D_g\sin(\theta))(1+\cos(\theta)) & (5.15)\\ Z_0(\theta) &= D_g(1+\cos(\theta))^2. & (5.16) \end{aligned}$$

Finally,

$$Q_g(\theta,t) = \psi_0(\theta)R_g(\theta,t) - Z_0(\theta)\partial_\theta R_g(\theta,t) \tag{5.17}$$

represents the flux in the new coordinates. The flux at the threshold $\theta = \pi$ is linked to the firing rate by the following condition of self-consistency:

$$\int dg Q_g(\pi,t)L(g) = 2\int dg R_g(\pi,t)L(g) = r(t) \tag{5.18}$$

Since we are now dealing with a phase variable it is natural to rewrite Eq. (5.14) in the Fourier space, the PDF reads as

$$R_g(\theta,t) = \frac{1}{2\pi}\left[1 + \sum_{m=1}^{\infty} a_m(t)\mathrm{e}^{-im\theta} + c.c.\right] \tag{5.19}$$

and the associated Kuramoto-Daido order parameters for the population synchronization are given by

$$z_m = \int dg \;\; a_m \;\; L(g) \tag{5.20}$$

the FPE in the Fourier space for the mode a_m reads as

$$\begin{aligned} \dot{a}_m &= m\left[i(A_g+1)a_m + \frac{i}{2}(A_g-1)(a_{m-1}+a_{m+1})\right] \\ &- D_g \left[\frac{3m^2}{2}a_m + (m^2 - \frac{m}{2})a_{m-1} + (m^2+\frac{m}{2})a_{m+1}\right. \\ &+ \left.\frac{m(m-1)}{4}a_{m-2} + \frac{m(m+1)}{4}a_{m+2}\right] \end{aligned} \tag{5.21}$$

and here, by definition, $a_0 = 1$, $a_{-m} = a_m^*$.
Thanks to the fact that we are considering a Lorentzian distribution for g the effect of this heterogeneity can be taken into account in an analytic manner by averaging over the parameter g. In particular by rewriting the distribution as

$$L(g) = \frac{1}{2i}\left[\frac{1}{(g-g_0)-i\Delta_g} - \frac{1}{(g-g_0)+i\Delta_g}\right]$$

we observe that it has two complex poles at $g = g_0 \pm i\Delta_g$. Therefore by employing the residues theorem one can estimate explicitly the Kuramoto-Daido order parameters as

$$z_m = \int dg \;\; a_m(g) \;\; L(g) = a_m(g_0 - i\Delta_g) \tag{5.22}$$

and by averaging Eq. (5.21) over the distribution of the parameters g one can find also the dynamical evolution of these quantities, namely

$$\begin{aligned}
\dot{z}_m &= m\left[(iA_{g_0} + i - r\Gamma)z_m + \frac{1}{2}(iA_{g_0} - i - r\Gamma)(z_{m-1} + z_{m+1})\right] \\
&- D_{g_0}(1 - \frac{i\Delta_g}{g_0})\left[\frac{3m^2}{2}z_m + (m^2 - \frac{m}{2})z_{m-1} + (m^2 + \frac{m}{2})z_{m+1}\right] \\
&- D_{g_0}(1 - \frac{i\Delta_g}{g_0})\left[\frac{m(m-1)}{4}z_{m-2} + \frac{m(m+1)}{4}z_{m+2}\right]
\end{aligned} \tag{5.23}$$

As shown in [10] the population firing rate r and the mean average membrane potential v can be obtained from the Kuramoto-Daido order parameters from the following series:

$$W \equiv \pi r + iv = 1 - 2\sum_{k=1}^{\infty}(-1)^{k+1} z_k^* \tag{5.24}$$

5.3.2 Ott-Antonsen Ansatz

If one neglects the fluctuations (i.e. $D_{g_0} = 0$) Eq. (5.23) reduces to the usual form where the Ott-Antonsen manifold $z_m = (z_1)^m$ is attracting [11, 82]. In this case one finds

$$2\dot{z}_1 = (iA_{g_0} - r\Gamma)[1 + z_1]^2 - i[1 - z_1]^2 \quad . \tag{5.25}$$

By applying the OA Anstanz to Eq. (5.24) one obtains the following conformal mapping transformation [10]:

$$z_1 = \frac{1 - W^*}{1 + W^*} \quad ; \tag{5.26}$$

which put in direct relationship the Kuramoto order parameter with the characteristic macroscopic functions describing the neural network dynamics, namely $v(t)$ and $r(t)$.
By applying this transformation to (5.25) one obtains the following ODEs for the dynamical evolution of $v(t)$ and $r(t)$

$$\begin{aligned} \dot{r} &= r(2v + \Gamma/\pi) \\ \dot{v} &= v^2 + \sqrt{K}(i_0 - g_0 r) - (\pi r)^2 \end{aligned} \tag{5.27}$$

These mean-field set of equations has been analyzed in [14], where it has been shown that it exhibits a stable focus solution for any parameter choice. However, the network dynamics reveal clear COs for sufficiently large in-degrees K. Therefore the neglected fluctuations are fundamental in order to capture the network dynamics at a macroscopic level.
Despite its inability to capture the emergence of COs the model (5.27) was able to give several correct previsions not only about the asynchronous state, but also for what concerns oscillatory dynamics. In particular, in [14] the authors have shown that the frequency of the damped oscillations towards the stable focus provide an accurate estimation of ν_{CO} over a wide range of parameters. Moreover, they have been able to provide, for sufficiently large in-degree K and I_0, the following asymptotic scaling law

$$\nu_{CO} \simeq I^{1/2} = I_0^{1/2} K^{1/4} \quad . \tag{5.28}$$

5.3.3 Circular Cumulants' Approximation

We can go beyond the OA Ansazt in presence of *weak* noise by considering the so called circular cumulant approximation as suggested in [16]. The authors of this paper noticed that the Kuramoto-Daido order parameters

$$z_m = \int dg \int d\theta R_g(\theta, t) L(g) \mathrm{e}^{im\theta} = \langle \mathrm{e}^{im\theta} \rangle \tag{5.29}$$

are the moments of the observable $\mathrm{e}^{i\theta}$. These moments can be determined via the moment-generating function

$$F(k) = \langle \exp\left(k\mathrm{e}^{i\theta}\right)\rangle \equiv \sum_{m=0}^{\infty} z_m \frac{k^m}{m!} \tag{5.30}$$

The circular cumulants κ_m can be obtained from the cumulant-generating function [16]

$$\Psi(k) = k\partial_k \ln F(k) \equiv \sum_{m=0}^{\infty} \kappa_m k^m \tag{5.31}$$

From (5.30) and (5.31) one can find the relationships among z_m and κ_m, namely

$$\kappa_N = z_N - \sum_{m=1}^{N-1} \binom{N-1}{m-1} \kappa_m z_{N-m} \tag{5.32}$$

from this the first two circular cumulants are simply given by

$$\kappa_1 = z_1 \qquad \kappa_2 = z_2 - z_1^2 \tag{5.33}$$

Whenever the OA Ansatz holds, i.e. the manifold $z_m = z_1^m$ is attracting, one simply obtains $F(k) = \mathrm{e}^{kz_1}$ and $\Psi(k) = kz_1$ and the only non zero circular cumulant is $\kappa_1 = z_1$. In general when the OA manifold is not attracting, as in presence of fluctuations, all the circular cumulants are non zero. Indeed in presence of a noise term of variance D_{g_0} in [16] it was shown that $\kappa_m \simeq D_{g_0}^{(m-1)}$, whenever $\kappa_1 \simeq \mathcal{O}(1)$ as in our case.
Therefore it makes sense to consider a simple approximation that takes into account only the first two cumulants κ_1 and κ_2, and in this case the Kuramoto-Daido order parameters are simply given by

$$z_m = z_1^m + \kappa_2 z_1^{m-2} \frac{m(m-1)}{2} \tag{5.34}$$

and this can be interpreted as a correction to the OA manifold in presence of noise.
The two circular cumulants' approximation for the FPE (5.23) correct to the order $o(D_{g_0})$ reads as

$$
\begin{aligned}
\dot{z}_1 &= z_1(iA_{g_0} + i - \Gamma r) + H(1 + \kappa_2 + z_1^2) + \\
&- \frac{D_{g_0}}{2}(1 - i\frac{\Delta_g}{g_0})(1 + z_1)^3 \\
\dot{\kappa}_2 &= 2(iA_{g_0} + i - \Gamma r)\kappa_2 + 4Hz_1\kappa_2 + \\
&- D_{g_0}(1 - i\frac{\Delta_g}{g_0})\left(\frac{1}{2}(1 + z_1)^4 + 6(1 + z_1)^2\kappa_2\right)
\end{aligned}
\tag{5.35}
$$

with:

$$
H = \frac{1}{2}\left[i(A_{g_0} - 1) - \Gamma r\right] \quad .
$$

In this approximation the firing rate r and the average membrane potential v can be obtained from Eq. (5.24) by limiting to the first two circular cumulants, namely:

$$
W^* = \pi r - iv = \frac{1 - z_1}{1 + z_1} + \frac{2\kappa_2}{(1 + z_1)^3} \tag{5.36}
$$

this is a generalization of the conformal transformations (5.26) to situation where the OA Ansatz is no more valid.

5.4 Homogeneous Case

Let us now limit our analysis to the homogeneous case where the in-degree has a constant value K for all the neurons, i.e. $\Delta_g = \Delta_0 = 0$. The fact that K is constant does not imply that there are no fluctuations in the system, indeed D_{g_0} is not zero, and this is due to the random distribution of the links: each neuron receives inputs from a different random ensemble of K pre-synaptic neurons [155]. In this case the Kuramoto-Daido order parameters will coincide with the coefficient of the Fourier expansion of the PDF $R_{g_0}(\theta, t)$, namely $z_m \equiv a_m(g_0)$.

5.4.1 Asynchronous State

In this sub-section we would like to characterize the asynchronous solution that one observes in the studied system for sufficiently small in-degrees

$K < K_c$, where $K_c \simeq 120$ for the parameter values considered in [14]. The asynchronous state corresponds to a stationary PDF $R^{(0)}(\theta)$ and it can be obtained by solving the stationary FPE in the Fourier space (5.21) truncated to some order M. In particular, we have solved iteratively the stationary FPE (5.21), which is simply a linear system in the coefficients a_m and a_m^*, with the following nonlinear consistency condition to be satisfied

$$r^{(0)} = 2R^{(0)}(\pi) = \frac{1}{\pi}\left[1 + \sum_{m=1}^{\infty}(-1)^{m+1}(a_m^{(0)} + a_m^{(0)^*})\right] \tag{5.37}$$

where the firing rate $r^{(0)}$ and the coefficients $\{a_m^{(0)}\}$ correspond to the stationary solution. The modulus of the obtained coefficients is shown in Fig. 5.1 for a certain choice of the parameters, we observe that the amplitude $|a_m|$ decays exponentially with m with an exponent that approaches $\simeq -0.564$ for sufficiently large m. Therefore, the truncation to $M = 64$ Fourier modes is already quite accurate, since it amounts to neglect terms $\mathcal{O}(10^{-12})$, and indeed we do not observe substantial differences by considering $M = 128$ or even $M = 256$.

In Fig. 5.2 we display for various in-degrees the results of the stationary solution of the FPE (5.21) obtained for $M = 64$ by considering for the synaptic current fluctuations σ_g either the Poisson approximation (Eq. (5.7)) or the renewal one (Eq. 5.8). In the same figure are reported the numerical estimations of $R^{(0)}(\theta)$ for $K = 20$, 40 and 80 with $N = 16000$. We have verified that $R^{(0)}(\theta)$ converges to an asymptotic profile by increasing N from 4000 to 16000, furthermore averaging the PDF over 20 different neurons was sufficient to reproduce the average PDF with negligible differences with respect to average over the whole ensemble of neurons.

The agreement between the numerical findings and the mean-field estimations is reasonably good. The main differences are present around the peak position of $R^{(0)}(\theta)$, the MF distributions are peaked at more negative θ-values with respect to the ones obtained by the direct simulation. For increasing K the positions of the peaks approach, as expected for MF results. However, the estimations, reported in Fig. 5.2, capture reasonably well the tail of the distributions $R^{(0)}(\theta)$, therefore also the average firing rate since $r^{(0)} = 2R^{(0)}(\pi)$ as reported in Table 5.1. In particular, the agreement improves noticeably by passing from the Poissonian to the renewal approximation with a value $CV = 0.8$, corresponding to the one measured in the network simulations for these parameter values.

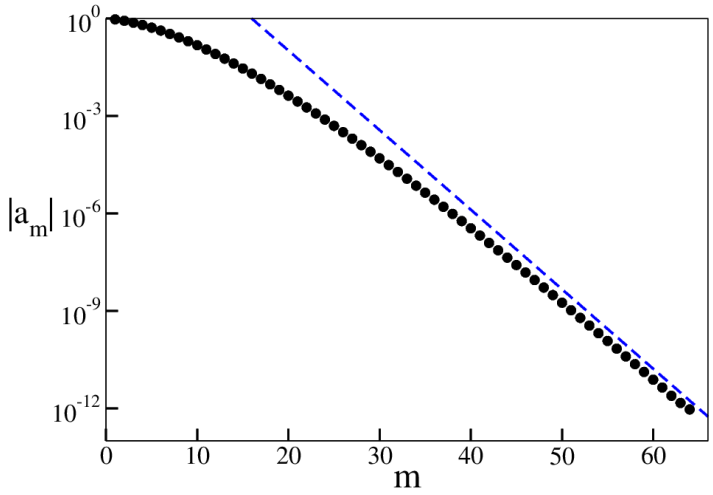

Figure 5.1: Modulus of the Fourier coefficients a_m. The blue dashed curve corresponds to an exponential decay law with exponent -0.564. Parameters $I_0 = 0.006$, $g_0 = 1$, $\Delta_g =$ and $K = 40$.

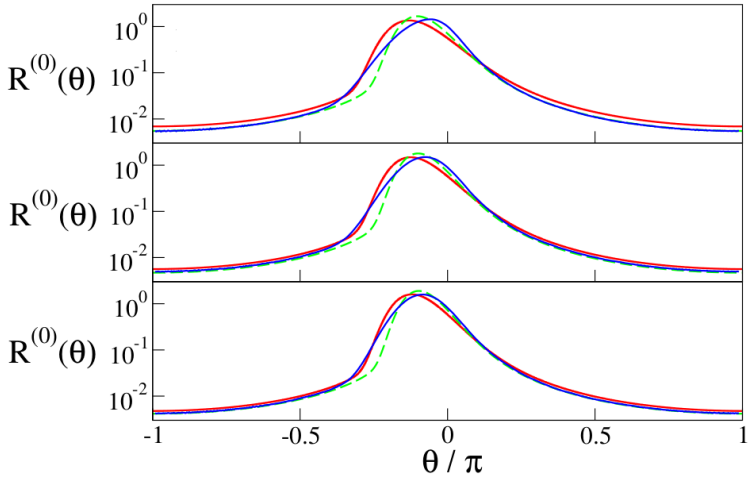

Figure 5.2: Stationary PDFs $R^{(0)}$ versus the angle θ estimated numerically from the network simulations (blue solid line) and theoretically from the FPE truncated at $M = 64$ by estimating the current fluctuations within the Poisson approximation Eq. (5.7) (red solid line) and within the renewal approximation Eq. (5.8) with $CV = 0.8$ (green dashed line). From top to bottom $K = 20$, 40 and 80. The numerical data are obtained for a network of size $N = 16000$ and by averaging over 20 different neurons. Parameters $I_0 = 0.006$, $g_0 = 1$ and $\Delta_g = 0$.

K	$\langle r \rangle$	$r^{(0)}$		r
	Network	FPE(P)	FPE(R)	2CCs
20	0.0114	0.0138	0.0110	0.0129
40	0.0100	0.0112	0.0094	0.0105
80	0.0089	0.0096	0.0084	0.0089

Table 5.1: Average firing rate versus the in-degree K for asynchronous dynamics. The second columns report $\langle r \rangle$ as estimated by averaging the activity of a network of $N = 16000$ neurons. The third and fourth columns report the estimation of the firing rate obtained by the stationary PDF, namely $r^{(0)} = 2R^{(0)}(\pi)$. In particular, the third (fourth) column displays the MF results obtained by the self-consistent solution of the stationary Eq. (5.21) for $M = 64$ with current fluctuations estimated within the Poisson approximation Eq. (5.7) (FPE(P)) (within the renewal approximation Eq.(5.8) with $CV = 0.8$ (FPE(R))). The fifth column refers to the two circular cumulants (2CCs) approximation where the expression (5.36) has been employed to estimate the population firing rate r. Parameters $I_0 = 0.006$, $g_0 = 1$ and $\Delta_g = 0$.

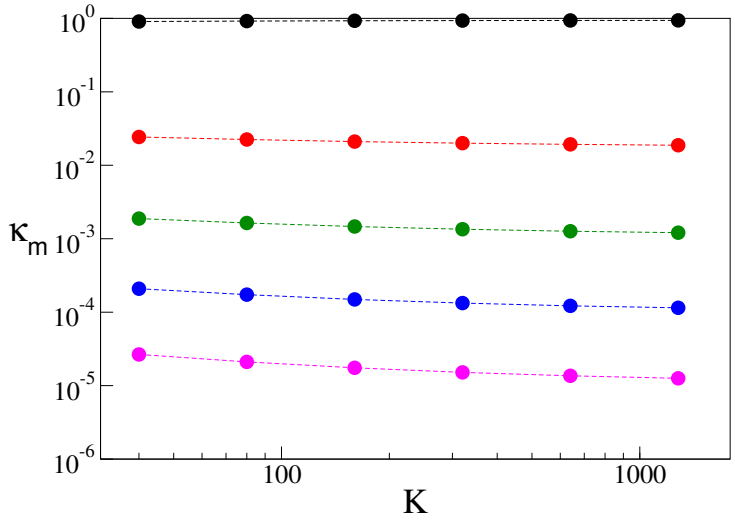

Figure 5.3: Circular cumulants κ_m as a function of the in-degree. From top to bottom κ_1, κ_2, κ_3, κ_4 and κ_5. The cumulants are estimated from the stationary solution $a_m^{(0)}$ of the FPE Eq. (5.21) wth $M = 64$. Parameters $I_0 = 0.006$, $g_0 = 1$ and $\Delta_g = 0$.

Let us now consider the two circular cumulants (2CCs) approximation for the homogeneous case. To verify that the approximation is indeed justified, we report in Fig. 5.3 the first five cumulants for different in-degree values. As expected $\kappa_1 \simeq \mathcal{O}(1)$, while for the other terms $\kappa_m \simeq \mathcal{O}(D_{g_0}^{m/2})$, therefore we can safely affirm that to neglect the cumulants beyond the second one is indeed justified. Furthermore, we observe that the circular cumulants scale as $\kappa_m \simeq K^{-\varepsilon(m)}$ with the mean in-degree with $\varepsilon(m) \simeq 0.030 + 0.046(m-1)$ for $m \geq 2$.
The two circular cumulants approximation can be used in the present context to estimate the average population firing rate r from Eq. (5.36). As shown in Table 5.1 the obtained values are in good agreement with the average firing rate measured form the network simulations.

5.4.2 Linear Stability of the Asynchronous State

In order to study the linear stability of the asynchronous state we consider the linearization of Eq. (5.21) around the stationary solution $\{a_m^{(0)}\}$, namely this corresponds to

$$\begin{aligned}
\delta\dot{a}_m &= m\left[(iA_{g_0}^{(0)}+i)\delta a_m + \frac{1}{2}(iA_{g_0}^{(0)}-i)(\delta a_{m-1}+\delta a_{m+1})\right] \\
&+ im\delta A_{g_0}\left[a_m^{(0)} + \frac{a_{m-1}^{(0)}+a_{m+1}^{(0)})}{2}\right] \\
&- D_{g_0}^{(0)}\left[\frac{3m^2}{2}\delta a_m + (m^2-\frac{m}{2})\delta a_{m-1} + (m^2+\frac{m}{2})\delta a_{m+1}\right] \\
&- D_{g_0}^{(0)}\left[\frac{m(m-1)}{4}\delta a_{m-2} + \frac{m(m+1)}{4}\delta a_{m+2}\right] \\
&- \delta D_{g_0}\left[\frac{3m^2}{2}a_m^{(0)} + (m^2-\frac{m}{2})a_{m-1}^{(0)} + (m^2+\frac{m}{2})a_{m+1}^{(0)}\right] \\
&- \delta D_{g_0}\left[\frac{m(m-1)}{4}a_{m-2}^{(0)} + \frac{m(m+1)}{4}a_{m+2}^{(0)}\right] \quad ; \qquad (5.38)
\end{aligned}$$

where $A_{g_0}^{(0)}$ and $D_{g_0}^{(0)}$ are estimated with the firing rate of the stationary solution $r^{(0)}$(5.37) and

$$\delta A_{g_0} = -\sqrt{K} g_0 \delta r \quad , \quad \delta D_{g_0} = \frac{g_0^2}{2} \delta r \tag{5.39}$$

$$\delta r = \frac{1}{\pi} \sum_{m=1}^{\infty} (-1)^{m+1} (\delta a_m + \delta a_m^*) \quad . \tag{5.40}$$

We have considered the system Eq. (5.38) truncated to order M and estimated the corresponding spectrum by solving the system for solutions like $\delta\mathbf{a}(t) = \mathrm{e}^{i\lambda_k t}\delta\mathbf{a}(0)$, where $\delta\mathbf{a} = (\delta a_1, \delta a_2, \ldots, \delta a_M)$ is the infinitesimal perturbation vector, with complex eigenvalues $\{\lambda_k\}$ $k = 1, \ldots M$. The asynchronous solution is stable (unstable) whenever $Re\{\lambda_k\} < 0$ $\forall k$ (at least one eigenvalue has $Re\{\lambda_k\} > 0$).
The estimated spectra for Poissonian noise are displayed in Fig. 5.4 (a) for different truncations of the Fourier expansion and for $K = 40$, instead in Fig. 5.4 (b) is reported the dependence of the spectra on the in-degrees K for $M = 64$. From the figures it is evident that each spectrum is symmetric with respect to the axis $Im\{\lambda\} = 0$ and therefore composed of couples of complex conjugate eigenvalues. Each part of the symmetric spectrum is then composed of two branches: a central one that approaches almost linearly the axis $Re\{\lambda\} = 0$ with $Im\{\lambda\} < 10$ and another branch at larger values of $Im\{\lambda\}$ that approaches tangentially the axis $Re\{\lambda\} = 0$ at very large values of $Im\{\lambda\}$. Furthermore, the spectrum displays two isolated couples of eigenvalues with $Re\{\lambda\} > -1$, it is the couple with the largest real part that crosses the axis $Re\{\lambda\} = 0$ for $K > K_c \simeq 330$ identifying the bifurcation to COs as a supercritical Hopf (see the inset of Fig. 5.4 (b)). The spectrum is composed also of several isolated couples of eigenvalues with very negative real parts, but these couples are irrelevant for the stability of the asynchronous state.

Furthermore, we noticed that by rescaling the real and imaginary part of the spectra for fixed K as a function of number of modes (namely, as $Re(\lambda) \to Re(\lambda)/M$ and $Im(\lambda) \to Im(\lambda)/M^{3/2}$) we obtain that the two main branches almost overlap. This indicates that this part of the spectrum can be considered as reliable and not affected by truncation errors.
From this analysis we have obtained also the two eigenvectors in Fourier space associated to the two dimensional unstable manifold: $\mathbf{e}_1$ and $\mathbf{e}_2$.
From the anti-Fourier transform of the linear combinations of these two eigenvectors $\mathbf{v} = a_1\mathbf{e}_1 + a_2\mathbf{e}_2$ we have reconstructed the shape of the perturbations

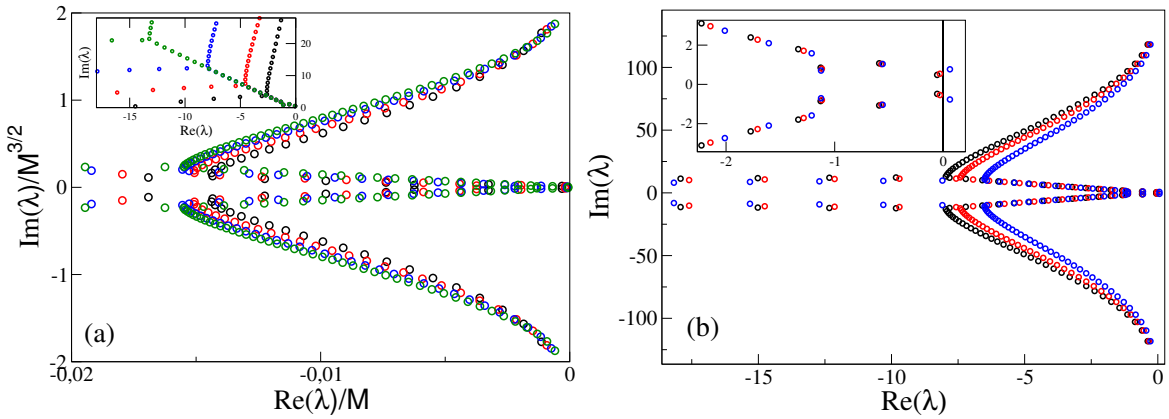

Figure 5.4: Real and imaginary part of the eigenvalues $\{\lambda_k\}$ of the asynchronous state. (a) In the main panel the axis are rescaled with the number of modes as $Re(\lambda)/M$ and $Im(\lambda)/M^{3/2}$, while these are not rescaled in the enlargement in the inset. The data refer to $K = 40$ for different truncation of the Fokker-Planck equation in Fourier space: namely, $M = 32$ (black circles), $M = 45$ (red circles), $M = 64$ (green circles) and $M = 90$ (blue circles). (b) The reported data refer to $K = 80$ (black circles), $K = 160$ (red circles) and $K = 1280$ (blue circles) for a truncation to $M = 64$ Fourier modes. The inset displays an enlargement of the central branch of the spectrum in proximity of the axis $Re\ \lambda = 0$. Here we considered the Poissonian approximation for the current fluctuations reported in Eq. (5.7). Parameters $I_0 = 0.006$, $g_0 = 1$ and $\Delta_g = 0$.

in the θ-space $p(\theta)$ leading to a destabilization of the asynchronous state. These functions $p(\theta)$ are perturbations to the stationary PDF $R^{(0)}(\theta)$ and therefore they should be at area zero, two examples are reported in Fig. 5.5 for $(a_1, a_2) = (1, 0)$ (orange solid line) and to $(a_1, a_2) = (0, 1)$ (blue solid line). In particular, their shapes (the amplitude is here arbitrary) resemble that of the first and second derivative of the PDF with respect to θ, shown as green and red dashed lines in Fig. 5.5.

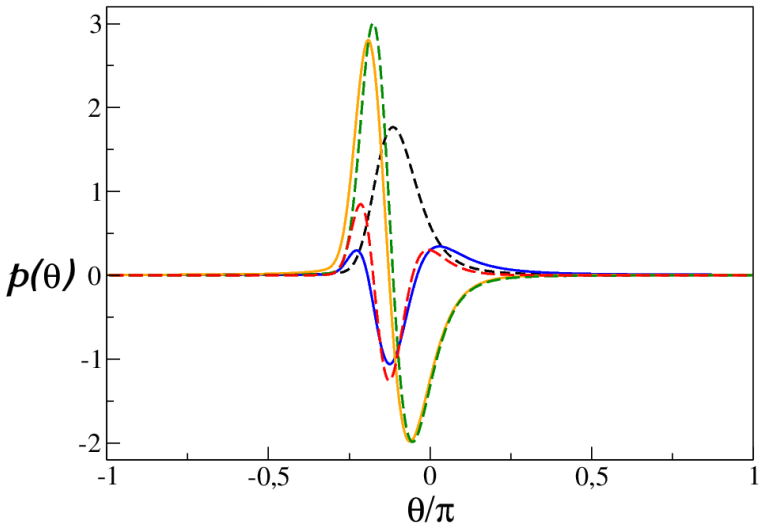

Figure 5.5: Perturbations $p(\theta)$ of the stationary PDF $R^{(0)}(\theta)$ (black dashed line) as a function of θ. The two reported perturbations corresponds to $(a_1, a_2) = (1, 0)$ (orange solid line) and to $(a_1, a_2) = (0, 1)$ (blue solid line). The green dashed line refers to $dR^{(0)}(\theta)/d\theta$ and the red dashed line to $d^2R^{(0)}(\theta)/d\theta^2$ reported in arbitrary units. Parameters as in Fig. 5.4.

The linear stability analysis of the asynchronous state can be performed also for the two CCs approximation, in this case the linear evolution of the system can be obtained from Eqs. (5.35), as

$$\delta\dot{z}_1 = \delta z_1(iA_{g_0} + i) + iz_1^{(0)}\delta A_{g_0} + \delta H(1 + \kappa_2^{(0)} + (z_1^{(0)})^2) + H^{(0)}(\delta\kappa_2 + 2z_1^{(0)}\delta z_1)$$
$$-\delta D_{g_0}\left[\frac{(1+z_1^{(0)})^3}{2}\right] - \frac{3}{2}D_{g_0}\left[\delta z_1(1+z_1^{(0)})^2\right]$$
$$\delta\dot{\kappa}_2 = 2(iA_{g_0} + i)\delta\kappa_2 + 2i\delta A_{g_0}\kappa_2^{(0)} + 4\delta H z_1\kappa_2 + 4H^{(0)}(\delta z_1\kappa_2^{(0)} + z_1^{(0)}\delta\kappa_2)$$
$$-\delta D_{g_0}\left[\frac{1}{2}(1+z_1^{(0)})^4 + 6\kappa_2^{(0)}(1+z_1^{(0)})^2\right]$$
$$-D_{g_0}\left[2(1+z_1^{(0)})\delta z_1\left((1+z_1^{(0)})^2 + 6\kappa_2\right) + 6\delta\kappa_2(1+z_1^{(0)})^2\right]$$

with the stationary values for A_{g_0} and D_{g_0} estimated with the stationary population firing rate, namely

$$r^{(0)} = \frac{1}{\pi}Re\left\{\left[\frac{1-z_1^{(0)}}{1+z_1^{(0)}} + \frac{2\kappa_2^{(0)}}{(1+z_1^{(0)})^3}\right]\right\} \tag{5.41}$$

and with

$$H^{(0)} = \frac{1}{2}\left[i(A_{g_0} - 1)\right]$$

Furthermore, the linearization of A_g and D_g are now given by

$$\delta A_{g_0} = -\sqrt{K}g_0\delta r \quad , \quad \delta D_{g_0} = \frac{g_0^2}{2}\delta r \tag{5.42}$$
$$\delta r = \frac{1}{\pi}Re\left\{\left[-\frac{\delta z_1}{(1+z_1^{(0)})^2} + \frac{\delta\kappa_2}{(1+z_1^{(0)})^3} - \frac{\kappa_2^{(0)}\delta z_1}{(1+z_1^{(0)})^4}\right]\right\}$$

5.4.3 Bifurcation to Collective Oscillations

As mentioned in the previous sub-section the instability of the asynchronous state leads to the emergence of COs in the system. The transition has been analyzed in the network by considering the indicator ρ introduced in Eq. (5.3) measured for increasing in-degrees K for different system sizes, namely $N = 2000$, 4000, 8000 and 16000. The numerical data are reported in Fig. 5.6 and reveals a transition from asynchronous dynamics to COs around $K_c \simeq 170 - 180$.

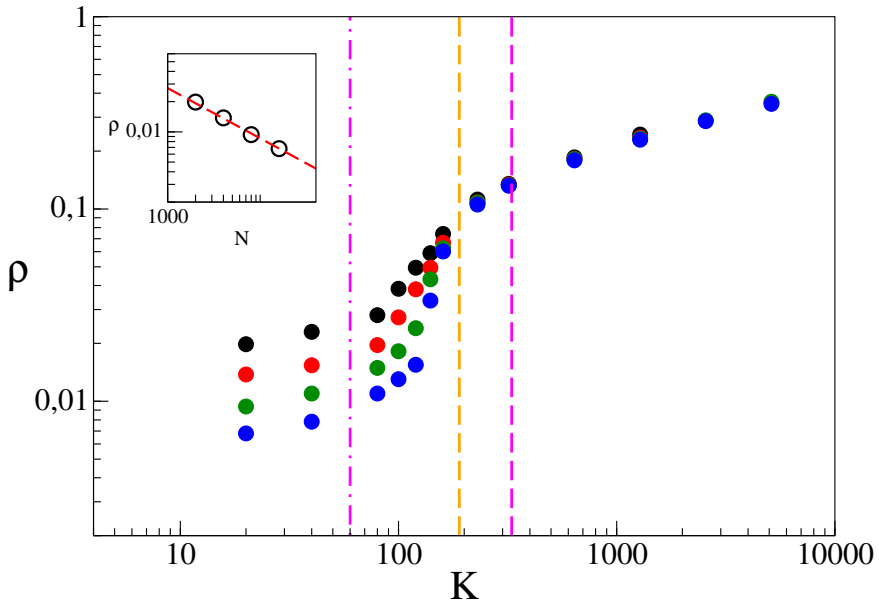

Figure 5.6: Order parameter ρ versus the in-degree K for different network sizes: namely $N = 2000$ (black circles), 4000 (red circles), 8000 (green circles) and 16000 (blue circles). The vertical magenta (orange) dashed line denotes K_c as estimated within a MF approach for the FPE truncated to $M = 64$ with a Poissonian (Renewal) approximation for the current fluctuations Eq. (5.7) (Eq.(5.8) with $CV = 0.8$). The dot-dashed vertical magenta line indicates K_c obtained within the two circular cumulants approximation. The inset report the scaling of ρ versus N for $K = 20$, the red dashed line corresponds to a power law $N^{-1/2}$. Parameters as in Fig. 5.4.

In the same figure are reported also the estimates of K_c found by the linear stability analysis of the FP solution for $M = 64$ with the Poissonian (Renewal) approximation for the noise fluctuations Eq. (5.7) (Eq.(5.8) with $CV = 0.8$). It is evident from the Renewal approximation with $CV = 0.8$ gives a very good estimation of $K_c \simeq 190$, while the Poissonian approximation was largely over estimating the transition point ($K_c \simeq 330$). For completeness, also K_c estimated within the 2CCs approximation is reported as a dash-dotted magenta line in Fig. 5.6. The result $K_c \simeq 50$ indicates that this approach has severe limitations in the homogeneous case, where the OA manifold is definitely not attracting.

Let us now analyze more in details the regime of COs. We have firstly

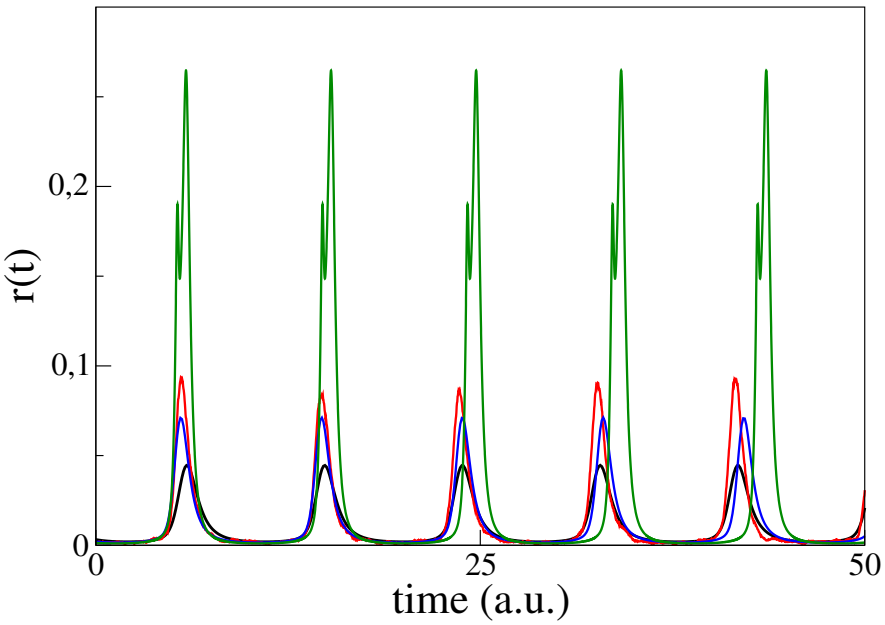

Figure 5.7: Instantaneous firing rate $r(t)$ versus time. The data refer to network simulations with $N = 16000$ (red line), to MF solutions obtained by truncating the FPE to $M = 64$ modes for the Poissonian noise (black line) or the Renewal approximation with $CV = 0.8$ (blue line), as well as to the 2CCs approximation (green line). Parameters as in Fig. 5.4 and $K = 640$.

considered the evolution of the instantaneous firing rate $r(t)$ reported in Fig. 5.7 for $K = 640$. We observe that the period of the COs is nicely captured by the FPE with $M = 64$ and Poissonian noise, however the amplitude of the oscillations is under-estimate by the MF results. On the other hand by taking in account the variance of the fluctuations within a Renewal approach wth $CV = 0.8$ allow to better reproduce the amplitude of the COs, but these results (blue line in Fig. 5.7) have a small drift with respect to the network simulations indicating a faster period of oscillation. The 2CCs approximation (displayed as a green line in Fig. 5.7) overestimates both the amplitude and the period of the COs.

As shown in Fig. 5.8, the frequency of the COs ν_{CO} measured in a network of $N = 8000$ neurons reveals a power-law increase with the in-degree with an exponent $\simeq 0.234$ (red filled circles) not too far from the exponent $1/4$ (dashed magenta line) predicted from the scaling-law in (5.28) [14]. In particular, this

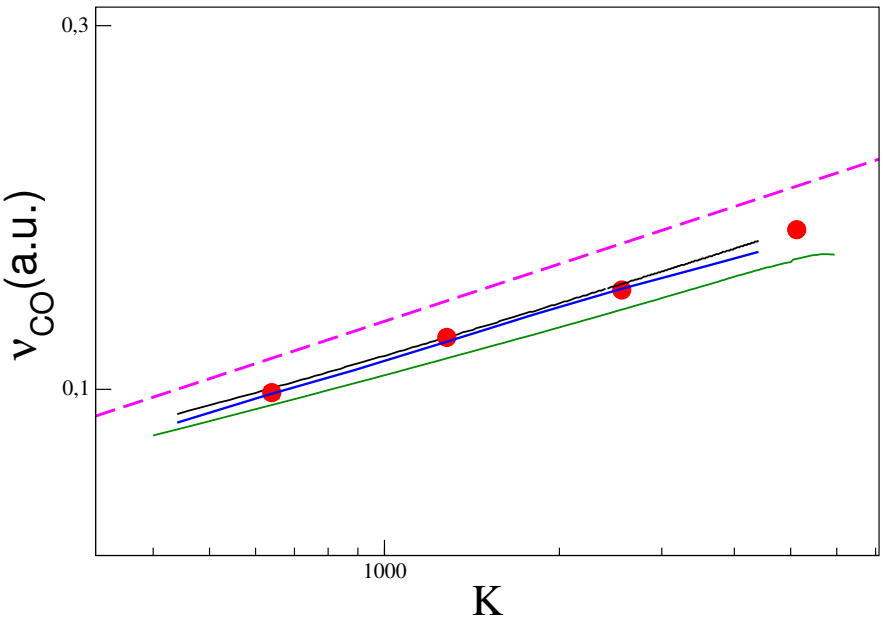

Figure 5.8: Frequency of the COs ν_{CO} versus the in-degree K. Numerical data refer to $N = 8000$ (red filled circles), the estimation based on the direct integration of the FPE with $M = 128$ modes are shown as black line (Poisson Approximation) and blue line (Renewal Approximation with $CV = 0.8$) and the 2CCs approximation as a green line. Parameters as in Fig. 5.4.

law was predicted analytically by considering the damped oscillation frequencies towards stable foci in the MF model (5.27). It should be however stressed that the latter MF model is unable to forecast the emergence of sustained COs via a super-critical Hopf bifurcation. The comparison with the estimations obtained by the FPE with $M = 128$ reveal an almost perfect agreement over the whole range of the considered in-degrees both within the Poissonian and the Renewal approximation, while the 2CCs slightly under-estimate ν_{CO} but also in this case the scaling with K is almost the same.

5.5 Heterogeneous case

5.5.1 Circular two cumulants' approach

In Fig. 5.9 and 5.10 we report direct simulations of the order parameter ρ for different system sizes to show various transitions from asynchronous dynamics to collective oscillations in presence of heterogeneity in the connectivity in-degree ($\Delta_0 > 0$). The estimations of the transition line in terms of the 2CCs Eq. (5.35) approach are also reported. These estimations are based on the linear stability of the asynchronous state and indicates when the state bifurcates to an oscillatory regime through a supercritical Hopf.
Asynchronous dynamics is observable also in the heterogeneous case for sufficiently sparse networks (small K), indeed a clear transition is observable from an asynchronous state to collective oscillations for K larger than a critical valuer K_c. As observable from Fig. 5.9, where we report the coherence indicator ρ as a function of K for various system sizes N, the transition from the asynchronous dynamics to COs is predicted by the 2CCs approximation. The numerical data obtained by network simulations reveals a transition from asynchronous dynamics to COs around $K_c \simeq 170 - 180$, while the 2CCs predicts a transition point around $K_c \simeq 200$.
The relevance of the microscopic fluctuations for the existence of the collective oscillations can be appreciated by considering the behavior of ρ as a function of the external current I_0 and of the parameter controlling the structural heterogeneity, namely Δ_0. The results of these analyses are shown in 5.10 (a) and (b) where we also report the transition point predicted by the 2CCs (red line). In both cases we fix an in-degree $K > K_c$ in order to observe collective oscillations and then we increase I_0 or Δ_0. We observe that for large I_0 (Δ_0) the microscopic dynamics is now imbalanced with few neurons firing regularly with high rates and the majority of neurons suppressed by this high activity. At large I_0 the dynamics of the network is controlled by neurons definitely suprathreshold and the dynamics becomes mean driven [14, 179, 180]. This occurs at a critical value $I_{0c} \simeq 0.6 - 0.8$.
The same occurs by increasing Δ_0, when the heterogeneity in the in-degree distribution becomes sufficiently large ($\Delta_{0c} \simeq 0.4 - 0.5$) only few neurons, the ones with in degrees in proximity of the mean K, can balance their activity, while for the remaining neurons it is no more possible to satisfy the balance conditions, as recently shown in Refs [188, 189, 224]. Even in these cases the 2CCs approximation is able to predict such a transition.

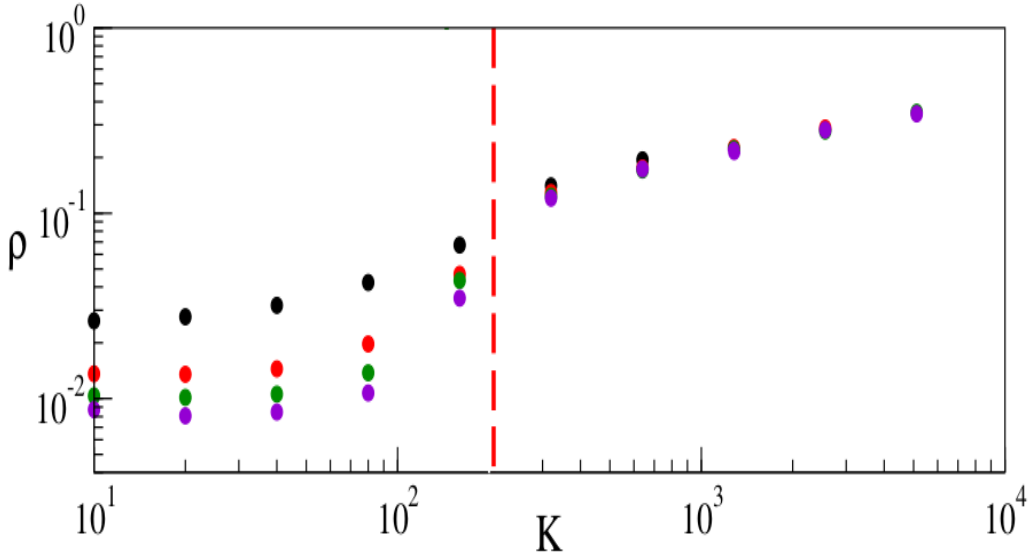

Figure 5.9: Transition for the heterogeneous case: order parameter ρ versus K. Symbols refer to direct simulations of the network for different system sizes: namely, $N = 2000$ (black), 5000 (red), 10000 (green) and 20000 (violet). The red dashed vertical line denotes the transition estimation obtained form the linear stability analysis of asynchronous state obtained within the 2CCs framework. Parameters $\Delta_0 = 0.1$, $I_0 = 0.006$, $g_0 = 1$.

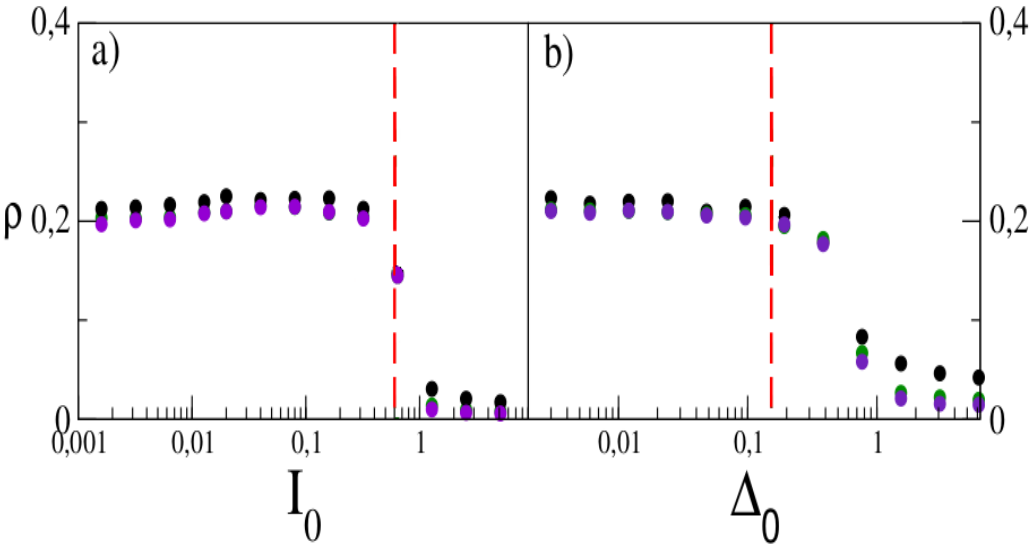

Figure 5.10: Transitions for heterogeneous case: order parameter ρ versus I_0 (a) and Δ_0 (b). Symbols refer to direct simulations of the network for different system sizes as in Fig. (5.9). The red dashed vertical line denotes the transition estimation obtained form the linear stability analysis of asynchronous state obtained within the 2CCs framework. approach. Parameters $K = 1000$, $I_0 = 0.006$, $g_0 = 1$ and $\Delta_0 = 0.1$, when not differently specified.

In particular 2CCs captures very well the transition point varying the external excitatory input ($I_{0_c} \simeq 0.6$) while it underestimates the transition point varying the heterogeneity ($\Delta_{0_c} \simeq 0.15$).

5.6 Conclusions

In this chapter we derived the Fokker-Planck equation associated to a sparse balanced inhibitory network of QIF neurons with instantaneous synapses in order to characterize the transition from the asyncronous state to collective oscillations. Specifically, we considered the noise terme entering in the Fokker-Planck equation in two different ways: namely, within a Poissonian approximation (FPE(P)) or within a renewal approximation (FPE(R)). We find that, in the homogeneous case, the transition occurs for sufficiently large in-degree and that FPE(R) captures more accurately the transition point compared to FPE(P). This is due to the fact that in the renewal approximation the fluctuating current term is better estimated in comparison with the Poissonian approximation, where the spike emissions are assumed to be completely uncorrelated. The linear stability analysis of the associated Fokker-Planck equation reveals that such a transition is due to a super-critical Hopf bifurcation. The effective mean-field model derived in [14] is not able to exhibit such a bifurcation, exhibiting a stable focus solution for any parameter choice, since in such mean-field model the sparseness was considered just as a quenched noise term changing the effective coupling of the neurons. However, in such approach the fluctuations of the input currents to the neurons were neglected. Anyway the frequency of the relaxation oscillations towards the stable focus, provided by the effective mean-field model, represents a good approximation of the frequency of the sustained collective oscillations observed in the network. Here we show that both FPE(P) and FPE(R) are able to reproduce almost perfectly the COs frequencies as a function of the median connectivity in-degree compared with the network simulations.
We also employ the Circular Cumulants approximation [16] truncated at the second cumulant order (2CCs), providing a mean-field model of two differential complex equations for the first and the second cumulant. We show that this model is able to display the transition from the asyncronous state to COs but the transition point is widely underestimated in the homogeneous case, since this approach is particularly suited for heterogeneous networks,

as shown in [16, 17]. Moreover, the 2CCs slightly underestimate COs frequencies but also in this case the scaling with the connectivity in-degree is in good agreement with network simulations.
We conclude that a sparse balanced inhibitory network of QIF neurons with instantaneous synapses is able to exhibit collective oscillations also for random networks with identical in-degree, enriching the result found in [14] where only the heterogeneous case was considered.
Our result shows the emergence of CO due to the presence of endogenous noise. In recent work, the emergence of CO has been reported by increasing the amount of heterogeneity in the excitabilities of neurons [225]. While this heterogeneity is different from the endogenous noise leading to CO in our model, the comparison between the differences form of disorder (annealed and quenched) deserves to be investigated in future works. In addition to the analysis referred to the homogeneous case we also investigate the transition from the asynchronous state to collective oscillations in presence of heterogeneity in the in-degree distribution by employing the 2CCs approximation. We find that this model reproduce quite well the transition from the asynchronous state to COs as a function of the median in-degree. Moreover, we also analyze how both the external excitatory input and the heterogeneity in the in-degree distribution affect the transition from asynchronous dynamic to COs. The impact of both the excitatory input and the heterogeneity in the connectivity in-degree manifest the relevance of the microscopic fluctuations in the network dynamics. As a result, COs disappear as soon as the microscopic fluctuations, due to balanced irregular spiking activity, vanish. The 2CCS approximation reproduces quite well all these transitions. However, further refinements of the mean-field approach can be obtained by considering higher order cumulants. This analysis will be subject of future studies.

Summary and perspectives

This thesis work is based on a neural mass model developed for spiking network of QIF neurons. The QIF neuronal model is extremely important becasue it respresents an excitable membrane model prototype of type I neurons [89]. In particular, we consider a neural mass model that is exaclty derived [10], this entails the description of the network in terms of average membrane potential and firing rate, unlike standard heuristic models [8] where only the firing rate is involved.
Chapters 1 and 2 are dedicated to a detailed review concerning the theory of phase oscillators with particular attention to the techniques of macroscopic reduction of networks of these oscillators based on the Ott-Antonsen ansatz [11]. Particularly relevant for the drafting of this thesis is the recent article by E. Montbrió, D. Pazó, A. Roxin [10] in which an exact mean field model is analytically derived from a microscopic network of fully-coupled QIF neurons. Specifically, the authors extended the approach developed by Ott and Antonsen for heterogeneous networks of phase oscillators to neural models. This is possible given that models of QIF neurons are essentially phase oscillators coupled together in an impulsive way. Thanks to this reduction methodology, the dynamic evolution of the mean membrane potential and of the firing rate of the neuronal population are perfectly reproduced with a model of only two ordinary differential equations.
In the rest of the thesis, namely in the chapters 3, 4 and 5, we take into consideration various network topologies and we study their dynamics. Our attention is particularly focused on the mechanisms that can give rise to collective oscillations in the gamma-band (30-90 Hz).
In Chapter 3 we study the dynamic of PING and ING fully-coupled configurations in order to reproduce the experimental data reported in [13]. We show that the corresponding mean-field model is able to reproduce part of these experiments but fails for others. In particular, we have shown that θ-nested γ

oscillations can emerge both in the PING and ING set-up under an external excitatory θ-drive in proximity of a super-critical and also a sub-critical Hopf bifurcations. As shown in Appendix A, in the latter case the amplitudes are no more symmetric with respect to the maximum value of the theta stimulation, analogously to the experimental findings reported in [13]. Furthermore, we have identified two different types of phase amplitude couplings (PACs): one characterized by a perfect locking between θ and γ-rhythms, corresponding to an overall periodic behaviour dictated by the slow forcing, the other one where the locking is imperfect and the dynamics is quasiperiodic or even chaotic. Our modelization of the PAC mechanism induced by an external θ-forcing is able to reproduce several experimental features reported for optogenetic experiments concerning the region CA1, CA3 of the hippocampus, as well as MEC [13,118–120]. In agreement with the experiments, we observe nested γ COs for forcing frequencies in the range $[1 : 10]$ Hz, whose amplitude grows proportionally to the forcing one. Furthermore, the γ-power and the frequency of the γ peak increase almost linearly with the forcing amplitude, i.e. with the input θ-power. However, the neural mass model in all the examined PING and ING set-ups is unable to reproduce the increase in frequency of the γ-power peak with the stimulation frequency reported in [13]. In order to get a similar increase in the neural mass model, we have been obliged to assume that the stimulation power (namely, the noise or the forcing amplitude) increases proportionally with the stimulation frequency.
Further studies, with the aim of reproducing experimental observations, can be addressed considering more complex set-ups. For example, in the case of the PING model, a synaptic time decay could be introduced. Furthermore, it is known that the structure of the network in the brain changes with our every-day experience, a mechanism called synaptic plasticity. An exciting future perspective is to include synaptic plasticity in our model, paving the way to a simple model to study the learning capacities and working memory ability (WM) of neural networks [226–228]. For example we would like to introduce short-term synaptic plasticity (STP), introduced by Mongillo et al. in [229], for which the corresponding exact neural mass model has recently been derived for heterogeneous spiking neural networks [230].
While in chapter 3 we consider ideal fully-coupled networks, a first step in the direction of more realistic models of brain circuits is to consider networks with randomly assigned connections between neurons, namely sparse networks, for which the exact reduction presented in chapter 2 is no longer valid. Indeed in Chapter 4 we consider an effective reduced neural mass

model reproducing a sparse network, where the random distribution of the number of presynaptic neurons is considered as a quenched disorder. We propose a minimal model capable of giving rise to the coexistence of fast and slow gamma oscillations considering a single sparse balanced inhibitory population. We also present a simple protocol to drive the system from slow gamma oscillations to fast ones (and vice versa) by injecting a fast external stimulus. This mechanism can allow a single inhibitory population to pass from a coding task to another following an external sensory stimulus. Indeed it has been shown that distinct gamma rhythms are involved in different coding processes: namely, fast gamma in new memory encoding, while slow gamma has been hypothized to promote memory retrieval [198].

We have analyzed the emergence of COs in our network also in presence of an external theta forcing. This in order to make a closer contact with recent experimental investigations devoted to analyse the emergence of gamma oscillations in several brain areas *in vitro* under sinusoidally modulated theta-frequency optogenetic stimulations [13,118,119]. For low forcing amplitudes, our network model displays theta-nested gamma COs at frequencies around 50 Hz joined with irregular spiking dynamics, analogously to the ones reported for the CA1 and CA3 areas of the hippocampus in [13, 118]. Furthermore, for intermediate forcing amplitudes we observe the coexistence of slow and fast gamma oscillations, which lock to different phases of the theta rhythm, analogously to what reported for the rat hippocampus during exploration and REM sleep [104, 105]. Finally, for sufficiently strong forcing, the model is driven in the fast gamma regime. These results can be useful in revealing the mechanism behind slow and fast gamma oscillations reported in several brain areas: namely, hippocampus [171], olfactory bulb [207], ventral striatum [208], visual cortical areas [209] and neocortex [170].

Future studies can be addressed considering intrinsic adaptation dynamics of the network. A slow adaptation variable could drive the system from one oscillatory state to the other without the need of external stimulus. In the same spirit, the coupling between this inhibitory population and an excitatory one could guide autonomously the system between one oscillatory state and the other. Due to the large variety of interneurons, present in the brain, a further step in rendering our model more realistic would consist in considering multiple inhibitory populations characterized by different neuronal parameters. By manipulating the influence of a population on the others it would be interesting to investigate the possible mechanisms to switch COs from one gamma rhythm to another.

In chapter 4 we have developed a low dimensional mean-field model for a sparse network, where the disorder has been considered only at the level of quenched random terms. However, we failed to include noise fluctuations that are present in the network. The fluctuations can be considered in the dynamical evolution by developing a Fokker-Planck formalism for the distribution of the membrane potentials of the QIF neurons. This has been done in Chapter 5, by developing the Fokker-Planck approach in Fourier space, thanks to the angular nature of the variable employed to describe the QIF neuron. Specifically, we solved the Fokker-Planck equation associated to a sparse balanced inhibitory network of QIF neurons with instantaneous synapses and we prove the transition from the asynchronous state to collective oscillations. However, this approach is infinite dimensional.
A promising low dimensional reduced mean-field model, successfully applied to noisy phase oscillators networks, is the Circular Cumulants approach [16, 17]. In particular, we have extended this methodology to the QIF sparse networks, where the noise has an endogenous nature. We showed that the reduced mean field model derived considering the second order cumulant is able to catch the transition between the asynchronous and the oscillatory state.
Furthermore, the theory could be extended by taking into account more biologically realistic characteristics, such as the presence of conductance-based synapses. Recently, mean field model have been developed [225, 231–233] in order to take into account such non-linearity in the dynamic, revealing that the network response depends on the state of the conductance. The extension of our approach to conductance-based synapses could clarify the role of this non-linearity for different regimes, such as fast oscillations. Indeed, even if preliminary results indicates that the introduction of conductances in our model does not represent any difficulty from the analytic point of view, their presence could radically change the response of the system. This new approach paves the way to a large variety of future studies. For example, by employing the Circular Cumulants approach we can envisage in the future to address excitatory-inhibitory sparse balance networks resembling realistic neural circuit [21].

Appendix A

PING set-up: sub-critical Hopf

In the PING set-up with only recurrent excitation (i.e. with $J^{(ee)} \neq 0$, $J^{(ii)} = 0$ and $J^{(ie)} = J^{(ei)} \neq 0$), it is possible to observe the emergence of COs also via a sub-critical Hopf bifurcation, by using $H^{(e)}$ as control parameter, as shown in Fig. A.1 (a). This is due to the nature of the Hopf bifurcation that can be modified by simply varying the value of $H^{(i)}$. In this case we observe three regimes: an asynchronous one for $H^{(e)} < H^{(e)}_{SN}$; an oscillatory one for $H^{(e)} > H^{(e)}_c$ and a bistable one in the range $[H^{(e)}_{SN} : H^{(e)}_c]$. The frequency of the COs $\nu^{(e)}$ is always in the γ-range with a minimal value $\simeq 36$ Hz achievable at the Hopf bifurcation, see the inset of Fig. A.1 (a).
If we consider the unforced system with $H^{(e)} < H^{(e)}_{SN}$ and we apply a θ-forcing, we observe PAC oscillations. However when considering $v^{(e)}$, the COs are now asymmetric with respect to the maximum of the stimulation current $I^{(e)} = I_\theta(t)$ (see Fig. A.1 (b)). This effect is even more pronounced by observing the wavelet spectrogram reported in Fig. A.1 (c), where a clear PFC is also observable. The asymmetry in the onset of the gamma oscillations is clearly visible in the continuous wavelet transform obtained from the experimental data and reported in Fig. 4G in [13]. This asymmetry can be explained in an adiabatic framework by considering the corresponding bifurcation diagram shown in Fig. A.1 (a). Indeed for the sub-critical Hopf, the COs will emerge for $I_\theta > [H^{(e)}_c - H^{(e)}]$, but they will disappear for a different value of the forcing, namely $I_\theta < [H^{(e)}_{SN} - H^{(e)}]$. Instead, for a super-critical, Hopf the emergence and disappearance of the oscillations will occur at the same forcing amplitude, namely $I_\theta = [H^{(e)}_c - H^{(e)}]$.

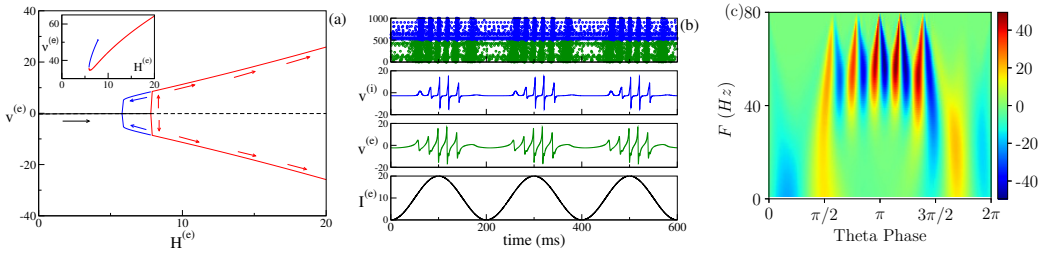

Figure A.1: (**PING set-up: subcritical Hopf**) (a) Bifurcation diagram of the neural mass model of the average membrane potential $v^{(e)}$ as a function of $H^{(e)}$. The black continuous (dashed) line identifies the stable (unstable) fixed point. The red lines denote the maxima and minima of the limit cycles. The subcritical Hopf bifurcation occurs at $H_c^{(e)} \simeq 7.8$ while the saddle-node of limit cycles occurs at $H_{SN}^{(e)} = 5.8$. In the inset the COs' frequency $\nu^{(e)}$ is displayed as a function of $H^{(e)}$. (b) From top to bottom: raster plot where green (blue) dots refer to excitatory (inhibitory) neurons in a network of 10000 neurons; average membrane potentials $v^{(i)}$ and $v^{(e)}$ as obtained by the evolution of the neural mass models and forcing current $I^{(e)}$ for $H^{(e)} = -5 < H_{SN}^{(e)}$ and $\nu_\theta = 5$ Hz. (c) Continuous wavelet transform over a single θ cycle for $v^{(e)}$ with system setting as in (b). The remaining system parameters are $J^{(ee)} = 8$, $J^{(ii)} = 0$, $J^{(ie)} = J^{(ei)} = 10$, $H^{(i)} = -8.0$ and the size of the excitatory (inhibitory) network is $N^{(e)} = 5000$ ($N^{(i)} = 5000$).

Appendix B

Different PING set-ups

In the main text we have considered a unique configuration giving rise to COs via the PING mechanism: namely, two cross coupled inhibitory and excitatory populations with recurrent excitation and no recurrent inhibition (i.e. $J^{(ee)} \neq 0$ and $J^{(ii)} = 0$). However, other network configurations can give rise to PING induced oscillatory regimes. In particular, we have observed such oscillations with only cross-couplings in the absence of recurrent excitation and inhibition (i.e. $J^{(ee)} = J^{(ii)} = 0$), as well as in the presence of recurrent inhibition only (i.e. $J^{(ee)} = 0$ and $J^{(ii)} \neq 0$). In the following we refer to the former configuration as PING_0 set-up, while the latter configuration with recurrent inhibition is identified as PING_I set-up. In both configurations the neural mass reproduces the emergence of γ oscillations via a super-critical Hopf bifurcation for increasing values of $H^{(e)}$, as shown in Figs. B.1 (a) and (b). Indeed the frequencies of the COs are in the range $[26 : 63.5]$ Hz ($[29.1 : 53.9]$ Hz) for PING_0 (PING_I) set-up. In both configurations the corresponding bifurcation, as a function of the parameter $H^{(i)}$, is sub-critical and COs disappear for sufficiently positive values of $H^{(i)}$, analogously to what is reported in the main text for the PING set-up with only recurrent excitation. It should be stressed that the standard Wilson-Cowan neural mass model gives rise to COs only in the presence of a recurrent excitation [8], thus being unable to reproduce the spiking network dynamics [138]. In the presence of an external θ-forcing with $\nu_\theta = 5$ Hz, we clearly observe θ-nested γ-oscillations, as shown in the raster plots reported in Figs. B.1 (top rows of panels (b) and (d)). These oscillations are phase amplitude modulated from the forcing, as it results to be evident from the shape of the mean membrane potentials $V^{(e)}$ and $V^{(i)}$ reported in the middle rows of Figs. B.1 (c) and (d).

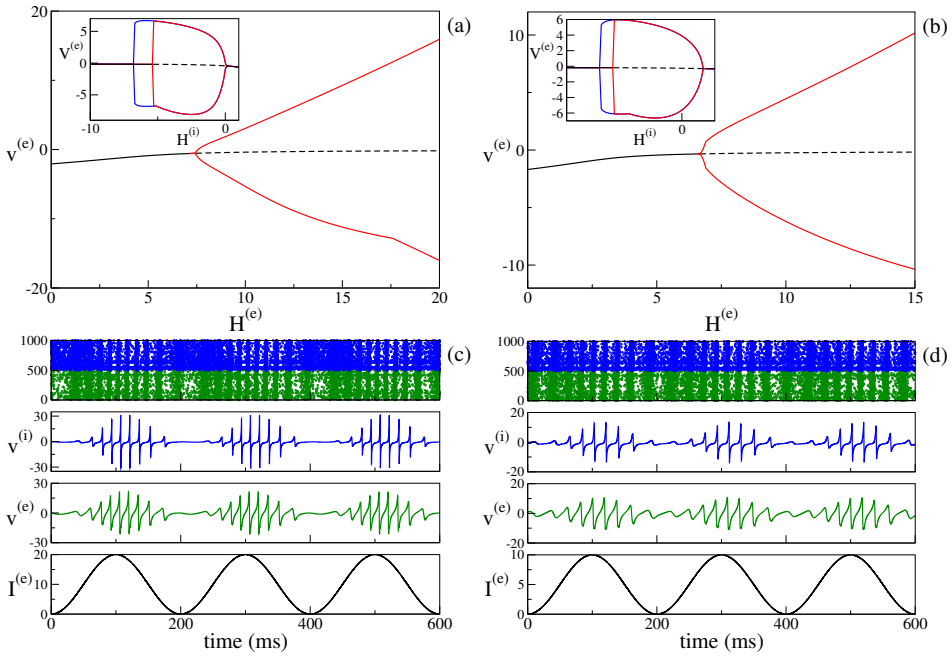

Figure B.1: (**Different PING set-ups**) Bifurcation diagram for the neural mass model versus $H^{(e)}$, for the PING_0 (a) and PING_I (b) set-ups for $H^{(i)} = -0.5$. The corresponding insets show the bifurcation diagrams as a function of $H^{(i)}$, for $H^{(e)} = 10$. θ-nested γ oscillations emerging in the PING_0 (c) and PING_I (d) configurations for $I_0 = 20$ and $\nu_\theta = 5$ Hz. From top to bottom the raster plot where green (blue) dots refer to excitatory (inhibitory) neurons in a network of 10000 neurons; the average membrane potentials $v^{(i)}$ and $v^{(e)}$ as obtained by the evolution of the neural mass models and the forcing currents $I^{(e)}$. Parameters for the PING_0 set-up are $J_{ee} = J_{ii} = 0$, while for PING_I are $J_{ee} = 0$ and $J_{ii} = 8$. In both cases $J_{ie} = J_{ei} = 10$ and $H^{(i)} = -0.5$. In the corresponding insets we set $H^{(e)} = 10$. The size of the excitatory (inhibitory) network shown in panels (c), (d) is $N^{(e)} = 5000$ ($N^{(i)} = 5000$).

Appendix C

Slow and fast gamma oscillations in Erdös-Renyi network

In order to compare the network simulations with the MF results we have considered in the article a Lorentzian distribution for the in-degrees. It is therefore important to show that the same phenomenology is observable by considering a more standard distribution, like the Erdös-Renyi (ER) one. The results of adiabatic simulations, reported in Fig. (C.1), confirm that also for ER networks a bistable regime, characterized by COs with different gamma-frequencies (see panel (b)), is indeed observable. In particular, slow gamma COs characterized by an average firing rate $\bar{r} \simeq 25$ Hz and irregular neuronal firings (as shown in panels (c) and (e)) coexist with almost synchronized fast gamma COs with neurons tonically firing with $\bar{r} \simeq 60$ Hz (see panels (d) and (f)).

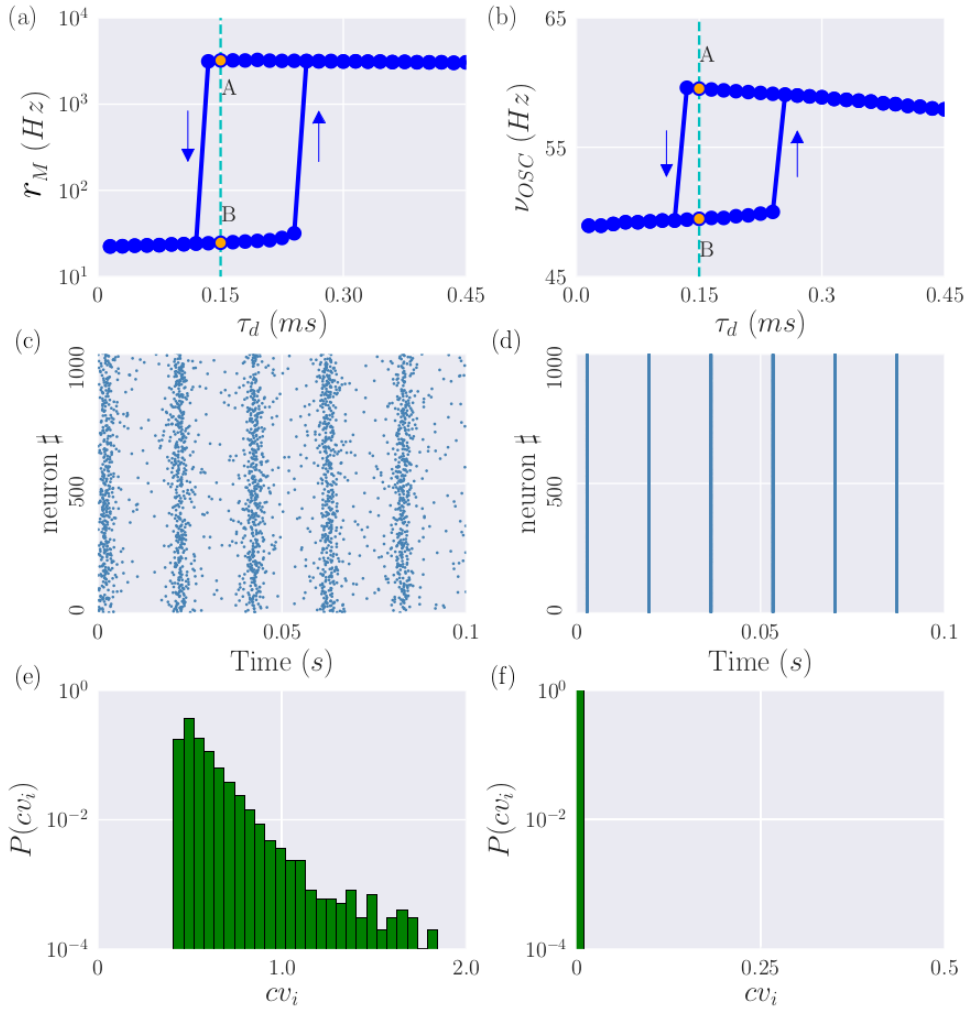

Figure C.1: **Erdös-Renyi Network** Results of adiabatic simulations for an ER network obtained by varying the synaptic time τ_d: (a) maximal firing rates r_M and (b) frequencies ν_{OSC} of the COs. Two coexisting states (A) and (B) are considered at $\tau_d = 0.15$ ms. In the left and right row are reported the raster plots (c,d) and the distributions of the cv_i (e,f) for the state (A) and (B), respectively. Parameters for the simulations are $N = 10000$, $K = 1000$, $I_0 = 0.25$, $J_0 = 1.0$ and $\Delta\tau_d = 0.015$ ms, $\tau_d^{(0)} = 0.015$ ms, $\tau_d^{(1)} = 0.45$ ms.

Appendix D

A general mechanism for the emergence of coexisting oscillations

We investigate here the generality of the mechanism for the coexistence of COs observed in the network of QIF neurons. In particular, we have shown that this phenomenon occurs when in the MF model we have a focus coexisting with a limit cycle, while in the sparse network we have fluctuations sustained by the dynamical balance. If this is the mechanism we expect to see a similar phenomenon whenever we consider a system in proximity of a sub-critical Hopf bifurcation and we add noise of constant amplitude to the dynamics.
Therefore, to asses the generality of the phenomenon we consider the normal form of a Hopf bifurcation in two dimensions leading to the birth of a limit cycle from an equilibrium, namely [234, 235]:

$$\tau_m \dot{x} = \beta x - y + \sigma x r^2 - (x + \gamma y) r^4 + I_1 \tag{D.1}$$
$$\tau_m \dot{y} = x + \beta y + \sigma y r^2 + (\gamma x - y) r^4 + I_2 \ , \tag{D.2}$$

where $r^2 = x^2 + y^2$, $\tau_m = 4$ ms is an arbitrary time scale, $I_1(t)$ and $I_2(t)$ are generic external time dependent forcing, β is the bifurcation parameter, the parameter σ sets the nature of the bifurcation and γ controls the frequency of the stable and unstable limit cycles. Notice that we added a quintic term, absent in the original normal form [234, 235], in order to maintain bounded

the values of x and y while keeping the same bifurcation structure. For $I_1 = I_2 = 0$ we will have a sub-critical (super-critical) Hopf for $\sigma = +1$ ($\sigma = -1$). In this case it is convenient to rewrite (D.2) in polar coordinates $(x, y) = (r\cos\phi, r\sin\phi)$, as follows:

$$\tau_m \dot{r} = \beta r + \sigma r^3 - r^5 \quad (D.3)$$

$$\tau_m \dot{\phi} = 1 + \gamma r^4 \quad . \quad (D.4)$$

The stationary solutions are $r = 0$ corresponding to stable focus characterized by relaxation oscillations with a frequency $\nu_D \simeq 39$ Hz and a stable and unstable limit cycles of amplitudes $r^2 = (\sigma \pm \sqrt{\sigma^2 + 4\beta})/2$.
In Fig. (D.1) (a) we report the bifurcation diagram for $\sigma = +1$ and $I_1 = I_2 = 0$. We observe that the sub-critical Hopf bifurcation occurs at $\beta = \beta_c = 0$ and for $\beta < 0$ it exists a region where a stable (green dots) and unstable (blue dashed line) limit cycles coexists with a stable focus (red line), exactly as it happens for the QIF MF model (see Fig. (4.7) (a)). The stable and unstable limit cycles merge at a SN bifurcation located at $\beta = -\sigma^2/4$.
As previously stated, the MF model cannot capture the endogenous fluctuations, naturally present in sparse balanced networks. In order to emulate this effect we consider $I_1(t)$ and $I_2(t)$ to be two i.i.d. Gaussian white noise processes (i.e. $I_q(t) = A_q\xi_q(t)$ with $q = 1, 2$, where $\xi_q(t)$ are random, Gaussian distributed, variables of zero average and unitary variance). In presence of these additive noise terms and in proximity of the Hopf bifurcation, we observe the coexistence of two oscillatory regimes as shown in Fig. (D.1) (b). One oscillation, characterized by higher amplitude (green line), corresponds to the limit cycle present in the non-noisy dynamics (green line in the bifurcation diagram reported in Fig. (D.1) (b).). The other oscillation is the result of a constructive role of noise that excites the stable focus thus generating robust oscillations at the frequency ν_D (red line). Analogously to what shown for the network of QIF neurons (see Fig. (4.8)), it is possible to switch between the two kind of oscillations via a pulse current of positive (negative) amplitude with respect to the baseline (see the dashed line in panel b)). Moreover the frequencies of the two oscillations, generated by two different mechanisms, corresponds to slow and fast gamma oscillations as observable in the corresponding power spectra $S(\nu)$ reported in the inset of Fig. (D.1) (b).

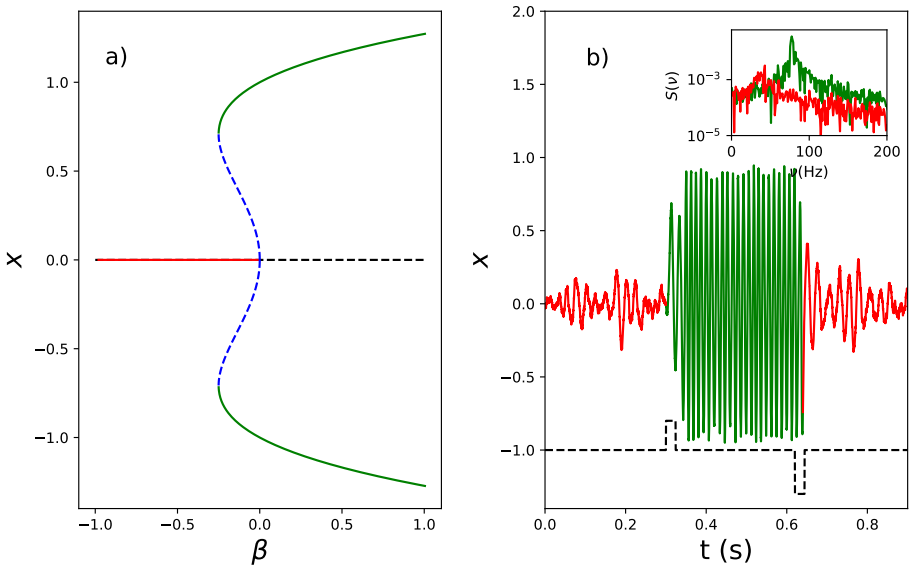

Figure D.1: a) Bifurcation diagram for the variable x as a function of the parameter β. Green (blue) lines indicate a stable (unstable) limit cycle and red (black) line a stable (unstable) focus. b) Fixing β in the bistability region we report the time trace of $x(t)$ in presence of a zero-mean gaussian noise of amplitude $A_1 = A_2 = 0.14$. An external pulse of current is added to the evolution equation for x in (D.2) for a time window of 56 ms to induce a switching between the oscillatory states (the black dashed line, shifted on the x axe to be visible while the actual baseline value is zero). In the inset we report the power spectrum of the two different oscillatory regimes obtained over long time traces (hundreds of seconds) in order to check that the oscillations persist in time. Parameters are $\beta = -0.16$, $\sigma = 1$, $\gamma = 1.5$.

Bibliography

[1] Duncan J Watts, Mark EJ Newman, and Albert-Làzlò Barabási. *The structure and dynamics of networks*. Princeton University Press, 2006.

[2] Paul C Matthews, Renato E Mirollo, and Steven H Strogatz. Dynamics of a large system of coupled nonlinear oscillators. *Physica D: Nonlinear Phenomena*, 52(2-3):293–331, 1991.

[3] Naoko Nakagawa and Yoshiki Kuramoto. From collective oscillations to collective chaos in a globally coupled oscillator system. *Physica D: Nonlinear Phenomena*, 75(1-3):74–80, 1994.

[4] Simona Olmi, Roberto Livi, Antonio Politi, and Alessandro Torcini. Collective oscillations in disordered neural networks. *Physical Review E*, 81(4):046119, 2010.

[5] Simona Olmi, Antonio Politi, and Alessandro Torcini. Collective chaos in pulse-coupled neural networks. *EPL (Europhysics Letters)*, 92(6):60007, 2011.

[6] Eugene M Izhikevich and Jeff Moehlis. Dynamical systems in neuroscience: The geometry of excitability and bursting. *SIAM review*, 50(2):397, 2008.

[7] Gustavo Deco, Viktor K Jirsa, Peter A Robinson, Michael Breakspear, and Karl Friston. The dynamic brain: from spiking neurons to neural masses and cortical fields. *PLoS computational biology*, 4(8), 2008.

[8] Hugh R Wilson and Jack D Cowan. Excitatory and inhibitory interactions in localized populations of model neurons. *Biophysical journal*, 12(1):1–24, 1972.

[9] Hugh R Wilson and Jack D Cowan. A mathematical theory of the functional dynamics of cortical and thalamic nervous tissue. *Kybernetik*, 13(2):55–80, 1973.

[10] Ernest Montbrió, Diego Pazó, and Alex Roxin. Macroscopic description for networks of spiking neurons. *Physical Review X*, 5(2):021028, 2015.

[11] Edward Ott and Thomas M Antonsen. Low dimensional behavior of large systems of globally coupled oscillators. *Chaos: An Interdisciplinary Journal of Nonlinear Science*, 18(3):037113, 2008.

[12] Diego Pazó and Ernest Montbrió. Low-dimensional dynamics of populations of pulse-coupled oscillators. *Physical Review X*, 4(1):011009, 2014.

[13] James L Butler, Philipe RF Mendonça, Hugh PC Robinson, and Ole Paulsen. Intrinsic cornu ammonis area 1 theta-nested gamma oscillations induced by optogenetic theta frequency stimulation. *Journal of Neuroscience*, 36(15):4155–4169, 2016.

[14] Matteo di Volo and Alessandro Torcini. Transition from asynchronous to oscillatory dynamics in balanced spiking networks with instantaneous synapses. *Phys. Rev. Lett.*, 121:128301, Sep 2018.

[15] Nicolas Brunel and Vincent Hakim. Fast global oscillations in networks of integrate-and-fire neurons with low firing rates. *Neural computation*, 11(7):1621–1671, 1999.

[16] Irina V Tyulkina, Denis S Goldobin, Lyudmila S Klimenko, and Arkady Pikovsky. Dynamics of noisy oscillator populations beyond the ott-antonsen ansatz. *Physical review letters*, 120(26):264101, 2018.

[17] Denis S Goldobin, Irina V Tyulkina, Lyudmila S Klimenko, and Arkady Pikovsky. Collective mode reductions for populations of coupled noisy oscillators. *Chaos: An Interdisciplinary Journal of Nonlinear Science*, 28(10):101101, 2018.

[18] Yoshiki Kuramoto. International symposium on mathematical problems in theoretical physics. *Lecture notes in Physics*, 30:420, 1975.

[19] Shinya Watanabe and Steven H Strogatz. Integrability of a globally coupled oscillator array. *Physical review letters*, 70(16):2391, 1993.

[20] Marco Segneri, Hongjie Bi, Simona Olmi, and Alessandro Torcini. Theta-nested gamma oscillations in next generation neural mass models. *Frontiers in Computational Neuroscience*, 14:47, 2020.

[21] Carl Van Vreeswijk and Haim Sompolinsky. Chaos in neuronal networks with balanced excitatory and inhibitory activity. *Science*, 274(5293):1724–1726, 1996.

[22] Alfonso Renart, Jaime De La Rocha, Peter Bartho, Liad Hollender, Néstor Parga, Alex Reyes, and Kenneth D Harris. The asynchronous state in cortical circuits. *science*, 327(5965):587–590, 2010.

[23] Michael Monteforte and Fred Wolf. Dynamic flux tubes form reservoirs of stability in neuronal circuits. *Physical Review X*, 2(4):041007, 2012.

[24] Hongjie Bi, Marco Segneri, Matteo di Volo, and Alessandro Torcini. Coexistence of fast and slow gamma oscillations in one population of inhibitory spiking neurons. *Physical Review Research*, 2(1):013042, 2020.

[25] Arthur T Winfree. *The geometry of biological time*, volume 12. Springer Science & Business Media, 2001.

[26] Steven H Strogatz. Exploring complex networks. *nature*, 410(6825):268–276, 2001.

[27] Michael Breakspear, JA Roberts, John R Terry, Serafim Rodrigues, N Mahant, and PA Robinson. A unifying explanation of primary generalized seizures through nonlinear brain modeling and bifurcation analysis. *Cerebral Cortex*, 16(9):1296–1313, 2006.

[28] C Liu, DW Feidman, and JL Pack. Weaver. *DR, Strogatz, SH and Reppert, SM*, pages 855–860, 1997.

[29] John Buck and Elisabeth Buck. Mechanism of rhythmic synchronous flashing of fireflies: Fireflies of southeast asia may use anticipatory time-measuring in synchronizing their flashing. *Science*, 159(3821):1319–1327, 1968.

[30] J Collins and I Stewart. J. nonlinear sci, 1993.

[31] SH Strogatz, DM Abrams, A McRobie, B Eckhardt, and E Ott. Enhanced flow in carbon nanotubes. *Nature*, 438(3), 2005.

[32] Steven H Strogatz, Richard E Kronauer, and Charles A Czeisler. Circadian pacemaker interferes with sleep onset at specific times each day: role in insomnia. *American Journal of Physiology-Regulatory, Integrative and Comparative Physiology*, 253(1):R172–R178, 1987.

[33] Jean-Christophe Leloup and Albert Goldbeter. Modeling the circadian clock: from molecular mechanism to physiological disorders. *Bioessays*, 30(6):590–600, 2008.

[34] PD Smolen and JH Byrne. Circadian rhythm models. *Encyclopedia of Neuroscience*, pages 957–963, 2009.

[35] Eder Zavala, Kyle CA Wedgwood, Margaritis Voliotis, Joël Tabak, Francesca Spiga, Stafford L Lightman, and Krasimira Tsaneva-Atanasova. Mathematical modelling of endocrine systems. *Trends in Endocrinology & Metabolism*, 2019.

[36] AK Ghosh, B Chance, and EK Pye. Metabolic coupling and synchronization of nadh oscillations in yeast cell populations. *Archives of biochemistry and biophysics*, 145(1):319–331, 1971.

[37] Sune Danø, Preben Graae Sørensen, and Finn Hynne. Sustained oscillations in living cells. *Nature*, 402(6759):320–322, 1999.

[38] Thomas M Massie, Bernd Blasius, Guntram Weithoff, Ursula Gaedke, and Gregor F Fussmann. Cycles, phase synchronization, and entrainment in single-species phytoplankton populations. *Proceedings of the National Academy of Sciences*, 107(9):4236–4241, 2010.

[39] Walter J Freeman. A proposed name for aperiodic brain activity: stochastic chaos. *Neural Networks*, 13(1):11–13, 2000.

[40] Christopher J Honey, Jean-Philippe Thivierge, and Olaf Sporns. Can structure predict function in the human brain? *Neuroimage*, 52(3):766–776, 2010.

[41] Alex Fornito, Andrew Zalesky, and Michael Breakspear. The connectomics of brain disorders. *Nature Reviews Neuroscience*, 16(3):159–172, 2015.

[42] Flavio Fröhlich. *Network neuroscience*. Academic Press, 2016.

[43] M Goodfellow, Christian Rummel, Eugenio Abela, MP Richardson, K Schindler, and JR Terry. Estimation of brain network ictogenicity predicts outcome from epilepsy surgery. *Scientific reports*, 6:29215, 2016.

[44] Steven Strogatz. *Sync: The emerging science of spontaneous order*. Penguin UK, 2004.

[45] Leon Glass. Synchronization and rhythmic processes in physiology. *Nature*, 410(6825):277–284, 2001.

[46] Florian Dörfler and Francesco Bullo. Synchronization in complex networks of phase oscillators: A survey. *Automatica*, 50(6):1539–1564, 2014.

[47] Michael J Kahana. The cognitive correlates of human brain oscillations. *Journal of Neuroscience*, 26(6):1669–1672, 2006.

[48] Klaus Lehnertz, Christian Geier, Thorsten Rings, and Kirsten Stahn. Capturing time-varying brain dynamics. *EPJ Nonlinear Biomedical Physics*, 5:2, 2017.

[49] J Fell and N Axmacher. O papel da sincronização de fase nos processos de memória. *Nature Reviews Neuroscience*, 12(2):105–118, 2011.

[50] Andreas K Kreiter and Wolf Singer. Stimulus-dependent synchronization of neuronal responses in the visual cortex of the awake macaque monkey. *Journal of neuroscience*, 16(7):2381–2396, 1996.

[51] XJ Wang. Introduction i, synchronization a, resonance b, subthreshold c, rhythms vs, et 27 al. *Neurophysiological and Computational Principles of Cortical Rhythms in Cognition*, 28:1195–1268.

[52] W Singer. St gray, –° m. anna. *Rev. Neurosci*, 18:555–586, 1995.

[53] Pascal Fries. A mechanism for cognitive dynamics: neuronal communication through neuronal coherence. *Trends in cognitive sciences*, 9(10):474–480, 2005.

[54] Eve Marder and Dirk Bucher. Central pattern generators and the control of rhythmic movements. *Current biology*, 11(23):R986–R996, 2001.

[55] Jeffrey C Smith, Howard H Ellenberger, Klaus Ballanyi, Diethelm W Richter, and Jack L Feldman. Pre-botzinger complex: a brainstem region that may generate respiratory rhythm in mammals. *Science*, 254(5032):726–729, 1991.

[56] Robert J Butera Jr, John Rinzel, and Jeffrey C Smith. Models of respiratory rhythm generation in the pre-botzinger complex. i. bursting pacemaker neurons. *Journal of neurophysiology*, 82(1):382–397, 1999.

[57] Peter J Uhlhaas and Wolf Singer. Neural synchrony in brain disorders: relevance for cognitive dysfunctions and pathophysiology. *neuron*, 52(1):155–168, 2006.

[58] Constance Hammond, Hagai Bergman, and Peter Brown. Pathological synchronization in parkinson's disease: networks, models and treatments. *Trends in neurosciences*, 30(7):357–364, 2007.

[59] Christian Rummel, Marc Goodfellow, Heidemarie Gast, Martinus Hauf, Frédérique Amor, Alexander Stibal, Luigi Mariani, Roland Wiest, and Kaspar Schindler. A systems-level approach to human epileptic seizures. *Neuroinformatics*, 11(2):159–173, 2013.

[60] Eugene M Izhikevich. *Dynamical systems in neuroscience*. MIT press, 2007.

[61] Stephen Coombes and Aine Byrne. Next generation neural mass models. In *Nonlinear Dynamics in Computational Neuroscience*, pages 1–16. Springer, 2019.

[62] Francisco A Rodrigues, Thomas K DM Peron, Peng Ji, and Jürgen Kurths. The kuramoto model in complex networks. *Physics Reports*, 610:1–98, 2016.

[63] Yoshiki Kuramoto. *Chemical oscillations, waves, and turbulence*. Courier Corporation, 2003.

[64] Juan A Acebrón, Luis L Bonilla, Conrad J Pérez Vicente, Félix Ritort, and Renato Spigler. The kuramoto model: A simple paradigm for synchronization phenomena. *Reviews of modern physics*, 77(1):137, 2005.

[65] Christian Bick, Marc Goodfellow, Carlo R Laing, and Erik Andreas Martens. Understanding the dynamics of biological and neural oscillator networks through mean-field reductions: A review. *arXiv preprint arXiv:1902.05307*, 2019.

[66] Steven H Strogatz and Renato E Mirollo. Collective synchronisation in lattices of nonlinear oscillators with randomness. *Journal of Physics A: Mathematical and General*, 21(13):L699, 1988.

[67] Steven H Strogatz and Renato E Mirollo. Phase-locking and critical phenomena in lattices of coupled nonlinear oscillators with random intrinsic frequencies. *Physica D: Nonlinear Phenomena*, 31(2):143–168, 1988.

[68] Kwok Yeung Tsang, Renato E Mirollo, Steven H Strogatz, and Kurt Wiesenfeld. Dynamics of a globally coupled oscillator array. *Physica D: Nonlinear Phenomena*, 48(1):102–112, 1991.

[69] Kurt Wiesenfeld, Pere Colet, and Steven H Strogatz. Frequency locking in josephson arrays: Connection with the kuramoto model. *Physical Review E*, 57(2):1563, 1998.

[70] Shinya Watanabe and Steven H Strogatz. Constants of motion for superconducting josephson arrays. *Physica D: Nonlinear Phenomena*, 74(3-4):197–253, 1994.

[71] James W Swift, Steven H Strogatz, and Kurt Wiesenfeld. Averaging of globally coupled oscillators. *Physica D: Nonlinear Phenomena*, 55(3-4):239–250, 1992.

[72] Edward Ott and Thomas M Antonsen. Long time evolution of phase oscillator systems. *Chaos: An interdisciplinary journal of nonlinear science*, 19(2):023117, 2009.

[73] Hidetsugu Sakaguchi. Cooperative phenomena in coupled oscillator systems under external fields. *Progress of theoretical physics*, 79(1):39–46, 1988.

[74] John David Crawford. Amplitude expansions for instabilities in populations of globally-coupled oscillators. *Journal of statistical physics*, 74(5-6):1047–1084, 1994.

[75] Yi Ming Lai and Mason A Porter. Noise-induced synchronization, desynchronization, and clustering in globally coupled nonidentical oscillators. *Physical Review E*, 88(1):012905, 2013.

[76] E Ott and BR Hunt. Tma jr.(2011), comment on long time evolution of phase oscillator systems [chaos 19, 023117 (2009)]. *Chaos: An Interdisciplinary Journal of Nonlinear Science*, 21(2):025–112.

[77] Bastian Pietras and Andreas Daffertshofer. Ott-antonsen attractiveness for parameter-dependent oscillatory systems. *Chaos: An Interdisciplinary Journal of Nonlinear Science*, 26(10):103101, 2016.

[78] Erik Andreas Martens, Ernest Barreto, Steven H Strogatz, Edward Ott, Paul So, and Thomas M Antonsen. Exact results for the kuramoto model with a bimodal frequency distribution. *Physical Review E*, 79(2):026204, 2009.

[79] Diego Pazó and Ernest Montbrió. Existence of hysteresis in the kuramoto model with bimodal frequency distributions. *Physical Review E*, 80(4):046215, 2009.

[80] Peter Ashwin, Christian Bick, and Oleksandr Burylko. Identical phase oscillator networks: bifurcations, symmetry and reversibility for generalized coupling. *Frontiers in Applied Mathematics and Statistics*, 2:7, 2016.

[81] Vladimir Vlasov, Michael Rosenblum, and Arkady Pikovsky. Dynamics of weakly inhomogeneous oscillator populations: perturbation theory on top of watanabe–strogatz integrability. *Journal of Physics A: Mathematical and Theoretical*, 49(31):31LT02, 2016.

[82] Renato E Mirollo. The asymptotic behavior of the order parameter for the infinite-n kuramoto model. *Chaos: An Interdisciplinary Journal of Nonlinear Science*, 22(4):043118, 2012.

[83] Wulfram Gerstner and Werner M Kistler. *Spiking neuron models: Single neurons, populations, plasticity*. Cambridge university press, 2002.

[84] Wolfgang Maass. Networks of spiking neurons: the third generation of neural network models. *Neural networks*, 10(9):1659–1671, 1997.

[85] Alan L Hodgkin and Andrew F Huxley. A quantitative description of membrane current and its application to conduction and excitation in nerve. *The Journal of physiology*, 117(4):500–544, 1952.

[86] Joaquin M Fuster. *Cortex and mind: Unifying cognition*. Oxford university press, 2003.

[87] Bard Ermentrout. Type i membranes, phase resetting curves, and synchrony. *Neural computation*, 8(5):979–1001, 1996.

[88] John Rinzel and G Bard Ermentrout. Analysis of neural excitability and oscillations. *Methods in neuronal modeling*, 2:251–292, 1998.

[89] G Bard Ermentrout and Nancy Kopell. Parabolic bursting in an excitable system coupled with a slow oscillation. *SIAM Journal on Applied Mathematics*, 46(2):233, 1986.

[90] Bard Ermentrout. Ermentrout-kopell canonical model. *Scholarpedia*, 3(3):1398, 2008.

[91] Christof Koch. *Biophysics of computation: information processing in single neurons*. Oxford university press, 2004.

[92] Peter Dayan and Laurence F Abbott. Theoretical neuroscience: computational and mathematical modeling of neural systems. 2001.

[93] Eric R Kandel, James H Schwartz, Thomas M Jessell, Department of Biochemistry, Molecular Biophysics Thomas Jessell, Steven Siegelbaum, and AJ Hudspeth. *Principles of neural science*, volume 4. McGraw-hill New York, 2000.

[94] Gabor Tamas, Eberhard H Buhl, and Peter Somogyi. Massive autaptic self-innervation of gabaergic neurons in cat visual cortex. *Journal of Neuroscience*, 17(16):6352–6364, 1997.

[95] Alberto Bacci, John R Huguenard, and David A Prince. Functional autaptic neurotransmission in fast-spiking interneurons: a novel form of feedback inhibition in the neocortex. *Journal of Neuroscience*, 23(3):859–866, 2003.

[96] Gyorgy Buzsaki. *Rhythms of the Brain*. Oxford University Press, 2006.

[97] György Buzsáki and Xiao-Jing Wang. Mechanisms of gamma oscillations. *Annual review of neuroscience*, 35:203–225, 2012.

[98] Pascal Fries, Danko Nikolić, and Wolf Singer. The gamma cycle. *Trends in neurosciences*, 30(7):309–316, 2007.

[99] Sylvain Williams and Patricia Boksa. Gamma oscillations and schizophrenia. *Journal of psychiatry & neuroscience: JPN*, 35(2):75, 2010.

[100] Marlene Bartos, Imre Vida, and Peter Jonas. Synaptic mechanisms of synchronized gamma oscillations in inhibitory interneuron networks. *Nature reviews neuroscience*, 8(1):45, 2007.

[101] Paul Tiesinga and Terrence J Sejnowski. Cortical enlightenment: are attentional gamma oscillations driven by ing or ping? *Neuron*, 63(6):727–732, 2009.

[102] Miles A Whittington, Roger D Traub, and John GR Jefferys. Synchronized oscillations in interneuron networks driven by metabotropic glutamate receptor activation. *Nature*, 373(6515):612–615, 1995.

[103] John Lisman. The theta/gamma discrete phase code occuring during the hippocampal phase precession may be a more general brain coding scheme. *Hippocampus*, 15(7):913–922, 2005.

[104] Laura Lee Colgin, Tobias Denninger, Marianne Fyhn, Torkel Hafting, Tora Bonnevie, Ole Jensen, May-Britt Moser, and Edvard I Moser. Frequency of gamma oscillations routes flow of information in the hippocampus. *Nature*, 462(7271):353, 2009.

[105] Mariano A Belluscio, Kenji Mizuseki, Robert Schmidt, Richard Kempter, and György Buzsáki. Cross-frequency phase–phase coupling between theta and gamma oscillations in the hippocampus. *Journal of Neuroscience*, 32(2):423–435, 2012.

[106] Alejandro Javier Pernía-Andrade and Peter Jonas. Theta-gamma-modulated synaptic currents in hippocampal granule cells in vivo define a mechanism for network oscillations. *Neuron*, 81(1):140–152, 2014.

[107] Laura Lee Colgin. Theta–gamma coupling in the entorhinal–hippocampal system. *Current opinion in neurobiology*, 31:45–50, 2015.

[108] Kevin Whittingstall and Nikos K Logothetis. Frequency-band coupling in surface eeg reflects spiking activity in monkey visual cortex. *Neuron*, 64(2):281–289, 2009.

[109] Ryan T Canolty, Erik Edwards, Sarang S Dalal, Maryam Soltani, Srikantan S Nagarajan, Heidi E Kirsch, Mitchel S Berger, Nicholas M Barbaro, and Robert T Knight. High gamma power is phase-locked to theta oscillations in human neocortex. *science*, 313(5793):1626–1628, 2006.

[110] Ryan T Canolty and Robert T Knight. The functional role of cross-frequency coupling. *Trends in cognitive sciences*, 14(11):506–515, 2010.

[111] John E Lisman and Ole Jensen. The theta-gamma neural code. *Neuron*, 77(6):1002–1016, 2013.

[112] Ole Jensen and Laura L Colgin. Cross-frequency coupling between neuronal oscillations. *Trends in cognitive sciences*, 11(7):267–269, 2007.

[113] Herbert Witte, Peter Putsche, Claudia Hemmelmann, Christoph Schelenz, and Lutz Leistritz. Analysis and modeling of time-variant amplitude–frequency couplings of and between oscillations of eeg bursts. *Biological Cybernetics*, 99(2):139–157, 2008.

[114] Mojtaba Chehelcheraghi, Cees van Leeuwen, Erik Steur, and Chie Nakatani. A neural mass model of cross frequency coupling. *PloS one*, 12(4), 2017.

[115] Alberto Mazzoni, Nicolas Brunel, Stefano Cavallari, Nikos K Logothetis, and Stefano Panzeri. Cortical dynamics during naturalistic sensory stimulations: experiments and models. *Journal of Physiology-Paris*, 105(1-3):2–15, 2011.

[116] Bradley Lega, John Burke, Joshua Jacobs, and Michael J Kahana. Slow-theta-to-gamma phase–amplitude coupling in human hippocampus supports the formation of new episodic memories. *Cerebral Cortex*, 26(1):268–278, 2016.

[117] P. Tass, M. G. Rosenblum, J. Weule, J. Kurths, A. Pikovsky, J. Volkmann, A. Schnitzler, and H.-J. Freund. Detection of $n : m$ phase locking from noisy data: Application to magnetoencephalography. *Phys. Rev. Lett.*, 81:3291–3294, Oct 1998.

[118] Thomas Akam, Iris Oren, Laura Mantoan, Emily Ferenczi, and Dimitri M Kullmann. Oscillatory dynamics in the hippocampus support dentate gyrus–ca3 coupling. *Nature neuroscience*, 15(5):763, 2012.

[119] Hugh Pastoll, Lukas Solanka, Mark CW van Rossum, and Matthew F Nolan. Feedback inhibition enables theta-nested gamma oscillations and grid firing fields. *Neuron*, 77(1):141–154, 2013.

[120] James L Butler, Y Audrey Hay, and Ole Paulsen. Comparison of three gamma oscillations in the mouse entorhinal–hippocampal system. *European Journal of Neuroscience*, 48(8):2795–2806, 2018.

[121] Anatol Bragin, Gábor Jandó, Zoltán Nádasdy, Jamille Hetke, K Wise, and Gy Buzsáki. Gamma (40-100 hz) oscillation in the hippocampus of the behaving rat. *Journal of Neuroscience*, 15(1):47–60, 1995.

[122] Wulfram Gerstner, Werner M. Kistler, Richard Naud, and Liam Paninski. *Neuronal Dynamics: From Single Neurons To Networks And Models Of Cognition*. Cambridge University Press, Cambridge, 2014.

[123] Federico Devalle, Alex Roxin, and Ernest Montbrió. Firing rate equations require a spike synchrony mechanism to correctly describe fast oscillations in inhibitory networks. *PLoS computational biology*, 13(12):e1005881, 2017.

[124] Carlo R Laing. Phase oscillator network models of brain dynamics. *Computational models of brain and behavior*, pages 505–517, 2017.

[125] Tanushree B Luke, Ernest Barreto, and Paul So. Complete classification of the macroscopic behavior of a heterogeneous network of theta neurons. *Neural computation*, 25(12):3207–3234, 2013.

[126] Carlo R Laing. Derivation of a neural field model from a network of theta neurons. *Physical Review E*, 90(1):010901, 2014.

[127] Paul So, Tanushree B Luke, and Ernest Barreto. Networks of theta neurons with time-varying excitability: Macroscopic chaos, multistability, and final-state uncertainty. *Physica D: Nonlinear Phenomena*, 267:16–26, 2014.

[128] Zachary P Kilpatrick. Wilson-cowan model. 2014.

[129] Angela CE Onslow, Matthew W Jones, and Rafal Bogacz. A canonical circuit for generating phase-amplitude coupling. *PloS one*, 9(8), 2014.

[130] Arkady Pikovsky and Antonio Politi. *Lyapunov exponents: a tool to explore complex dynamics*. Cambridge University Press, 2016.

[131] Giancarlo Benettin, Luigi Galgani, Antonio Giorgilli, and Jean-Marie Strelcyn. Lyapunov characteristic exponents for smooth dynamical systems and for hamiltonian systems; a method for computing all of them. part 1: Theory. *Meccanica*, 15(1):9–20, 1980.

[132] Willy Govaerts, Yuri A Kuznetsov, and Bart Sautois. Matcont. *Scholarpedia*, 1(9):1375, 2006.

[133] Alexandre Hyafil, Anne-Lise Giraud, Lorenzo Fontolan, and Boris Gutkin. Neural cross-frequency coupling: connecting architectures, mechanisms, and functions. *Trends in neurosciences*, 38(11):725–740, 2015.

[134] JJ Chrobak and G Buzsáki. Gamma oscillations in the entorhinal cortex of the freely behaving rat. *Journal of Neuroscience*, 18(1):388–398, 1998.

[135] Andrea Ceni, Simona Olmi, Alessandro Torcini, and David Angulo-Garcia. Cross frequency coupling in next generation inhibitory neural mass models. *arXiv preprint arXiv:1908.07954*, 2019.

[136] Robson Scheffer-Teixeira and Adriano BL Tort. On cross-frequency phase-phase coupling between theta and gamma oscillations in the hippocampus. *Elife*, 5:e20515, 2016.

[137] Akihiko Akao, Yutaro Ogawa, Yasuhiko Jimbo, G Bard Ermentrout, and Kiyoshi Kotani. Relationship between the mechanisms of gamma rhythm generation and the magnitude of the macroscopic phase response function in a population of excitatory and inhibitory modified quadratic integrate-and-fire neurons. *Physical Review E*, 97(1):012209, 2018.

[138] Grégory Dumont and Boris Gutkin. Macroscopic phase resetting-curves determine oscillatory coherence and signal transfer in inter-coupled neural circuits. *PLoS computational biology*, 15(5):e1007019, 2019.

[139] Grégory Dumont, G Bard Ermentrout, and Boris Gutkin. Macroscopic phase-resetting curves for spiking neural networks. *Physical Review E*, 96(4):042311, 2017.

[140] Omar J Ahmed and Mayank R Mehta. Running speed alters the frequency of hippocampal gamma oscillations. *Journal of Neuroscience*, 32(21):7373–7383, 2012.

[141] Alex Sheremet, JP Kennedy, Yu Qin, Yuchen Zhou, Sarah D Lovett, Sara N Burke, and Andrew P Maurer. Theta-gamma cascades and running speed. *Journal of neurophysiology*, 121(2):444–458, 2019.

[142] Gregory R Richard, Ali Titiz, Anna Tyler, Gregory L Holmes, Rod C Scott, and Pierre-Pascal Lenck-Santini. Speed modulation of hippocampal theta frequency correlates with spatial memory performance. *Hippocampus*, 23(12):1269–1279, 2013.

[143] Caroline Haimerl, David Angulo-Garcia, Vincent Villette, Susanne Reichinnek, Alessandro Torcini, Rosa Cossart, and Arnaud Malvache. Internal representation of hippocampal neuronal population spans a time-distance continuum. *Proceedings of the National Academy of Sciences*, 116(15):7477–7482, 2019.

[144] Urszula Sławińska and Stefan Kasicki. The frequency of rat's hippocampal theta rhythm is related to the speed of locomotion. *Brain research*, 796(1-2):327–331, 1998.

[145] Arkady Pikovsky and Michael Rosenblum. Dynamics of globally coupled oscillators: Progress and perspectives. *Chaos: An Interdisciplinary Journal of Nonlinear Science*, 25(9):097616, 2015.

[146] Yoshiki Kuramoto. *Chemical oscillations, waves, and turbulence*, volume 19. Springer Science & Business Media, 2012.

[147] Hyunsuk Hong, Hugues Chaté, Hyunggyu Park, and Lei-Han Tang. Entrainment transition in populations of random frequency oscillators. *Physical review letters*, 99(18):184101, 2007.

[148] Steven H Strogatz. From kuramoto to crawford: exploring the onset of synchronization in populations of coupled oscillators. *Physica D: Nonlinear Phenomena*, 143(1-4):1–20, 2000.

[149] Julien Barre and David Métivier. Bifurcations and singularities for coupled oscillators with inertia and frustration. *Physical review letters*, 117(21):214102, 2016.

[150] Pascal Fries, John H Reynolds, Alan E Rorie, and Robert Desimone. Modulation of oscillatory neuronal synchronization by selective visual attention. *Science*, 291(5508):1560–1563, 2001.

[151] Jürgen Fell, Peter Klaver, Klaus Lehnertz, Thomas Grunwald, Carlo Schaller, Christian E Elger, and Guillén Fernández. Human memory formation is accompanied by rhinal–hippocampal coupling and decoupling. *Nature neuroscience*, 4(12):1259, 2001.

[152] Andreas K Engel and Wolf Singer. Temporal binding and the neural correlates of sensory awareness. *Trends in cognitive sciences*, 5(1):16–25, 2001.

[153] Wilson Truccolo, Omar J Ahmed, Matthew T Harrison, Emad N Eskandar, G Rees Cosgrove, Joseph R Madsen, Andrew S Blum, N Stevenson Potter, Leigh R Hochberg, and Sydney S Cash. Neuronal ensemble synchrony during human focal seizures. *Journal of Neuroscience*, 34(30):9927–9944, 2014.

[154] N Kopell and GB Ermentrout. Mechanisms of phase-locking and frequency control in pairs of coupled neural oscillators. *Handbook of dynamical systems*, 2:3–54, 2002.

[155] Nicolas Brunel. Dynamics of sparsely connected networks of excitatory and inhibitory spiking neurons. *Journal of Computational Neuroscience*, 8(3):183–208, May 2000.

[156] Imre Vida, Marlene Bartos, and Peter Jonas. Shunting inhibition improves robustness of gamma oscillations in hippocampal interneuron networks by homogenizing firing rates. *Neuron*, 49(1):107–117, 2006.

[157] C. van Vreeswijk and H. Sompolinsky. Chaos in neuronal networks with balanced excitatory and inhibitory activity. *Science*, 274(5293):1724–1726, 1996.

[158] Alfonso Renart, Jaime de la Rocha, Peter Bartho, Liad Hollender, Néstor Parga, Alex Reyes, and Kenneth D. Harris. The asynchronous state in cortical circuits. *Science*, 327(5965):587–590, 2010.

[159] Ashok Litwin-Kumar and Brent Doiron. Slow dynamics and high variability in balanced cortical networks with clustered connections. *Nat Neurosci*, 15(11):1498–1505, 11 2012.

[160] Robert Rosenbaum and Brent Doiron. Balanced networks of spiking neurons with spatially dependent recurrent connections. *Physical Review X*, 4(2):021039, 2014.

[161] Jonathan Kadmon and Haim Sompolinsky. Transition to chaos in random neuronal networks. *Phys. Rev. X*, 5:041030, Nov 2015.

[162] Rune W Berg, Aidas Alaburda, and Jørn Hounsgaard. Balanced inhibition and excitation drive spike activity in spinal half-centers. *Science*, 315(5810):390–393, 2007.

[163] Jérémie Barral and Alex D Reyes. Synaptic scaling rule preserves excitatory–inhibitory balance and salient neuronal network dynamics. *Nature neuroscience*, 19(12):1690, 2016.

[164] Nicolas Brunel and Xiao-Jing Wang. What determines the frequency of fast network oscillations with irregular neural discharges? i. synaptic

dynamics and excitation-inhibition balance. *Journal of neurophysiology*, 90(1):415–430, 2003.

[165] Michael Monteforte and Fred Wolf. Dynamical entropy production in spiking neuron networks in the balanced state. *Phys. Rev. Lett.*, 105:268104, Dec 2010.

[166] Sven Jahnke, Raoul-Martin Memmesheimer, and Marc Timme. Stable irregular dynamics in complex neural networks. *Physical Review Letters*, 100(4):048102, 2008.

[167] Chenguang Zheng, Kevin Wood Bieri, Sean Gregory Trettel, and Laura Lee Colgin. The relationship between gamma frequency and running speed differs for slow and fast gamma rhythms in freely behaving rats. *Hippocampus*, 25(8):924–938, 2015.

[168] Kevin Wood Bieri, Katelyn N Bobbitt, and Laura Lee Colgin. Slow and fast gamma rhythms coordinate different spatial coding modes in hippocampal place cells. *Neuron*, 82(3):670–681, 2014.

[169] Chenguang Zheng, Kevin Wood Bieri, Yi-Tse Hsiao, and Laura Lee Colgin. Spatial sequence coding differs during slow and fast gamma rhythms in the hippocampus. *Neuron*, 89(2):398–408, 2016.

[170] Anton Sirota, Sean Montgomery, Shigeyoshi Fujisawa, Yoshikazu Isomura, Michael Zugaro, and György Buzsáki. Entrainment of neocortical neurons and gamma oscillations by the hippocampal theta rhythm. *Neuron*, 60(4):683–697, 2008.

[171] Laura Lee Colgin. Rhythms of the hippocampal network. *Nature Reviews Neuroscience*, 17(4):239, 2016.

[172] Erik W Schomburg, Antonio Fernández-Ruiz, Kenji Mizuseki, Antal Berényi, Costas A Anastassiou, Christof Koch, and György Buzsáki. Theta phase segregation of input-specific gamma patterns in entorhinal-hippocampal networks. *Neuron*, 84(2):470–485, 2014.

[173] Andre Fisahn, Fenella G Pike, Eberhard H Buhl, and Ole Paulsen. Cholinergic induction of network oscillations at 40 hz in the hippocampus in vitro. *Nature*, 394(6689):186, 1998.

[174] Roger D Traub, Mark O Cunningham, T Gloveli, Fiona EN LeBeau, A Bibbig, EH Buhl, and MA Whittington. Gaba-enhanced collective behavior in neuronal axons underlies persistent gamma-frequency oscillations. *Proceedings of the National Academy of Sciences*, 100(19):11047–11052, 2003.

[175] Alexander NJ Pietersen, Peter D Ward, Nicholas Hagger-Vaughan, James Wiggins, John GR Jefferys, and Martin Vreugdenhil. Transition between fast and slow gamma modes in rat hippocampus area ca1 in vitro is modulated by slow ca3 gamma oscillations. *The Journal of physiology*, 592(4):605–620, 2014.

[176] Michael T Craig and Chris J McBain. Fast gamma oscillations are generated intrinsically in ca1 without the involvement of fast-spiking basket cells. *Journal of Neuroscience*, 35(8):3616–3624, 2015.

[177] Stephen Keeley, André A Fenton, and John Rinzel. Modeling fast and slow gamma oscillations with interneurons of different subtype. *Journal of neurophysiology*, 117(3):950–965, 2016.

[178] Stephen Keeley, Áine Byrne, André Fenton, and John Rinzel. Firing rate models for gamma oscillations. *Journal of neurophysiology*, 121(6):2181–2190, 2019.

[179] Alfonso Renart, Rubén Moreno-Bote, Xiao-Jing Wang, and Néstor Parga. Mean-driven and fluctuation-driven persistent activity in recurrent networks. *Neural computation*, 19(1):1–46, 2007.

[180] David Angulo-Garcia, Stefano Luccioli, Simona Olmi, and Alessandro Torcini. Death and rebirth of neural activity in sparse inhibitory networks. *New Journal of Physics*, 19(5):053011, 2017.

[181] Diego Pazó and Ernest Montbrió. From quasiperiodic partial synchronization to collective chaos in populations of inhibitory neurons with delay. *Physical review letters*, 116(23):238101, 2016.

[182] B. Ermentrout. XPPAUT. *Scholarpedia*, 2(1):1399, 2007. revision #136177.

[183] Günther Sperk, Sabine Furtinger, Christoph Schwarzer, and Susanne Pirker. Gaba and its receptors in epilepsy. In *Recent advances in epilepsy research*, pages 92–103. Springer, 2004.

[184] Marco I González, Heidi L Grabenstatter, Christian A Cea-Del Rio, Yasmin Cruz Del Angel, Jessica Carlsen, Rick P Laoprasert, Andrew M White, Molly M Huntsman, and Amy Brooks-Kayal. Seizure-related regulation of gabaa receptors in spontaneously epileptic rats. *Neurobiology of disease*, 77:246–256, 2015.

[185] R Dickinson, S Awaiz, MA Whittington, WR Lieb, and NP Franks. The effects of general anaesthetics on carbachol-evoked gamma oscillations in the rat hippocampus in vitro. *Neuropharmacology*, 44(7):864–872, 2003.

[186] David A McCormick and David A Prince. Two types of muscarinic response to acetylcholine in mammalian cortical neurons. *Proceedings of the National Academy of Sciences*, 82(18):6344–6348, 1985.

[187] Charles J Frazier, Amber V Buhler, Jeffrey L Weiner, and Thomas V Dunwiddie. Synaptic potentials mediated via α-bungarotoxin-sensitive nicotinic acetylcholine receptors in rat hippocampal interneurons. *Journal of Neuroscience*, 18(20):8228–8235, 1998.

[188] Ryan Pyle and Robert Rosenbaum. Highly connected neurons spike less frequently in balanced networks. *Physical Review E*, 93(4):040302, 2016.

[189] Itamar D Landau, Robert Egger, Vincent J Dercksen, Marcel Oberlaender, and Haim Sompolinsky. The impact of structural heterogeneity on excitation-inhibition balance in cortical networks. *Neuron*, 92(5):1106–1121, 2016.

[190] Simona Olmi, Antonio Politi, and Alessandro Torcini. Stability of the splay state in networks of pulse-coupled neurons. *The Journal of Mathematical Neuroscience*, 2(1):12, 2012.

[191] RA Nicoll, JC Eccles, T Oshima, and F Rubia. Prolongation of hippocampal inhibitory postsynaptic potentials by barbiturates. *Nature*, 258(5536):625, 1975.

[192] Roger D Traub, Nelson Spruston, Ivan Soltesz, Arthur Konnerth, Miles A Whittington, and John GR Jefferys. Gamma-frequency oscillations: a neuronal population phenomenon, regulated by synaptic and intrinsic cellular processes, and inducing synaptic plasticity. *Progress in neurobiology*, 55(6):563–575, 1998.

[193] Anne E Campbell, Petroc Sumner, Krish D Singh, and Suresh D Muthukumaraswamy. Acute effects of alcohol on stimulus-induced gamma oscillations in human primary visual and motor cortices. *Neuropsychopharmacology*, 39(9):2104, 2014.

[194] György Buzsáki. Theta oscillations in the hippocampus. *Neuron*, 33(3):325–340, 2002.

[195] Paul L Nunez, Ramesh Srinivasan, et al. *Electric fields of the brain: the neurophysics of EEG*. Oxford University Press, USA, 2006.

[196] Greg A. Worrell, Landi Parish, Stephen D. Cranstoun, Rachel Jonas, Gordon Baltuch, and Brian Litt. High frequency oscillations and seizure generation in neocortical epilepsy. *Brain*, 127(7):1496–1506, 07 2004.

[197] Ekkehard Ullner and Antonio Politi. Self-sustained irregular activity in an ensemble of neural oscillators. *Physical Review X*, 6(1):011015, 2016.

[198] Alexandra J Mably and Laura Lee Colgin. Gamma oscillations in cognitive disorders. *Current opinion in neurobiology*, 52:182–187, 2018.

[199] Ashwini Oswal, Peter Brown, and Vladimir Litvak. Synchronized neural oscillations and the pathophysiology of parkinson's disease. *Current opinion in neurology*, 26(6):662–670, 2013.

[200] Joel S Perlmutter and Jonathan W Mink. Deep brain stimulation. *Annu. Rev. Neurosci.*, 29:229–257, 2006.

[201] Sorin Breit, Jörg B Schulz, and Alim-Louis Benabid. Deep brain stimulation. *Cell and tissue research*, 318(1):275–288, 2004.

[202] Coralie De Hemptinne, Nicole C Swann, Jill L Ostrem, Elena S Ryapolova-Webb, Marta San Luciano, Nicholas B Galifianakis, and

Philip A Starr. Therapeutic deep brain stimulation reduces cortical phase-amplitude coupling in parkinson's disease. *Nature neuroscience*, 18(5):779, 2015.

[203] Peter A Tass. Desynchronization of brain rhythms with soft phase-resetting techniques. *Biological cybernetics*, 87(2):102–115, 2002.

[204] Oleksandr V Popovych, Christian Hauptmann, and Peter A Tass. Effective desynchronization by nonlinear delayed feedback. *Physical review letters*, 94(16):164102, 2005.

[205] Russell J Andrews. Neuromodulation: advances in the next five years. *Annals of the New York Academy of Sciences*, 1199(1):204–211, 2010.

[206] Viktor K Jirsa, William C Stacey, Pascale P Quilichini, Anton I Ivanov, and Christophe Bernard. On the nature of seizure dynamics. *Brain*, 137(8):2210–2230, 2014.

[207] Leslie M Kay. Two species of gamma oscillations in the olfactory bulb: dependence on behavioral state and synaptic interactions. *Journal of integrative neuroscience*, 2(01):31–44, 2003.

[208] Matthijs AA Van Der Meer and A David Redish. Low and high gamma oscillations in rat ventral striatum have distinct relationships to behavior, reward, and spiking activity on a learned spatial decision task. *Frontiers in integrative neuroscience*, 3:9, 2009.

[209] Andre Moraes Bastos, Julien Vezoli, Conrado Arturo Bosman, Jan-Mathijs Schoffelen, Robert Oostenveld, Jarrod Robert Dowdall, Peter De Weerd, Henry Kennedy, and Pascal Fries. Visual areas exert feedforward and feedback influences through distinct frequency channels. *Neuron*, 85(2):390–401, 2015.

[210] Caroline Geisler, Nicolas Brunel, and Xiao-Jing Wang. Contributions of intrinsic membrane dynamics to fast network oscillations with irregular neuronal discharges. *Journal of neurophysiology*, 94(6):4344–4361, 2005.

[211] Balázs Hangya, Zsolt Borhegyi, Nóra Szilágyi, Tamás F Freund, and Viktor Varga. Gabaergic neurons of the medial septum lead the hippocampal network during theta activity. *Journal of Neuroscience*, 29(25):8094–8102, 2009.

[212] Federico Devalle, Ernest Montbrió, and Diego Pazó. Dynamics of a large system of spiking neurons with synaptic delay. *Physical Review E*, 98(4):042214, 2018.

[213] György Buzsáki. Hippocampal sharp wave-ripple: A cognitive biomarker for episodic memory and planning. *Hippocampus*, 25(10):1073–1188, 2015.

[214] Gianmaria Maccaferri and Jean-Claude Lacaille. Interneuron diversity series: Hippocampal interneuron classifications–making things as simple as possible, not simpler. *Trends in neurosciences*, 26(10):564–571, 2003.

[215] Philipp Thomas, Arthur V Straube, Jens Timmer, Christian Fleck, and Ramon Grima. Signatures of nonlinearity in single cell noise-induced oscillations. *Journal of Theoretical Biology*, 335:222–234, 2013.

[216] Rachel Kuske, Luis F Gordillo, and Priscilla Greenwood. Sustained oscillations via coherence resonance in sir. *Journal of theoretical biology*, 245(3):459–469, 2007.

[217] AF Rozenfeld, CJ Tessone, E Albano, and HS Wio. On the influence of noise on the critical and oscillatory behavior of a predator–prey model: coherent stochastic resonance at the proper frequency of the system. *Physics Letters A*, 280(1-2):45–52, 2001.

[218] OV Ushakov, H-J Wünsche, F Henneberger, IA Khovanov, Lutz Schimansky-Geier, and MA Zaks. Coherence resonance near a hopf bifurcation. *Physical review letters*, 95(12):123903, 2005.

[219] José MG Vilar, Hao Yuan Kueh, Naama Barkai, and Stanislas Leibler. Mechanisms of noise-resistance in genetic oscillators. *Proceedings of the National Academy of Sciences*, 99(9):5988–5992, 2002.

[220] Duccio Fanelli, Francesco Ginelli, Roberto Livi, Niccoló Zagli, and Clement Zankoc. Noise-driven neuromorphic tuned amplifier. *Physical Review E*, 96(6):062313, 2017.

[221] D. Golomb. Neuronal synchrony measures. *Scholarpedia*, 2(1):1347, 2007.

[222] Henry Clavering Tuckwell. *Introduction to theoretical neurobiology. Vol. 1, Linear cable theory and dendritic structure*. Cambridge University Press, 1988.

[223] Martin Paul Nawrot. Analysis and interpretation of interval and count variability in neural spike trains. In *Analysis of parallel spike trains*, pages 37–58. Springer, 2010.

[224] Farzad Farkhooi and Wilhelm Stannat. Complete mean-field theory for dynamics of binary recurrent networks. *Physical review letters*, 119(20):208301, 2017.

[225] Matteo di Volo and Alain Destexhe. Optimal responsiveness and collective oscillations emerging from the heterogeneity of inhibitory neurons. *arXiv preprint arXiv:2005.05596*, 2020.

[226] Marcel A Just and Patricia A Carpenter. A capacity theory of comprehension: individual differences in working memory. *Psychological review*, 99(1):122, 1992.

[227] Patricia S Goldman-Rakic. Cellular basis of working memory. *Neuron*, 14(3):477–485, 1995.

[228] Randall W Engle, Stephen W Tuholski, James E Laughlin, and Andrew RA Conway. Working memory, short-term memory, and general fluid intelligence: a latent-variable approach. *Journal of experimental psychology: General*, 128(3):309, 1999.

[229] Gianluigi Mongillo, Omri Barak, and Misha Tsodyks. Synaptic theory of working memory. *Science*, 319(5869):1543–1546, 2008.

[230] Halgurd Taher, Alessandro Torcini, and Simona Olmi. Exact neural mass model for synaptic-based working memory. *bioRxiv*, 2020.

[231] Sami El Boustani and Alain Destexhe. A master equation formalism for macroscopic modeling of asynchronous irregular activity states. *Neural computation*, 21(1):46–100, 2009.

[232] Yann Zerlaut, Sandrine Chemla, Frederic Chavane, and Alain Destexhe. Modeling mesoscopic cortical dynamics using a mean-field model of conductance-based networks of adaptive exponential integrate-and-fire neurons. *Journal of computational neuroscience*, 44(1):45–61, 2018.

[233] Matteo Di Volo, Alberto Romagnoni, Cristiano Capone, and Alain Destexhe. Biologically realistic mean-field models of conductance-based networks of spiking neurons with adaptation. *Neural computation*, 31(4):653–680, 2019.

[234] Aleksandr Aleksandrovich Andronov. *Theory of bifurcations of dynamic systems on a plane*, volume 554. Israel Program for Scientific Translations;[available from the US Dept. of ?, 1971.

[235] Yuri A Kuznetsov. *Elements of applied bifurcation theory*, volume 112. Springer Science & Business Media, 2013.